

AD-A250 182

1



**THE STRUCTURE AND ENERGETICS OF AMAZON SQUALL LINES**

Harold Lloyd Massie, Jr.  
Madison Heights, Virginia

**DTIC**  
**ELECTE**  
**MAY 7 1992**  
**S C D**

B.S., Lynchburg College, 1973  
M.S., University of Virginia, 1984

A Dissertation Presented to the Graduate  
Faculty of the University of Virginia  
in Candidacy for the Degree of  
Doctor of Philosophy

Department of Environmental Sciences

University of Virginia  
August 1991

Michael Garstang  
Major Advisor

Bruce P. Hayden

Henry H. Shugart

Jeffrey B. Morton

**DISTRIBUTION STATEMENT A**  
Approved for public release;  
Distribution Unlimited

92 5 01 007

92-11925



REPORT DOCUMENTATION PAGE			Form Approved OMB No. 0704-0188	
Public reporting burden for this collection of information is estimated to average 1 hour per response, including the time for reviewing instructions, searching existing data sources, gathering and maintaining the data needed, and completing and reviewing the collection of information. Send comments regarding this burden estimate or any other aspect of this collection of information, including suggestions for reducing this burden, to Washington Headquarters Services, Directorate for Information Operations and Reports, 1215 Jefferson Davis Highway, Suite 1204, Arlington, VA 22202-4302, and to the Office of Management and Budget, Paperwork Reduction Project (0704-0188), Washington, DC 20503.				
1. AGENCY USE ONLY (Leave blank)	2. REPORT DATE August 1991	3. REPORT TYPE AND DATES COVERED <del>XXXXX</del> DISSERTATION		
4. TITLE AND SUBTITLE The Structure and Energetics of Amazon Squall Lines			5. FUNDING NUMBERS	
6. AUTHOR(S) Harold L. Massie, Jr., Major				
7. PERFORMING ORGANIZATION NAME(S) AND ADDRESS(ES) AFIT Student Attending: University of Virginia			8. PERFORMING ORGANIZATION REPORT NUMBER AFIT/CI/CIA-91-027D	
9. SPONSORING / MONITORING AGENCY NAME(S) AND ADDRESS(ES) AFIT/CI Wright-Patterson AFB OH 45433-6583			10. SPONSORING / MONITORING AGENCY REPORT NUMBER	
11. SUPPLEMENTARY NOTES				
12a. DISTRIBUTION / AVAILABILITY STATEMENT Approved for Public Release IAW 190-1 Distributed Unlimited ERNEST A. HAYGOOD, Captain, USAF Executive Officer			12b. DISTRIBUTION CODE	
13. ABSTRACT (Maximum 200 words)				
14. SUBJECT TERMS			15. NUMBER OF PAGES 194	
			16. PRICE CODE	
17. SECURITY CLASSIFICATION OF REPORT	18. SECURITY CLASSIFICATION OF THIS PAGE	19. SECURITY CLASSIFICATION OF ABSTRACT	20. LIMITATION OF ABSTRACT	

**THE STRUCTURE AND ENERGETICS OF AMAZON SQUALL LINES**

Harold Lloyd Massie, Jr.

**ABSTRACT**

The role of the Amazon Basin as a global center of action for deep convection is quantified in the context of the planet's heat balance. Mesoscale heat and moisture budgets are presented for three synoptic-scale coastal originating systems (COS) over the Amazon Basin during the 1987 wet season. The budgets are obtained from volumetric analyses of mesoscale rawinsonde data from the April-May 1987 Amazon Boundary Layer Experiment (ABLE-2B).

Classification of cloud and rainfall components is based on data from Portable Automated Mesonet (PAM) towers, GOES images, and radar. Satellite measurements of the total active cloud area, coupled with the mesoscale budget calculations, are used to determine the system-wide vertical transport of heat as a function of the COS life cycle.

Maximum heat transport occurs in the COS mature stage when the system has its maximum spatial extent. The instantaneous heat transport for the 300-100 mb layer in a mature COS equals nearly 20% of the theoretical heat export requirement for the equatorial trough zone. A little more than half of the system-wide transport occurs in the dynamically active anvil cloud.

Session For	
IS 0101	
CO 248	
Announced	
Justification	
By	
Distribution/	
Availability Code	
Dist	Avail and/or Special
A-1	



**DEDICATION**

To my wife Donna and children Courtney, Emily, and  
Mary Ellen for their love, support, and patience.

## ACKNOWLEDGEMENTS

The Air Force Institute of Technology has sponsored my doctoral program at the University of Virginia. This work would not have been possible without the support of Cols. Gary Zeigler, Bob Dumont, and Jim Sands and Lt. Col. Cliff Matsumoto, who made it possible for me to participate in the field phase of ABLE-2B.

I am grateful to Jeff Halverson for his assistance in reducing the rawinsonde data and for offering valuable comments on the results.

I deeply appreciate the encouragement and support of my major advisor Mike Garstang and thank him for inviting me to participate in ABLE-2B. I thank the members of my committee, especially Bruce Hayden and George Hornberger, for their critical reviews which noticeably improved the presentation of these results.

Rich Kochendarfer, my friend and former colleague at the Babcock & Wilcox Company, helped me prepare the numerous figures. I would like to thank Professor Julius Sigler of Lynchburg College for many helpful discussions during the course of this work.

Grants awarded by the National Aeronautics and Space Administration to the University of Virginia supported this work.

## TABLE OF CONTENTS

	Page
ABSTRACT.....	ii
DEDICATION.....	iii
ACKNOWLEDGEMENTS.....	iv
CONTENTS.....	v
LIST OF FIGURES.....	vii
LIST OF TABLES.....	xvii
CHAPTER 1: INTRODUCTION.....	1
CHAPTER 2: DATA SOURCES.....	5
A: General.....	5
B. Portable Automated Mesonetwork (PAM).....	8
C. Rawinsonde.....	9
D. Satellite.....	10
E. Radar.....	11
CHAPTER 3: METHODS OF ANALYSIS.....	12
A. Data Classification.....	12
B. Heat and Moisture Budgets.....	14
C. Divergence and Vertical Velocity.....	16
D. Storage and Advection.....	18
E. Radiational Heating and Cooling.....	19
CHAPTER 4: CASE STUDIES.....	25
A. Weakening COS, 26 April 1987.....	25
B. Mature COS, 1 May 1987.....	66
C. Regenerating COS, 6 May 1987.....	98
D. Fair Weather Cumulus, 4 May 1987.....	131

	vi
CHAPTER 5: APPRAISAL OF RESULTS.....	165
A. COS Life Cycle.....	165
B. Kinematic and Thermodynamic Structure.....	168
C. Energy Transfer Characterisitcs.....	172
CHAPTER 6: SUMMARY AND CONNCLUSIONS.....	180
REFERENCES.....	186

## LIST OF FIGURES

		Page
Figure 1:	The ABLE-2B basin-scale network .....	6
Figure 2:	The ABLE-2B mesoscale triangle network .....	7
Figure 3:	The GOES full disk IR image at 2100 UTC, 25 April 1987.....	26
Figure 4:	The GOES MB-enhanced IR image at 2000 UTC, 25 April 1987.....	27
Figure 5:	The GOES full disk IR image at 1800 UTC, 26 April 1987.....	28
Figure 6:	The GOES full disk IR image at 0300 UTC, 27 April 1987.....	29
Figure 7:	The GOES MB-enhanced IR image at 1400 UTC, 26 April 1987.....	31
Figure 8:	CAPPI radar scan of building cumulus in the mesoscale network at 1530 UTC, 26 April 1987	32
Figure 9:	CAPPI radar scan of squall line in the meso- scale network at 1644 UTC, 26 April 1987....	34
Figure 10:	PAM time series of total rainfall on 26 April 1987.....	35
Figure 11:	PAM time series of rainfall rate on 26 April 1987.....	36
Figure 12:	PAM time series of peak winds on 26 April 1987.....	37
Figure 13:	PAM time series of $p$ on 26 April 1987.....	38

## List of Figures (cont.)

	Page
Figure 14: PAM time series of $T$ on 26 April 1987.....	39
Figure 15: PAM time series of $q$ on 26 April 1987.....	40
Figure 16: PAM time series of $\theta_e$ on 26 April 1987.....	41
Figure 17: PAM time series of $u$ on 26 April 1987.....	42
Figure 18: PAM time series of $v$ on 26 April 1987.....	43
Figure 19: CAPPI radar scan of COS squall line in the mesoscale network at 1750 UTC, 26 April 1987.....	44
Figure 20: Vertical time cross section of $u$ in the mesoscale network on 26 April 1987.....	46
Figure 21: Vertical time cross section of $v$ in the mesoscale network on 26 April 1987.....	47
Figure 22: Vertical time cross section of $\theta_e$ in the mesoscale network on 26 April 1987.....	48
Figure 23: Vertical time cross section of divergence in the mesoscale network on 26 April 1987...	49
Figure 24: Vertical time cross section of $\omega$ in the mesoscale network on 26 April 1987.....	50
Figure 25: Vertical time cross section of relative humidity in the mesoscale network on 26 April 1987.....	52
Figure 26: Apparent sensible heat source in the mesoscale network at 1500 UTC, 26 April 1987.....	53

## List of Figures (cont.)

	Page
Figure 27: Apparent moisture sink in the mesoscale network at 1500 UTC, 26 April 1987.....	54
Figure 28: Rate of temperature change in the mesoscale network due to longwave radiation at 1500 UTC, 26 April 1987.....	56
Figure 29: Rate of temperature change in the mesoscale network due to shortwave radiation at 1500 UTC, 26 April 1987.....	57
Figure 30: Vertical eddy flux of total heat in the mesoscale network at 1500 UTC, 26 April 1987	58
Figure 31: Apparent sensible heat source in the mesoscale network at 1800 UTC, 26 April 1987	60
Figure 32: Apparent moisture sink in the mesoscale network at 1800 UTC, 26 April 1987.....	61
Figure 33: Rate of temperature change in the mesoscale network due to longwave radiation at 1800 UTC, 26 April 1987.....	62
Figure 34: Rate of temperature change in the mesoscale network due to shortwave radiation at 1800 UTC, 26 April 1987.....	63
Figure 35: Vertical eddy flux of total heat in the mesoscale network at 1800 UTC, 26 April 1987	64
Figure 36: The GOES full disk IR image at 1800 UTC, 30 April 1987.....	67

## List of Figures (cont.)

	Page
Figure 37: The GOES MB-enhanced IR image at 1700 UTC, 30 April 1987.....	68
Figure 38: The GOES MB-enhanced IR image at 2130 UTC, 30 April 1987.....	69
Figure 39: The GOES MB-enhanced IR image at 0230 UTC, 1 May 1987.....	71
Figure 40: PAM time series of $\theta_e$ on 1 May 1987.....	72
Figure 41: Vertical time cross section of $u$ in the mesoscale network on 1 May 1987.....	73
Figure 42: Vertical time cross section of $v$ in the mesoscale network on 1 May 1987.....	74
Figure 43: Vertical time cross section of relative humidity in the mesoscale network on 1 May 1987.....	75
Figure 44: Vertical time cross section of $\theta_e$ in the mesoscale network on 1 May 1987.....	76
Figure 45: PAM time series of total rainfall on 1 May 1987.....	77
Figure 46: PAM time series of peak winds on 1 May 1987.	79
Figure 47: PAM time series of $u$ on 1 May 1987.....	80
Figure 48: PAM time series of $v$ on 1 May 1987.....	81
Figure 49: Vertical time cross section of divergence in the mesoscale network on 1 May 1987.....	83

## List of Figures (cont.)

	Page
Figure 50: Vertical time cross section of $\omega$ in the mesoscale network on 1 May 1987.....	85
Figure 51: Apparent sensible heat source in the mesoscale network at 1200 UTC, 1 May 1987.....	86
Figure 52: Apparent moisture sink in the mesoscale network at 1200 UTC, 1 May 1987.....	88
Figure 53: Rate of temperature change due to longwave radiation in the mesoscale network at 1200 UTC, 1 May 1987.....	89
Figure 54: Rate of temperature change due to shortwave radiation in the mesoscale network at 1200 UTC, 1 May 1987.....	90
Figure 55: Vertical eddy flux of total heat in the mesoscale network at 1200 UTC, 1 May 1987...	91
Figure 56: Apparent sensible heat source in the mesoscale network at 1800 UTC, 1 May 1987.....	93
Figure 57: Apparent moisture sink in the mesoscale network at 1800 UTC, 1 May 1987.....	94
Figure 58: Rate of temperature change in the mesoscale network due to longwave radiation at 1800 UTC, 1 May 1987.....	95
Figure 59: Rate of temperature change in the mesoscale network due to shortwave radiation at 1800 UTC, 1 May 1987.....	96

## List of Figures (cont.)

	Page
Figure 60: Vertical eddy flux of total heat in the mesoscale network at 1800 UTC, 1 May 1987...	97
Figure 61: The GOES full disk IR image at 1100 UTC, 6 May 1987.....	99
Figure 62: The GOES full disk IR image at 1500 UTC, 6 May 1987.....	100
Figure 63: The GOES MB-enhanced IR image at 1900 UTC, 6 May 1987.....	101
Figure 64: CAPPI radar scan of the COS convective component in the mesoscale network at 1528 UTC, 6 May 1987.....	102
Figure 65: PAM time series of total rainfall on 6 May 1987.....	104
Figure 66: PAM time series of rainfall rate on 6 May 1987.....	105
Figure 67: PAM time series of $T$ on 6 May 1987.....	106
Figure 68: PAM time series of $q$ on 6 May 1987.....	107
Figure 69: PAM time series of peak winds on 6 May 1987.	108
Figure 70: PAM time series of $u$ on 6 May 1987.....	109
Figure 71: PAM time series of $v$ on 6 May 1987.....	110
Figure 72: PAM time series of $p$ on 6 May 1987.....	111
Figure 73: PAM time series of $\theta_e$ on 6 May 1987.....	112
Figure 74: Vertical time cross section of $u$ in the mesoscale network on 6 May 1987.....	114

## List of Figures (cont.)

	Page
Figure 75: Vertical time cross section of $v$ in the mesoscale network on 6 May 1987.....	115
Figure 76: Vertical time cross section of $\theta_e$ in the mesoscale network on 6 May 1987.....	116
Figure 77: Vertical time cross section of divergence in the mesoscale triangle on 6 May 1987.....	117
Figure 78: Vertical time cross section of $\omega$ in the mesoscale network on 6 May 1987.....	118
Figure 79: Vertical time cross section of relative humidity in the mesoscale network on 6 May 1987.....	119
Figure 80: Apparent sensible heat source in the mesoscale network at 1500 UTC, 6 May 1987.....	121
Figure 81: Apparent moisture sink in the mesoscale network at 1500 UTC, 6 May 1987.....	122
Figure 82: Rate of temperature change in the mesoscale network due to longwave radiation at 1500 UTC, 6 May 1987.....	123
Figure 83: Rate of temperature change in the mesoscale network due to shortwave radiation at 1500 UTC, 6 May 1987.....	124
Figure 84: Vertical eddy flux of total heat in the mesoscale network at 1500 UTC, 6 May 1987...	125

## List of Figures (cont.)

	Page
Figure 85: Apparent sensible heat source in the meso- scale network at 1800 UTC, 6 May 1987.....	126
Figure 86: Apparent moisture source in the mesoscale network at 1800 UTC, 6 May 1987.....	127
Figure 87: Rate of temperature change in the mesoscale network due to longwave radiation at 1800 UTC, 6 May 1987.....	128
Figure 88: Rate of temperature change in the mesoscale network due to shortwave radiation at 1800 UTC, 6 May 1987.....	129
Figure 89: Vertical eddy flux of total heat in the mesoscale network at 1800 UTC, 6 May 1987...	130
Figure 90: The GOES full disk IR image at 1200 UTC, 4 May 1987.....	132
Figure 91: The GOES full disk IR image at 1731 UTC, 4 May 1987.....	133
Figure 92: The GOES .5 NM resolution visible image at 1230 UTC, 4 May 1987.....	134
Figure 93: The GOES .5 NM resolution visible image at 1731 UTC, 4 May 1987.....	135
Figure 94: PAM time series of $u$ on 4 May 1987.....	137
Figure 95: PAM time series of $v$ on 4 May 1987.....	138
Figure 96: PAM time series of peak winds on 4 May 1987.	139
Figure 97: PAM time series of $q$ on 4 May 1987.....	140

## List of Figures (cont.)

	Page
Figure 98: PAM time series of $T$ on 4 May 1987.....	141
Figure 99: PAM time series of $\theta_e$ on 4 May 1987.....	142
Figure 100: Profile of $u$ in the mesoscale network at 1200 UTC, 4 May 1987.....	144
Figure 101: Profile of $u$ in the mesoscale network at 1800 UTC, 4 May 1987.....	145
Figure 102: Profile of $v$ in the mesoscale network at 1200 UTC, 4 May 1987.....	146
Figure 103: Profile of $v$ in the mesoscale network at 1800 UTC, 4 May 1987.....	147
Figure 104: Profile of $\theta_e$ in the mesoscale network at 1200 UTC, 4 May 1987.....	148
Figure 105: Profile of $\theta_e$ in the mesoscale network at 1800 UTC, 4 May 1987.....	149
Figure 106: Relative humidity profile in the mesoscale network at 1200 UTC, 4 May 1987.....	150
Figure 107: Relative humidity profile in the mesoscale network at 1800 UTC, 4 May 1987.....	151
Figure 108: Divergence profile in the mesoscale network at 1200 UTC, 4 May 1987.....	153
Figure 109: Vertical velocity profile in the mesoscale network at 1800 UTC, 4 May 1987.....	154
Figure 110: Divergence profile in the mesoscale network at 1800 UTC, 4 May 1987.....	155

## List of Figures (cont.)

	Page
Figure 111: Vertical velocity profile in the mesoscale network at 1800 UTC, 4 May 1987.....	156
Figure 112: Apparent sensible heat source in the mesoscale network at 1200 UTC, 4 May 1987.....	157
Figure 113: Apparent moisture sink in the mesoscale network at 1200 UTC, 4 May 1987.....	158
Figure 114: Vertical eddy flux of total heat in the mesoscale network at 1200 UTC, 4 May 1987..	159
Figure 115: Apparent sensible heat source in the mesoscale network at 1800 UTC, 4 May 1987.....	161
Figure 116: Apparent moisture sink in the mesoscale network at 1800 UTC, 4 May 1987.....	162
Figure 117: Vertical eddy flux of total heat in the mesoscale network at 1800 UTC, 4 May 1987..	163

LIST OF TABLES

	Page
Table 1: ABLE-2B weather classification criteria.....	14
Table 2: Vertical transport of total heat in COS cloud components based on vertical integration of $F$ for five ABLE-2B cases.....	173
Table 3: Total heat transport in a mature COS over the central Amazon basin on 1 May 1987.....	176
Table 4: Total heat transport in a weakening COS over the central Amazon basin on 1 May 1987.....	176
Table 5: Total heat transport in a regenerating COS over the central Amazon basin on 1 May 1987...	176
Table 6: The COS vertical heat transport in the 300-100 mb upper-level outflow layer as a percentage of the equatorial heat export requirement.....	177
Table 7: The GOES analysis of equatorial trough con- vective activity from 12 April-9 May 1987....	178

**CHAPTER 1**  
**INTRODUCTION**

Amazon squall lines of coastal origin (Molion, 1987), described as "Coastal Occurring Systems" (COS) by Greco et al. (1990), rank among the largest and most frequent synoptic tropical disturbances. They often reach a length of 3500 km (Greco et al., 1990) with 500-1000 km being active deep convection.

This study evaluates mesoscale heat transport associated with three COS sampled during the April-May 1987 Amazon Boundary Layer Experiment (ABLE-2B) (Harris et al., 1990). The transport is extrapolated to the synoptic scale with a simple model developed from analysis of images from the Geosynchronous Operational Environmental Satellite (GOES). It is found that a mature COS provides substantial heat for upper level export from the Amazon Basin. It will be shown that the upper level heating by COS has global importance compared to the equatorial heat balance requirements (Riehl and Malkus, 1958).

While Riehl and Malkus (1958) invoke the "hot tower" hypothesis to account for the needed upward transfer of heat from the lower to upper atmosphere, they do not require the convective towers to be concentrated within specific regions of the tropics. They state that the required transport occurs in 1500-5000 giant clouds active at once and distrib-

uted in approximately 30 synoptic-scale disturbances located throughout tropics.

The Amazon Basin plays a recognized role as a global "center of action" for thunderstorms (Newell et al., 1972) with the storms often concentrated in synoptic disturbances (Molion, 1987; Kousky, 1981; Greco et al., 1990). Until now, insufficient rawinsonde and other measurements from the vast, relatively inaccessible Brazilian rain forests have precluded a definitive treatment of COS structure and energetics.

This study uses intensive mesoscale surface and rawinsonde measurements from ABLE-2B (Garstang et al., 1990) to assess COS structure and energetics. It finds that substantial upper level heating occurs in a typical mature COS compared to the global heat balance requirements for the equatorial trough zone (Riehl and Malkus, 1958).

It will be shown that about one-third of the global heat requirement can be met by vertical heat transport concentrated in COS over the Amazon Basin. Furthermore, calculations of massive heat transport within large, dynamically active anvil shields will imply that they share an important role with convective hot towers in providing the necessary heat transport to the upper troposphere.

Besides COS, Greco et al. (1990) identify two other modes of Amazon wet season convection: "Basin Occurring Systems" (BOS) and "Locally Occurring Systems" (LOS). In

terms of scale, longevity, and effects upon the lower atmosphere, COS are by far the most impressive Amazon convective rainfall systems. From 21 April to 14 May 1987, 11 COS accounted for 41% of the total rainfall and produced marked changes in the kinematic and thermodynamic structure of the atmosphere, according to Greco et al. (1990).

Recent budget studies of tropical squall lines have substantiated and clarified a dynamic role for extensive anvil cloud layers (Johnson, 1984; Houze, 1989). By partitioning the squall-line analysis into convective hot tower and anvil components, they show that a steady upward circulation in the anvil permits dynamic communication of heat to the upper troposphere.

The ABLE-2B mesoscale budget analyses, extended to the scale of an entire COS, will show that about half of the vertical heat export by these huge Amazon systems can occur in anvils. It will be revealed that the total amount of heat transport in the anvil varies as a function of the active cloud area during the systems's life cycle, consisting of six possible stages over a maximum lifetime of 48 hours. The COS life cycle will be defined in Chapter 5.

The evaluation of COS structure and energetics will require detailed analyses of surface, upper air, satellite, and radar data. The ABLE-2B data networks (Harris et al., 1990) were specifically designed to provide intensive mesoscale measurements of the convectively "active" atmosphere.

For the first time, ABLE-2B has provided rawinsonde measurements for a mesoscale volume extending from the surface to the tropopause over the Amazon Basin.

Comprehensive mesoscale case studies of three COS days and one fair weather day will appear in Chapter 4. In Chapter 5, a simple model based on case-study results and satellite analyses of active cloud area will allow evaluations of vertical heat transport as a function of the COS life cycle. With the aid of the case studies, the synoptic transport model, and satellite cloud analyses, this dissertation will address the following questions:

(1) Does substantial heat transport to the upper levels occur in COS compared to the global heat balance requirements of the equatorial trough zone?

(2) Does substantial heat transport occur in the anvil cloud during all stages of the COS life cycle?

(3) Is there more deep convection over the Amazon Basin during ABLE-2B than over the equatorial western Atlantic and equatorial eastern Pacific?

Satellite images show three COS at different stages of the life cycle may exist at once. It will be hypothesized that the Amazon basin may account for nearly one-third of the tropical heat export requirement.

## CHAPTER 2

### DATA SOURCES

This chapter describes the ABLE-2B meteorological networks, instruments, and methods of sampling that provided the data used in this research.

#### A. General

The ABLE-2B meteorological networks (Harris et al., 1990) have provided the most intensive synoptic and meso-scale observations ever made of convective systems over the vast, relatively inaccessible Amazon rain forests. The measurement systems providing data for this study include: rawinsonde, Portable Automated Mesonet (PAM) stations from the National Center for Atmospheric Research (NCAR), the Geosynchronous Operational Environmental Satellite (GOES), and a 3-cm weather radar. This study uses data from 26 April, 1 May, 4 May, and 6 May 1987.

Rawinsondes were released simultaneously every 6 h (0000, 0600, 1200, 1800 UT) from five locations around the perimeter of the Amazon Basin and at one location near the center of the basin (Figure 1). A 1000 km<sup>2</sup> triangle network (Figure 2) near Manaus, provided mesoscale surface and upper air observations near the center of the basin. Rawinsonde and PAM stations were collocated at each corner of the triangle. A fourth PAM station was located near the center of the triangle. There were simultaneous rawinsonde releases

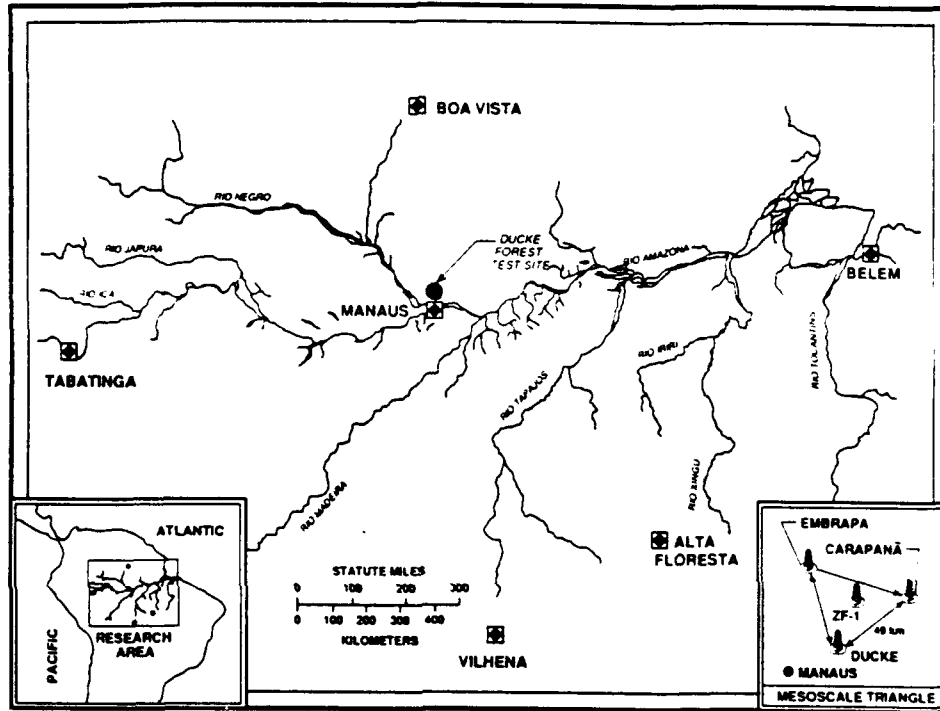


Figure 1. The ABLÉ-2B basin-scale network. Rawinsonde stations were located at Belem (1), Alta Floresta (2), Vilhena (3), Tabatinga (4), Boa Vista (5), and Embrapa (6).

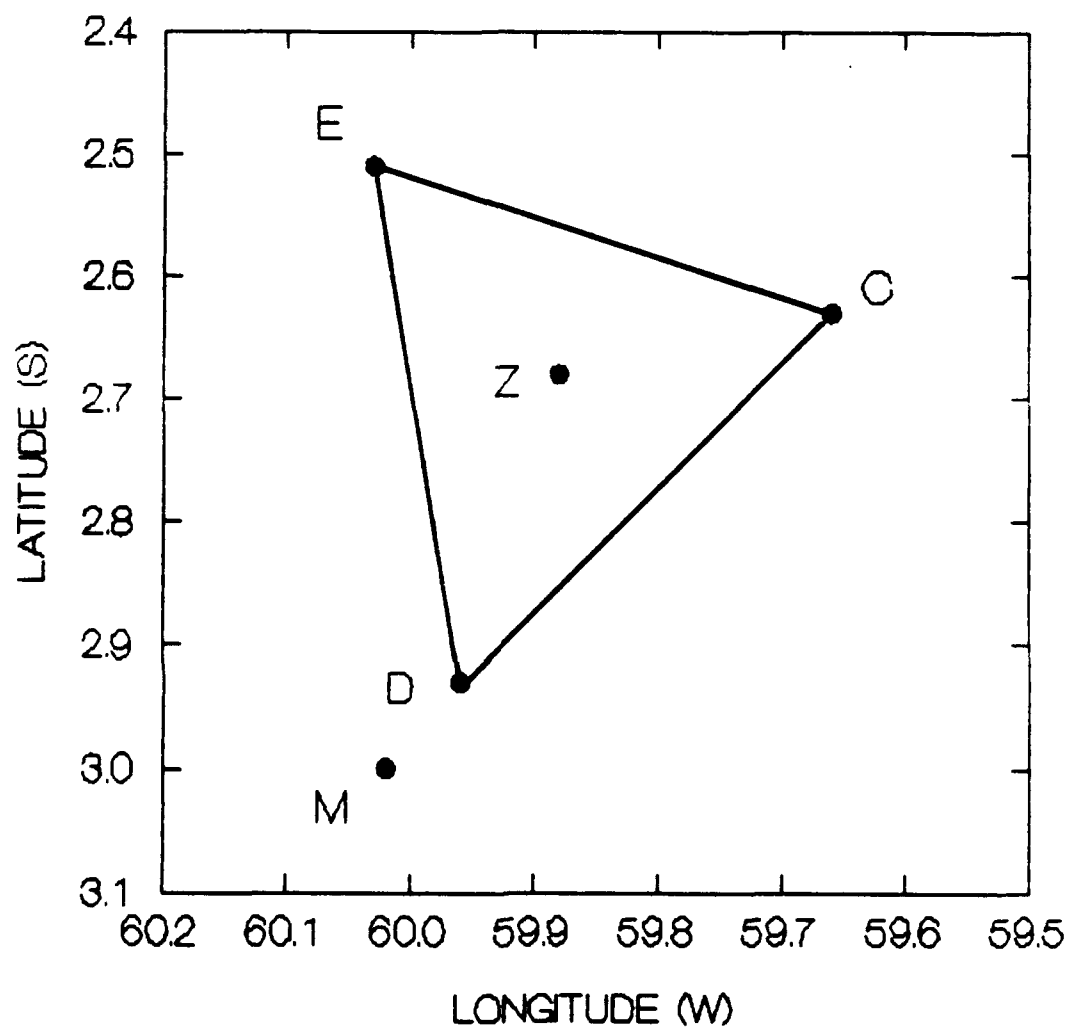


Figure 2. The ABL-2B mesoscale triangle network. Portable Automated Mesonet (PAM) towers and rawinsonde stations were collocated at Ducke (D), Embrapa (E), and Carapana (C). The ZF-1 site only had a PAM station. M denotes the city of Manaus.

in the mesoscale network at 1200, 1500, 1800, and 2100 UT (0800, 1100, 1400, and 1700 LT).

The GOES centered over the Amazon Basin monitored convective activity throughout the experiment. A telecommunications downlink furnished hourly visible and infrared imagers including special enhancements via the Digital Weather Image Processing System (DWIPS). The DWIPS can store 120 images and allows the user to create animation loops and magnify image sectors.

The remainder of this chapter addresses specific aspects of sampling methods that are important to this study.

#### **B. PAM**

The single-level PAM stations, located about 5 m above the rain forest canopy on 40-m towers, measured the horizontal wind velocity, temperature, humidity, pressure, and rainfall. The measurements, taken at 1 Hz and stored as 1-min averages, were telemetered real-time via satellite to NCAR for processing and storage. Satellite-ground communications links permitted near real-time display and use of the PAM data on a graphics terminal at the operations center.

The combination of PAM rainfall measurements at .25-mm resolution and PAM measurements of temperature, humidity, and wind velocity facilitate the identification of COS squall fronts and the transition from convective and to stratiform rain. Neither satellite images, which only

monitor cloud-top conditions, nor 3-cm radar, which attenuates in heavy rain and has range limitations, can match the quality of surface detail offered by the PAM network.

The PAM communications link operated flawlessly except for brief interruptions during heavy rain and lightning. Missing data in the PAM time series during these interruptions do not create problems for this study.

### C. Rawinsonde

Basin network stations (Figure 1) located at Boa Vista, Belem, Alta Floresta, Vilhena, Tabatinga, and Embrapa made four soundings per day (0000, 0600, 1200, 1800 UTC). In the triangle network (Figure 2), Ducke and Carapana made four soundings per day at 1200, 1500, 1800, 2100 UTC while Embrapa took six soundings per day at 0000, 0600, 1200, 1500, 1800, 2100 UTC. Both networks conducted simultaneous operations from 13 April to 12 May with many soundings reaching the stratosphere (approximately 17 km).

Checks against climatology and temperature profiles from the basins-scale stations revealed significant pressure offset problems in mesoscale triangle soundings. In the raw data, these offsets cause errors in pressure and temperature above 400 mb, and thus in values of geopotential, mixing ratio, and wind velocity, which depend upon accurate assignments of pressure. The error in wind velocity is due to the incorrect assignment of the height of the observation and is not due to any inherent problems in tracking the sonde. The

cause of the pressure offset was traced to bad instrument calibrations by the manufacturer of rawinsondes.

Statistical comparisons of the mesoscale soundings to the project-mean sounding for Belem revealed heteroscedastic variance (Davis, 1986) in the pressure offset above 700 mb. Thus, a least squares procedure based on the mean temperature profile at Belem is used to develop a procedure for adjusting and editing the mesoscale soundings. After the pressure offset is determined, temperatures are reasigned to adjusted pressure levels. Next geopotential, mixing ratio, and wind velocity are recalculated at 25 mb intervals from the surface to 100 mb. The wind calculations employ smoothed azimuth, elevation, and balloon ascent rate by using three-point moving averages (Davis, 1986) to reduce noise introduced by antenna errors.

Some soundings during thunderstorms show data losses due to lightning or icing problems. Usually these soundings terminate near the freezing level. These weather-related problems prevented budget calculations for several strong COS which passed through the mesoscale network. The cases selected for study either had no problems or they had problems which could easily be handled by the above procedures.

#### D. Satellite

The DWIPS provided full-disk 4- and 8-km resolution visible and infrared images as well as 2-km high resolution visible images, all centered on Manaus (3°S, 60°W). User-

defined loops stored the most recent 40 images which were animated, magnified, and enhanced, as needed, to study the features of mesoscale and synoptic-scale convective systems. This study uses thermal-facsimile GOES images processed on the DWIPS.

#### **E. Radar**

A 3-cm CAPPI (constant-altitude plan-position indicator) radar from the McGill Radar Weather Observatory made scans at 5-min intervals during selected periods of the experiment. The radar coverage provided good coverage of the 26 April COS, a large, well-organized system with strong squall front features as it passed through the mesoscale network.

Attenuation of the CAPPI data during heavy rain precluded accurate estimates of rainfall rates. The radar data have primarily been used to supplement the PAM and GOES data in partitioning the budget calculations into convective hot tower and anvil components.

## CHAPTER 3

### METHODS OF ANALYSIS

The methods described in this chapter will be used to study the structure and energetics of COS on 26 April, 1 May, and 6 May and fair weather cumulus on 4 May.

#### A. Data Classification

Many squall-line budget studies (e.g. Yanai et al., 1973; Reed and Recker, 1971; and Thompson et al., 1979) have not partitioned heating and moistening distributions into cumulus hot towers and stratiform anvils (Johnson, 1984). In the above studies, the rawinsonde networks were not conducive to partitioning because the station arrays were much larger than the squall-line cloud components.

The ABLE-2B triangle is smaller than either the hot tower or anvil parts of a COS. Thus, the network is capable of giving rawinsonde and surface measurements made entirely within each cloud component. Other advantages of the ABLE-2B sampling methods include PAM time series of rainfall and GOES enhanced infrared (IR) images to aid in identifying cloud and precipitation components.

The COS have the following features which satisfy Zipser's (1977) criteria for a tropical "squall system":

(1) a squall front that propagates with considerable speed with respect to the low-level ambient winds,

(2) large decreases in surface temperature and water vapor mixing ratio behind the squall front,

(3) large increases in surface wind speed and pressure associated with squall front passage,

(4) heavy convective rainfall from deep cumulonimbi (Cb) existing just behind the squall front,

(5) propagation of the squall system into the environment ahead by development and growth of new convective cells along the squall front, and

(6) blending of old Cb towers into an extensive stratiform anvil cloud mass, with Cb bases rapidly giving way to anvil cloud bases from which light rain falls into a shallow pool of cool, dry air in the lower levels.

Four general categories described in Table 1 are used to classify ABLE-2B data: fair weather cumulus, rapidly building pre-squall cumulus, leading edge Cb, and stratiform anvil. The cases discussed in Chapter 4 also contain other precise indicators imbedded in the PAM time series of rainfall, temperature, mixing ratio, and winds.

**Table 1. ABLE-2B Weather Classification Criteria**

Type	Conditions	Clouds	Precipitation
1	Non-squall	Fair weather cumulus	None
2	Pre-squall	Towering cumulus	None
3	Squall front	Deep cumulus towers	Heavy rain starts as squall front passes
4	Anvil	Deep layers of middle and high stratiform clouds	Light to moderate stratiform rain falls into cool dry air behind squall front

## B. Heat and Moisture Budgets

Equations derived by Nitta (1972) and Yanai et al. (1973) and used in tropical studies by Thompson et al. (1979), Johnson and Young (1983), Johnson (1984), and Chen (1987), among others, are applied in heat and moisture budget calculations for the mesoscale triangle. The equations for sensible heat source ( $Q_1$ ) and latent heat sink ( $Q_2$ ), respectively, are (Johnson and Young, 1983):

$$\begin{aligned} Q_1 &\equiv \frac{\partial \bar{s}}{\partial t} + \bar{\mathbf{V}} \cdot \nabla \bar{s} + \bar{\omega} \frac{\partial \bar{s}}{\partial p} \\ &= -\frac{\partial}{\partial p} \overline{\omega' s'} + \bar{Q}_s + \bar{Q}_R \end{aligned} \quad (1)$$

$$\begin{aligned} Q_2 &\equiv -L \left( \frac{\partial \bar{q}}{\partial t} + \bar{\mathbf{V}} \cdot \nabla \bar{q} + \bar{\omega} \frac{\partial \bar{q}}{\partial p} \right) \\ &= L \frac{\partial}{\partial p} \overline{\omega' q'} - L \bar{Q}_q \end{aligned} \quad (2)$$

where the symbols are:

- $Q_1$       apparent sensible heat source
- $Q_2$       apparent moisture sink
- $Q_R$       net radiative heating rate
- $Q_s$       sources of heat

$Q_q$	sources of water vapor
$s$	dry static energy [ $=c_p T + gz$ ]
$c_p$	specific heat at constant pressure
$T$	temperature
$g$	acceleration of gravity
$z$	geopotential height
$q$	specific humidity
$V$	horizontal wind velocity
$\omega$	vertical velocity in pressure coordinates [ $\equiv dp/dt$ ]
$p$	pressure
$t$	time
$L$	latent heat of condensation
$\overline{[ ]}$	area average of a quantity
$[ ]'$	deviation of a quantity from the area average

The source terms, including processes associated with phase changes in liquid water, water vapor, and ice, are

$$Q_s = L_v(c-e) + (L_v+L_v')(d-s_*) + L_f(f-m)$$

and

$$Q_q = e - c - d + s_*$$

where  $L_v$  and  $L_f$  are the latent heats of vaporization and fusion and  $c$ ,  $e$ ,  $d$ ,  $s_*$ ,  $f$  and  $m$  are the rates of condensation, evaporation, deposition, sublimation, freezing, and

melting, respectively (Johnson and Young, 1983).

The equation obtained from Eqs. (1) and (2) for the budget of total heat at a specific pressure level is

$$Q_1 - Q_2 - Q_R = -\frac{\partial}{\partial p} \overline{(s' + Lq')\omega'} = -\frac{\partial}{\partial p} \overline{h'\omega'} \quad (3)$$

where  $h$  is moist static energy and  $\overline{h'\omega'}$  is the vertical eddy transport of total heat, a quantity used to evaluate convective activity (Yanai et al., 1973). The integration of Eq. (3) from the tropopause pressure  $p_t$  to a given level  $p$  gives the following equation for the vertical eddy flux of total heat  $F$  (Yanai et al., 1973)

$$F = g^{-1} \int_{p_t}^p (Q_1 - Q_2 - Q_R) dp.$$

### C. Divergence and Vertical Velocity

Horizontal divergence at a single pressure level in the mesoscale network area  $A$  is calculated as follows from the line integral of wind components normal to each leg of the mesoscale triangle (Brümmer, 1978; Gamache and Houze, 1982; and Esbensen, 1975)

$$D_o(p) = \frac{1}{A} \oint V_n dl \quad (4)$$

where the  $V_n$  are horizontal wind components normal to leg  $dl$ . Average wind velocity is the linear average of the observed winds at each end point of a leg. Divergence is calculated from 1000 to 100 mb in 25 mb intervals. A first estimate of the vertical velocity  $\omega$  is obtained from

$$\omega(p) = - \int_{p_s}^p D_o(p) dp. \quad (5)$$

The vertical velocity calculation uses a lower boundary condition of zero vertical motion at the surface.

Rawinsonde measurements of horizontal winds deteriorate as elevation angle decreases (Duvedal, 1962). Consequently, divergence and vertical velocity errors increase with altitude and reach a maximum at the highest level.

Vertical velocity at each level was corrected by adjusting divergence through the column according to the method of O'Brien (1970). This procedure gives results that compare well with physically realistic estimates of vertical motion from adiabatic and isentropic methods (Haltiner and Martin, 1957). O'Brien's method assumes vertical-velocity errors result from linear-divergence errors which increase uniformly from a surface minimum to a maximum at the highest level reached. Gamache and Houze (1982) obtain acceptable results by applying these procedures to tropical squall lines. The equation for corrected divergence is

$$D_c(p) = D(p) + \epsilon(p-p_s)$$

where  $\epsilon$  is a constant with units of  $s^{-1}mb^{-1}$ . Substituting  $D_c(p)$  for  $D(p)$  in Eq. (5) gives the equation for adjusted vertical velocity

$$\begin{aligned} \omega_c(p) &= - \int_{p_s}^p D(p) dp - \epsilon \int_{p_s}^p (p_s - p) dp \\ &= - \int_{p_s}^p D(p) dp + .5\epsilon(p_s - p)^2. \end{aligned}$$

A top boundary condition of  $\omega(p_t)=0$ , where  $p_t$  is 100 mb, forces mass balance upon the column and gives the following equation for  $\epsilon$ :

$$\epsilon = \frac{2 \int_{p_s}^p D(p) dp}{(p_s - p_t)^2}.$$

Adjusted values of divergence and vertical velocity are obtained by substituting  $\epsilon$  into Eqs. (4) and (5).

#### D. Storage and Advection

Calculations of  $Q_1$  and  $Q_2$  include storage ( $\partial/\partial t$ ), horizontal advection ( $V \cdot \nabla$ ) and vertical advection ( $\omega \partial/\partial p$ ) of  $s$  and  $q$ , respectively. Storage calculations use forward-in-time differences while vertical advection calculations

use centered-in-space differences. Horizontal advection is found by applying least squares objective analysis to rawinsonde measurements of  $s$ ,  $q$ ,  $u$  and  $v$  in the triangle (Thompson et al., 1979; Johnson and Young, 1983).

The relatively small size of the triangle network and well-known limitations of rawinsonde systems cause unavoidable errors in  $Q_1$  and  $Q_2$ . These errors are smaller and less significant during convectively active periods (Thompson et al., 1979; Johnson and Young, 1983) when the vertical advection terms increase by an order of magnitude and dominate over storage and horizontal advection.

#### **E. Radiational Heating and Cooling**

Tropical budget studies (e.g. Thompson et al., 1978; Chen, 1987) and methods of convective parameterization based upon them (Frank, 1978; Betts, 1986) have emphasized diabatic processes related to water, water vapor, and ice phase changes over radiation. Winter MONEX studies indicate that large differences in net radiation between the base and top of anvil clouds cannot be ignored in the total heat budget of tropical cloud systems (Webster and Stephens, 1980). The MONEX heating and cooling rates are an order of magnitude larger than the area averaged rates used in budget studies of the GATE B-scale area (e.g. Thompson et al., 1978).

The net radiative heating due to longwave and short-wave radiative processes in the triangle volume is calculat-

ed by the following methods, which are described in Pielke (1978, Ch. 8).

The area-averaged longwave radiative flux in clear air at vertical level  $k$  is

$$\bar{R}(k) \simeq \sigma \left( \bar{\epsilon}_b \bar{T}_b^4 - \bar{\epsilon}_a \bar{T}_a^4 \right)$$

where  $\sigma$  is the Stephan-Boltzman constant and  $\bar{\epsilon}$  and  $\bar{T}$  are the radiative emissivity and temperature, respectively, for the adjacent vertical layers below (subscript  $b$ ) and above (subscript  $a$ ) level  $k$ . Layer  $a$  is bounded by levels  $(k+1)$  and  $k$  while layer  $b$  is bounded by levels  $(k-1)$  and  $k$ . The total emissivity of a layer, expressed as the sum of the emissivities attributed to the primary infrared constituents, e.g. water vapor ( $H_2O$ ) and carbon dioxide ( $CO_2$ ), is

$$\epsilon = \epsilon_{H_2O} + \epsilon_{CO_2}$$

The Atwater (1974) and Kondratyev (1969) algorithms are used for the emissivities of water vapor and carbon dioxide, respectively. The water vapor algorithm derives emissivity from precipitable water; the algorithm for carbon dioxide emissivity uses optical depth expressed as a function of pressure. The calculations neglect the spectral overlap of water vapor and carbon dioxide since the effect on radiational heating rates is small over periods of 3-6 h in cloudy air (Staley and Jurica, 1970). The ABLE-2B radiation

profiles obtained by these methods resemble those obtained in Winter MONEX convective systems by Webster and Stephens (1980).

If clouds are present at level  $k$ , the longwave radiative flux is

$$\bar{R}_c(k) = \sigma \left( \epsilon_{cb} \bar{T}^4 - \epsilon_{ca} \bar{T}^4 \right)$$

The radiative emissivities below and above the level  $k$  in a cloud are (Stephens, 1978a):

$$\epsilon_{cb} = 1 - e^{-A_b W_b}$$

$$\epsilon_{ca} = 1 - e^{-A_a W_a}$$

where  $A_b = 0.130 \text{ m}^2\text{g}^{-1}$  and  $A_a = 0.158 \text{ m}^2\text{g}^{-1}$  and  $W_b$  and  $W_a$  are the integrated liquid water content in the cloud layer below and above the level  $k$ , respectively. In the calculations of  $W_b$  and  $W_a$  it is assumed that the cloud water content varies as a function of pressure (Cox and Griffith, 1979).

Fractional cloud cover  $\sigma_c$  at each pressure level in the mesoscale network is determined from the area-averaged relative humidity measured by rawinsonde. The method is generally based on cloud analysis procedures discussed in Air Weather Service Manual 105-124 (1969). The cloud analysis procedure employs a linear relationship between cloud cover and relative humidity. It is assumed that clouds form at a relative humidity of 90% and that the triangle is to-

tally covered by clouds at a relative humidity of 100%. Relative humidities above the freezing level are based upon the frost point instead of dew point. The cloud analysis is checked for consistency against surface observations and satellite images.

For levels partially covered by clouds, the longwave radiative flux for the combination of clouds and cloud-free air is

$$\bar{R}_{lw} = \sigma_c \bar{R}_c + (1 - \sigma_c) \bar{R}$$

Shortwave irradiance in the atmosphere includes both direct and diffuse radiation. The direct component is the shortwave radiation not absorbed or scattered by the atmosphere. In cloud-free air, ozone, water vapor, and other gases, e.g. diatomic oxygen, absorb shortwave radiation. Water vapor is the main source of tropospheric heating due to shortwave absorption. Under a clear sky, total shortwave irradiance absorbed at the surface is

$$\bar{R}_{SWG} = (t - a)(1 - A)R_{SW0}$$

where  $t$  is fractional transmissivity,  $a$  is fractional loss due to water vapor absorption,  $A$  is surface albedo, and  $R_{SW0}$  is shortwave irradiance at the top of the atmosphere. This study uses  $R_{SW0} = 1376 \text{ W m}^{-2}$  and  $A = 0.15$  for the tropical rain forest. The relations for  $t$  (Atwater and Brown, 1974; Kondratyev, 1969) and  $a$  (McCumber, 1980; McDonald, 1960) are

$$t = 1.03 - 0.08 \left( [0.000949p + 0.051]/\cos Z \right)^{0.5}$$

and

$$a = 0.077(\delta P/\cos Z)^{0.3}$$

where  $Z$  is zenith angle and  $\delta P$  is the total vertical depth of liquid water in  $g\ cm^{-2}$ . The equation for  $t$  accounts for downward Rayleigh scattering as well as absorption caused by ozone, diatomic oxygen, and carbon dioxide. Shortwave irradiance above the earth's surface is

$$\bar{R} = (t - a)R_{SW0}. \quad (6)$$

The shortwave irradiance in cloud is

$$\bar{R}_{SWC} = t_c \bar{R}_{SWCT} \quad (7)$$

where  $t_c$ , the shortwave transmissivity in cloud is obtained by the Stephens (1978) procedure and the shortwave irradiance at the cloud top  $\bar{R}_{SWCT}$  comes from Eq. (6). For a single cloud layer, the shortwave irradiance at the ground equals the shortwave irradiance exiting downward from the cloud base minus the extinction in the atmosphere between the cloud base and the ground. For multiple cloud layers, the procedure involves repeated use of Eq. (7) for each cloud layer. If clouds only cover a fraction of the network area, the calculation of irradiance weights the cloudy and cloudfree areas, i.e.

$$\bar{R}_{\text{SWT}} = \sigma_c \bar{R}_{\text{SWC}} + (1 - \sigma_c) \bar{R}_{\text{SW}}.$$

These methods neglect backscattered radiation from the ground and overlying clouds, cloud shading, and the effects of cloud shape.

At a specific pressure level, the local time change in temperature due to radiative processes is

$$\frac{\partial \bar{T}}{\partial t} \Big|_{\text{rad}} = -\frac{1}{\rho c_p} \left( \frac{\partial \bar{R}}{\partial z} \Big|_{lw} + \frac{\partial \bar{R}}{\partial z} \Big|_{sw} \right).$$

The methods described in this chapter will now be applied in energy budget and heat transport case studies for four days during ABLE-2B.

**CHAPTER 4**  
**CASE STUDIES**

**A. Weakening COS, 26 April 1987**

On 26 April 1987, between 1500 and 2100 UTC, a weakening COS passed through the mesoscale triangle. Satellite images show it had just passed the mature stage but still had a strong squall front when it reached the mesoscale network. Major kinematic and thermodynamic changes occurred in the triangle volume.

The GOES IR images (Figures 3-5) illustrate the system's life cycle. It formed along the northern coast of Brazil during the afternoon of 25 April (Figure 3), coinciding with a marked increase in deep convection over the equatorial Atlantic. Shortly after it formed, the COS had quasi-linear features.

Satellite analysis indicates westward propagation at a 24-hour average speed of  $55 \text{ km hr}^{-1}$  with leading edge cumulonimbi and convective rain entering the mesoscale triangle at approximately 1600 UTC on 26 April. A decrease in size along with a more ragged appearance of the convective clusters on GOES images indicates the COS was weakening over the triangle. Full disk IR images show the COS regenerated over the western Amazon Basin and entered a second mature stage on 27 April (Figure 6) when its length and width grew to 3500 km and 400 km, respectively.

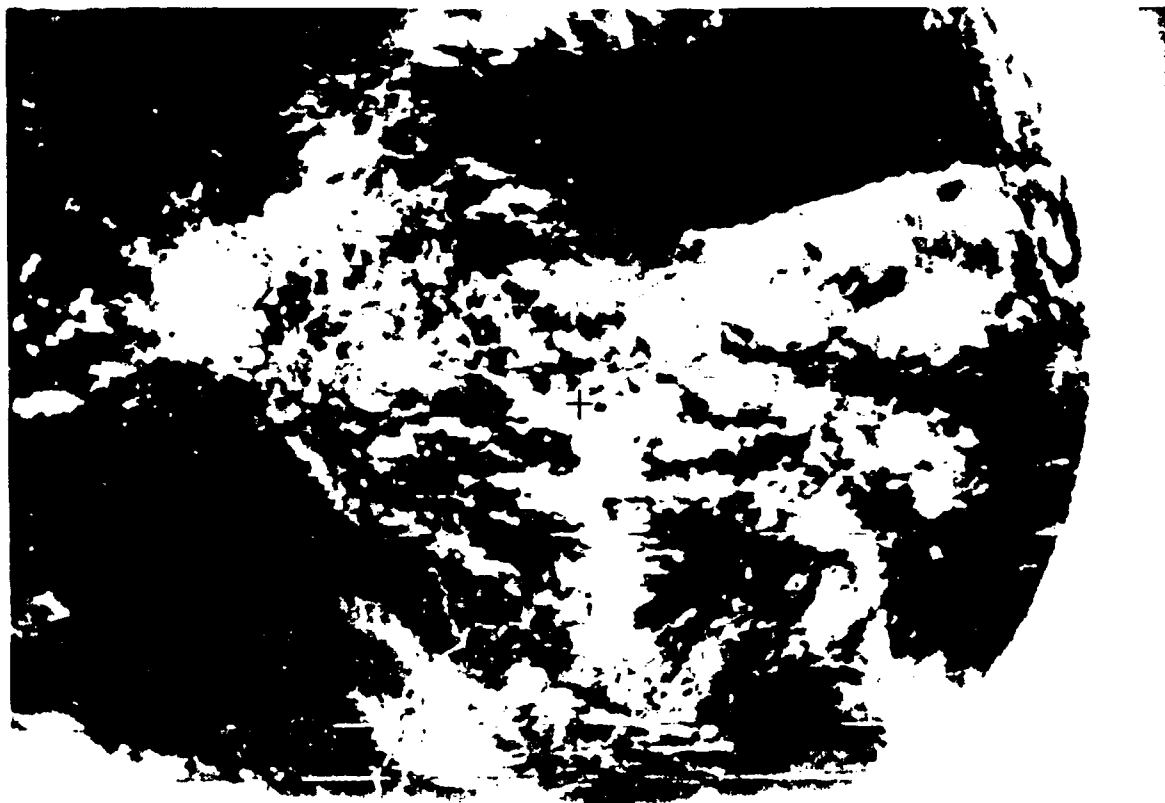
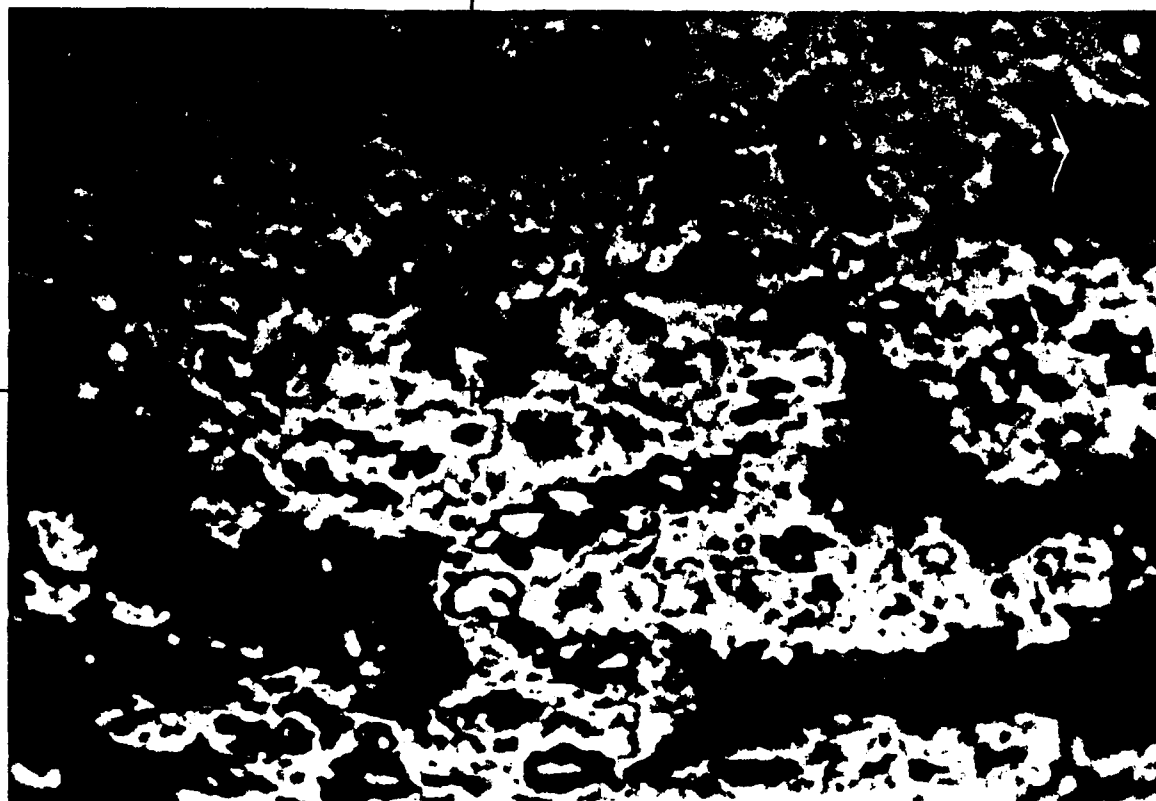


Figure 3. GOES full disk IR image at 2100 UTC, 25 April 1987 showing COS in intensifying stage over the northeast coast of Brazil. The + denotes 3°S, 60°W, the coordinates of Manaus.



500 km

Figure 4. The GOES MB-enhanced IR image at 2000 UTC, 25 April 1987 showing COS (see upper right corner) in the intensifying stage over the northeast coast of Brazil. The + denotes 3°S, 60°W.



Figure 5. The GOES full disk IR image at 1800 UTC, 26 April 1987 showing COS just after it begins to weaken over the central Amazon basin. The + denotes 3°S, 60°W.

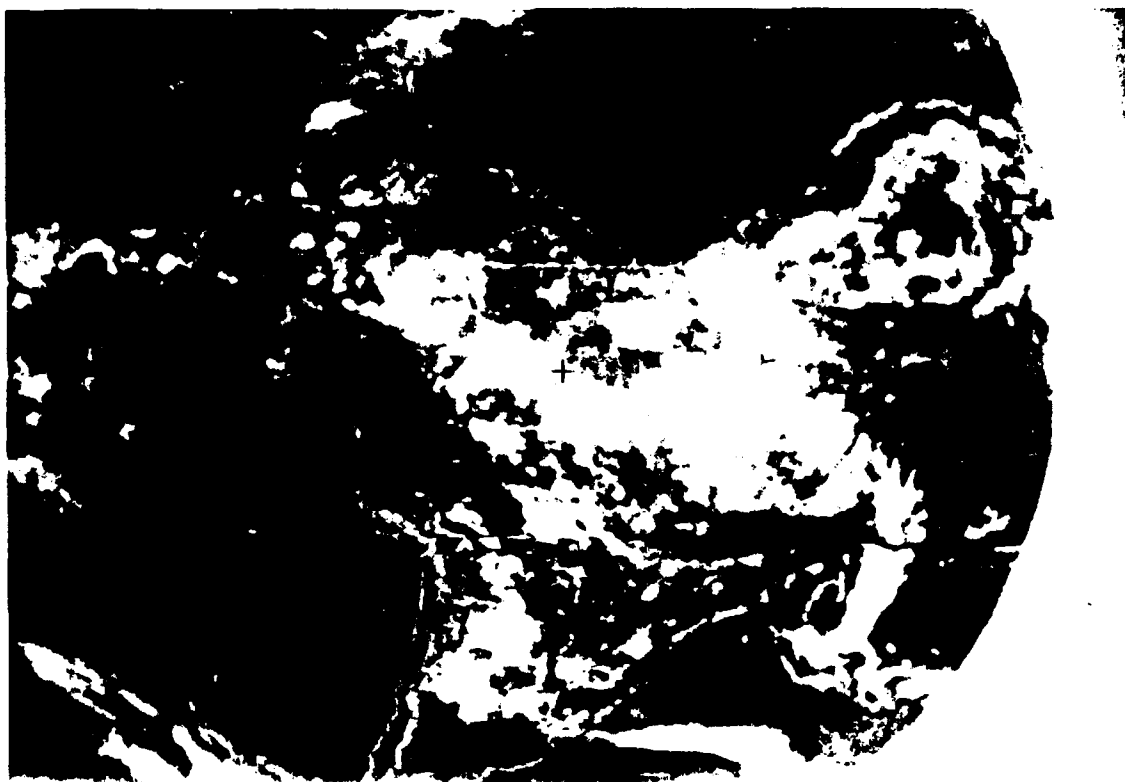
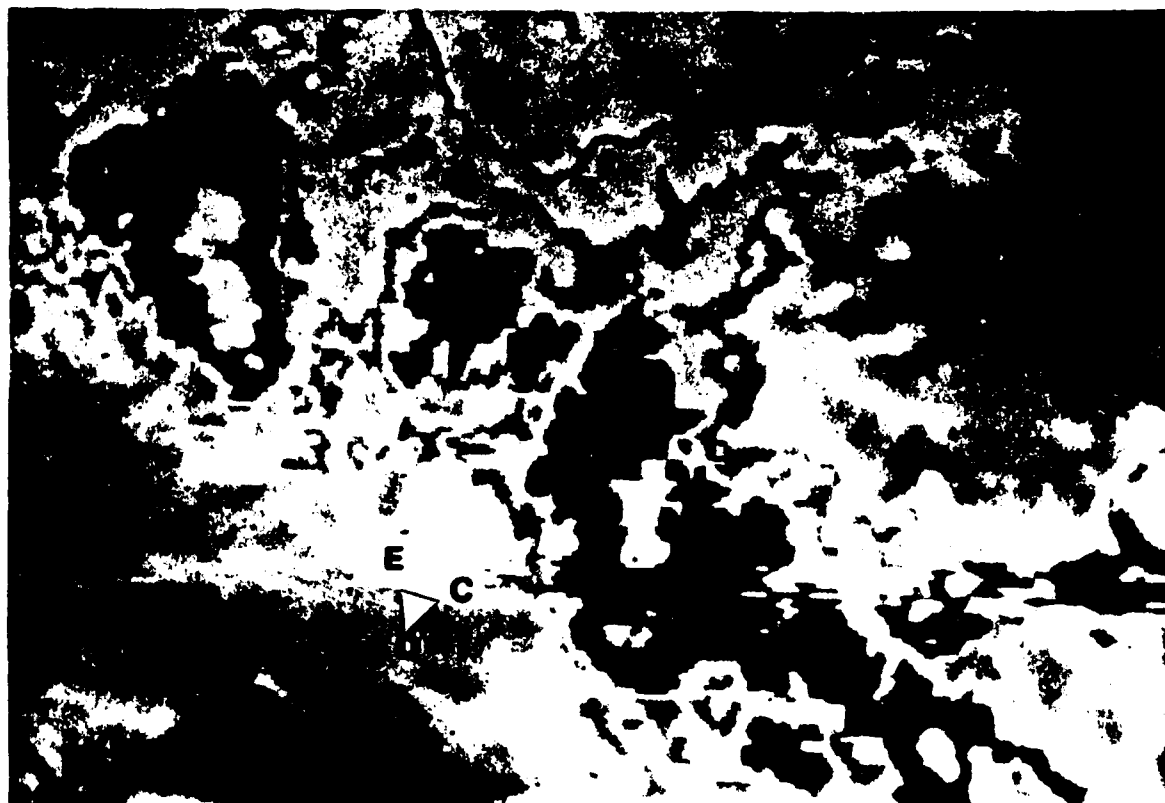


Figure 6. The GOES full disk IR image at 0300 UTC, 27 April 1987 showing COS regenerating across the entire Amazon basin. The + denotes 3°S, 60°W.

The IR satellite image at 1400 UTC on 26 April (Figure 7) uses the MB-enhancement curve (Carlson, 1981) to improve the resolution of cloud-top temperatures. The COS appears as a convective line oriented from northwest to southeast shortly before it enters the triangle. Its markedly linear features include distinct mesoscale cloud clusters in the black and dark gray shades, indicating areas of convective and stratiform rain (Carlson, 1981). Each cluster is comprised of cumulus hot towers (Riehl and Malkus, 1958) along the leading edge of the system and layers of stratiform anvil clouds that surround the convective cells and extend far to the rear (Houze, 1982).

The COS anvils are identical to those described in GATE (e.g. Houze, 1977; Leary and Houze, 1982), MONEX (e.g. Johnson, 1984; Webster and Stephens, 1980), VIMHEX (e.g. Miller and Betts, 1977), and COPT 81 (Chong et al., 1987). Thick anvil layers protrude horizontally from the convective towers and merge with each other to form the sharply defined clusters seen on the MB images. Thin anvil clouds extend from each cluster and combine with those from neighboring clusters to form the characteristic synoptic-scale cloud line on the full-disk GOES IR images.

The CAPPI radar provides further detail on the system's structure. Isolated echoes appear in the triangle at 1530 UTC (Figure 8) and are followed by increases in cell number, area, and intensity during the next hour. By 1644



500 km

---

Figure 7. The GOES MB-enhanced IR image at 1400 UTC, 26 April 1987 showing mature COS located just to the east of the mesoscale network (denoted by white triangle and the first letter of each rawinsonde site).

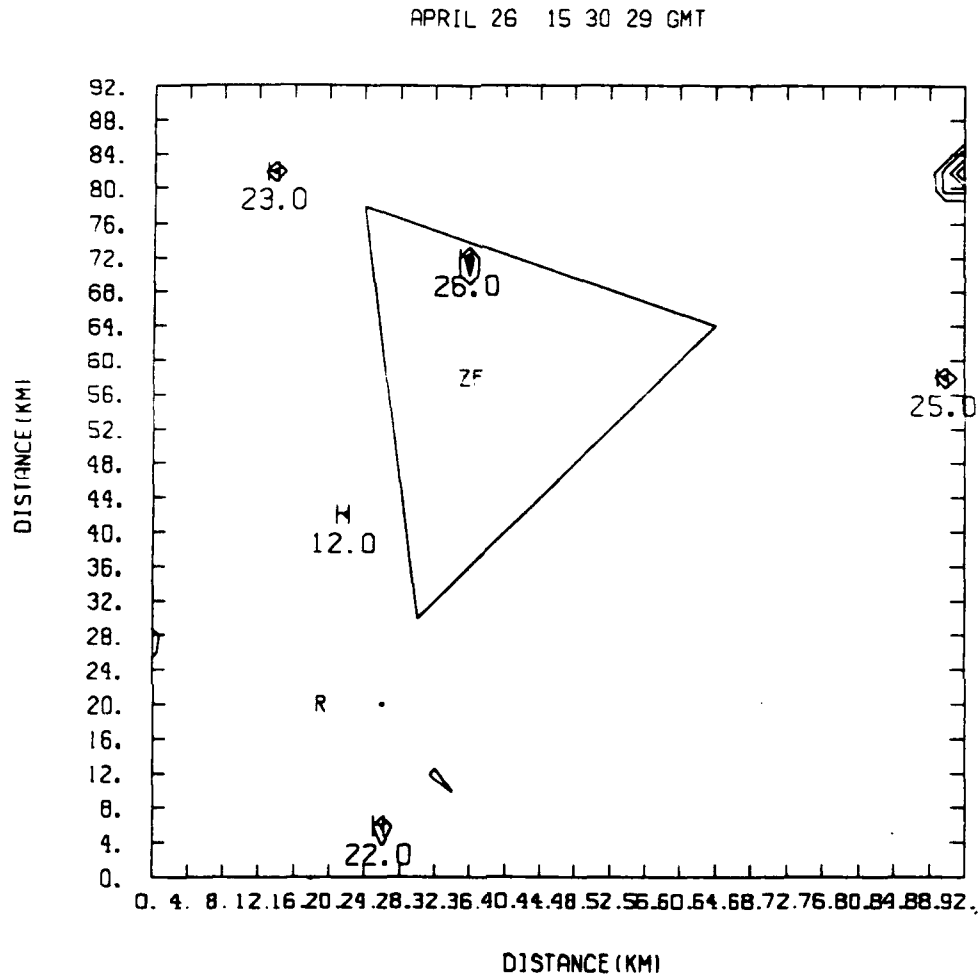


Figure 8. CAPPI radar scan of building cumulus cells in the mesoscale triangle at 1530 UTC, 26 April 1987.

UTC (Figure 9) a northwest-to-southeast oriented line of cells, each about 25 km wide, is centered on the southeast leg of the triangle.

The PAM time series (Figures 10-18) have well-defined convective and stratiform rainfall components (Figures 10-11). They support satellite and radar analyses of a line disturbance moving to the southwest. Rainfall begins at Carapana around 1630 UTC and then spreads westward to ZF-1, Embrapa, and Ducke. Although rain occurs at all four stations, only a trace falls at Ducke. The radar scans, which show several convective cells barely missed Ducke (Figure 19), substantiate the PAM rain gauge measurements.

At squall front passage, there are abrupt increases in wind speed (Figure 12), sharp jumps in pressure (Figure 13), and rapid decreases in  $T$ ,  $q$ , and  $\theta_e$  (Figures 14-16, respectively). Changes occur first at Carapana as the system propagates to the southwest. Horizontal winds (Figures 17-18) shift from southwesterlies ahead of to northeasterlies behind the squall front. The system's 24-h average forward speed of movement, determined from satellite analysis, is  $15 \text{ m s}^{-1}$  or slightly larger than the area-averaged peak winds of  $13.5 \text{ m s}^{-1}$  in the triangle. The time lag in squall-front features between PAM stations indicates a forward speed of  $13.9 \text{ m s}^{-1}$  in the mesoscale network.

The protracted effects of cold, dry convective downdrafts from cumulus hot towers continue at the surface long

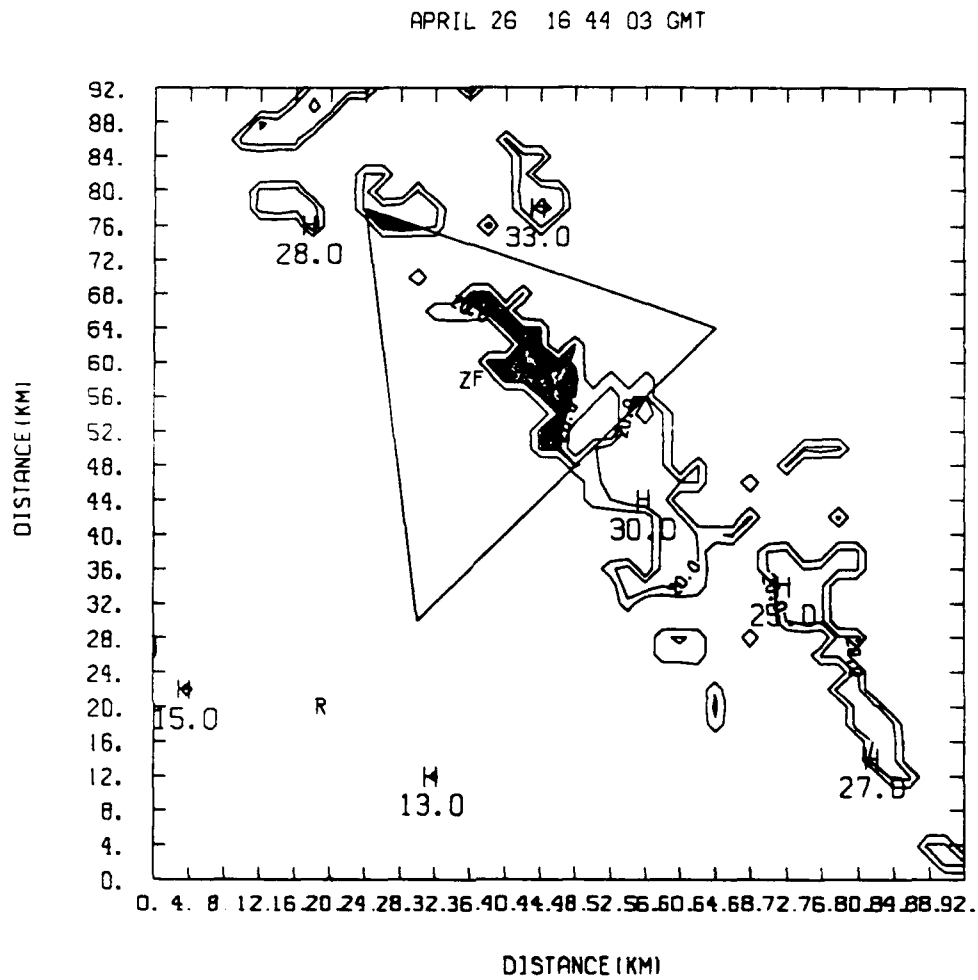


Figure 9. CAPPI radar scan of COS squall line in the mesoscale triangle at 1644 UTC, 26 April 1987.

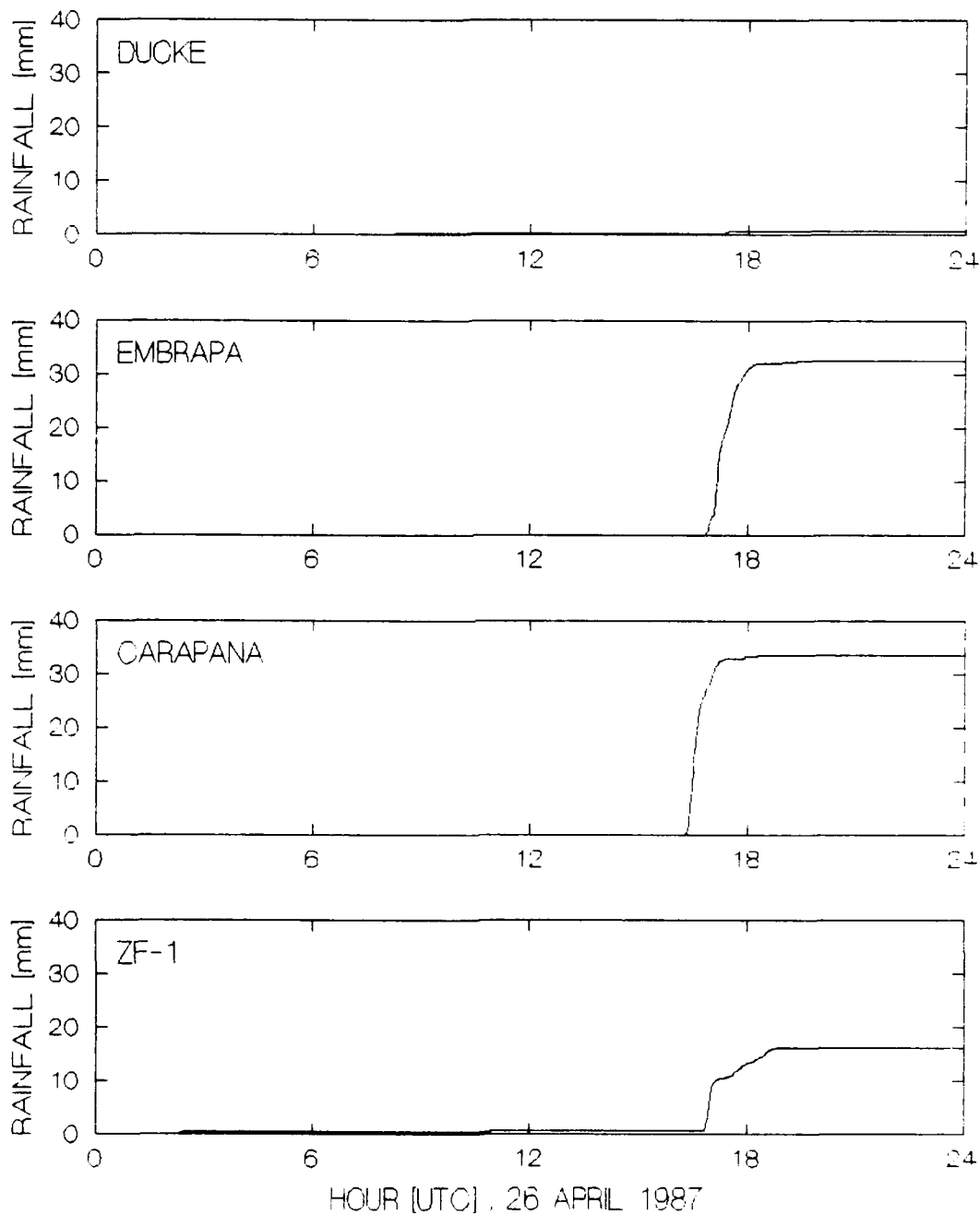


Figure 10. PAM time series of total rainfall (mm) on 26 April 1987.

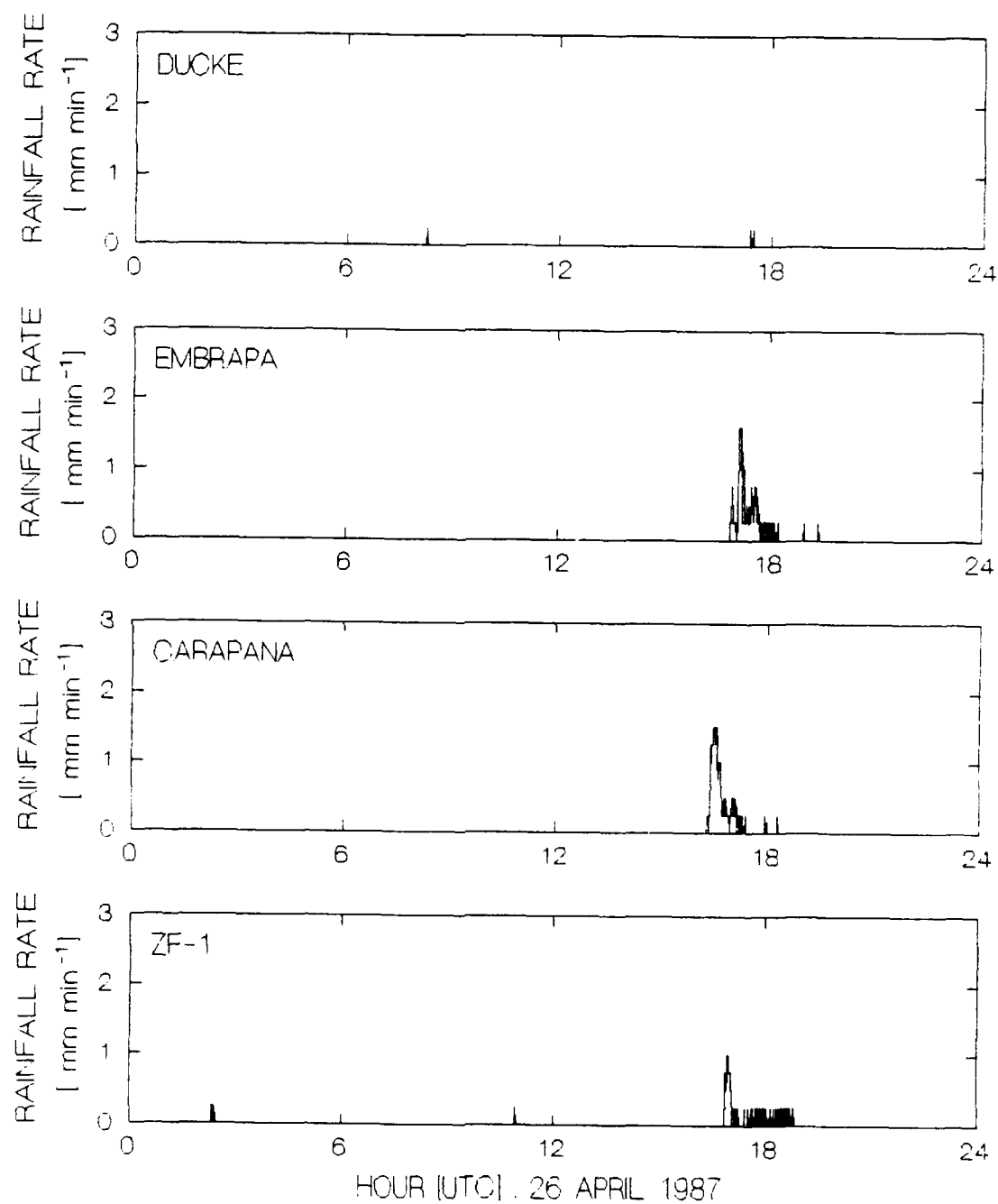


Figure 11. PAM time series of rainfall rate (mm min<sup>-1</sup>) on 26 April 1987.

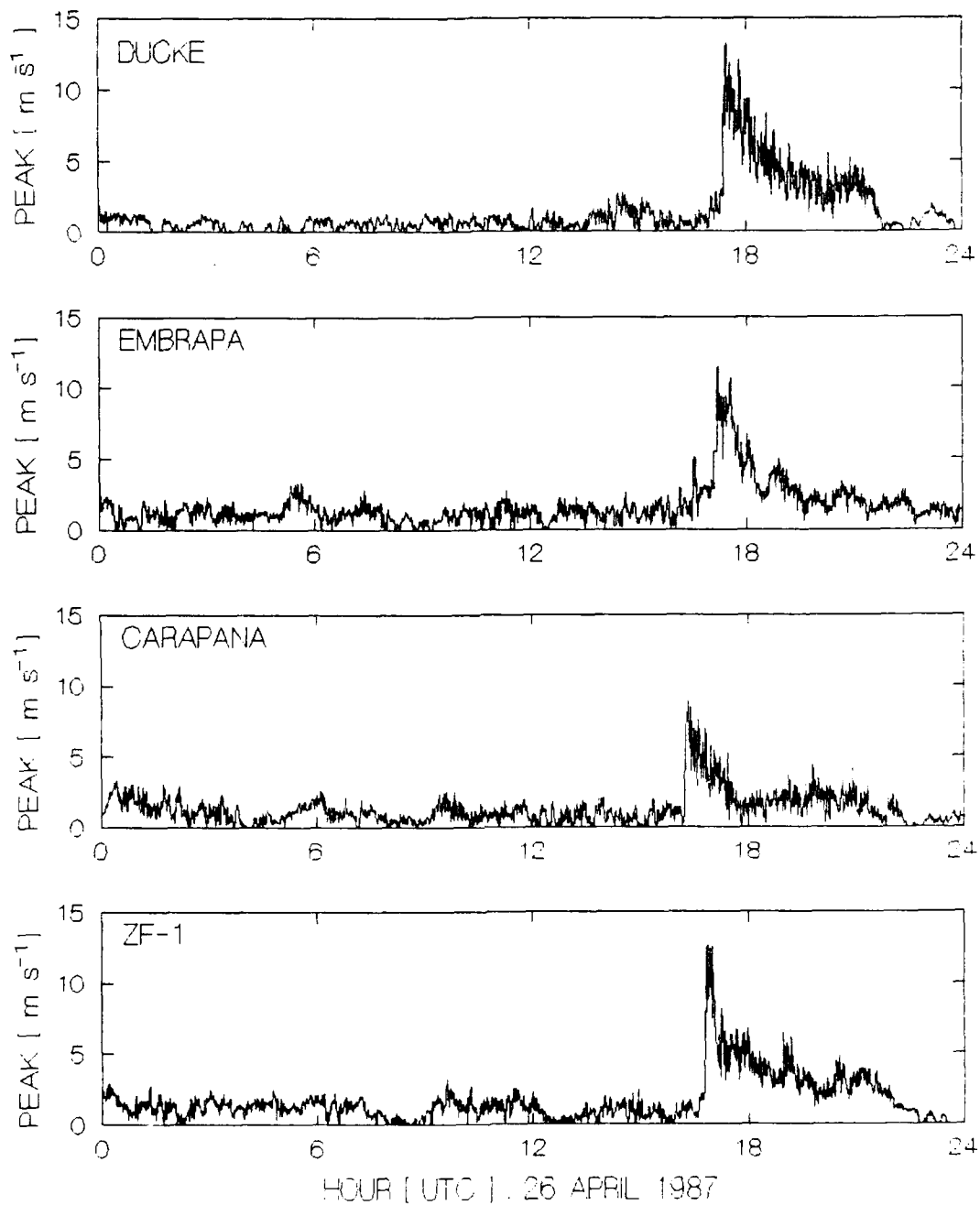


Figure 12. PAM time series of peak wind speed ( $\text{m s}^{-1}$ ) on 26 April 1987.

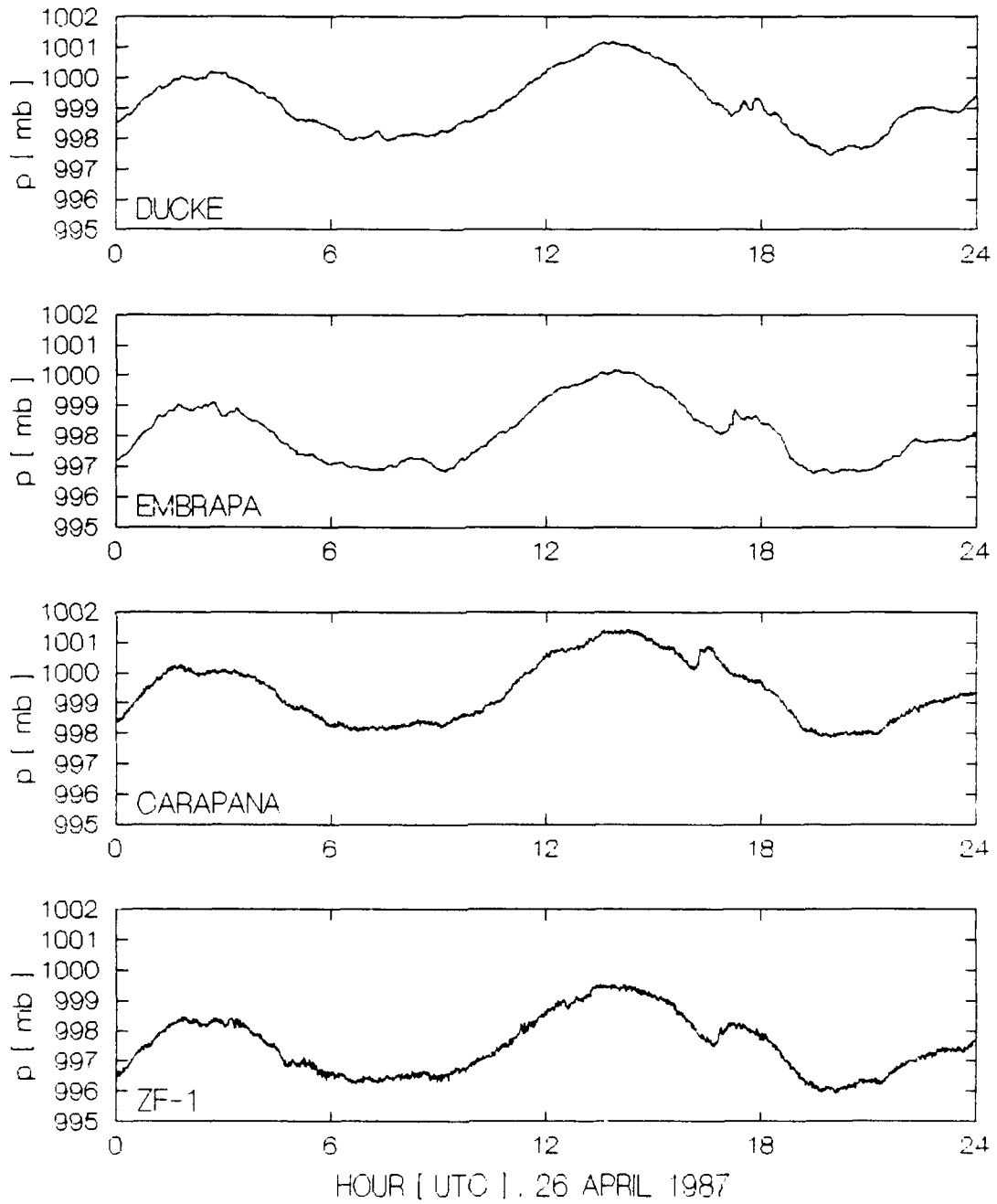


Figure 13. PAM time series of  $p$  (mb) on 26 April 1987.

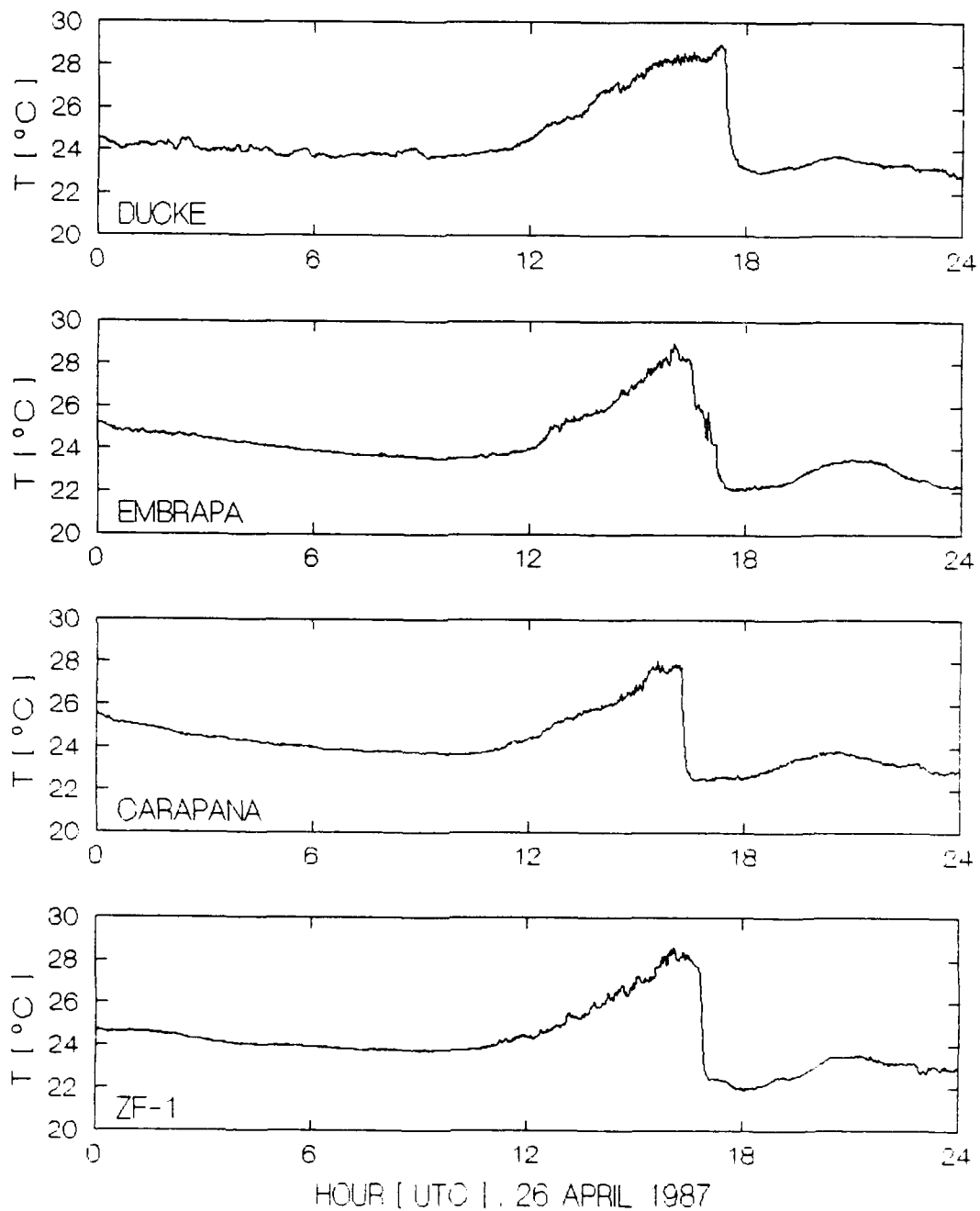


Figure 14. PAM time series of  $T$  (deg C) on 26 April 1987.

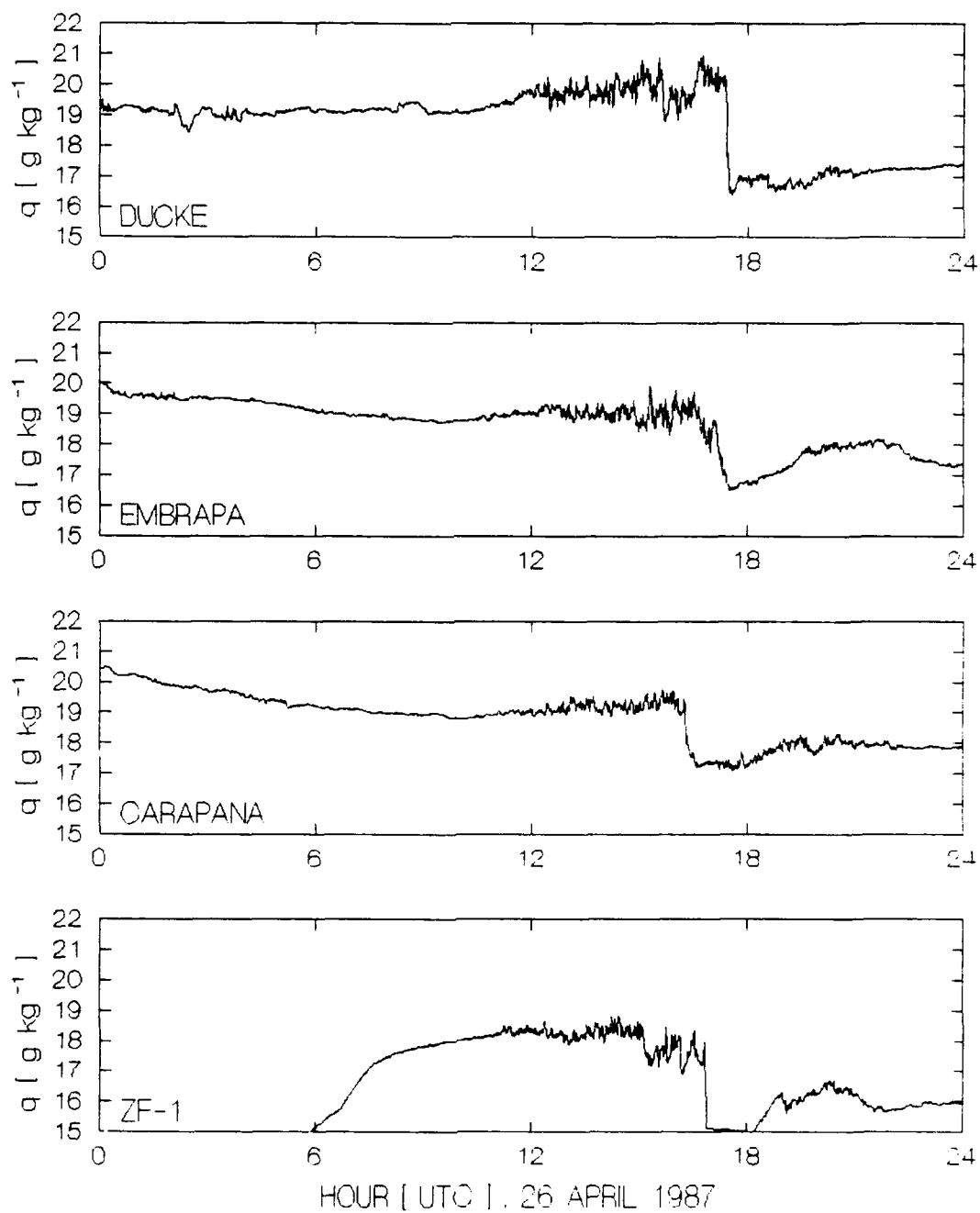


Figure 15. PAM time series of  $q$  ( $\text{g kg}^{-1}$ ) on 26 April 1987.

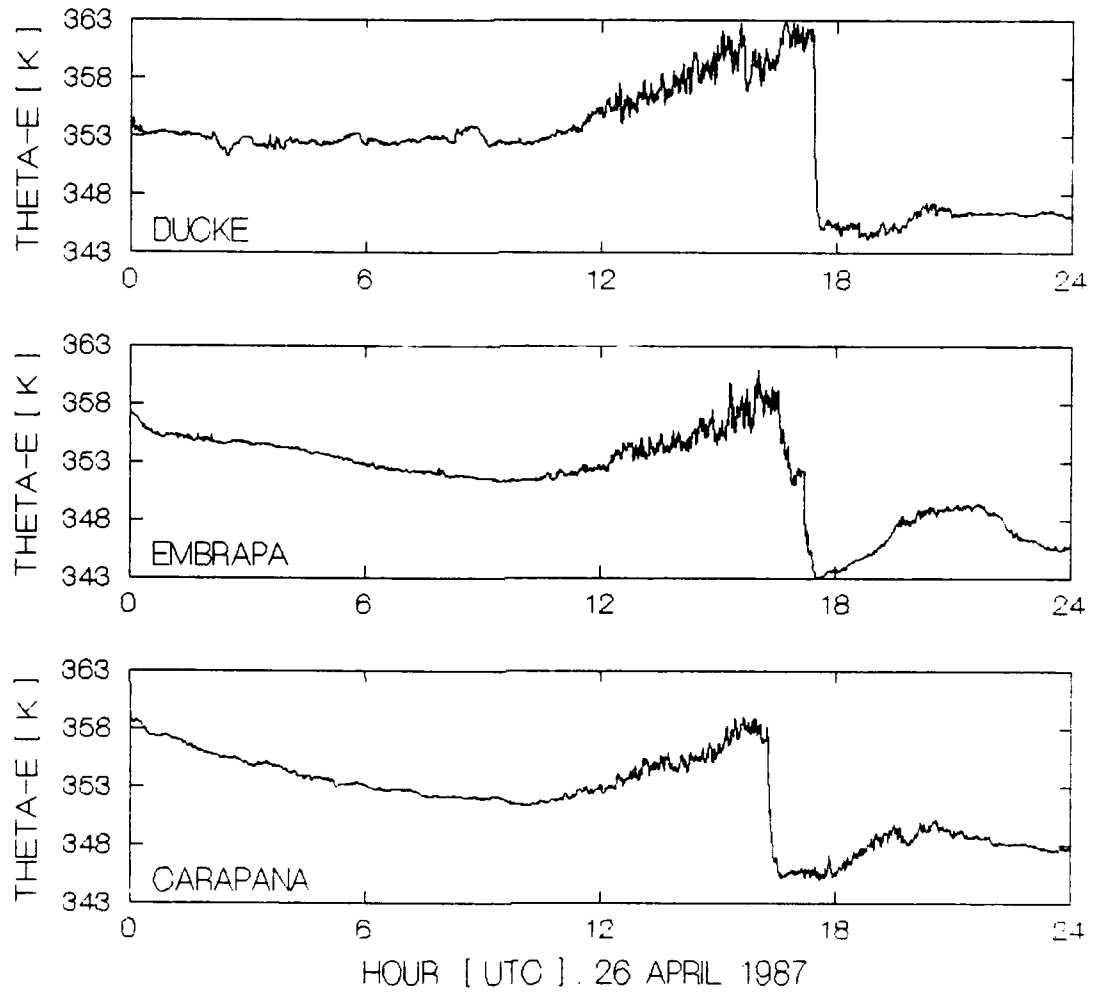


Figure 16. PAM time series of  $\theta_e$  (deg K) on 26 April 1987.

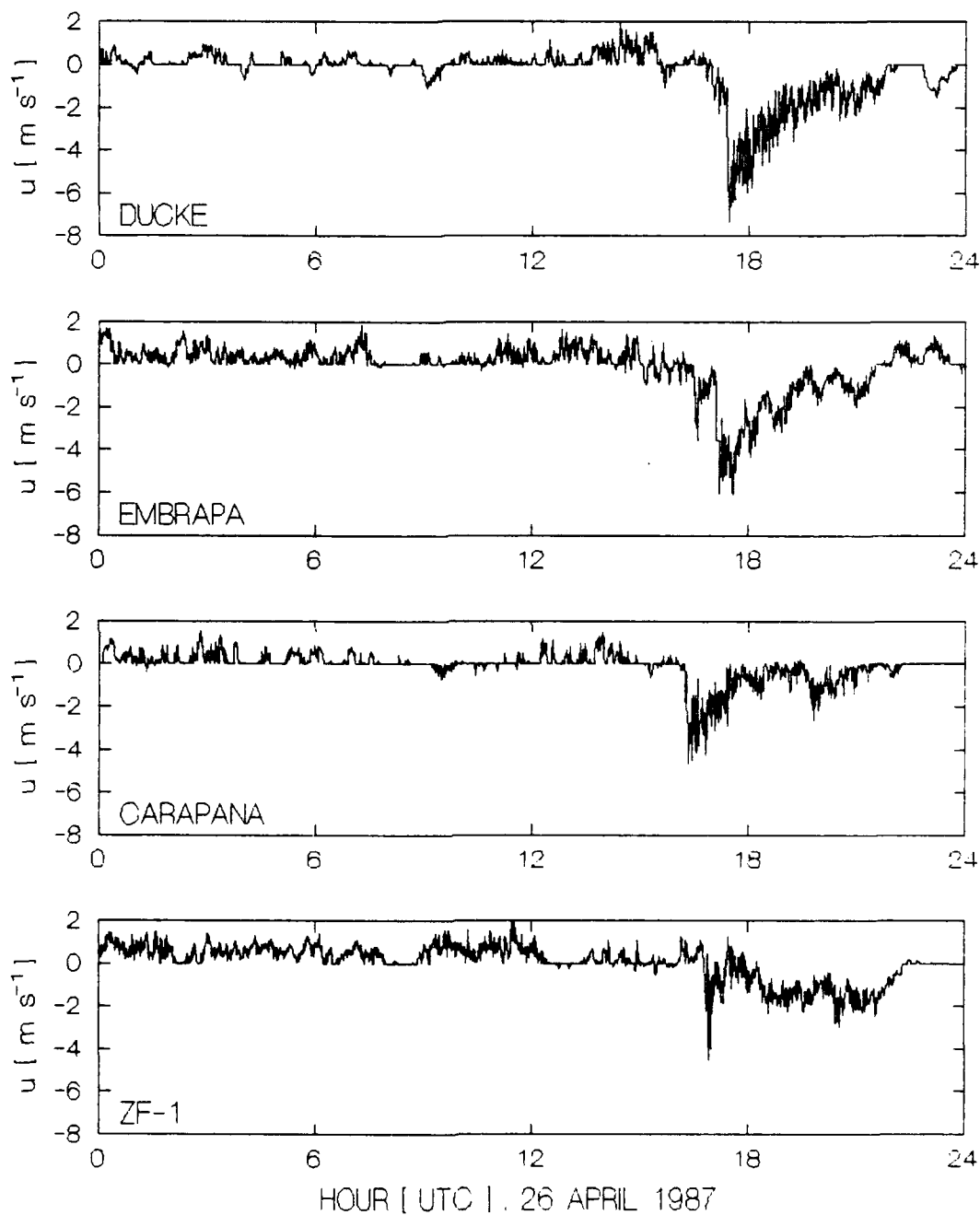


Figure 17. PAM time series of  $u$  ( $\text{m s}^{-1}$ ) on 26 April 1987.

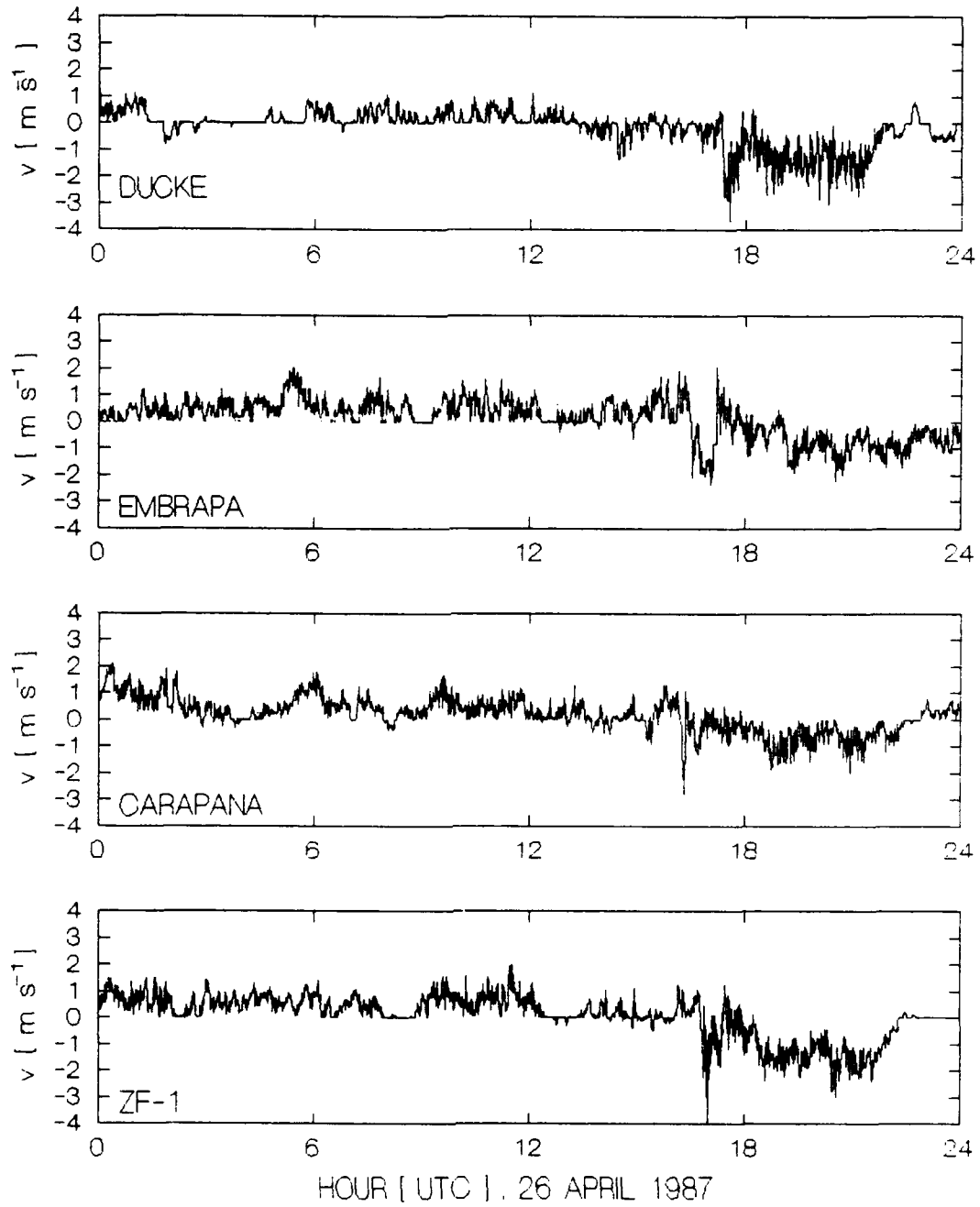


Figure 18. PAM time series of  $v$  ( $\text{m s}^{-1}$ ) on 26 April 1987.

26 APRIL 1987 17 20 50 GMT

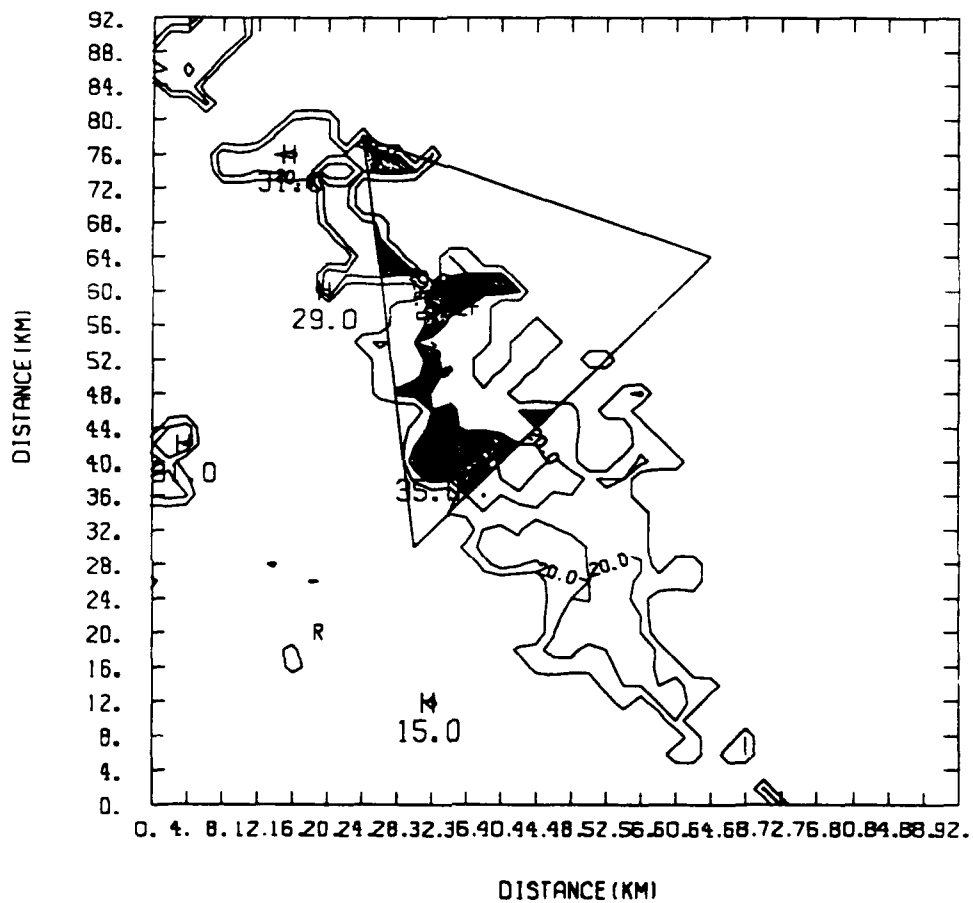


Figure 19. CAPPI radar scan of COS squall line in the mesoscale triangle at 1721 UTC, 26 April 1987.

after the squall front. In the post-squall environment at 27 April 0000 UTC,  $q$  is 2-2.6 g kg<sup>-1</sup> lower,  $T$  is 1-1.5°C lower, and  $\theta_e$  is 8-12 K lower than 24 h earlier at the start of the period. It took nearly five hours for surface winds to return to pre-squall levels.

Vertical time sections of rawinsonde data show pronounced changes in  $u$ ,  $v$ , and  $\theta_e$  (Figures 20-22, respectively). At squall front passage around 1630 UTC,  $u$  (Figure 20) shifts from westerly to easterly in the lower levels and vertical wind shear increases. The meridional winds (Figure 21) shift from southerly to northerly.

Low-level convergence ahead of the squall front is replaced by divergence under the anvil (Figure 23). Upward vertical motion (Figure 24), limited to the lower levels in the pre-squall environment, extends through the whole column as the squall front enters the triangle. Strong subsidence near 300 mb is a well-defined kinematic feature of the pre-squall troposphere. Downward vertical motion occurs in the anvil subcloud region while upward motion exists in mid- and upper-level cloud layers.

Since the rawinsonde release times did not correspond with squall front passage, the vertical time cross sections do not resolve hot towers passing through the triangle between 1630-1730 UTC. Composite analyses of GATE squall lines have shown upward vertical motion increases by an order of magnitude within the cumulus hot tower region

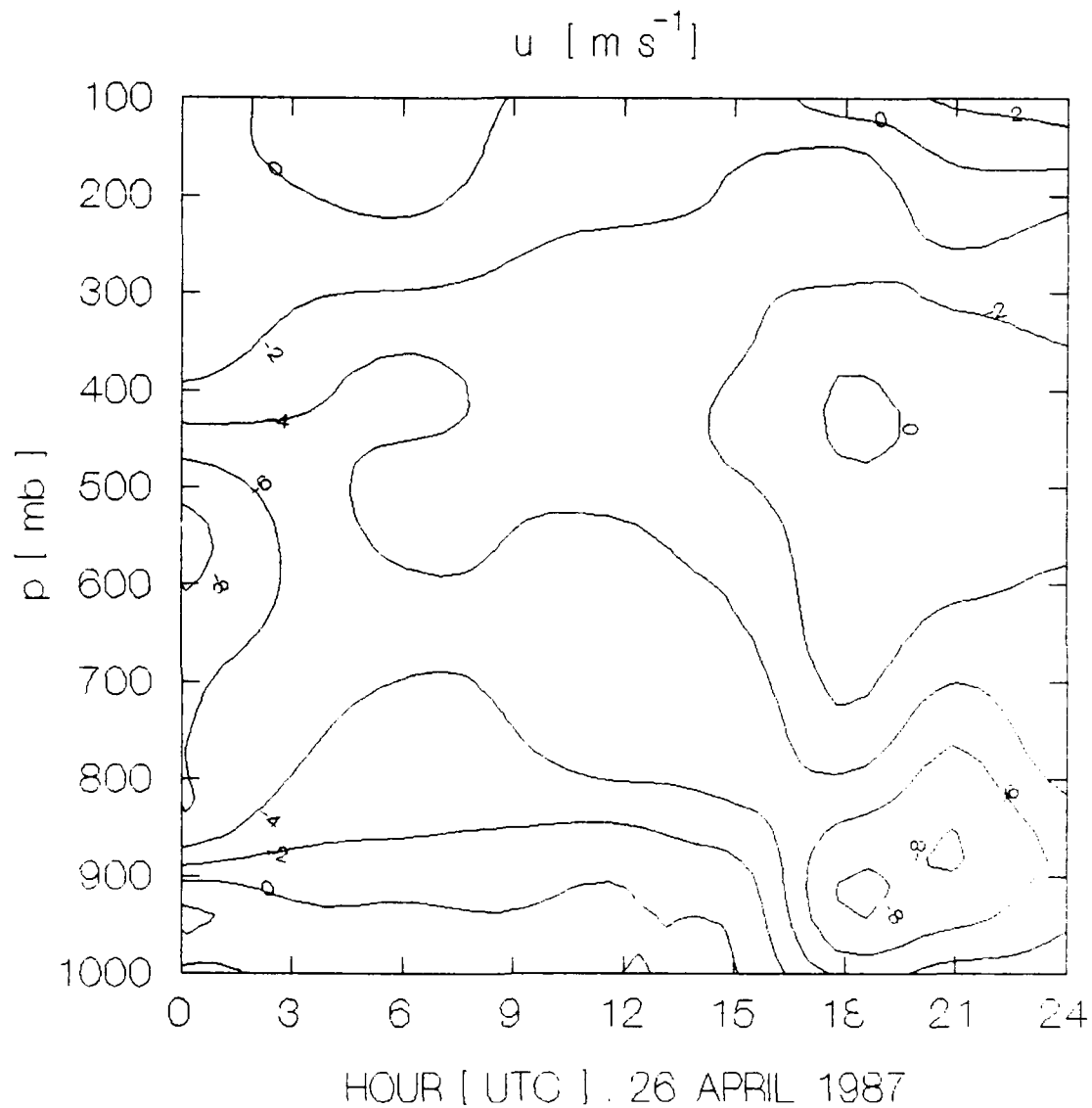


Figure 20. Vertical time cross section of  $\bar{u}$  ( $\text{m s}^{-1}$ ) in the mesoscale triangle on 26 April 1987. The contour interval is  $2 \text{ m s}^{-1}$ .

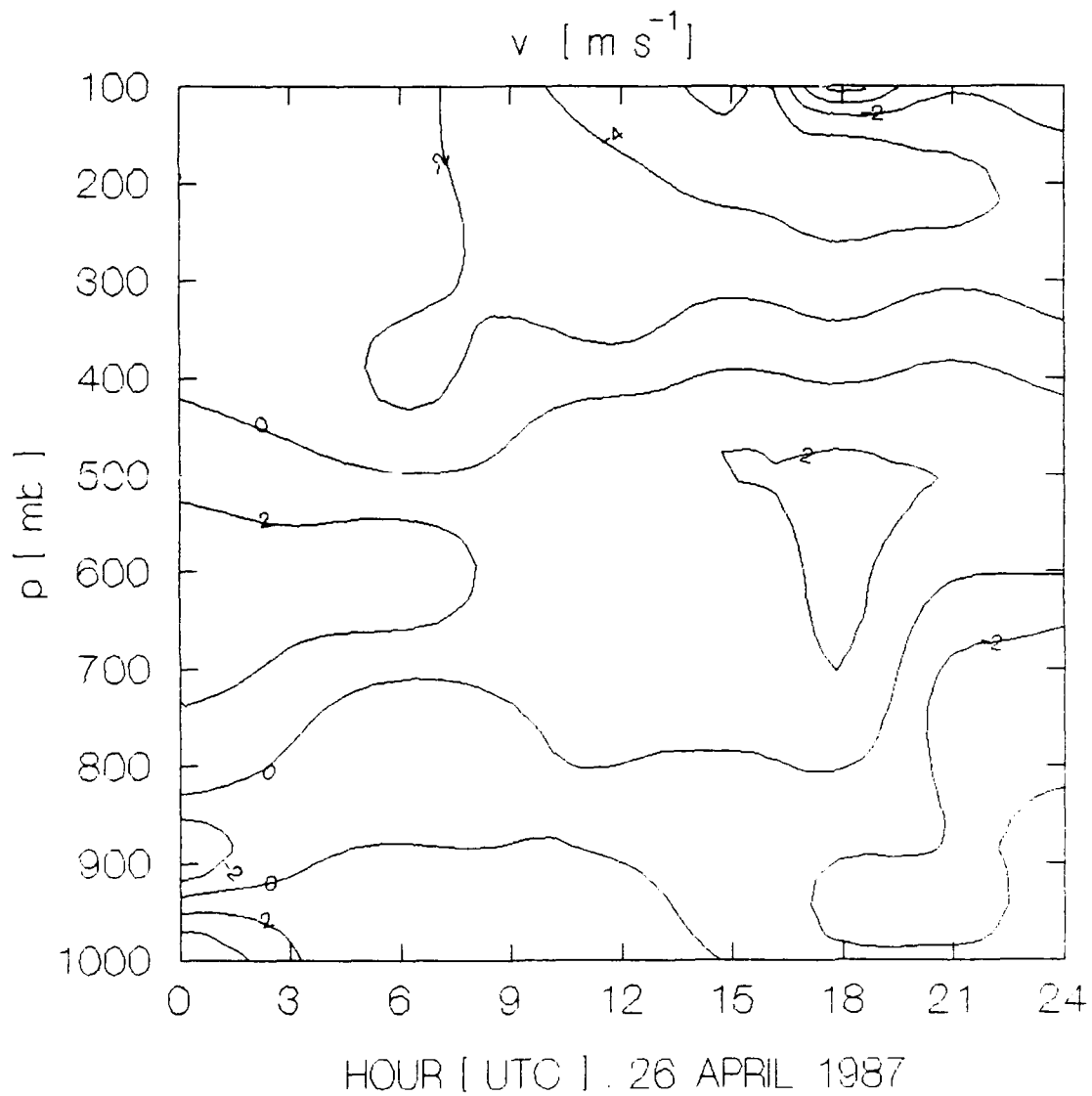


Figure 21. Vertical time cross section of  $\bar{v}$  ( $\text{m s}^{-1}$ ) in the mesoscale triangle on 26 April 1987. The contour interval is  $2 \text{ m s}^{-1}$ .

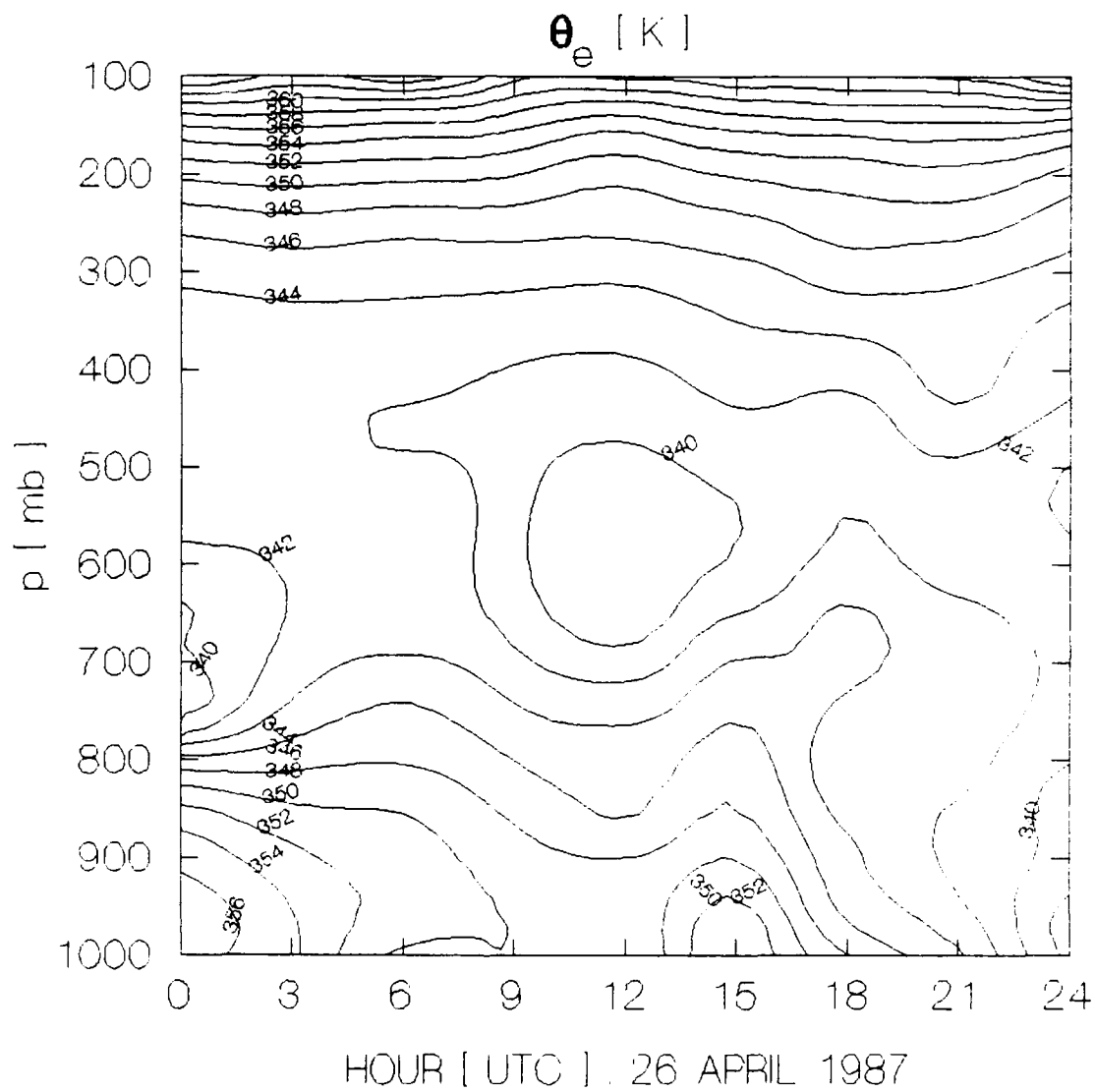


Figure 22. Vertical time cross section of  $\theta_e$  (deg K) in the mesoscale network on 26 April 1987. The contour interval is 2 K.

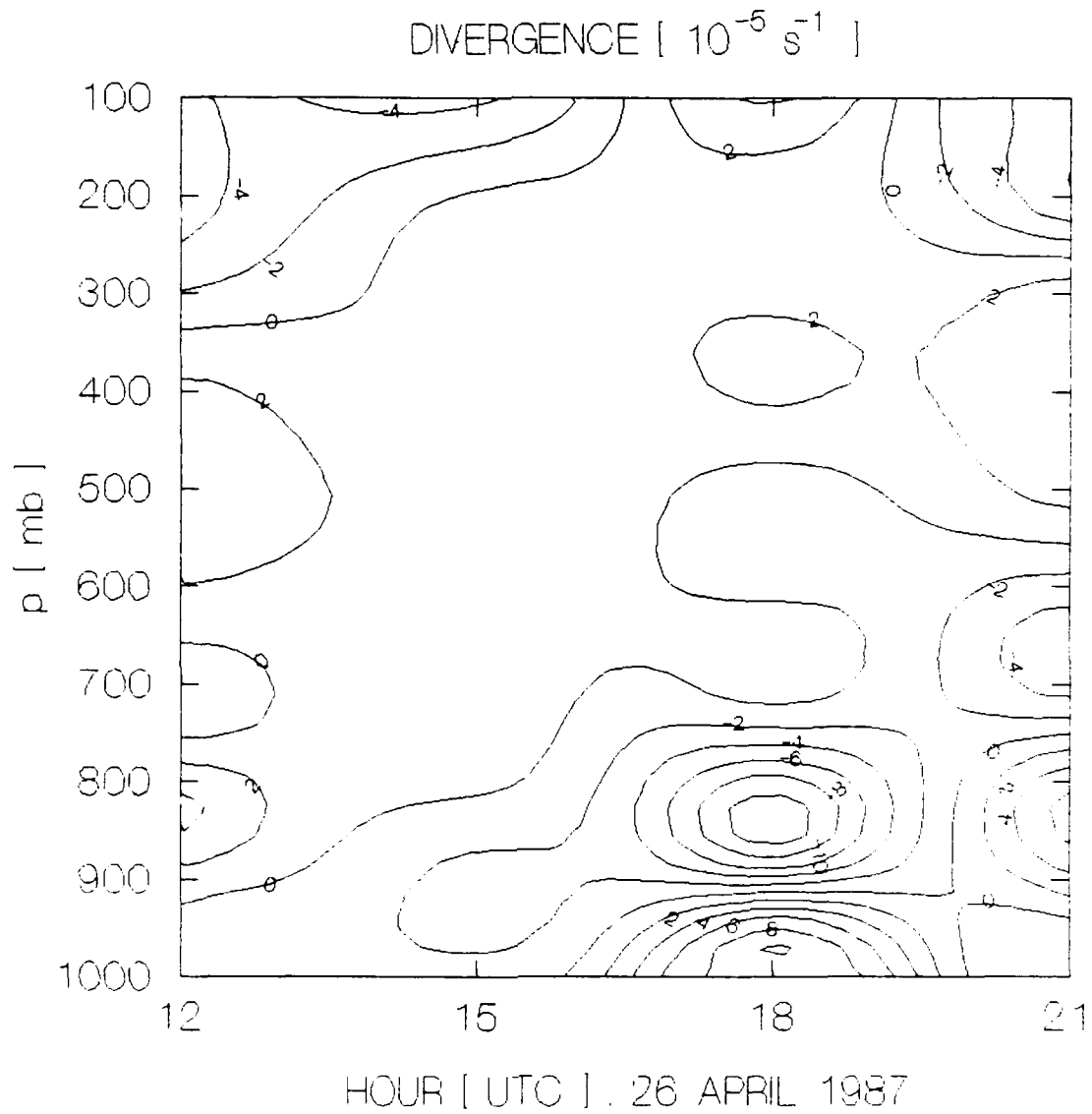


Figure 23. Vertical time cross section of divergence ( $10^{-5} \text{ s}^{-1}$ ) in the mesoscale triangle on 26 April 1987. The contour interval is  $2 \times 10^{-5} \text{ s}^{-1}$ .

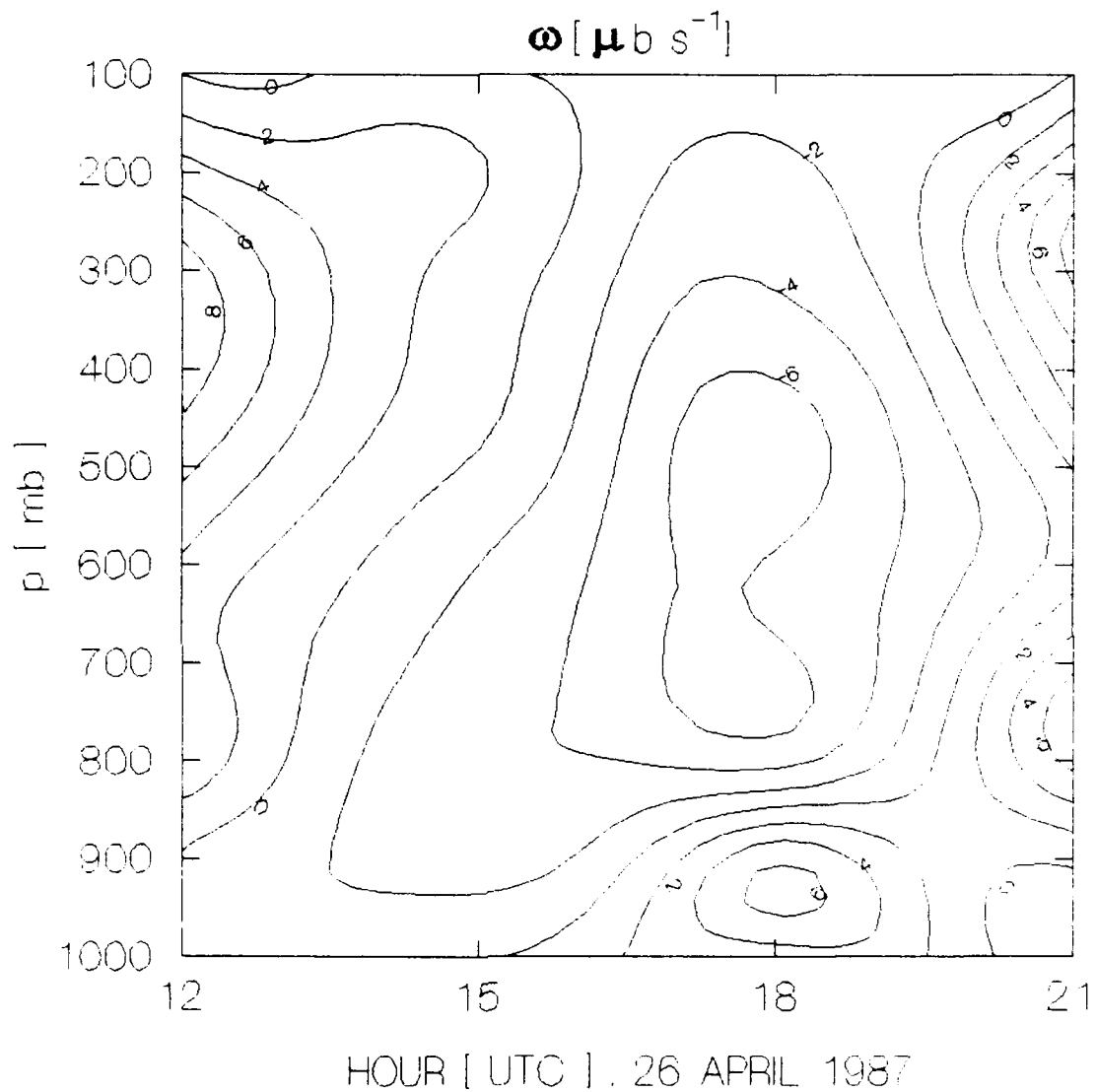


Figure 24. Vertical time cross section of vertical velocity  $\omega$  (microbars  $\text{s}^{-1}$ ) in the mesoscale triangle on 26 April 1987. The contour interval is 2 microbars  $\text{s}^{-1}$ .

(Gamache and Houze, 1982). This feature is not present in the vertical velocity cross section (Figure 24).

Pre-squall relative humidities exceed 90% from the surface to 900 mb (Figure 25). Above this shallow humid layer, a deep dry layer extends to the tropopause and has a minimum relative humidity of less than 30% near 300 mb. Collocation of enhanced upper-level dryness with deep subsidence suggests dynamic communication between the COS and the atmosphere well ahead of the squall front.

The  $\theta_e$  cross section (Figure 22) shows the effects of two different scales of storm updrafts and downdrafts in the convective and stratiform components. At the low levels, a pre-squall  $\theta_e$  maximum is replaced by low  $\theta_e$  under the anvil. Identical patterns for  $\theta_e$  are typically observed in tropical squall lines (Miller and Betts, 1977; Houze, 1982). Intense, localized convective downdrafts transport cool, dry air from the mid levels to replace warm, moist air rising in updrafts. The downdrafts produce a shallow pool of cold, dry air that spreads near the surface in the form of density current. Moistening and further cooling occurs as light stratiform precipitation falls from the anvil and evaporates. This cooling is partially offset by adiabatic warming in broad area of steady subsidence beneath the anvil.

Profiles of the heat and moisture budgets in building cumuli are shown in Figures 26-27, respectively. The sensible heat source (Figure 26) indicates mid- and low-

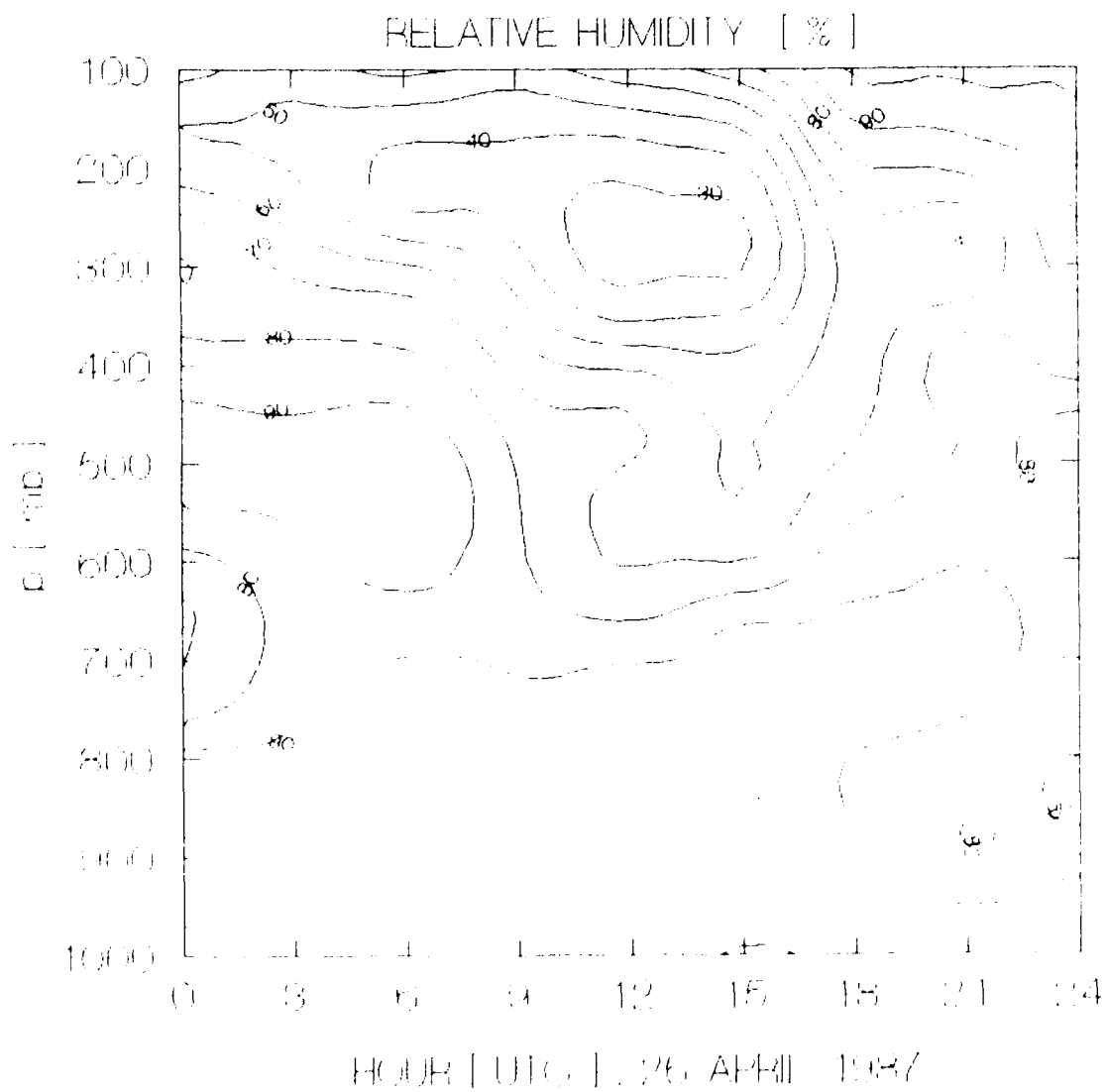


Figure 25. Vertical time cross section of area mean relative humidity (%) in the mesoscale triangle on 26 April 1987. The contour interval is 10%.

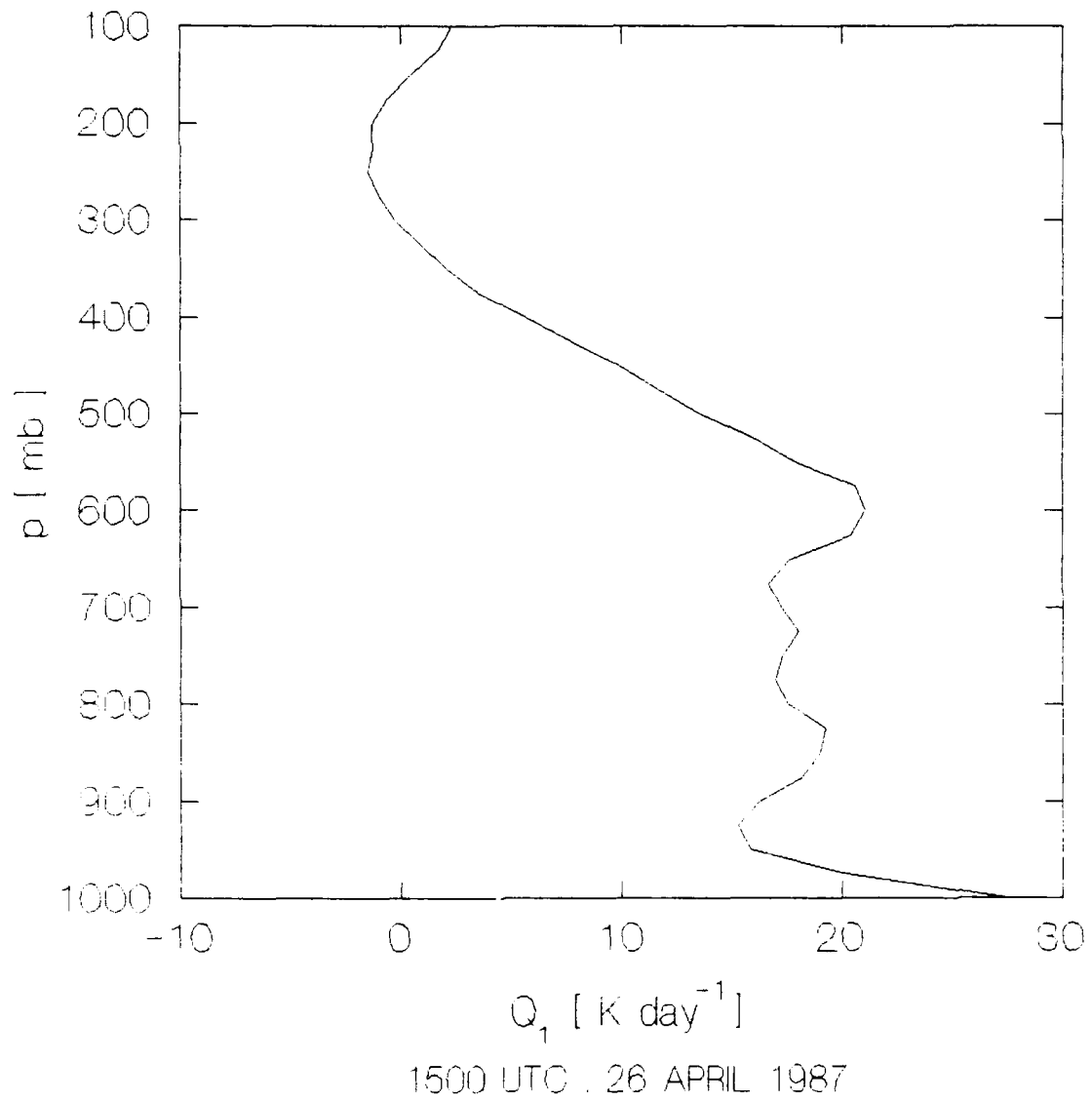


Figure 26. Apparent sensible heat source (K day<sup>-1</sup>) in the mesoscale triangle during the COS building cumulus component at 1500 UTC, 26 April 1987.

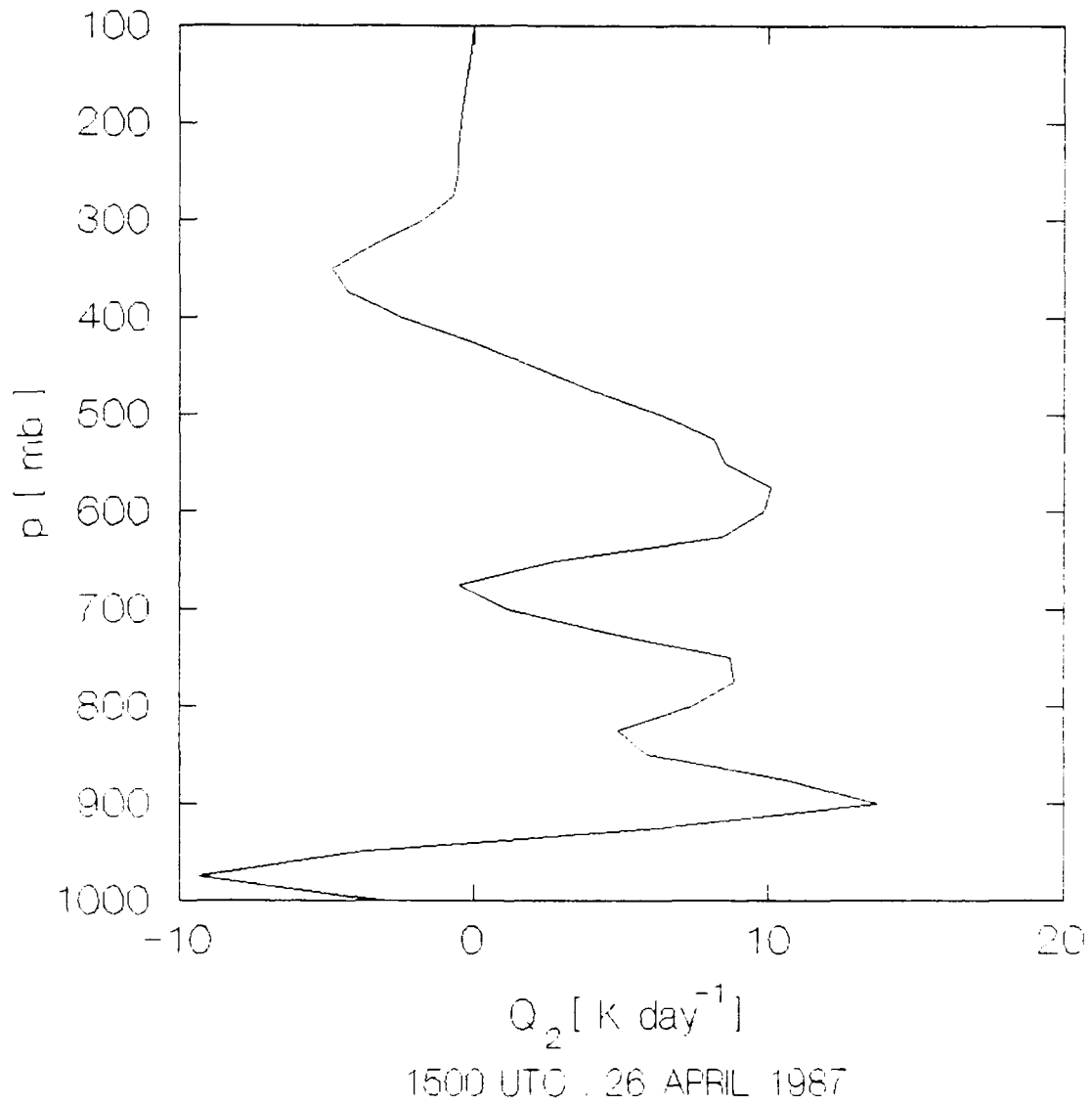


Figure 27. Apparent moisture sink (K day<sup>-1</sup>) in the meso-scale triangle during the COS building cumulus component at 1500 UTC, 26 April 1987.

Heating and moistening in building cumuli are shown in Figures 26-27, respectively. Low- and mid-level heating (Figure 26) result mainly from vertical advection of  $s$ . The moisture budget shows moistening below 925 mb and drying between 925 and 400 mb (Figure 27). The low-level moistening results from evaporation in the rain forest and convergence. Subsidence mainly accounts for the upper level drying.

Heating profiles for long- and shortwave radiation are shown in Figures 28-29, respectively. A longwave cooling of  $\sim 15 \text{ K day}^{-1}$  at cloud top and a longwave warming of  $\sim 4 \text{ K day}^{-1}$  at cloud base agree well with radiational heating and cooling rates observed in winter MONEX anvils by Webster and Stephens (1980). The net effect of radiation warms the cloud bases and cools the cloud tops.

The vertical eddy flux of total heat (Figure 30) decreases from a maximum surface value of  $\sim 900 \text{ W m}^{-2}$  to small values in the upper troposphere. The diagnosed total surface energy flux exceeds the maximum midday values reported at Ducke in September 1983 by Shuttleworth et al. (1984) and approximately equals the maximum midday values observed in July 1985 by Fitzjarrald et al. (1987).

Heat and moisture budgets for the anvil (1800 UTC) are shown in Figures 31-32, respectively. In the anvil subcloud layer,  $Q_1$  (Figure 31) shows a maximum cooling rate of  $\sim 45 \text{ K day}^{-1}$  near 925 mb. In the anvil, there is strong

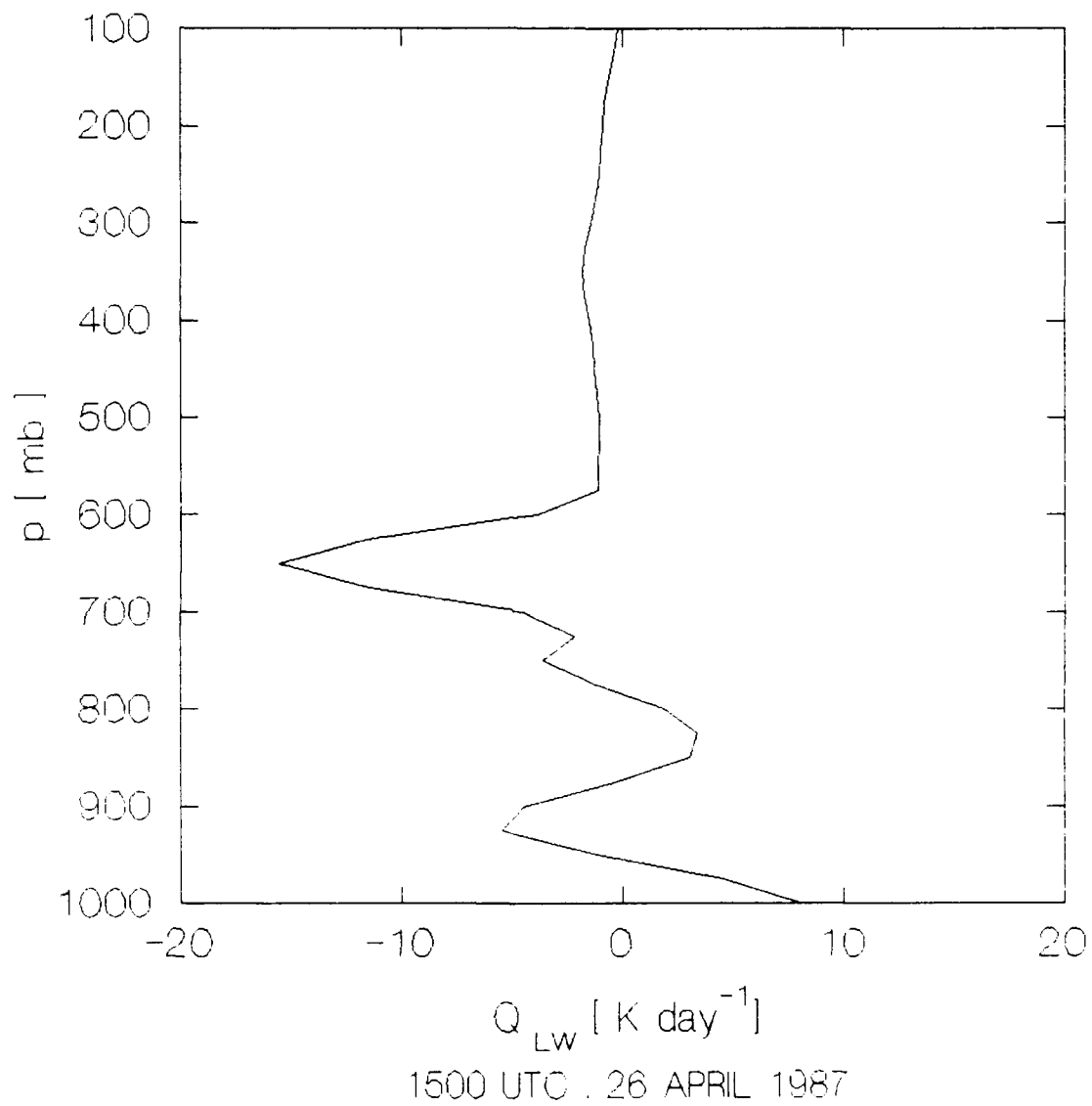


Figure 28. Rate of temperature change ( $\text{K day}^{-1}$ ) due to longwave radiation in the mesoscale triangle during the COS building cumulus component at 1500 UTC, 26 April 1987.

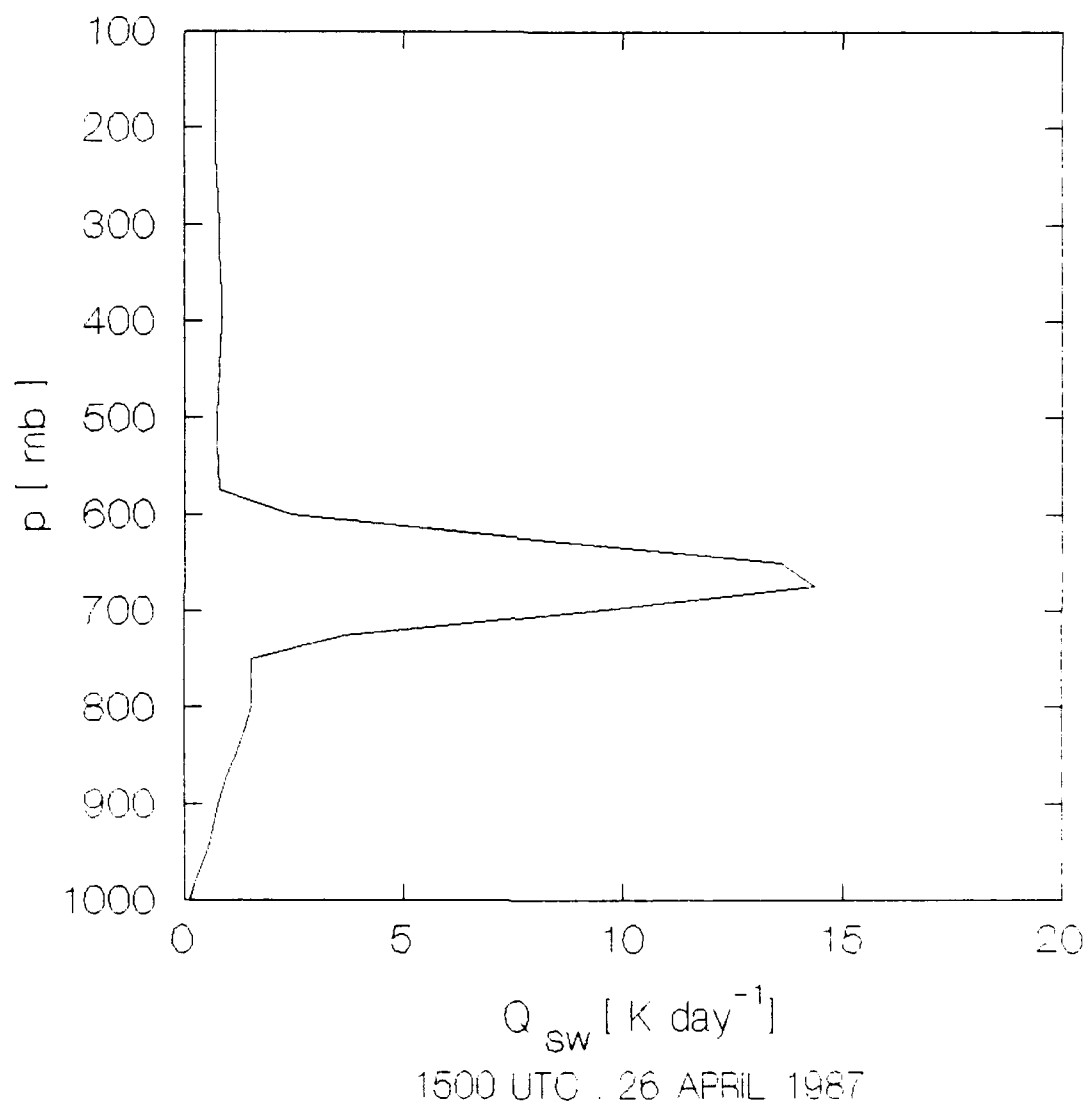


Figure 29. Rate of temperature change (K day<sup>-1</sup>) due to shortwave radiation in the mesoscale triangle during the COS building cumulus component at 1500 UTC, 26 April 1987.

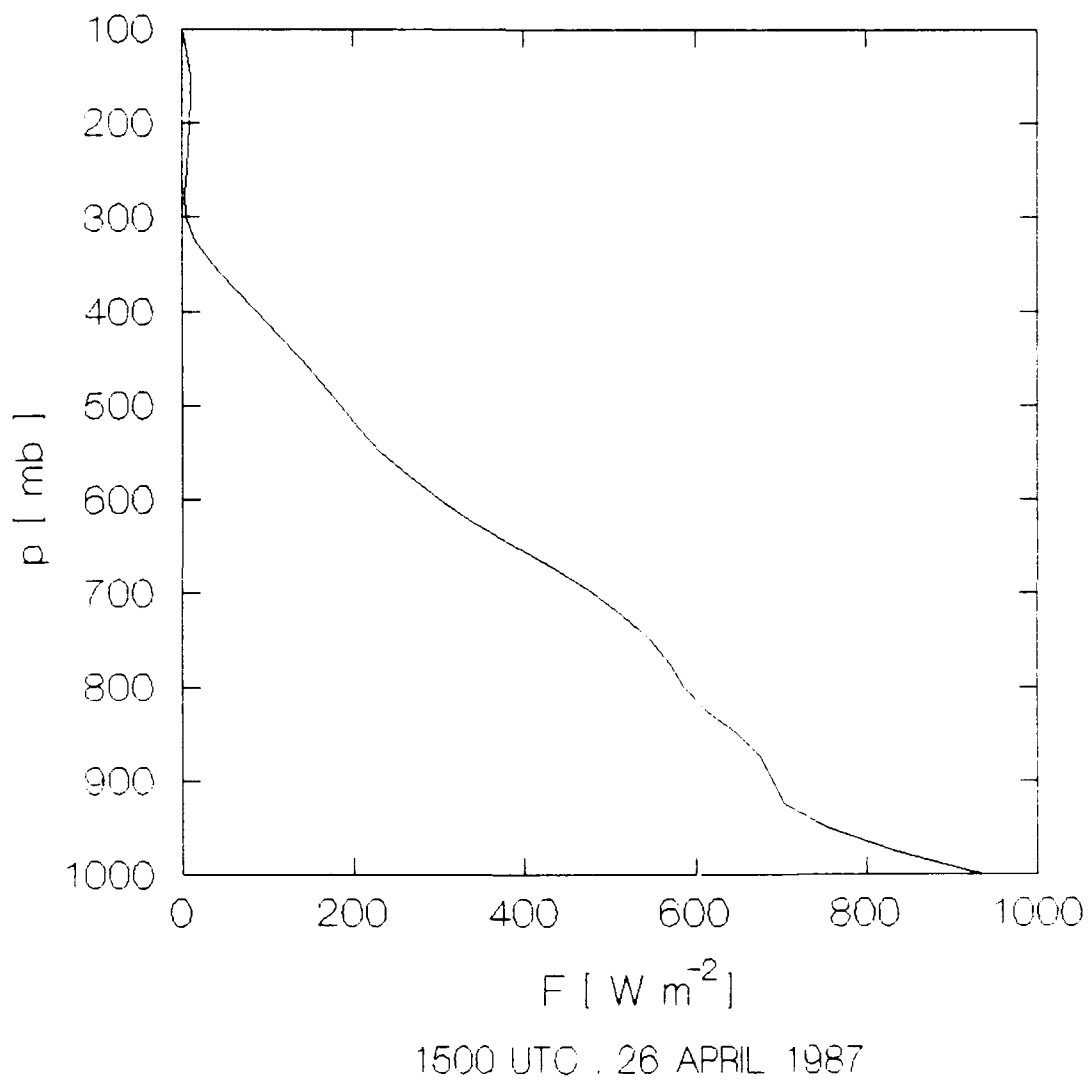


Figure 30. Vertical eddy flux of total heat ( $\text{W m}^{-2}$ ) in the mesoscale triangle during the COS building cumulus component at 1500 UTC, 26 April 1987.

heating with maxima of  $\sim 40 \text{ K day}^{-1}$  and  $30 \text{ K day}^{-1}$  at 700 mb and 500 mb, respectively. The  $Q_1$  profile resembles those obtained from budget calculations for Winter MONEX anvils by Johnson and Young (1983). Houze (1982) attributes the heating maximum in the anvil to condensation and freezing. According to Houze (1982), the evaporation and melting of precipitation in dry air below the anvil largely explains the low-level cooling.

The  $Q_2$  profile (Figure 32) reveals low-level moistening from the surface to 900 mb, above which there is strong drying with maxima near 800 mb and 500 mb, respectively. The profile resembles  $Q_2$  profiles obtained by Johnson and Young (1983) for Winter MONEX anvils.

The relative humidity cross section (Figure 25) indicates two stratiform cloud layers comprise the COS anvil region. The lower layer extends from 800 to 500 mb while the upper layer reaches from 200 to 100 mb. The GOES MB images show some cloud tops extend to about 125 mb. Longwave radiation (Figure 33) cools the upper part of each cloud layer. However, warming from shortwave absorption (Figure 34) nearly equals longwave cooling. The net result is little temperature change in the anvil due to radiation.

The total surface energy flux of  $\sim 100 \text{ W m}^{-2}$  (Figure 35) is substantially smaller in the anvil than in building cumuli. The eddy flux increases through the subcloud layer to a maximum of  $\sim 800 \text{ W m}^{-2}$  near 750 mb and

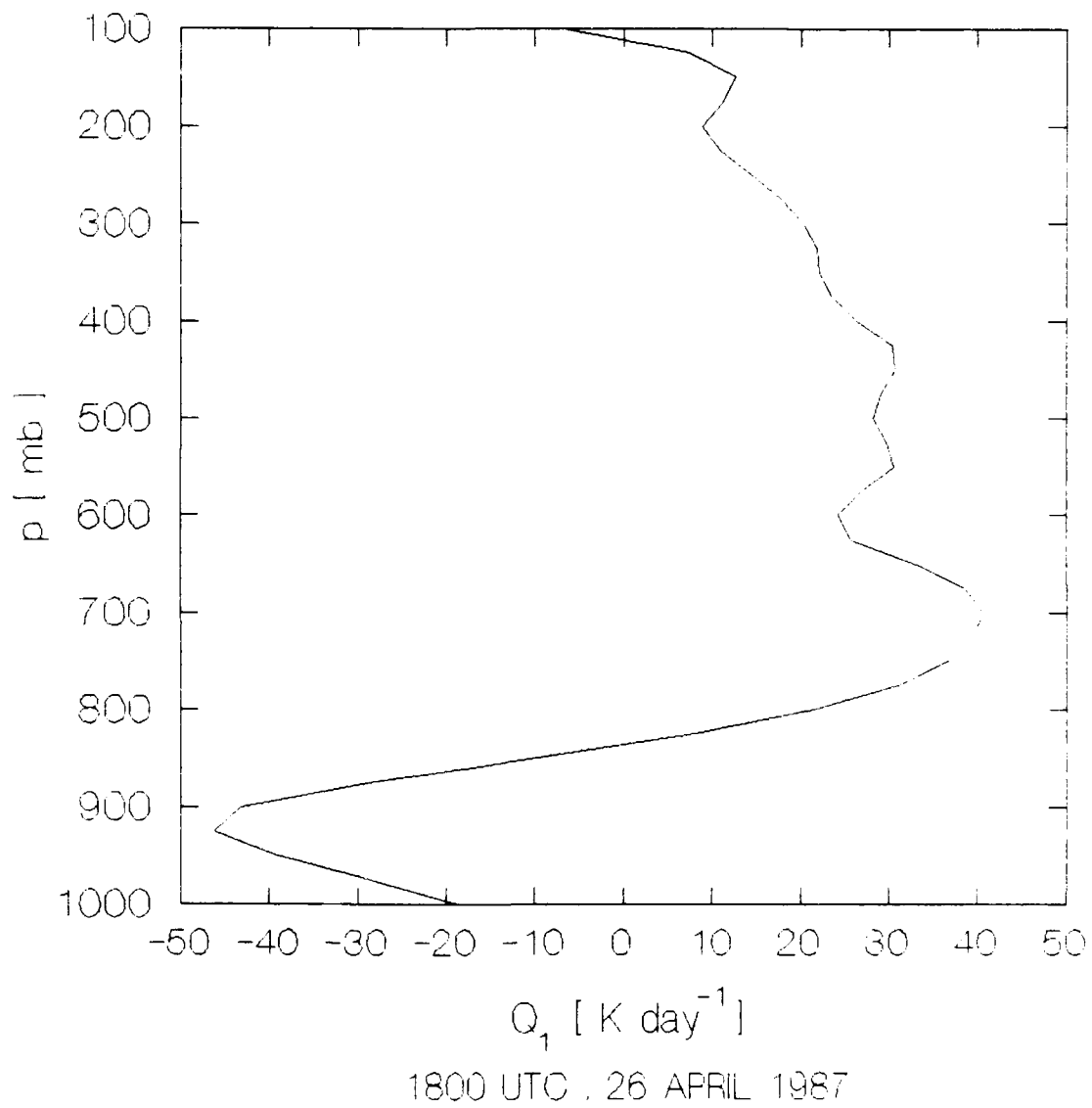


Figure 31. Apparent sensible heat source ( $\text{K day}^{-1}$ ) in the mesoscale triangle during the COS anvil component at 1800 UTC, 26 April 1987.

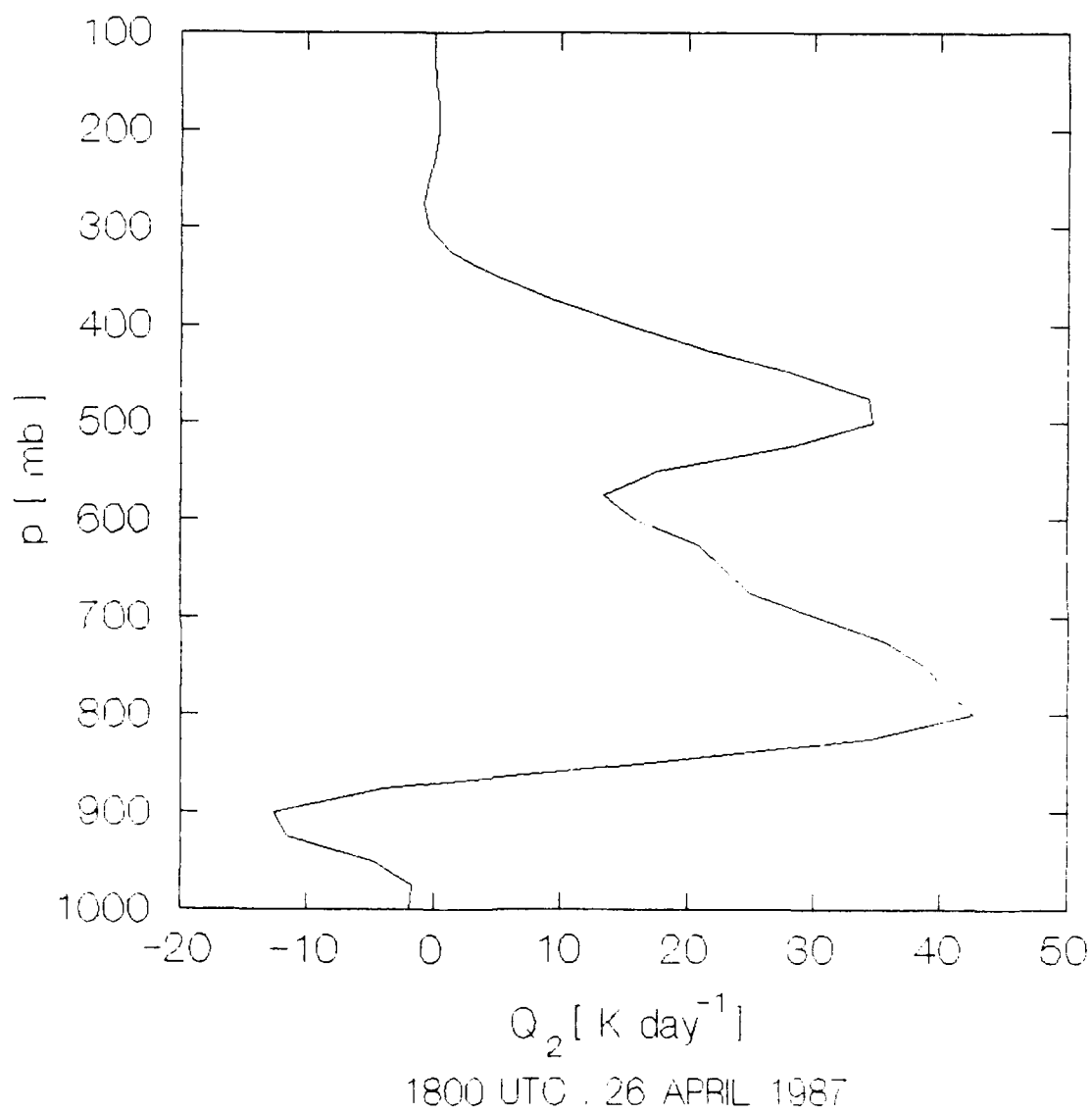


Figure 32. Apparent moisture sink ( $K \text{ day}^{-1}$ ) in the meso-scale triangle during the COS anvil component at 1800 UTC, 26 April 1987.

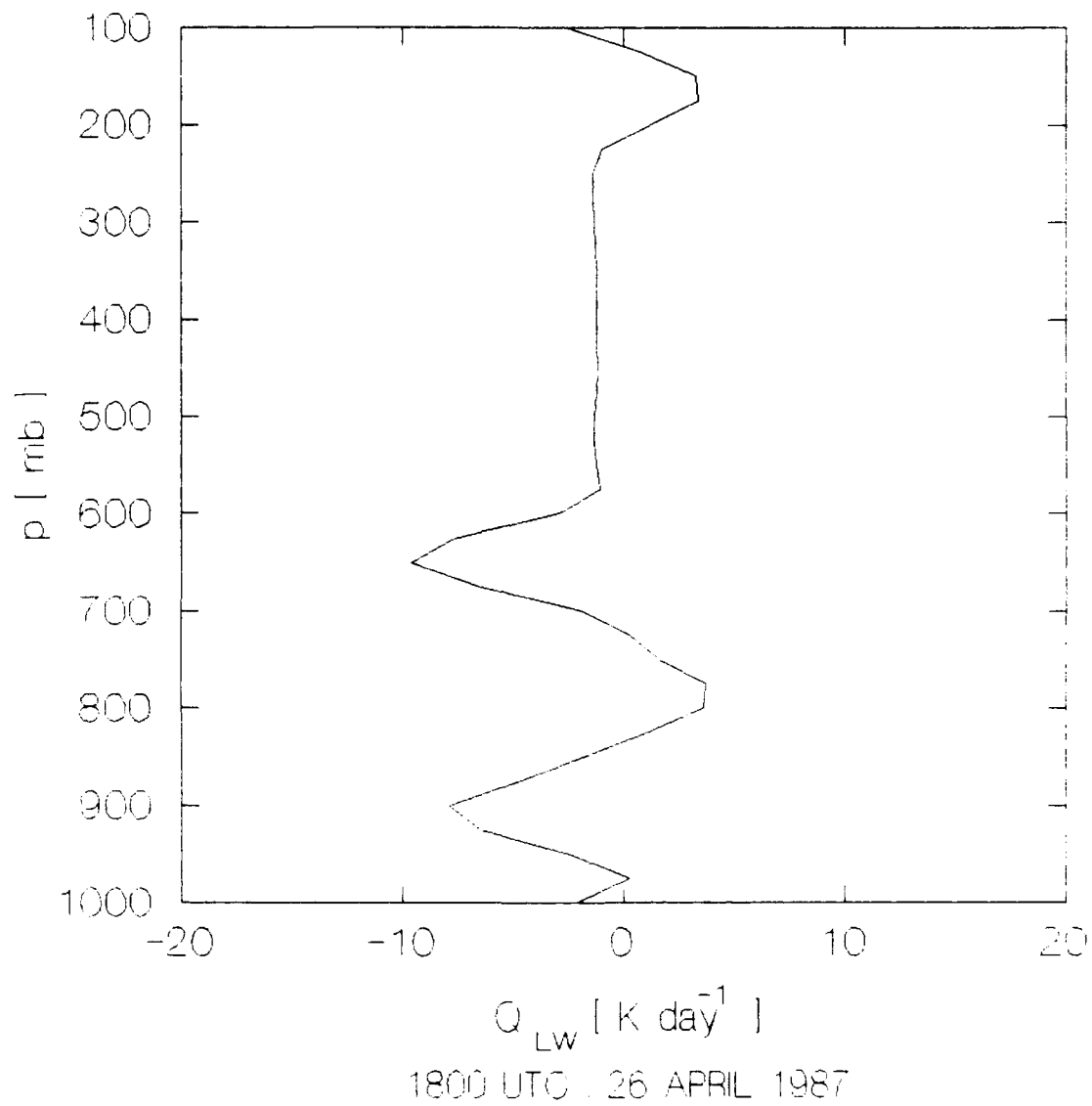


Figure 33. Rate of temperature change due to longwave radiation in the mesoscale triangle during the COS anvil component at 1800 UTC, 26 April 1987.

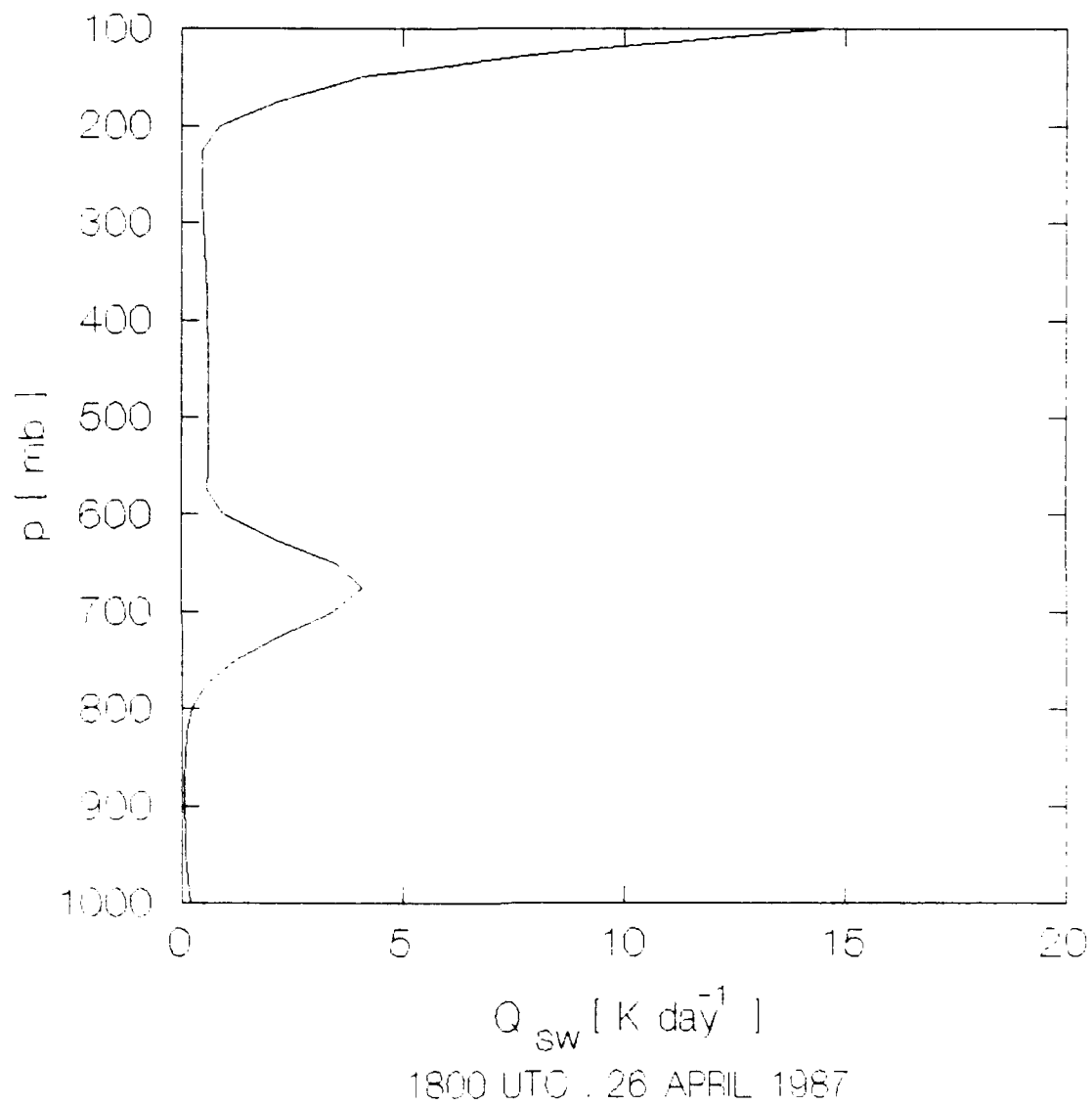
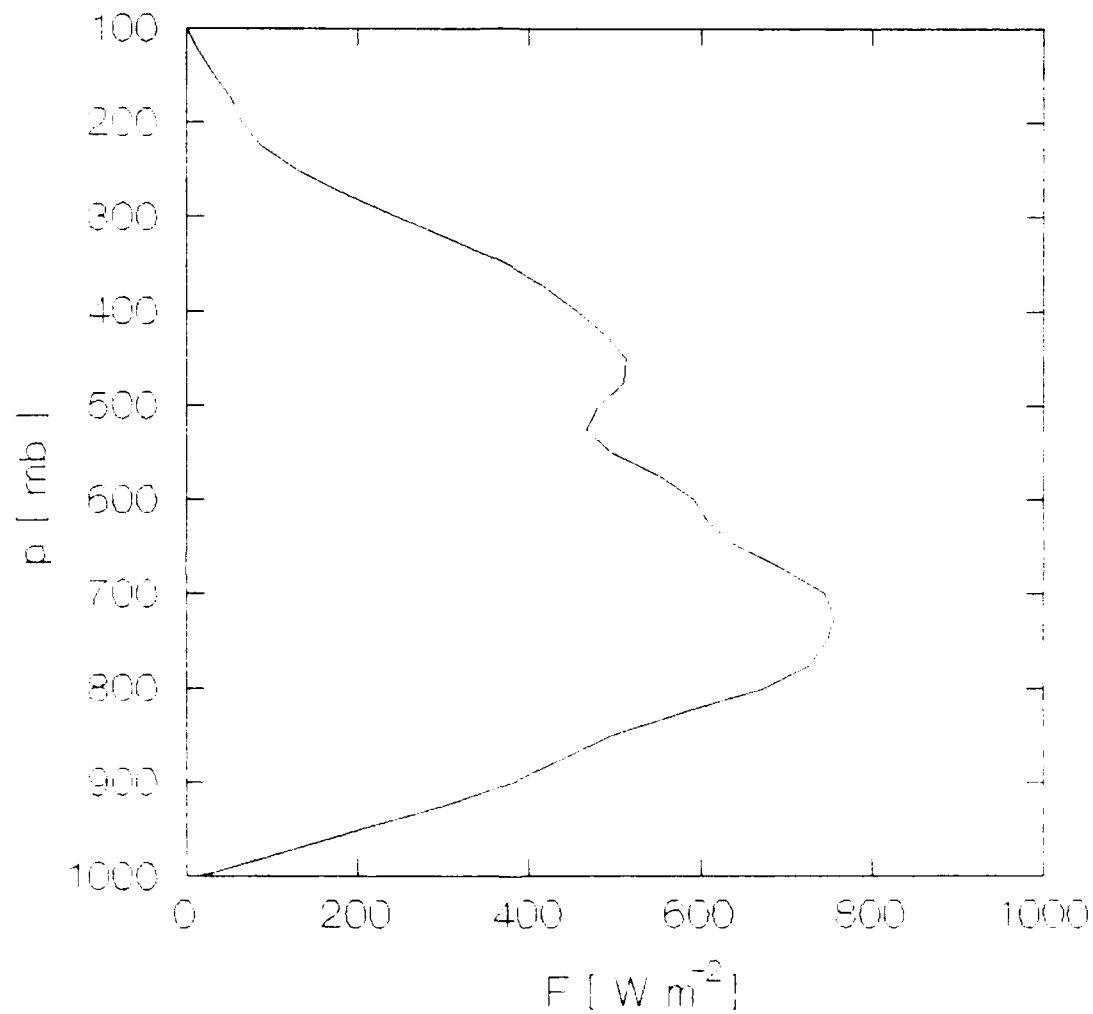


Figure 34. Rate of temperature change due to shortwave radiation in the mesoscale triangle during the COS anvil component at 1800 UTC, 26 April 1987.



1800 UTC, 26 APRIL 1987

Figure 35. Vertical eddy flux of total heat ( $\text{W m}^{-2}$ ) in the mesoscale triangle during the COS anvil component at 1800 UTC, 26 April 1987.

then decreases in the upper levels. These values of  $F$  are up to seven times greater than those diagnosed in either the GATE B-scale network (Nitta, 1977; Thompson et al., 1979) or in the western Pacific Kwajalein-Eniwetok-Ponape triangle network (Reed and Recker, 1971). They are slightly less than the values of  $F$  diagnosed by Gallus and Johnson (1991) in mid-latitude anvils.

**B. Mature COS, 1 May 1987**

On 1 May 1987, from ~ 1200-2100 UTC, the cumulus hot towers and anvils of a mature COS passed through the triangle. From ~ 0500-0800 UTC a mesoscale convective cloud cluster well ahead of the COS produced thunderstorms and heavy rain in the northern part of the triangle. However, it will be shown that the effects of the earlier cluster are minimal compared to those observed after passage of the COS squall front.

A telecommunications failure during thunderstorms caused a six-hour interruption in PAM data during the passage of the COS squall front and part of the anvil. Satellite images, surface observations from Eduardo Gomes Airport in Manaus, and triangle soundings are combined with the fragmented PAM time series to classify the cloud and rainfall components.

The COS formed during the afternoon of 30 April along the northern coast of Brazil and coincided with a marked increase in deep convection over the equatorial Atlantic (Figure 36-37). The MB image at 1700 UTC (Figure 37) shows numerous small convective clusters located north and south of a larger mesoscale cluster near the mouth of the Amazon river.

By 2130 UTC (Figure 38), the smaller clusters, had grown rapidly and merged to form a synoptic bow-shaped COS

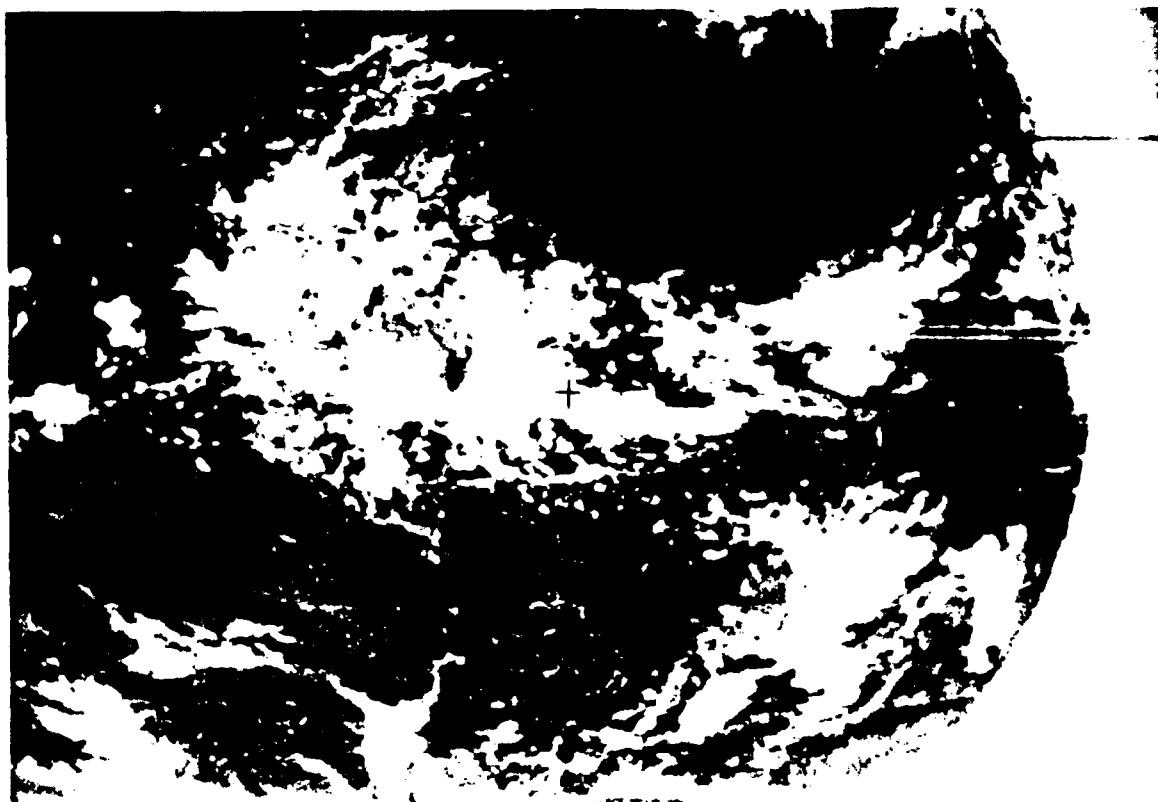
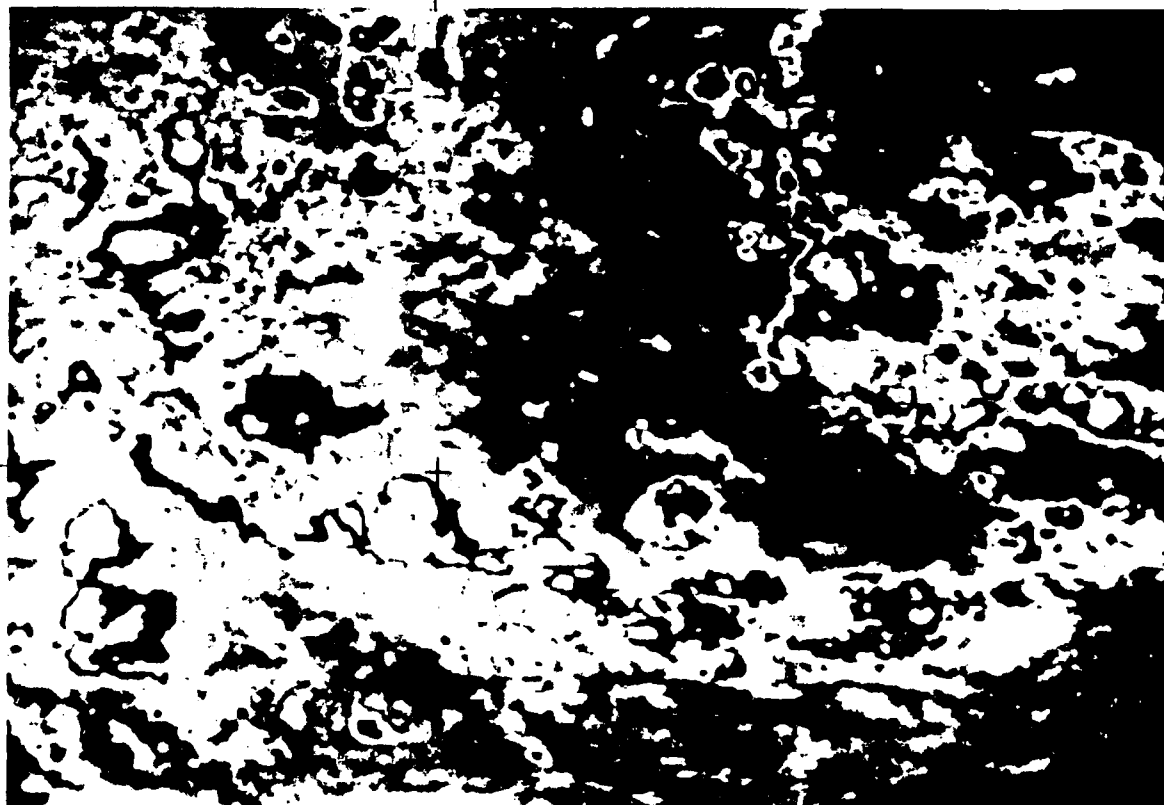
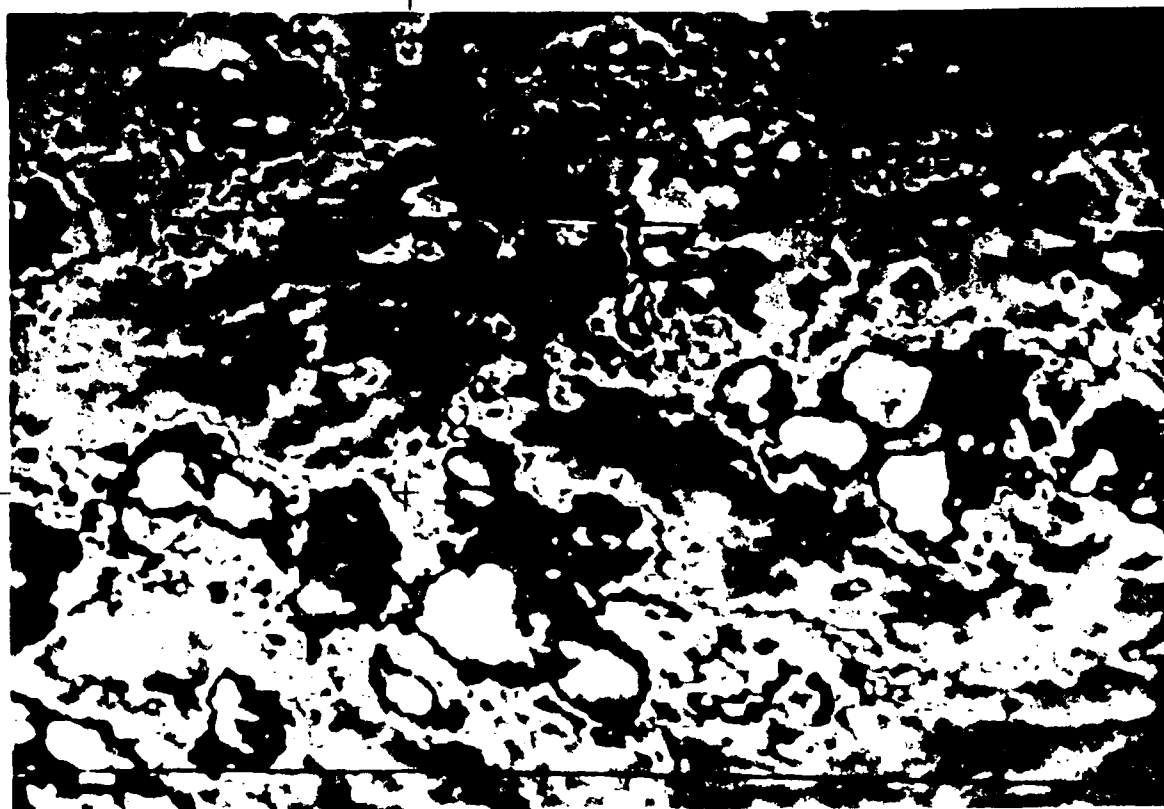


Figure 36. The GOES full disk IR image at 1800 UTC, 30 April 1987 showing COS in the intensifying stage over the northeast coast of Brazil. The + denotes 3°S, 60°W.



500 km

Figure 37. The GOES MB-enhanced IR image at 1700 UTC, 30 April 1987 showing COS (upper right part of figure) in the intensifying stage over the northeast coast of Brazil. The + denotes 3°S, 60°W.



500 km

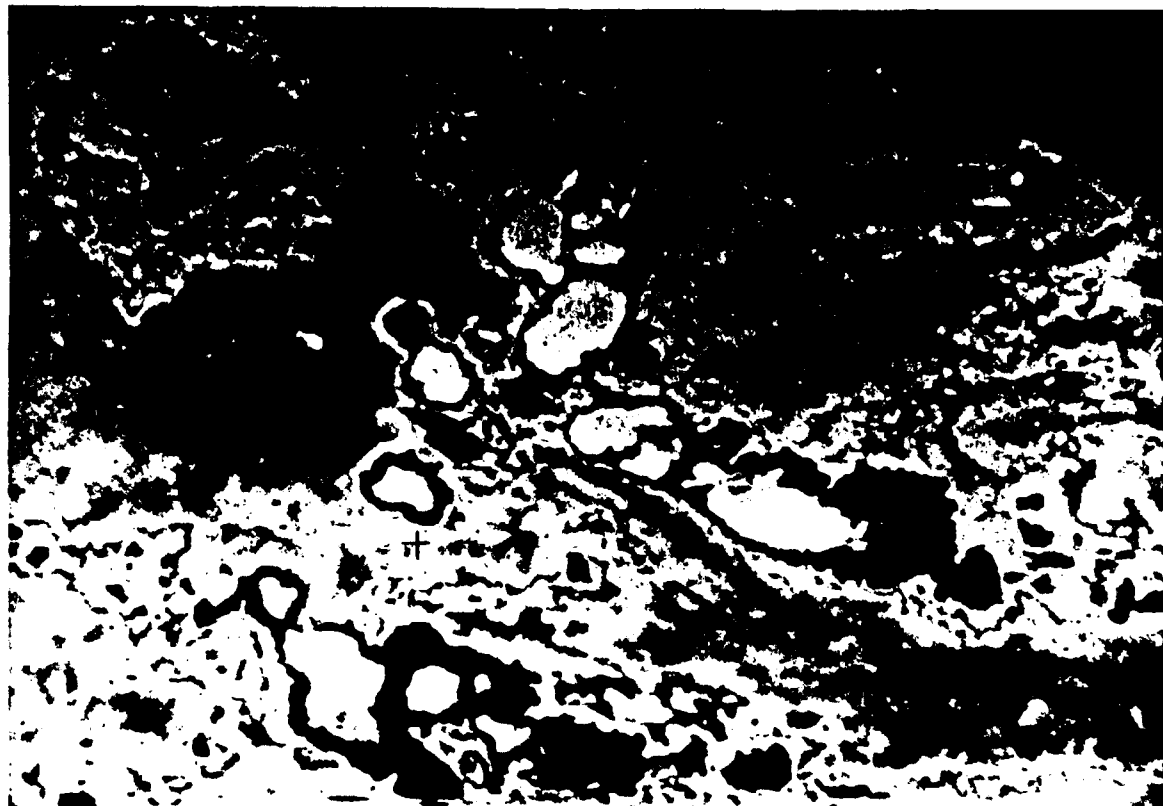
Figure 38. The GOES MB-enhanced IR image at 2130 UTC, 30 April 1987 showing COS (upper right part of figure) as it propagates inland from the northeast coast of Brazil. A second COS is also seen in the lower left part of the figure. The + denotes 3°S, 60°W.

with quasi-linear features as in the 26 April system. Cloud areas in white surrounded by black and dark gray indicate intense thunderstorms. By 0230 UTC (Figure 39) a group of smaller mesoscale clusters had formed ~ 250 km ahead of the COS squall front. The mesoscale clusters produced heavy rain in the northern part of the triangle six hours before COS passage.

Satellite analysis reveals the COS propagated southwestward with a forward speed of ~ 65 km h<sup>-1</sup>. The squall front arrived at the airport around 1300 UTC when hourly observations showed mean winds of 12 m s<sup>-1</sup>, recent thunderstorms, and moderate rain. Airport data indicate the squall front moved through the triangle between 1200-1300 UTC with peak winds of ~ 15 m s<sup>-1</sup> and convective rain.

Airport observations are consistent with the time series of  $\theta_e$  (Figure 40) before and after the PAM interruption. They also agree well with the vertical time sections of rawinsonde winds, relative humidity, and  $\theta_e$  (Figures 41-44, respectively).

The PAM time series of total rain (Figure 45) show heavy rain at Embrapa, Carapana, and ZF-1 from ~ 0500-0700 UTC, followed by data interruption at all sites. The total rainfall measurements show no precipitation either at Ducke or at the airport during the data interruption. It is evident the earlier rain fell mainly in the northern part of



500 km

---

Figure 39. The GOES MB-enhanced IR image at 0230 UTC, 1 May 1987 showing mature COS (center of figure) as it propagates westward towards the mesoscale triangle. The + denotes 3°S, 60°W.

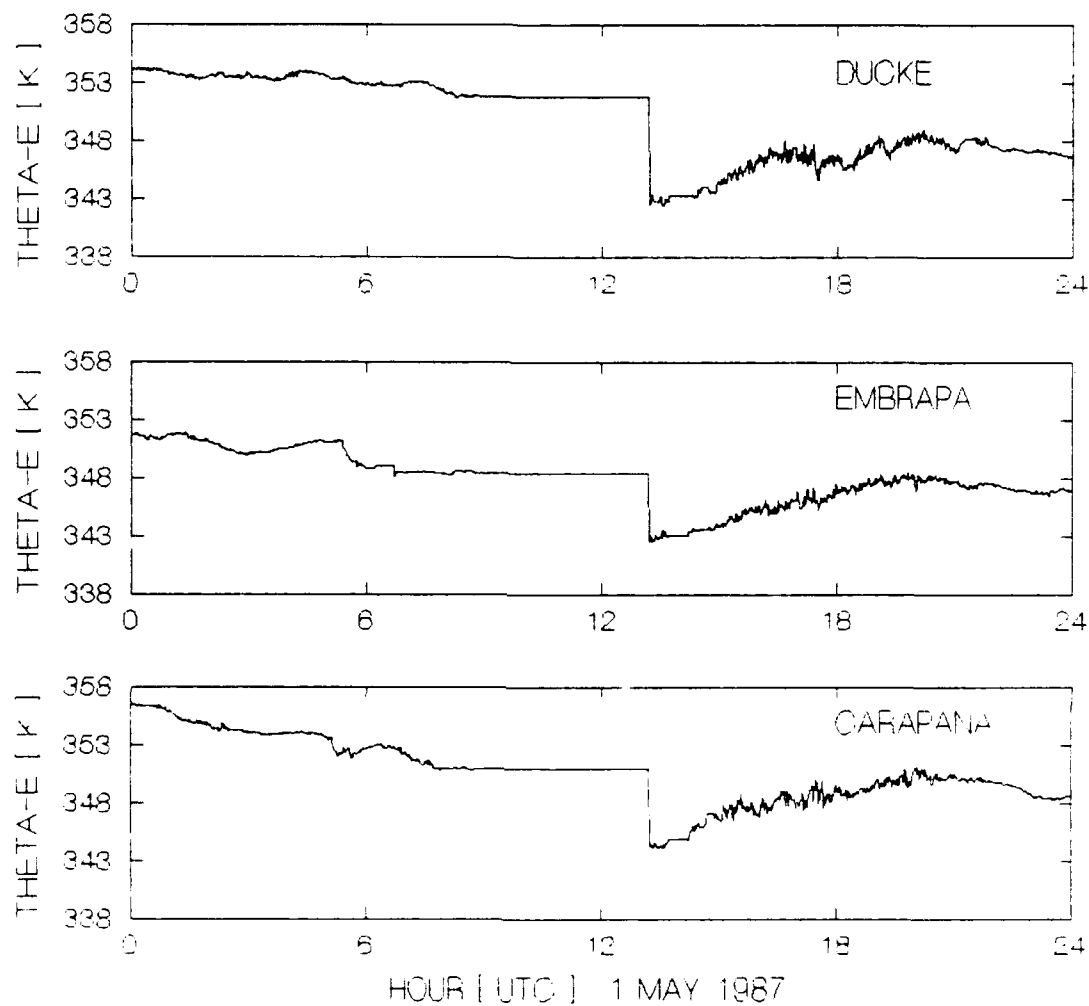


Figure 40. PAM times series of  $\theta_e$  (deg K) on 1 May 1987.  
Lightning interrupted PAM measurements from  
approximately 0900-1300 UTC.

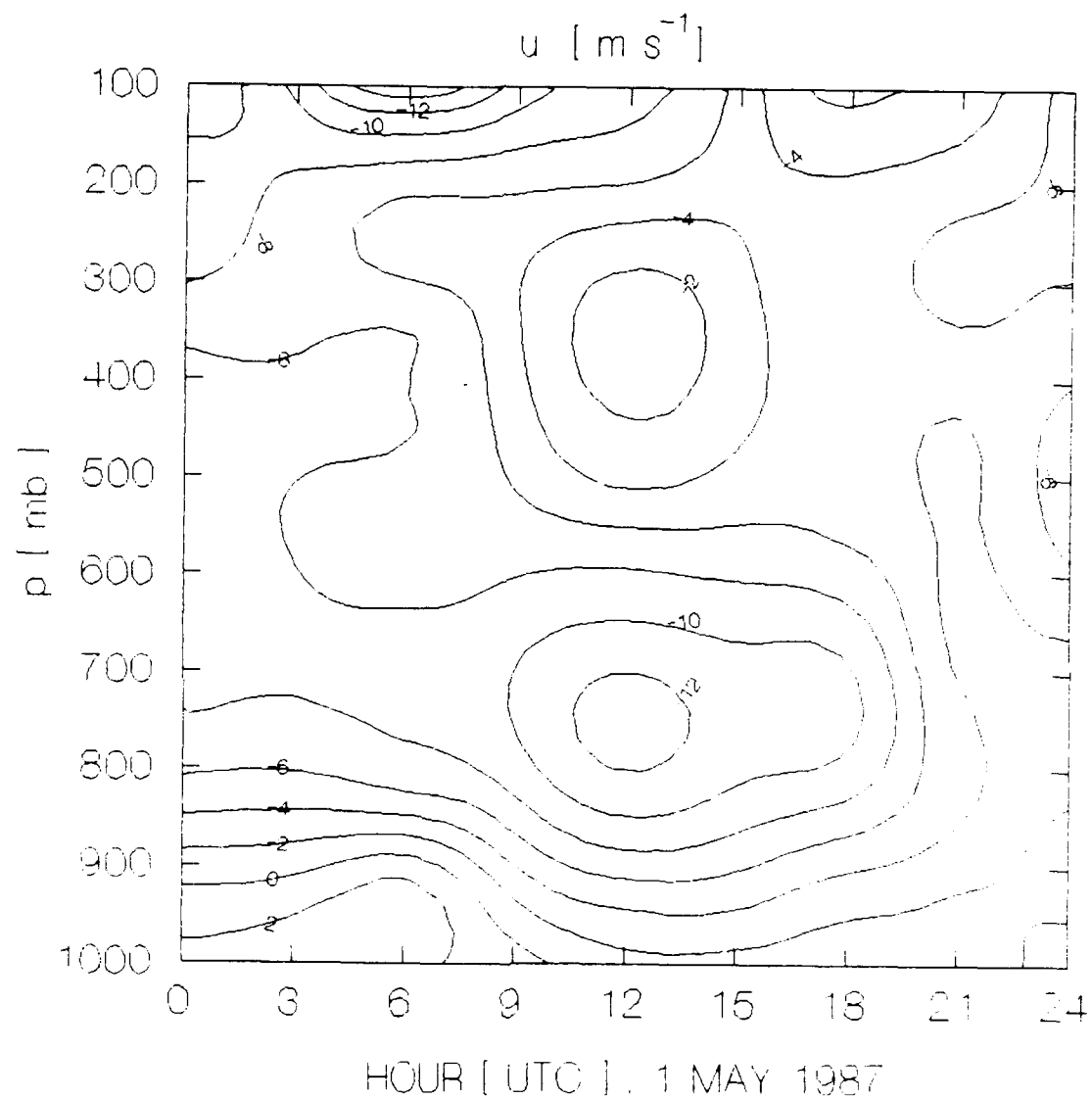


Figure 41. Vertical time cross section of  $\bar{u}$  ( $\text{m s}^{-1}$ ) in the mesoscale triangle on 1 May 1987. The contour interval is  $2 \text{ m s}^{-1}$ .

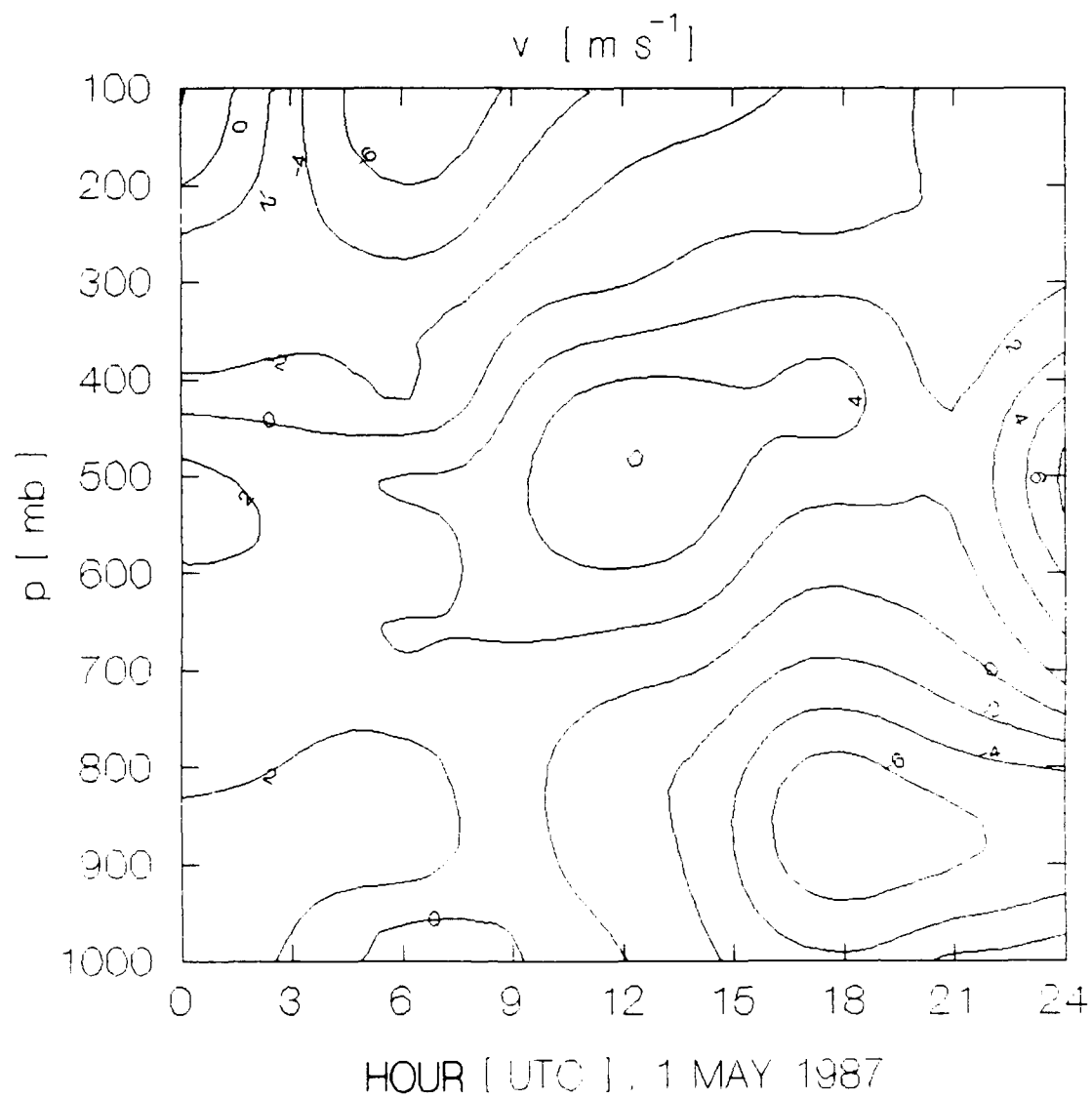


Figure 42. Vertical time cross section of  $\bar{v}$  ( $\text{m s}^{-1}$ ) in the mesoscale triangle on 1 May 1987. The contour interval is  $2 \text{ m s}^{-1}$ .

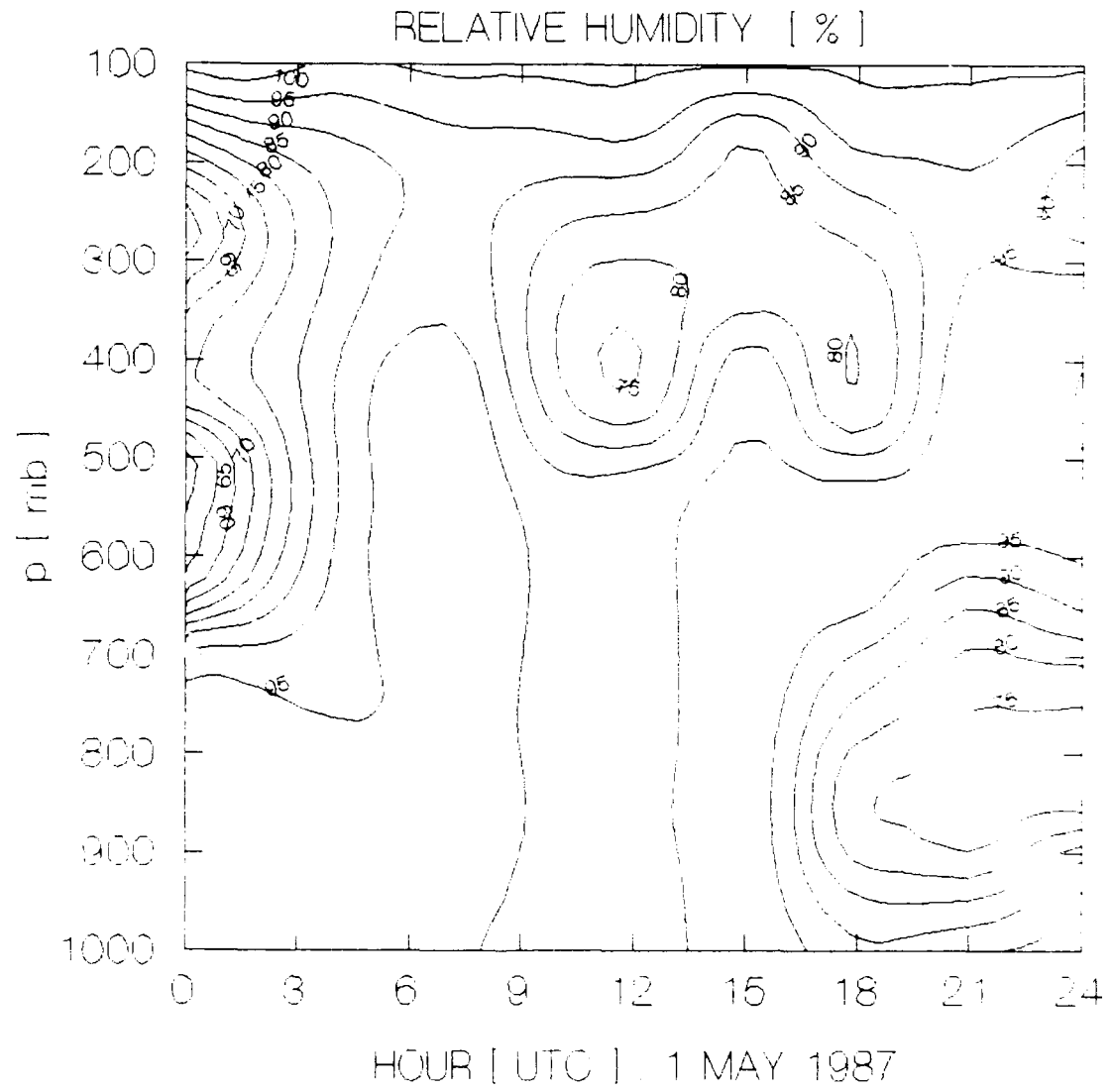


Figure 43. Vertical time cross section of mean relative humidity (%) in the mesoscale triangle on 1 May 1987. The contour interval is 5%.



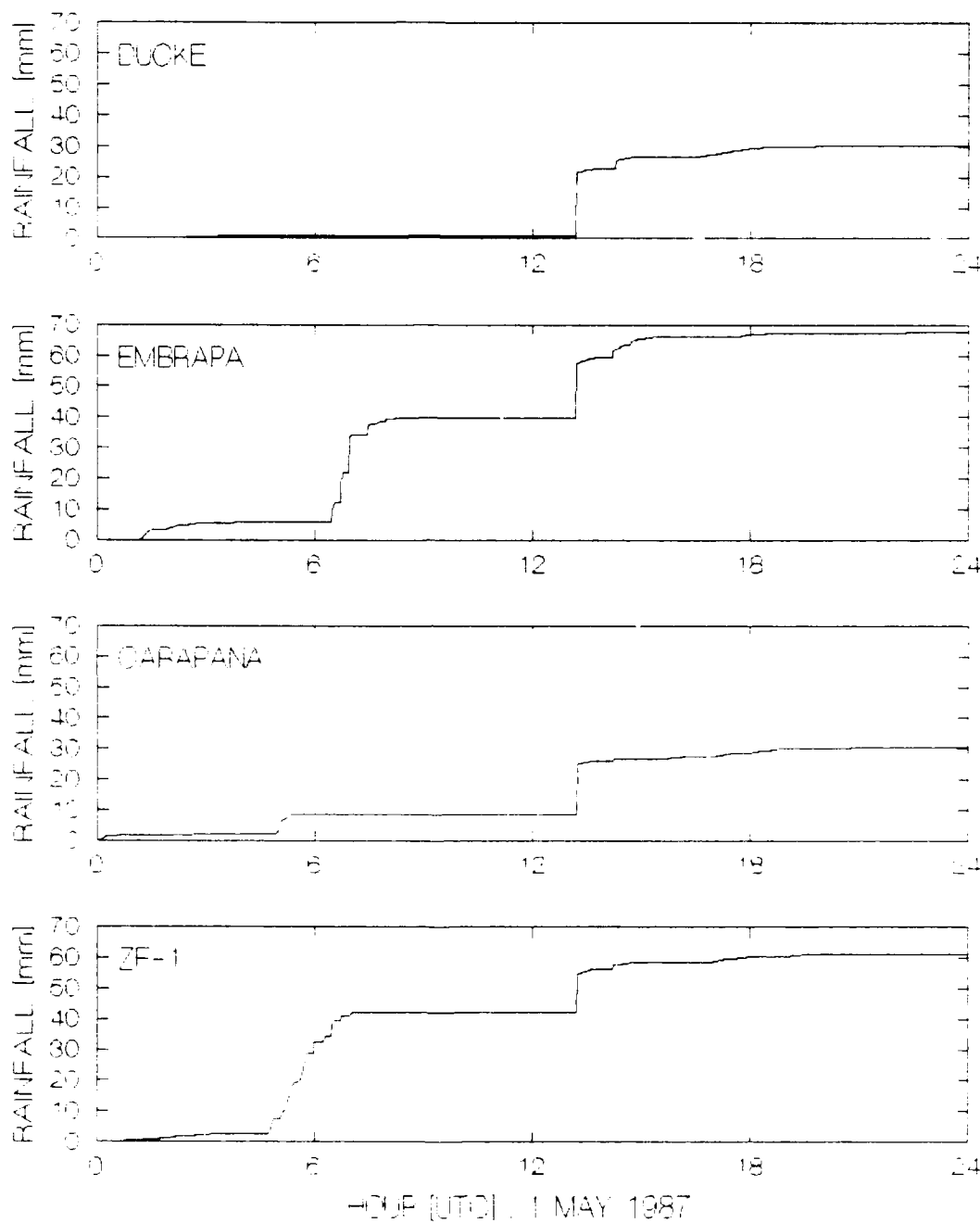


Figure 45. PAM time series of total rainfall (mm) on 1 May 1987. Lightning caused an interruption in the data from approximately 0900-1300 UTC.

the triangle and was associated with the mesoscale cluster ahead of the COS. The PAM data delineate small  $\theta_e$  changes associated with the first period of rain. The values of  $\theta_e$  derived from rawinsonde and airport observations decrease sharply after convective rain in the COS squall front.

Peak winds,  $u$ , and  $v$  (Figures 47-49, respectively) exhibit non-squall, non-wave characteristics during the earlier rain. Behind the COS squall front, all four PAM stations show pronounced shifts in  $u$  and  $v$ . The lack of strong surface and upper changes indicate the earlier mesoscale cloud clusters are not part of the COS. However, there may be a connection between the clusters and the synoptic-scale convergence that triggered and organized the COS.

The  $\theta_e$  time series (Figure 40) resemble those on 26 April; lower values persist after squall front passage. The effects of downdrafts and cloudiness on total energy at the surface are revealed by comparing  $\theta_e$  at 0000 UTC on 2 May to values 24 hours earlier. Values of  $\theta_e$  remain  $\sim 5-8$  K lower in the mesoscale anvil region during the afternoon as the anvil suppresses surface fluxes of heat and moisture.

Large changes in the vertical kinematic and thermodynamic structure resemble those on 26 April. While the patterns are similar, more coherent changes in time occur on 1 May.

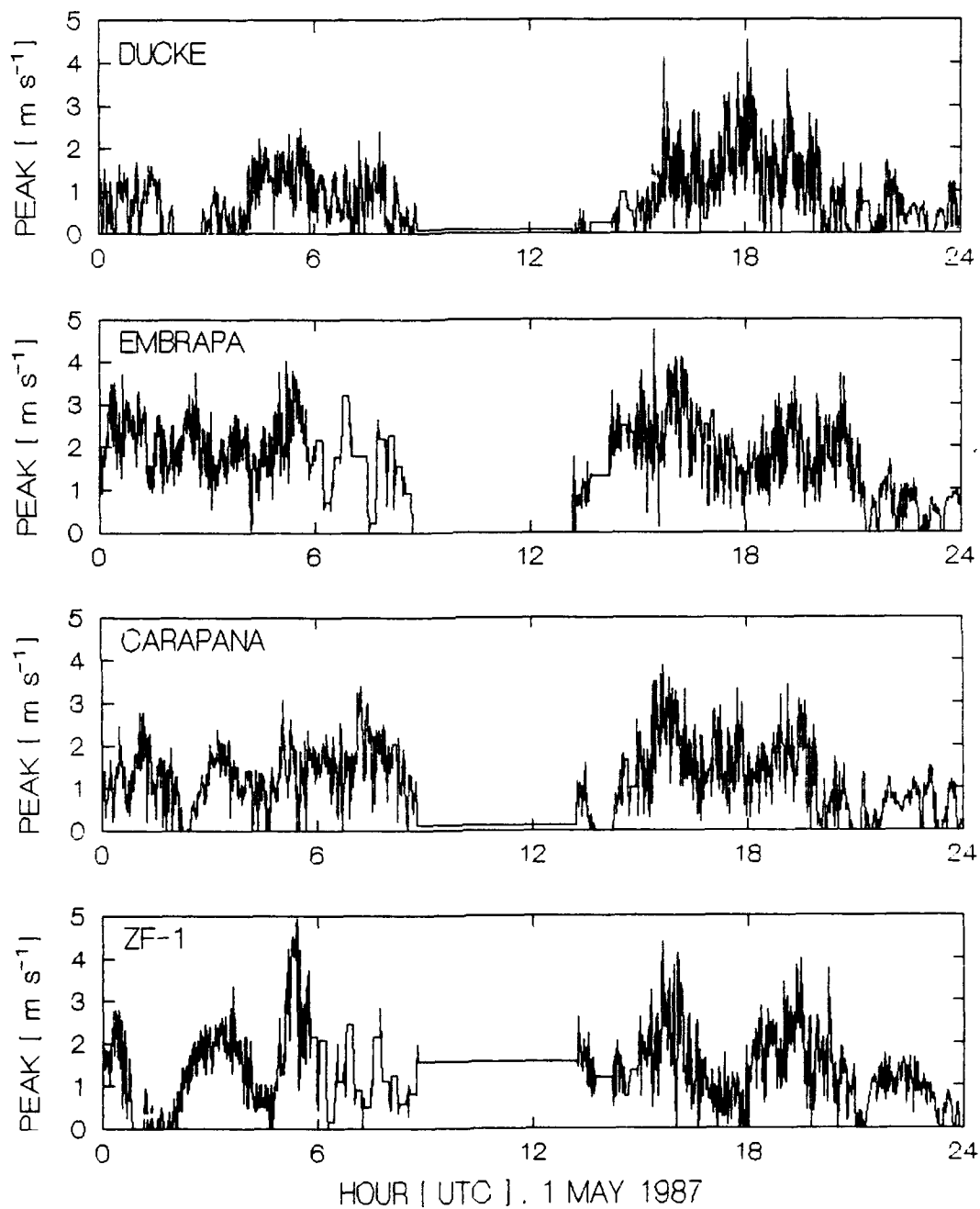


Figure 46. PAM time series of peak winds ( $\text{m s}^{-1}$ ) on 1 May 1987. Lightning caused an interruption in the data from approximately 0900-1300 UTC.

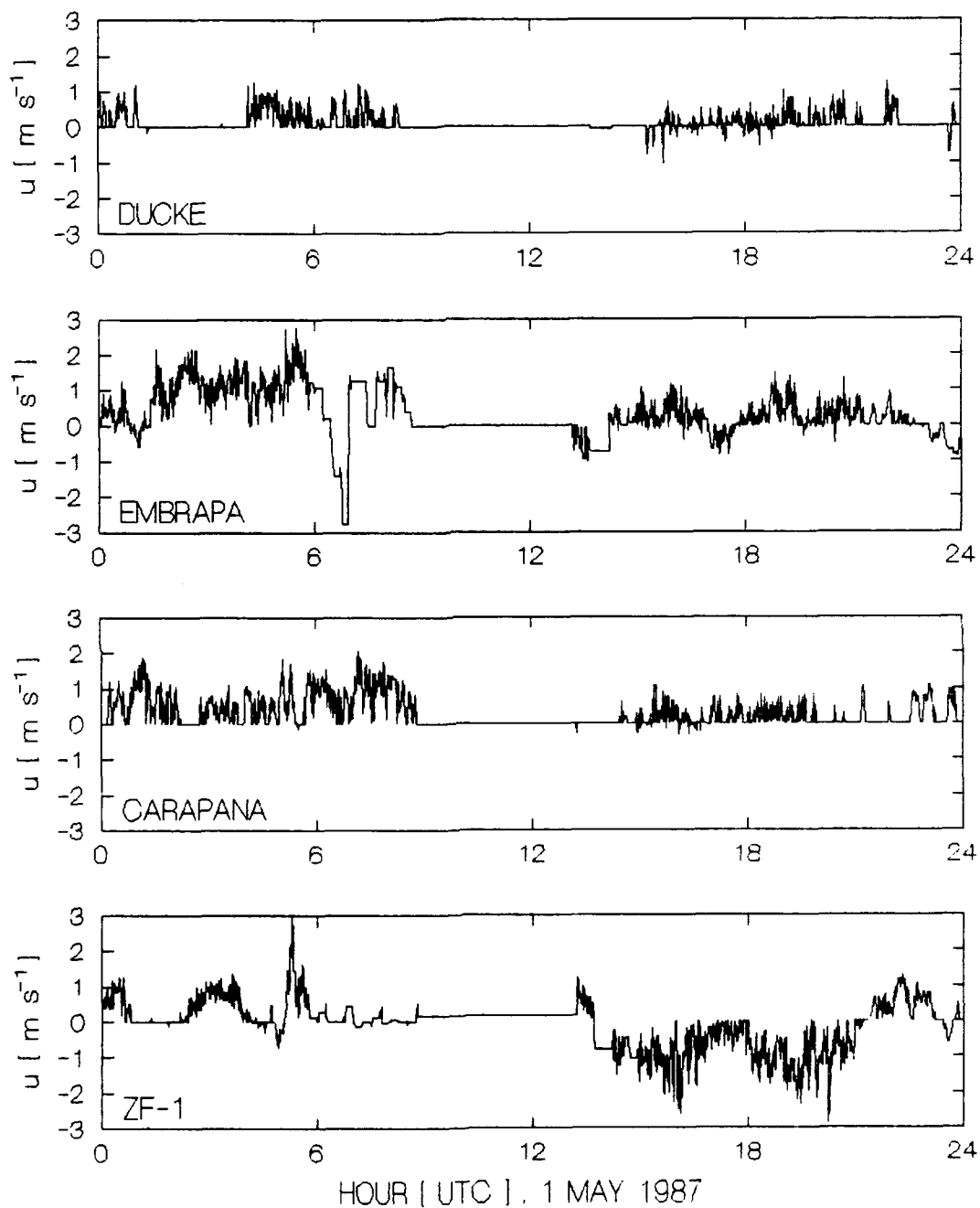


Figure 47. PAM time series of  $u$  ( $\text{m s}^{-1}$ ) on 1 May 1987.

Lightning caused an interruption in the data  
from approximately 0900-1300 UTC.

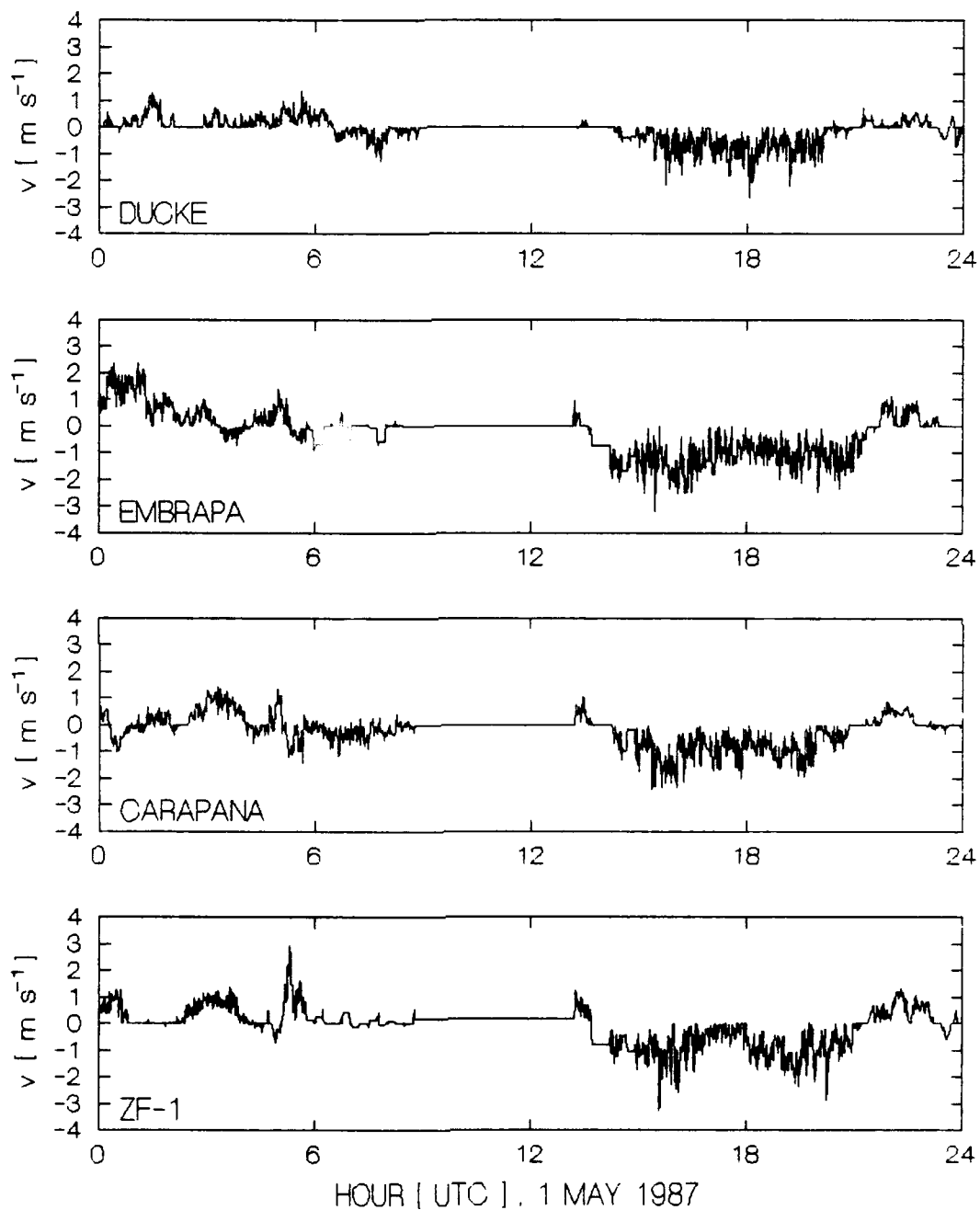


Figure 48. PAM time series of  $v$  ( $\text{m s}^{-1}$ ) on 1 May 1987.  
Lightning caused an interruption in the data  
from approximately 0900-1300 UTC.

The upper levels are more humid on 1 May (Figure 43) but the general structure of the humidity field in time is similar. Before 0600 UTC, a moist layer with humidity greater than 95% extends from the surface to 700 mb. A deep dry layer with humidity minima near 500 mb and 250 mb appears in the mid and upper troposphere ahead of the mesoscale clusters. The upper-level humidity increases during passage of the mesoscale cluster, then decreases in the hot tower and anvil regions of the COS. In the anvil stage, the low levels become drier as the humidity drops below 75%. The mature COS on 1 May thrives in a moisture-rich environment with higher relative humidities at all levels than on 26 April.

The downward transport of low  $\theta_e$  air from the mid to lower troposphere (Figure 44) by hot tower and anvil downdrafts has a strong effect on total heat in the column. The earlier mesoscale clusters actually increase the total heat in the column while the COS squall front causes overturning of mid- and low-level air.

The main changes in  $u$  and  $v$  (Figures 41-42, respectively) are directional shifts and enhanced vertical shear after passage of the squall front. In the mid and upper troposphere, the easterly component is weaker in the anvil.

The vertical time section of divergence is shown in Figure 49. In the squall front region (1200 UTC), convergence occurs in the lower troposphere with maximum conver-



gence near 650 mb. In the upper levels, divergence characterizes the squall-front region with a maximum near 375 mb. Low-level divergence occurs in the anvil subcloud region (2100 UTC). Mid- and upper-level convergence in the anvil layer weakens and increases in height with time.

In the region of COS hot towers, upward vertical motion (Figure 50) has a maximum of about  $40 \mu\text{b s}^{-1}$  at 650 mb and decreases at the upper levels. There is mid- and upper-level upward vertical motion in the stratiform cloud layers and downward motion in the subcloud layer.

The divergence and vertical motion in this disturbance are consistent with the kinematics of tropical squall lines described by Gamache and Houze (1982). They attribute the decrease in upper-level ascent in the hot-tower region to strong mid- and upper-level outflow from active thunderstorms.

In the COS hot-tower component,  $Q_1$  (Figure 51) shows heating through the entire column with a maximum heating rate of  $\sim 280 \text{ K day}^{-1}$  at 500 mb. Normalizing by rainfall rate allows comparison of the heating rate with other studies (Chong and Hauser, 1990; Johnson, 1984). The rainfall rate used in the normalization is expressed in  $\text{cm day}^{-1}$ . The normalization rate is obtained by extrapolating the convective rainfall rate in  $\text{mm min}^{-1}$  to 24 hours. A rainfall rate of  $16 \text{ cm day}^{-1}$  on 1 May gives a normalized value for

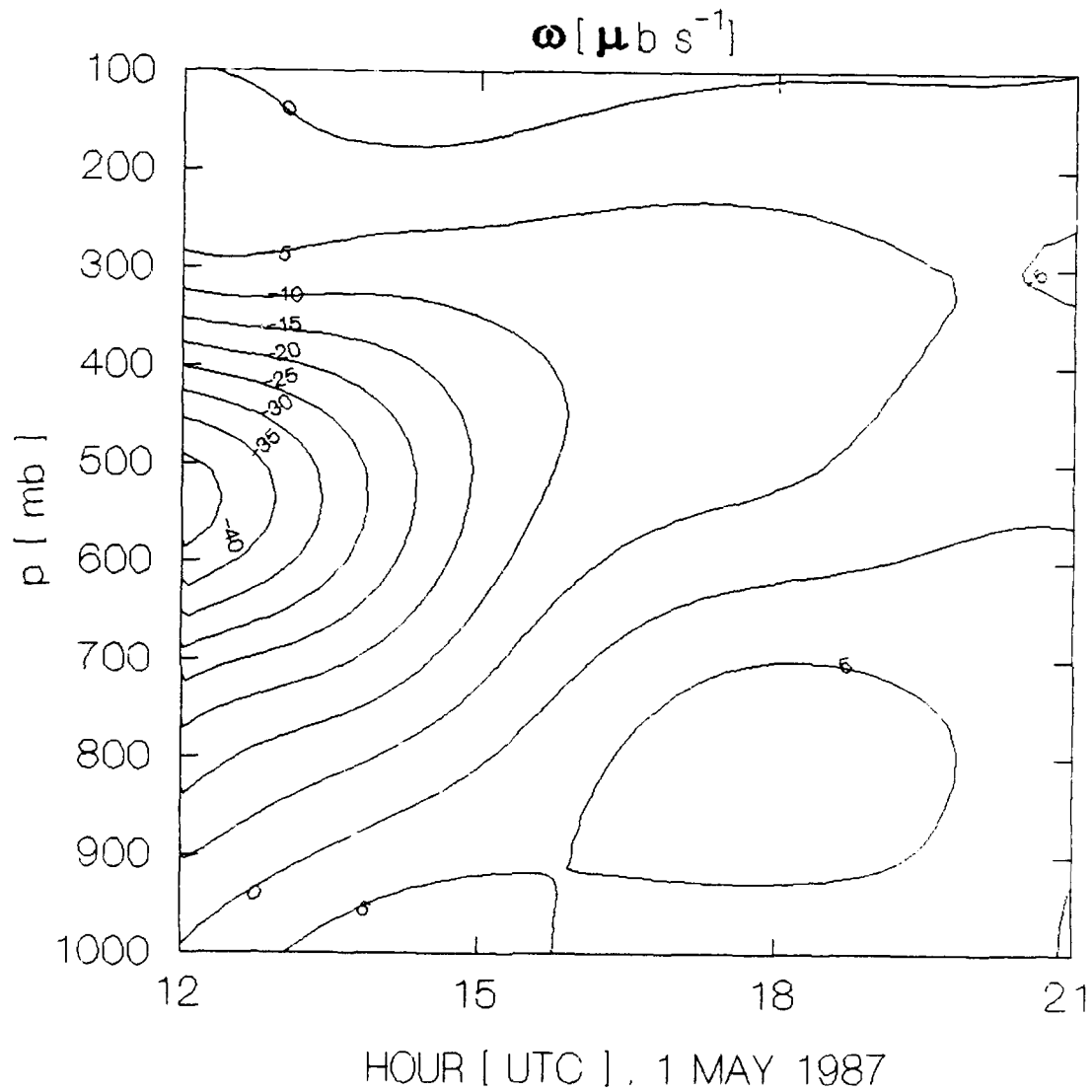
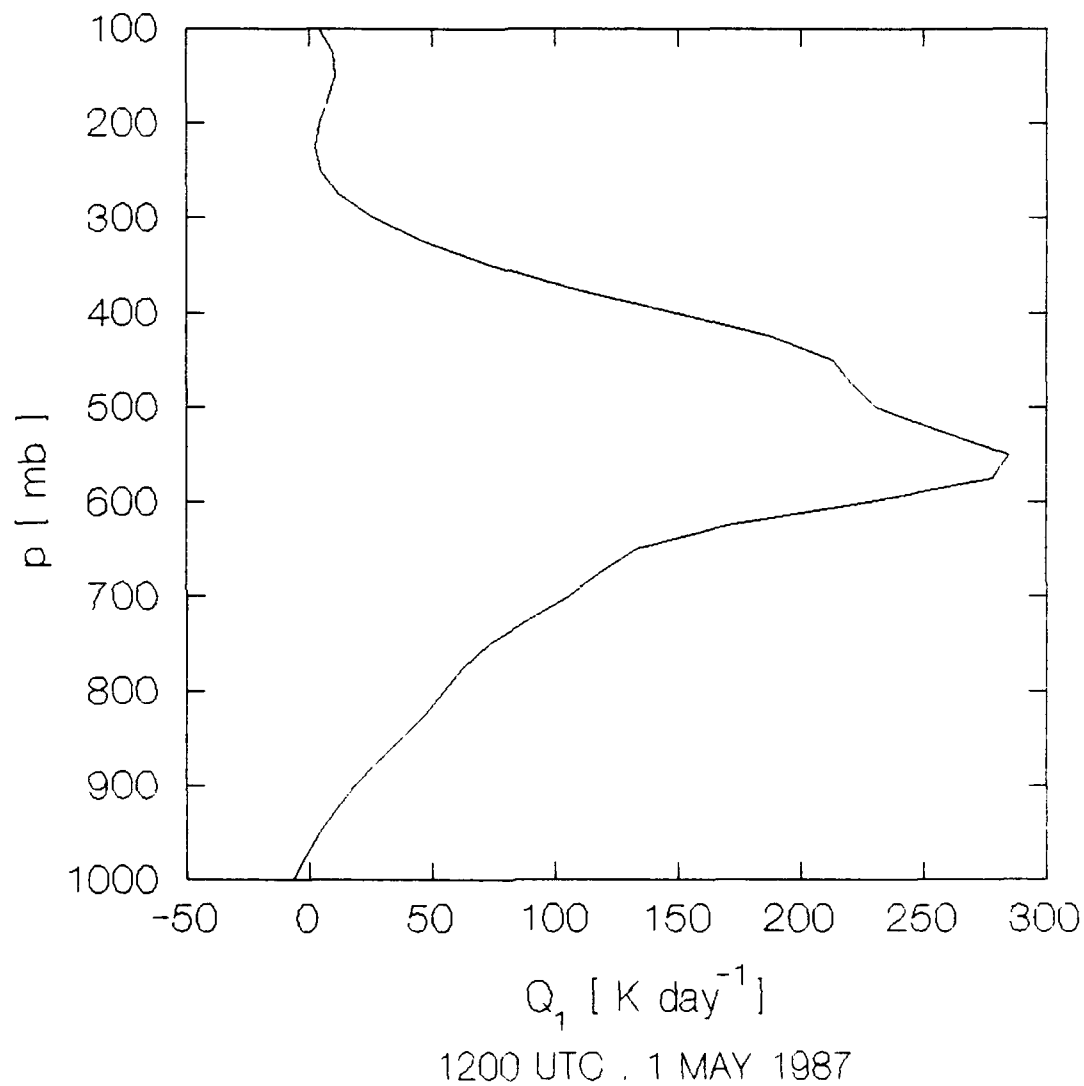


Figure 50. Vertical time cross section of  $\omega$  (microbars  $\text{s}^{-1}$ ) in the mesoscale triangle on 1 May 1987. The contour interval is 5 microbars  $\text{s}^{-1}$ .



**Figure 51.** Apparent sensible heat source (K day<sup>-1</sup>) in the mesoscale triangle during the COS convective component at 1200 UTC, 1 May 1987.

the  $Q_1$  maximum of  $17.5 \text{ K day}^{-1}/\text{cm day}^{-1}$  at 1200 UTC. This value is 1.7 times larger than the value of  $10.1 \text{ K day}^{-1}/\text{cm day}^{-1}$  for a squall line over West Africa during COPT 81 (Chong and Hauser, 1990). The COPT maximum vertical velocity of  $\sim 100 \mu\text{b s}^{-1}$  is about 2.1 times larger than calculated in the 1 May COS convective component.

The  $Q_2$  profile in the COS convective region on 1 May (Figure 52) shows drying everywhere in the column with a maximum of  $\sim 320 \text{ K day}^{-1}$  near 500 mb. The maximum normalized drying rate is  $20 \text{ K day}^{-1}/\text{cm day}^{-1}$ . This value is 1.9 times larger than in the COPT disturbance (Chong and Hauser, 1990).

The rates of temperature change due to long- and shortwave radiation are shown in Figures 53-54, respectively. Main cloud types in the analysis are cumulus towers and mid- to high-level stratiform anvils. The radiation profiles show net cooling from the surface to the top of the cloud layer at 500 mb. In the cirrus layer near the tropopause there is net warming due to radiation. These results show the sensitivity of the radiation model to time of day and upper level layers of cirrus.

The  $F$  profile (Figure 55) has a maximum at  $\sim 1400 \text{ W m}^{-2}$  near the levels of strongest upward vertical motion.

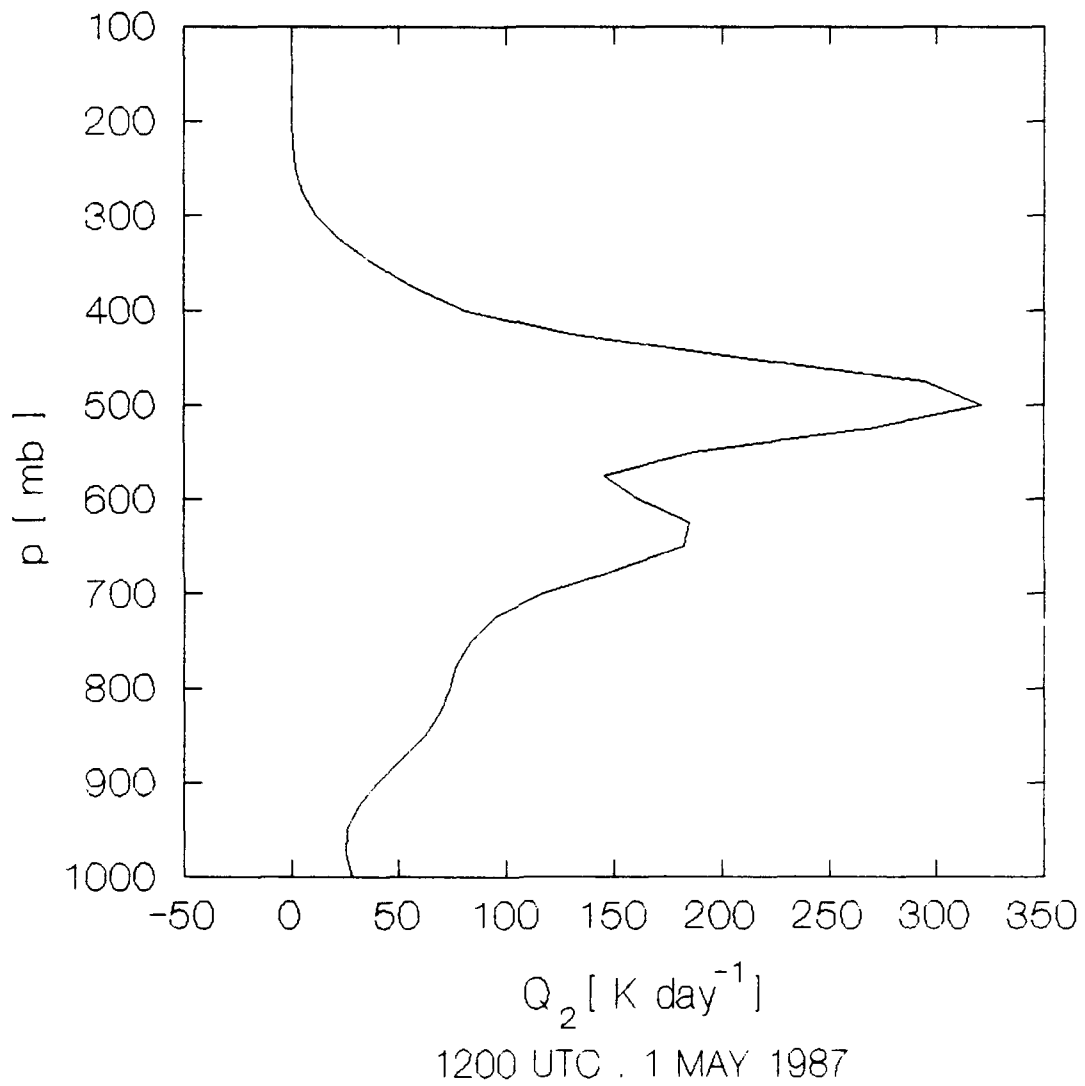


**Figure 52.** Apparent moisture sink (K day<sup>-1</sup>) in the meso-scale triangle during the COS convective component at 1200 UTC, 1 May 1987.

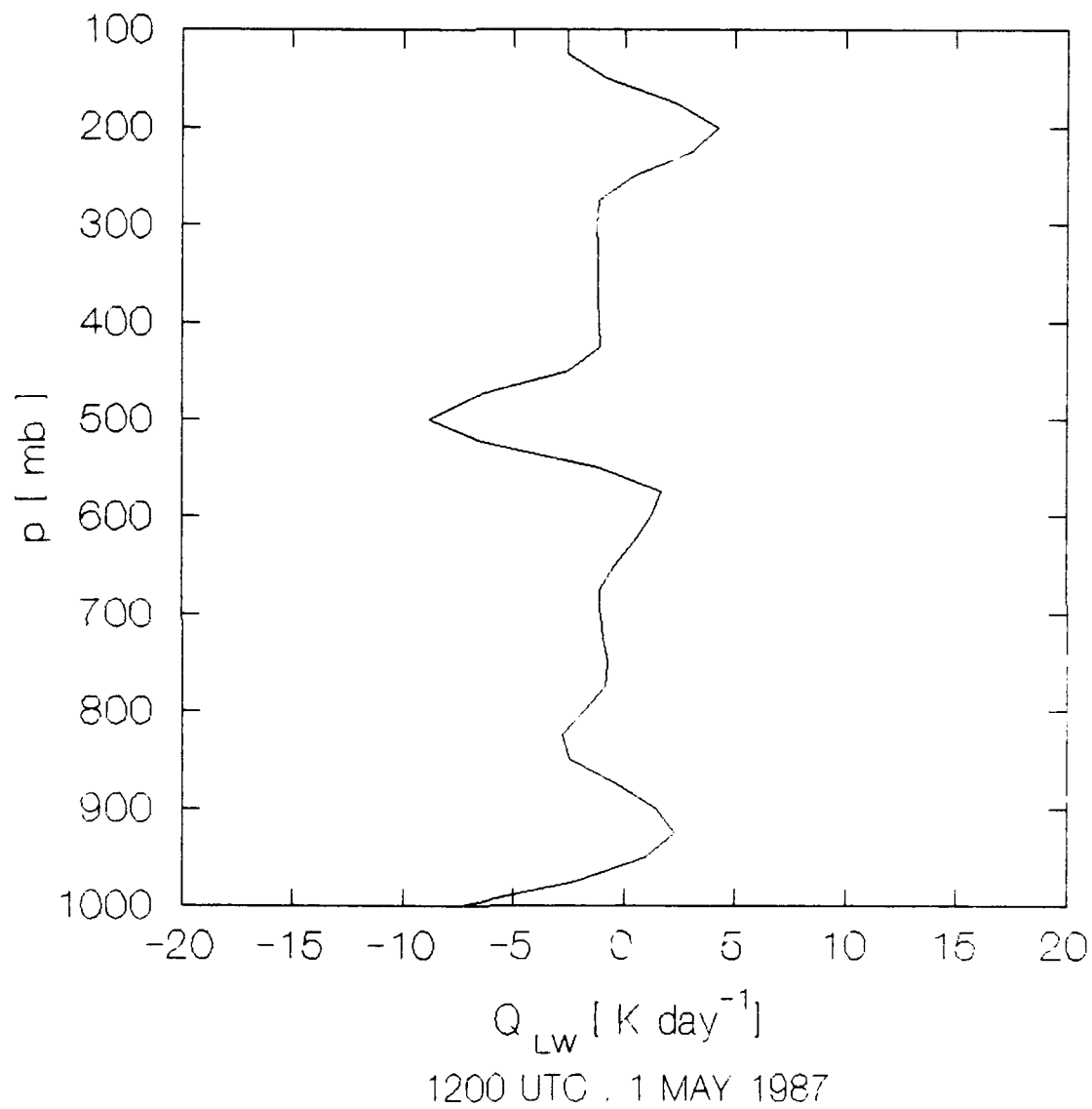


Figure 53. Rate of temperature change (K day<sup>-1</sup>) due to longwave radiation in the mesoscale triangle during the COS convective component at 1200 UTC, 1 May 1987.

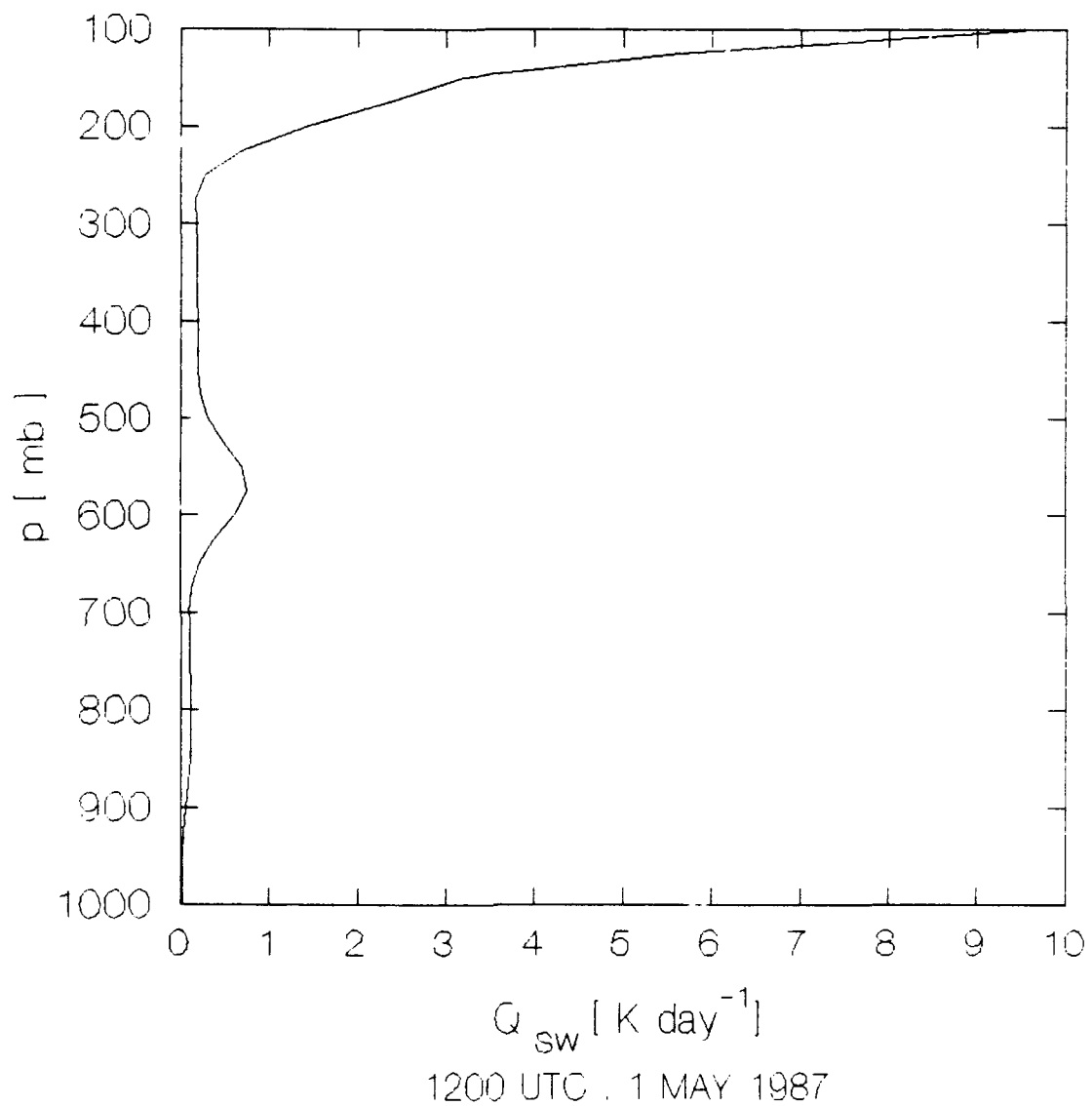
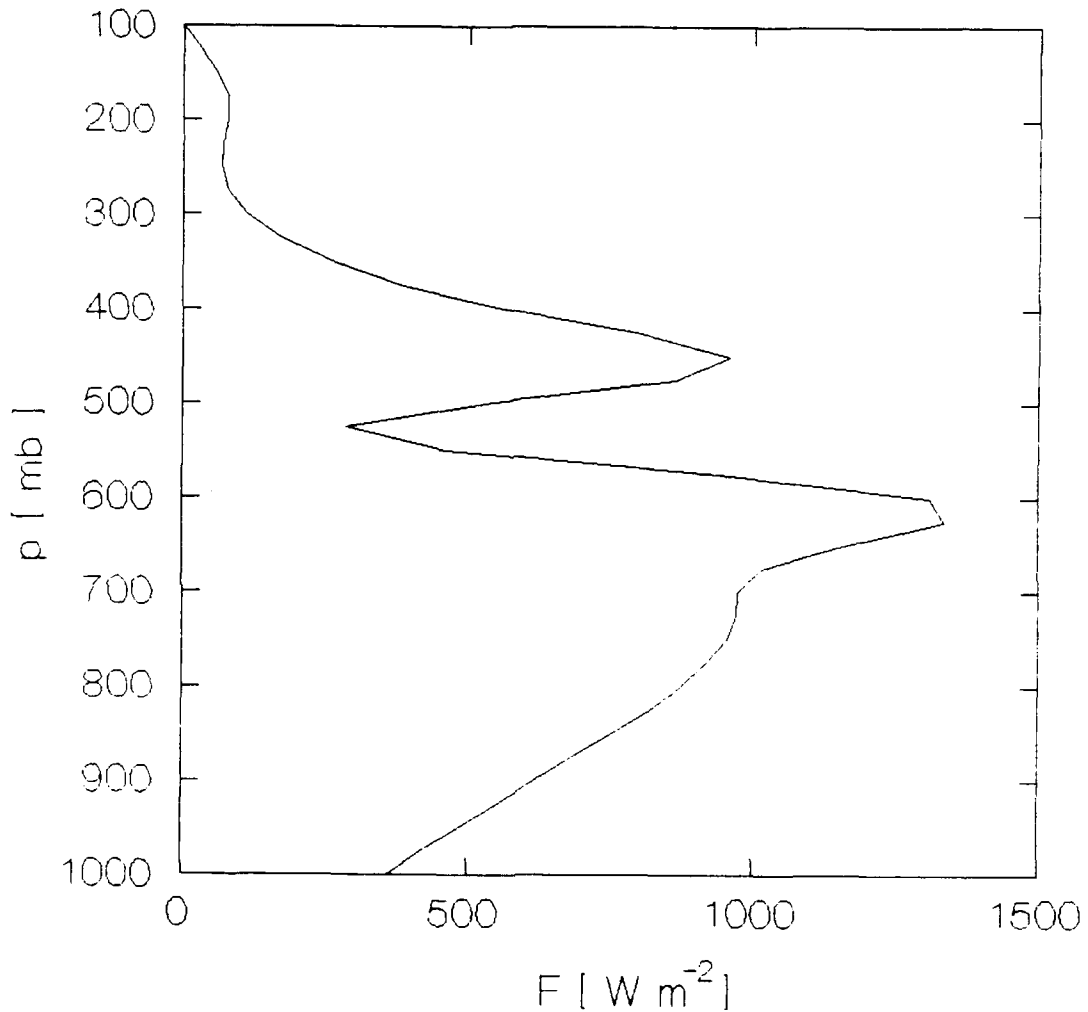


Figure 54. Rate of temperature change (K day<sup>-1</sup>) due to shortwave radiation in the mesoscale triangle during the COS convective component at 1200 UTC, 1 May 1987.



1200 UTC . 1 MAY 1987

Figure 55. Vertical eddy flux of total heat ( $\text{W m}^{-2}$ ) in the mesoscale triangle during the COS convective component at 1200 UTC, 1 May 1987.

A sharp change in  $F$  at 525 mb is related to the effects of layered clouds on the vertical advection of water vapor in the triangle volume.

Profiles of  $Q_1$  and  $Q_2$  in the COS anvil at 1800 UTC (Figures 56-57, respectively) resemble those diagnosed by Johnson (1984) and Johnson and Young (1983) in GATE and Winter MONEX anvils. There is a mid-level drying maximum of about  $50 \text{ K day}^{-1}$  in the anvil. The low levels have a maximum moistening rate of about  $22 \text{ K day}^{-1}$  (Figure 57). Low-level cooling of nearly  $30 \text{ K day}^{-1}$  occurs in the subcloud layer while the mid levels show heating of about  $50 \text{ K day}^{-1}$  near 450 mb (Figure 56). Another region of pronounced drying occurs near 750 mb. According to Johnson (1984), double-peak drying is caused by the combined effects of anvils and cumulus towers.

Radiation heating rates (Figures 58-59) show the net effect of radiation in anvil cloud layers is to cool the atmosphere. The net cooling primarily results from longwave radiation at the top of each cloud deck.

The  $F$  profile (Figure 60) shows relatively low surface energy fluxes behind the squall front. Above the surface,  $F$  decreases to a minimum near 900 mb and then increases to a maximum of about  $800 \text{ W m}^{-2}$  near the 800 mb level.

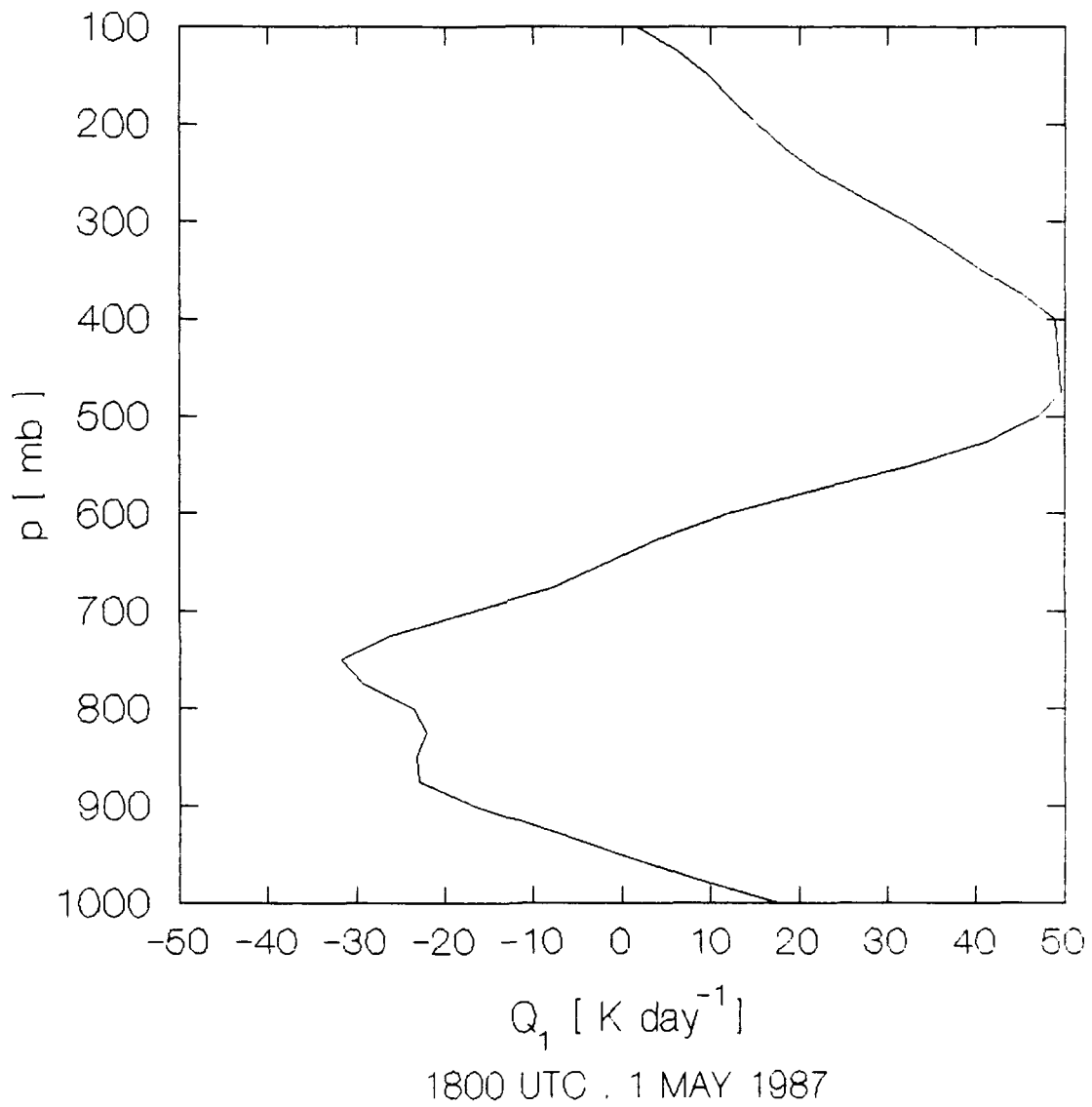


Figure 56. Apparent sensible heat source ( $\text{K day}^{-1}$ ) in the mesoscale triangle during the COS anvil component at 1800 UTC, 1 May 1987.

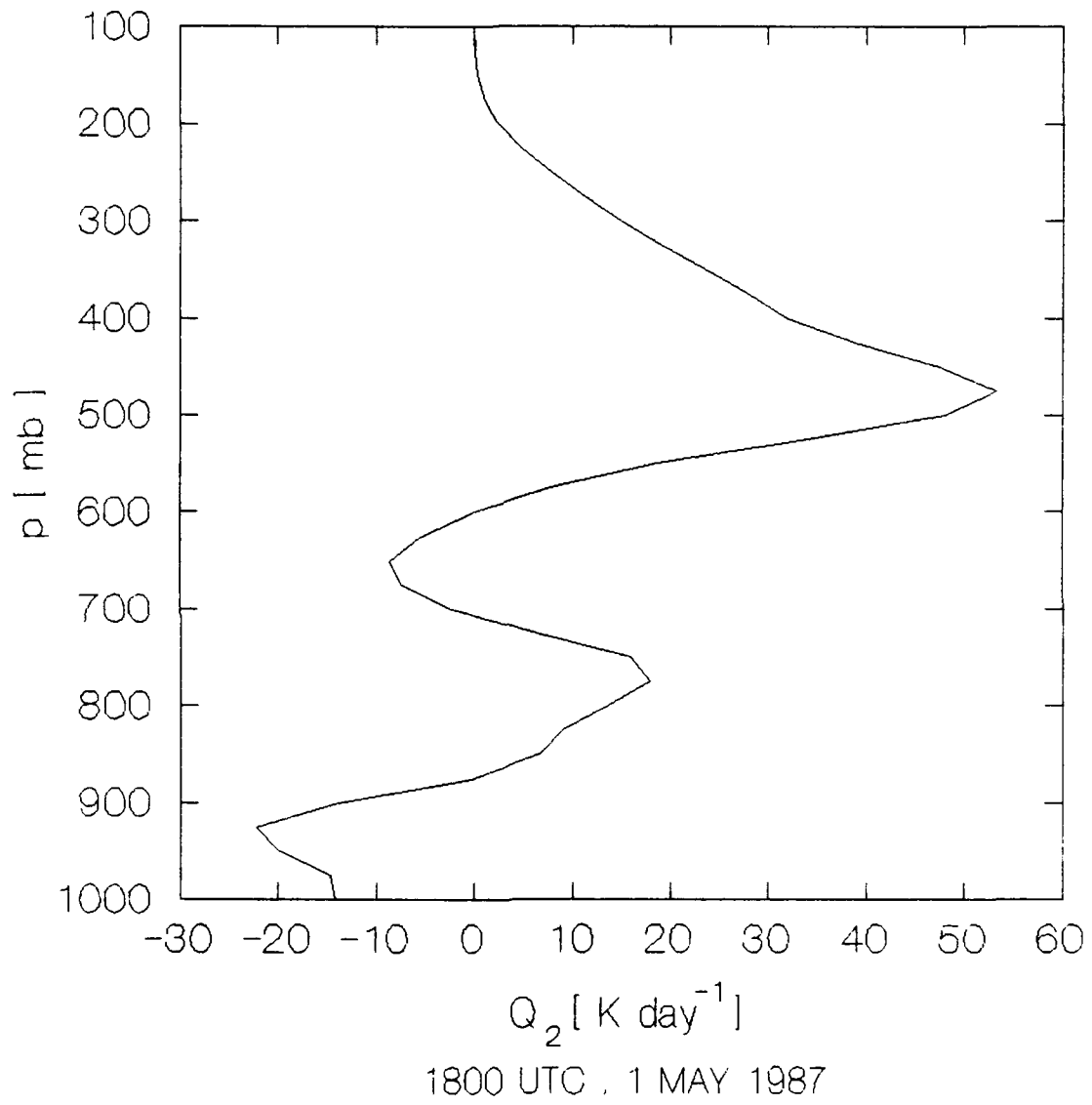


Figure 57. Apparent moisture sink ( $\text{K day}^{-1}$ ) in the meso-scale triangle during the COS anvil component at 1800 UTC, 1 May 1987.

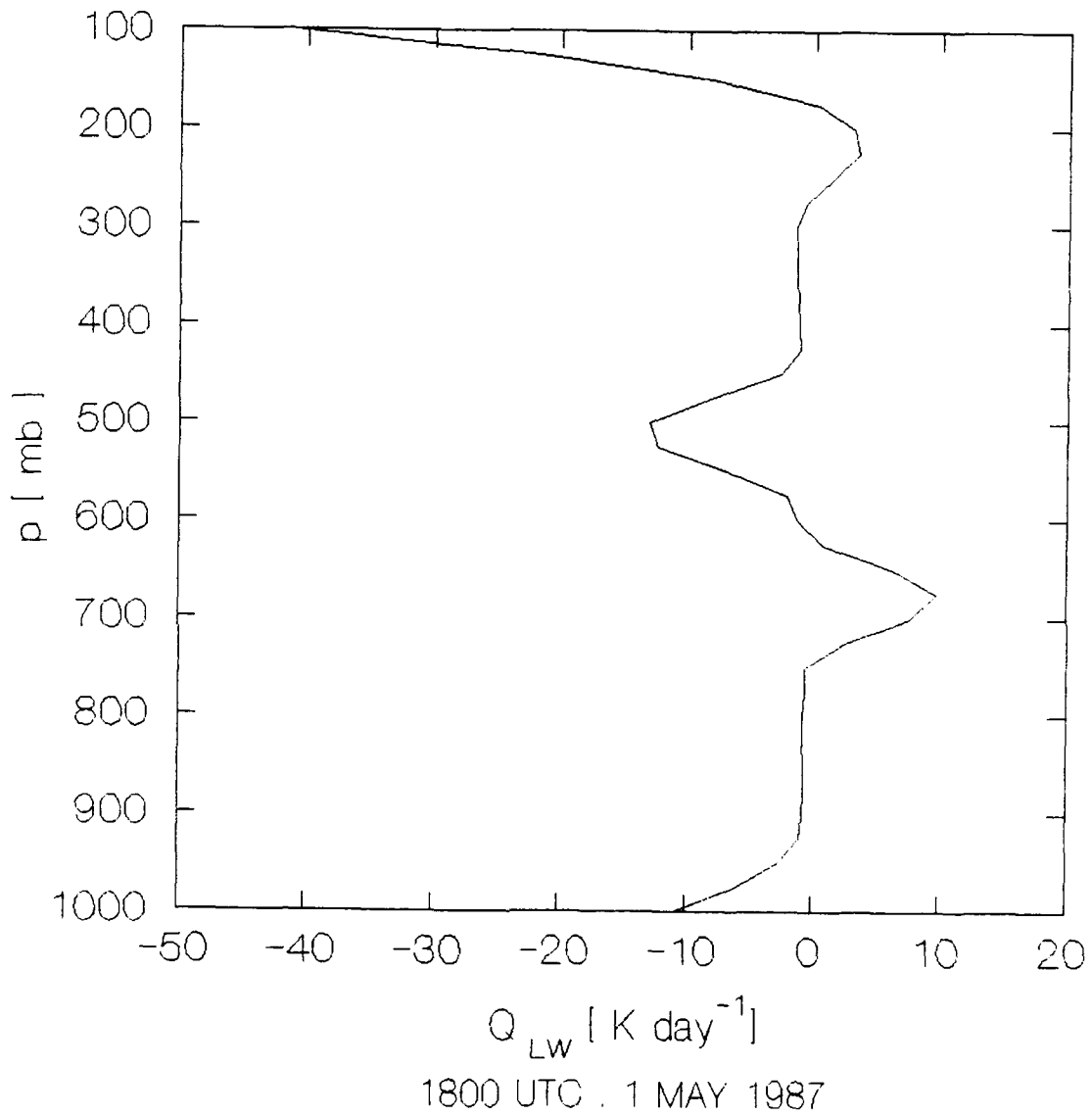
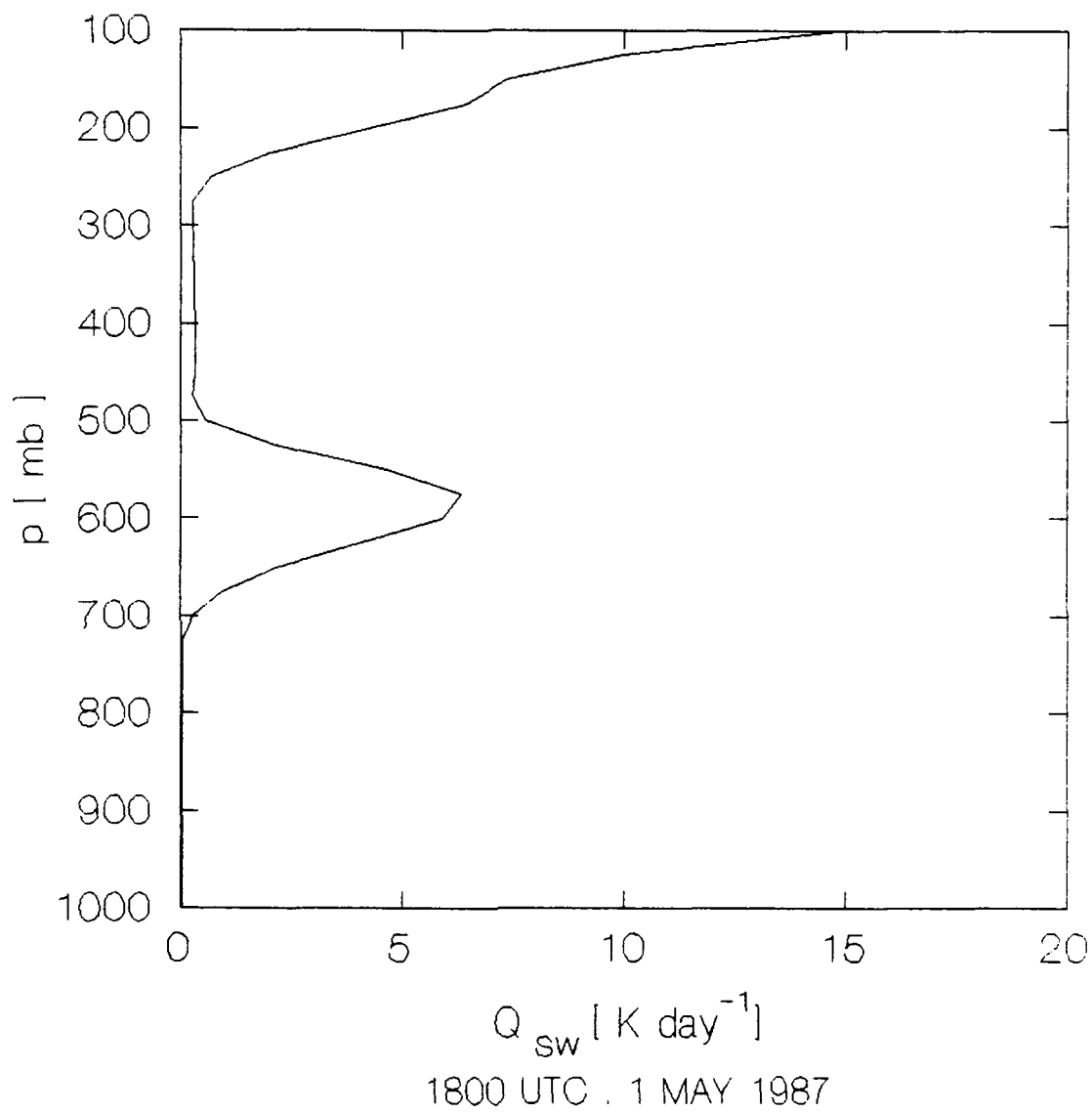
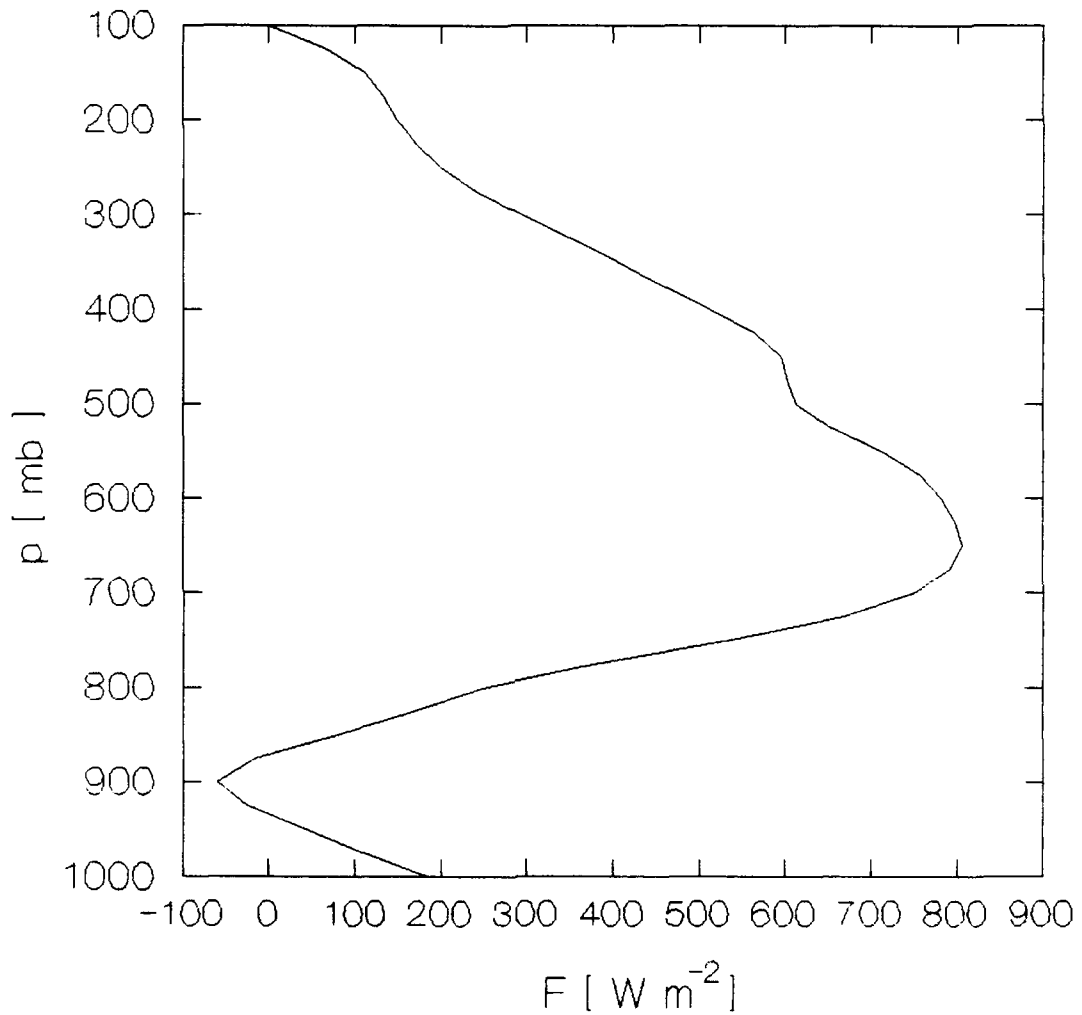


Figure 58. Rate of temperature change ( $\text{K day}^{-1}$ ) due to longwave radiation in the mesoscale triangle during the COS anvil component at 1800 UTC, 1 May 1987.



**Figure 59.** Rate of temperature change (K day<sup>-1</sup>) due to shortwave radiation in the mesoscale triangle during the COS anvil component at 1800 UTC, 1 May 1987.



1800 UTC, 1 MAY 1987

Figure 60. Vertical eddy flux of total heat ( $\text{W m}^{-2}$ ) in the mesoscale triangle during the COS anvil component at 1800 UTC, 1 May 1987.

### C. Regenerating COS, 6 May 1987

A regenerating COS passed through the triangle network on 6 May 1987, from ~ 1500-1800 UTC. Satellite images indicate the convection was rapidly intensifying as the system entered the triangle. However, the system had a relatively weak squall front compared to those occurring on 26 April and 1 May.

The GOES images show the system formed with distinct linear features along the northeast coast of Brazil on the afternoon of 5 May. Development of the COS coincided with an increase in deep convection over the equatorial Atlantic. The disturbance initially weakened after moving inland with an average forward speed of  $55 \text{ km h}^{-1}$ . The COS had poorly organized cloud structure at 1100 UTC on 6 May (Figure 61) but by 1500 UTC (Figure 62) it quickly regenerated as it neared the triangle. Satellite images show the COS matured to the west of the triangle around 2100 UTC and then rapidly weakened and dissipated by 1200 UTC on 7 May.

The MB image at 1900 UTC (Figure 63) shows the northwest-to-southeast oriented COS near the time it leaves the mesoscale triangle. The broad band of individual convective clusters and merging anvils gives the COS its distinctive linear features on the GOES full disk IR images.

The CAPPI radar scans at 1528 UTC (Figure 64) show convective elements in the triangle at the time of squall

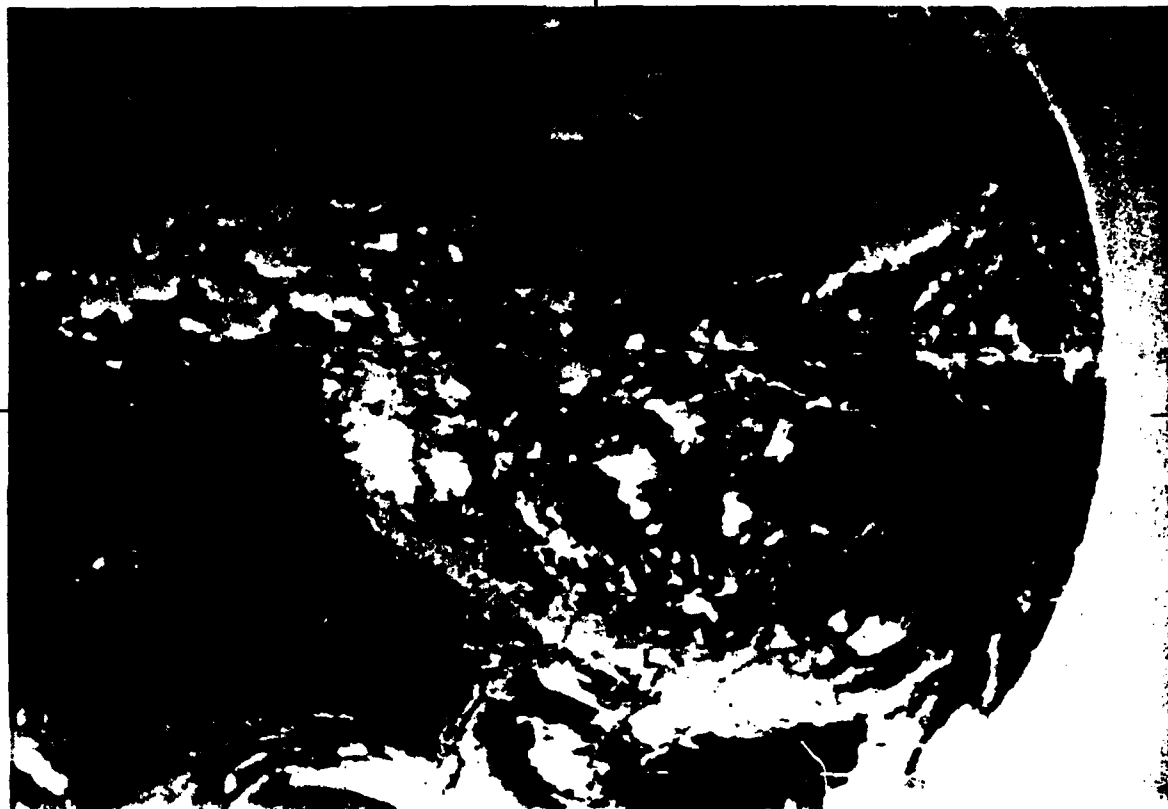


Figure 61. The GOES full disk IR image at 1101 UTC, 6 May 1987 showing weakened COS prior to regeneration over the central Amazon basin. The + denotes 3°S, 60°W.

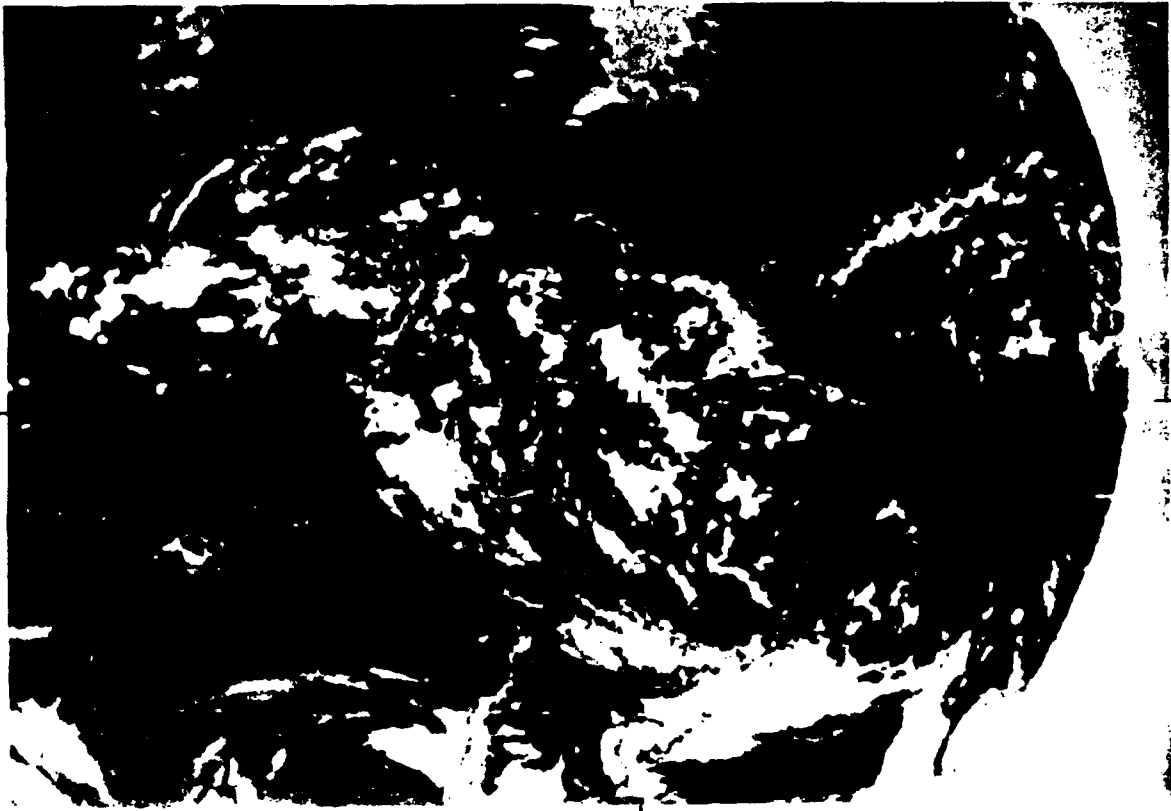
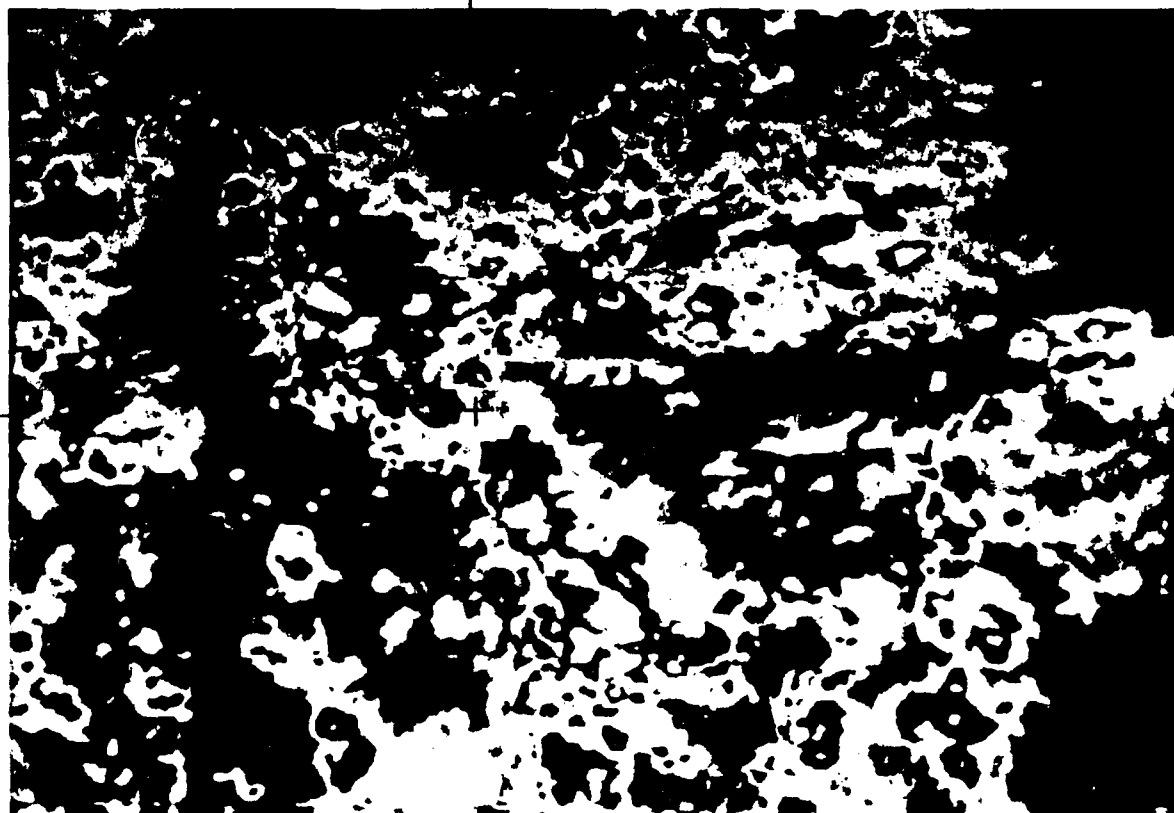


Figure 62. The GOES full disk IR image at 1501 UTC, 6 May 1987 showing COS regenerating over the central Amazon basin. The + denotes 3°S, 60°W.



500 km

Figure 63. The GOES MB-enhanced IR image at 1901 UTC, 6 May 1987 showing regenerating COS as it intensifies just west of the mesoscale triangle. The + denotes 3°S, 60°W.

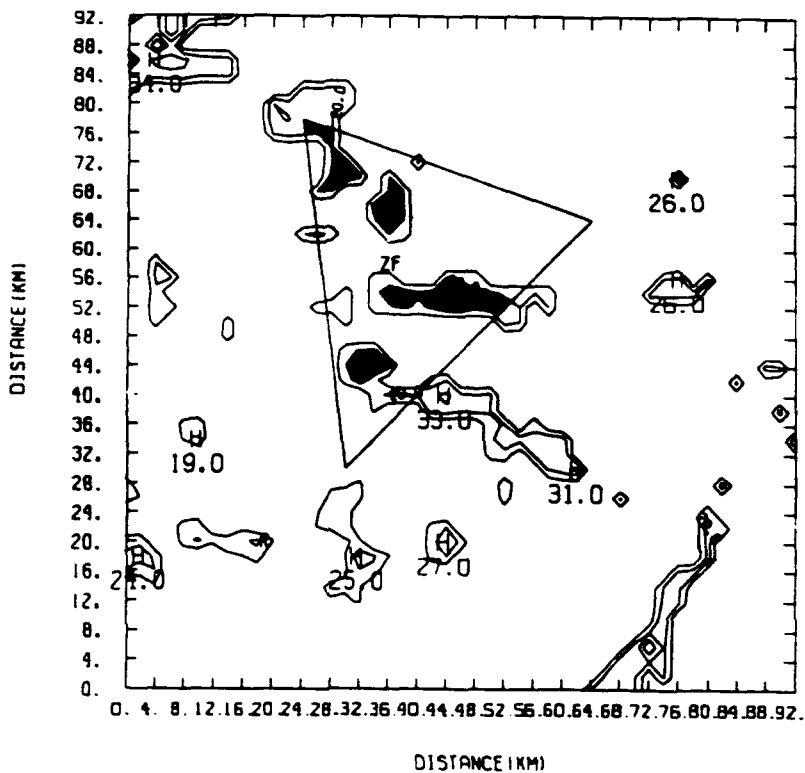


Figure 64. CAPPI radar scan of the regenerating COS convective component in the mesoscale triangle at 1528 UTC, 6 May 1987. The contour interval of reflectivity is 10 dBz. The location of the radar in the lower left part of the figure is denoted by the letter R.

front passage. The convective hot towers do not form a solid line of clouds.

The PAM time series (Figures 65-73) show evidence of a southwestward moving squall front having much weaker features than those observed in the 26 April and 1 May COS. Both the total rainfall (Figure 65) and the rainfall rate (Figure 66) are small in this system. The decreases in  $T$  (Figure 67), ranging from  $4^{\circ}\text{C}$  at Carapana to  $6^{\circ}\text{C}$  at Ducke, are considerably less than the  $10^{\circ}\text{C}$  drops behind the squall front on 26 April. Changes in mixing ratio (Figure 68) range from a small  $2\text{ g kg}^{-1}$  decrease at Ducke and Embrapa to a slight increase at Carapana. Embrapa and Ducke, with peak winds of  $15$  and  $10\text{ m s}^{-1}$ , respectively (Figure 69), are the only two stations measuring significant wind gusts during passage of the convective front. There are no persistent directional shifts in the horizontal winds (Figures 70-71). The PAM time series show a time-lagged pressure jump (Figure 72) moves across the network with the pressure increase being coincident with the start of convective rain at each site. The jumps are not as pronounced as those on 26 April.

The protracted effects of storm downdrafts upon surface heat and moisture are not as evident on 6 May as they are in the 26 April and 1 May disturbances. The comparisons of  $\theta_e$  (Figure 73),  $T$  (Figure 67), and  $q$  (Figure 68) at 0000 UTC on 6 May to measurements 24 hours later show

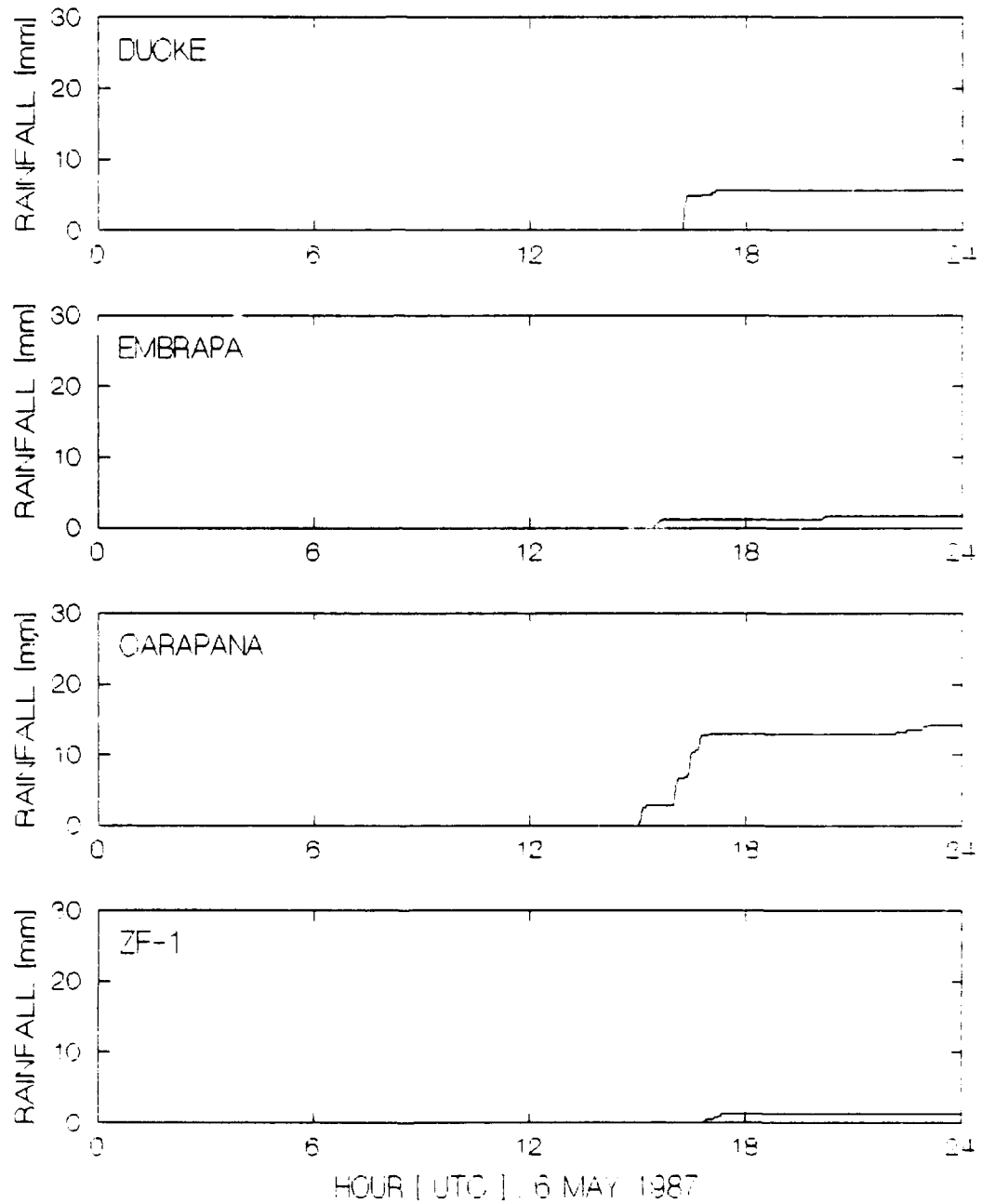


Figure 65. PAM time series of total rainfall (mm) on 6 May 1987.

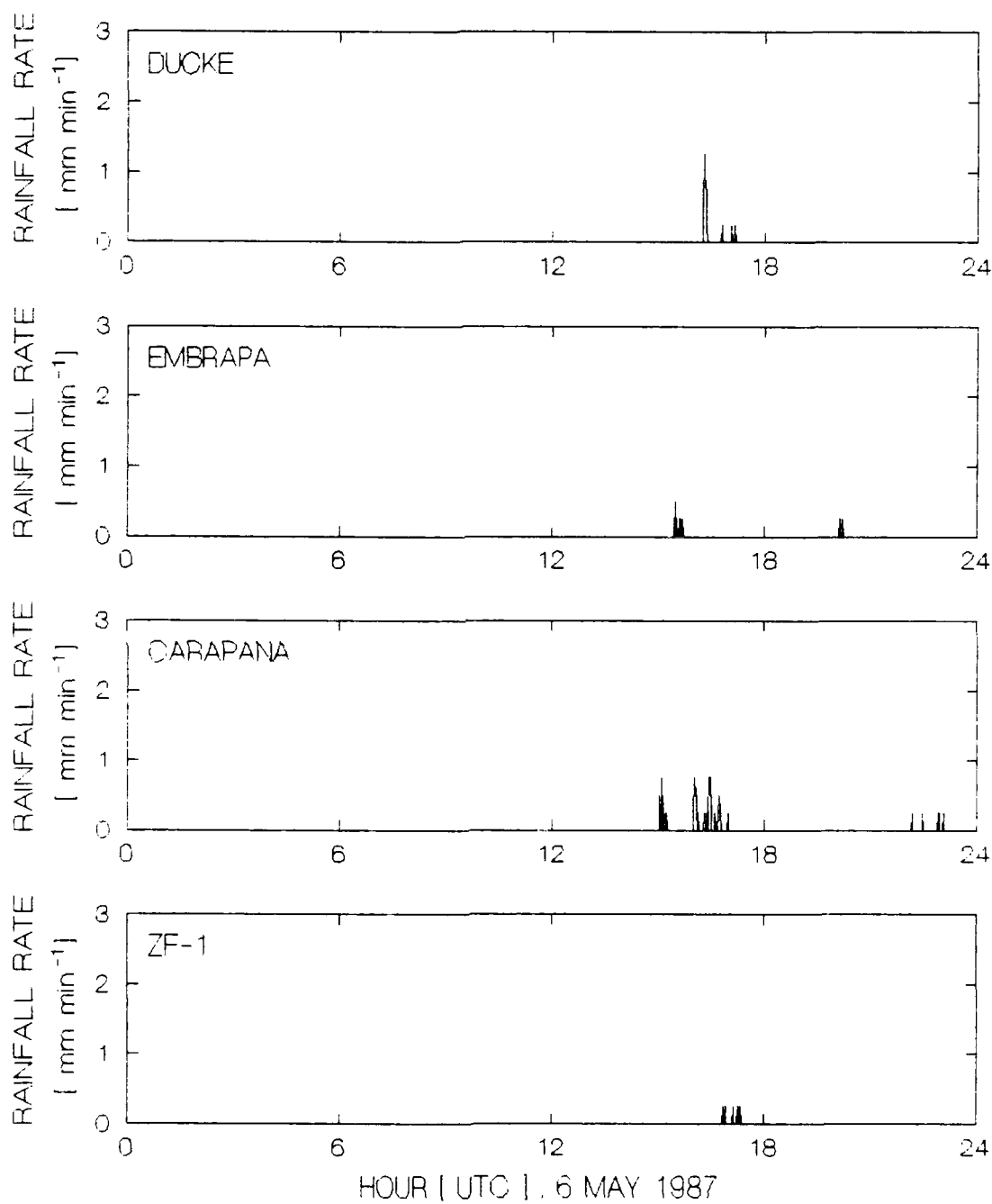


Figure 66. PAM time series of rainfall rate ( $\text{mm min}^{-1}$ ) on 6 May 1987.

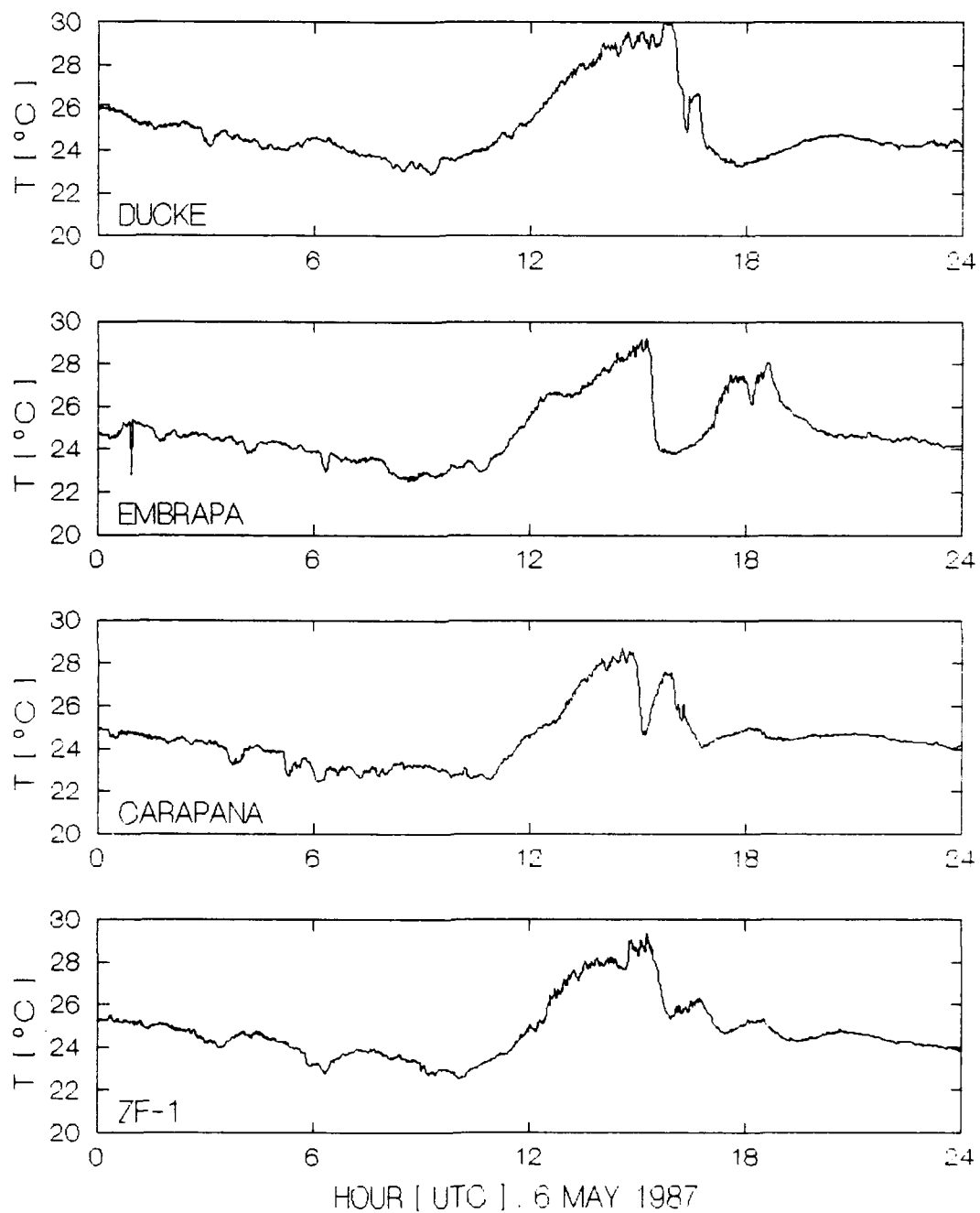


Figure 67. PAM time series of  $T$  (deg C) on 6 May 1987.

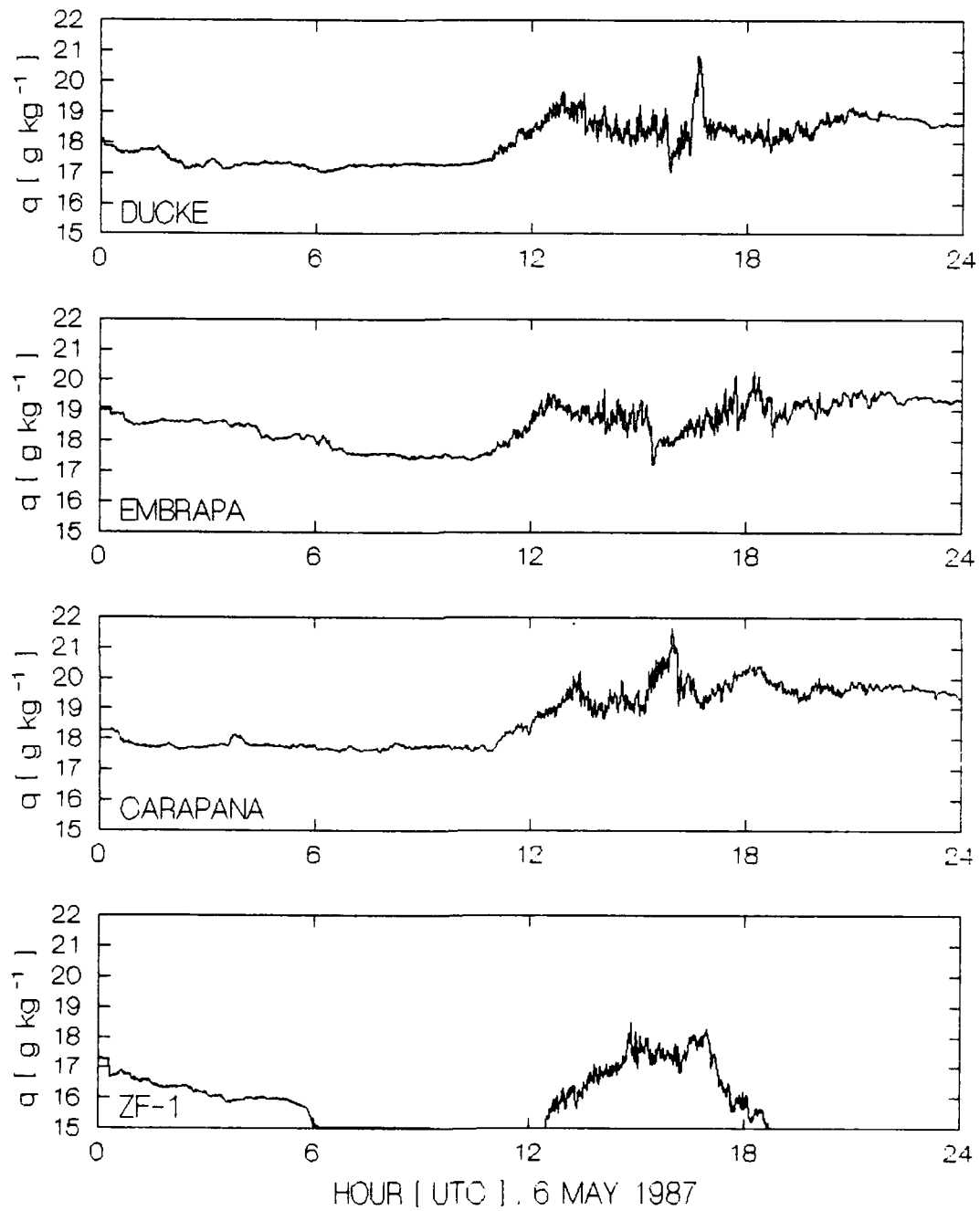


Figure 68. PAM time series of  $q$  ( $\text{g kg}^{-1}$ ) on 6 May 1987.

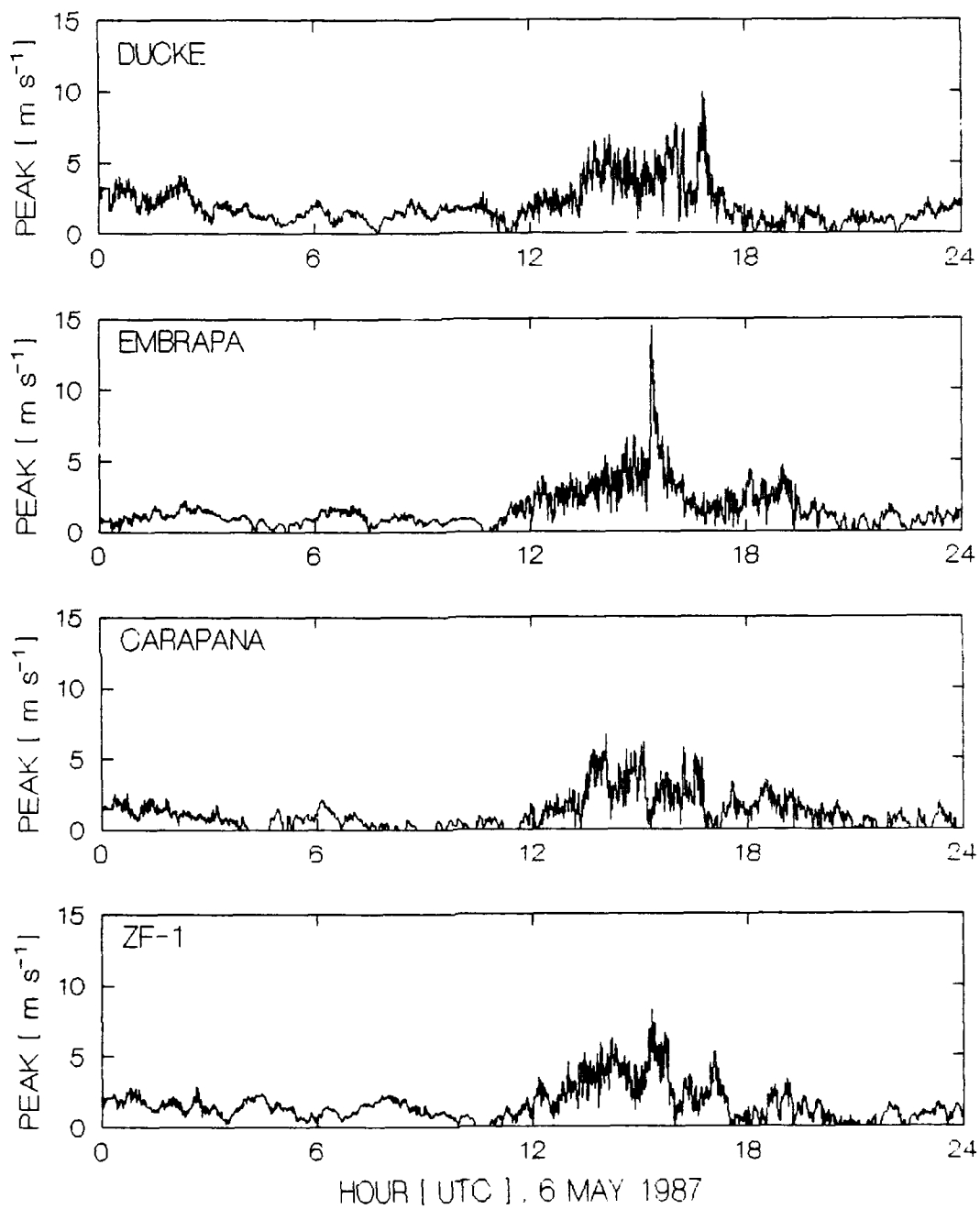


Figure 69. PAM time series of peak winds ( $\text{m s}^{-1}$ ) on 6 May 1987.

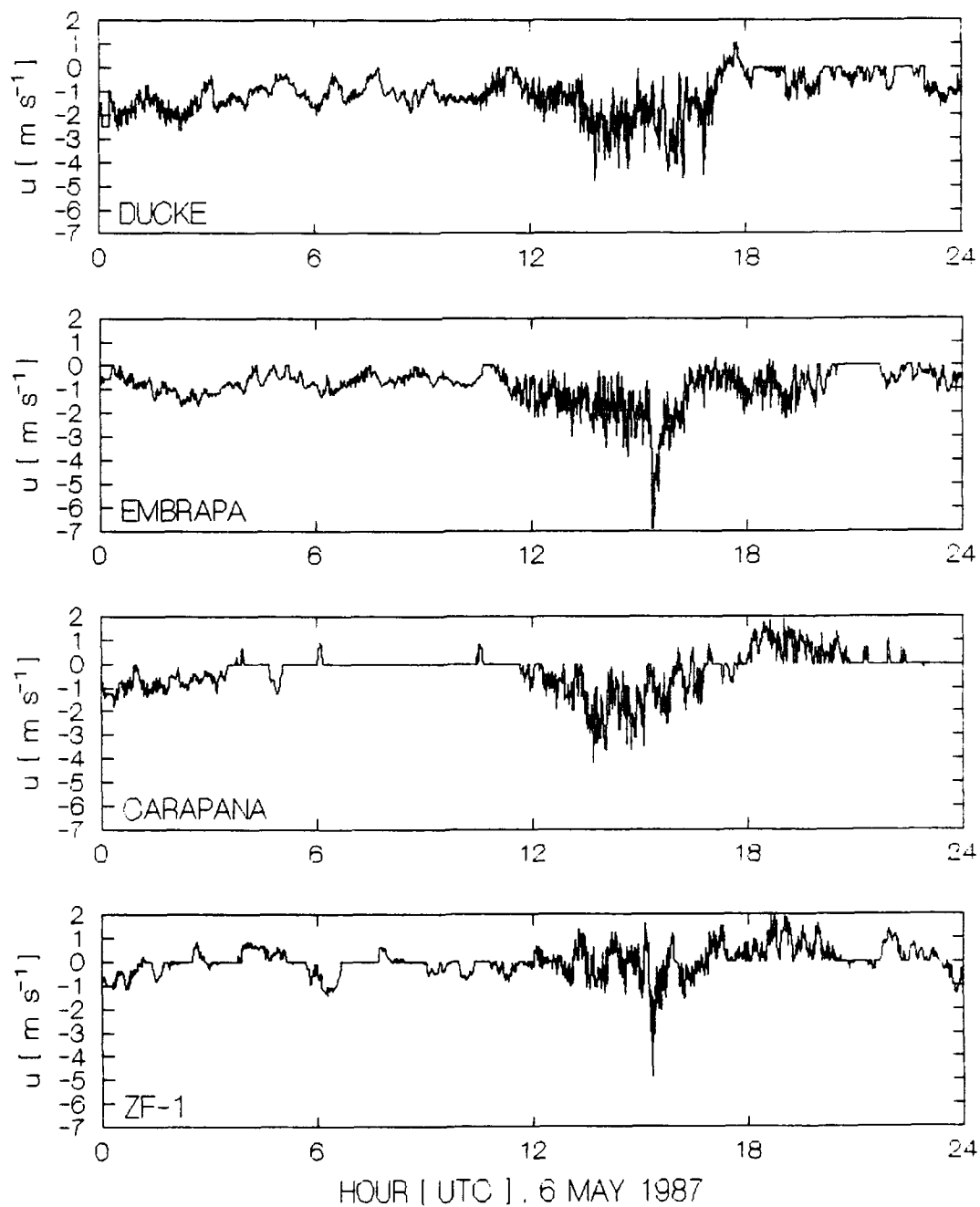


Figure 70. PAM time series of  $u$  ( $\text{m s}^{-1}$ ) on 6 May 1987.

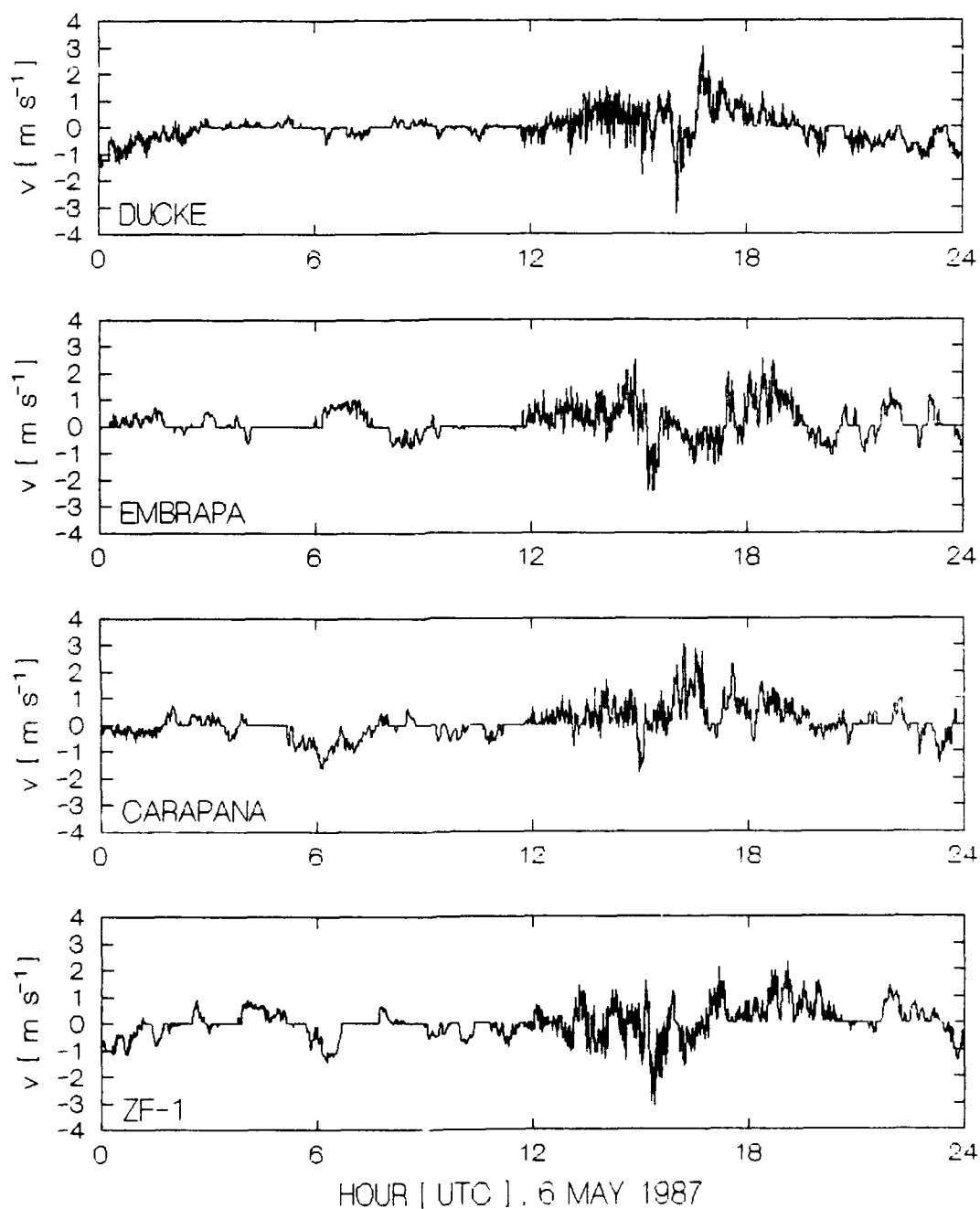


Figure 71. PAM time series of  $v$  ( $\text{m s}^{-1}$ ) on 6 May 1987.

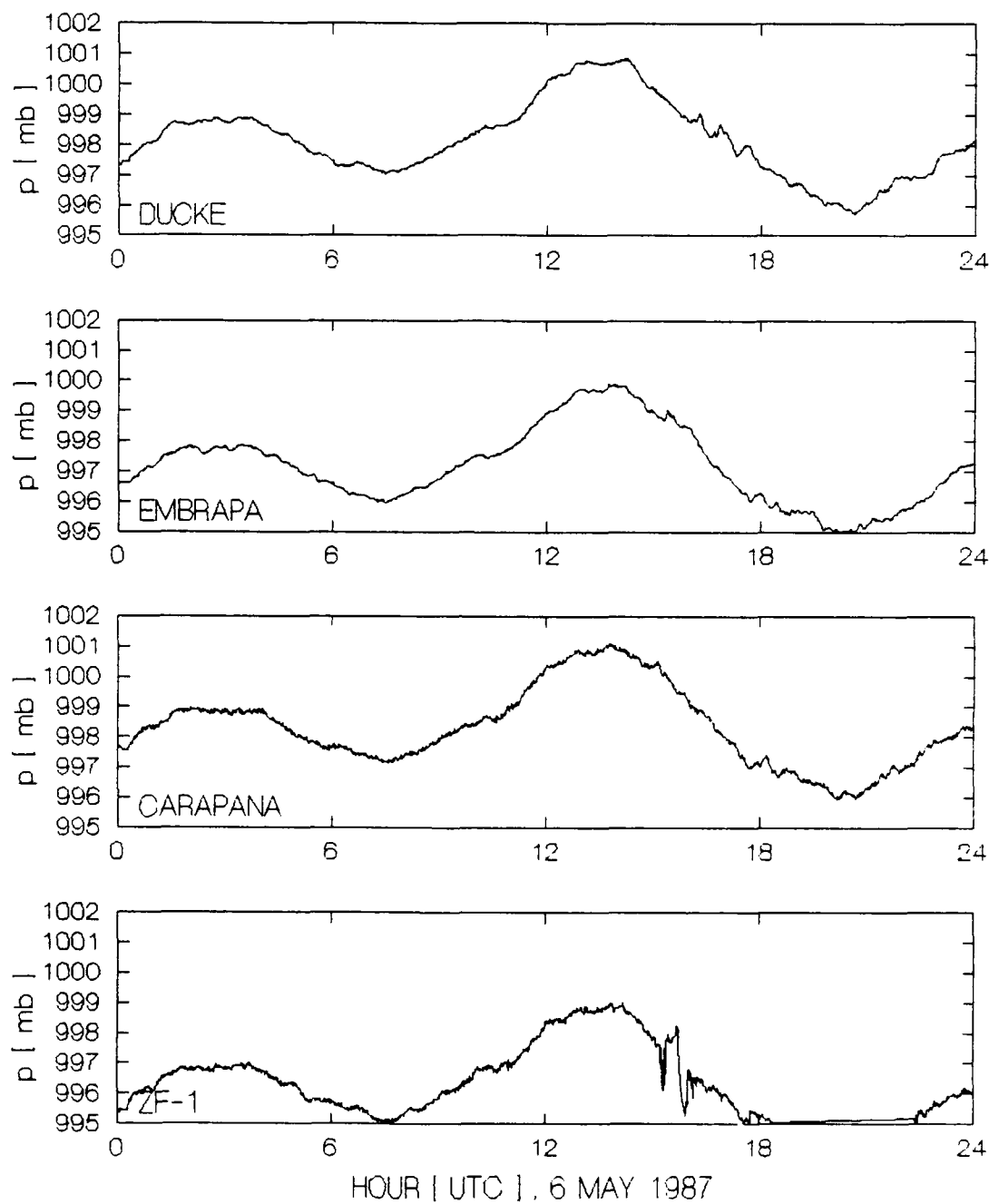


Figure 72. PAM time series of  $p$  (mb) on 6 May 1987.

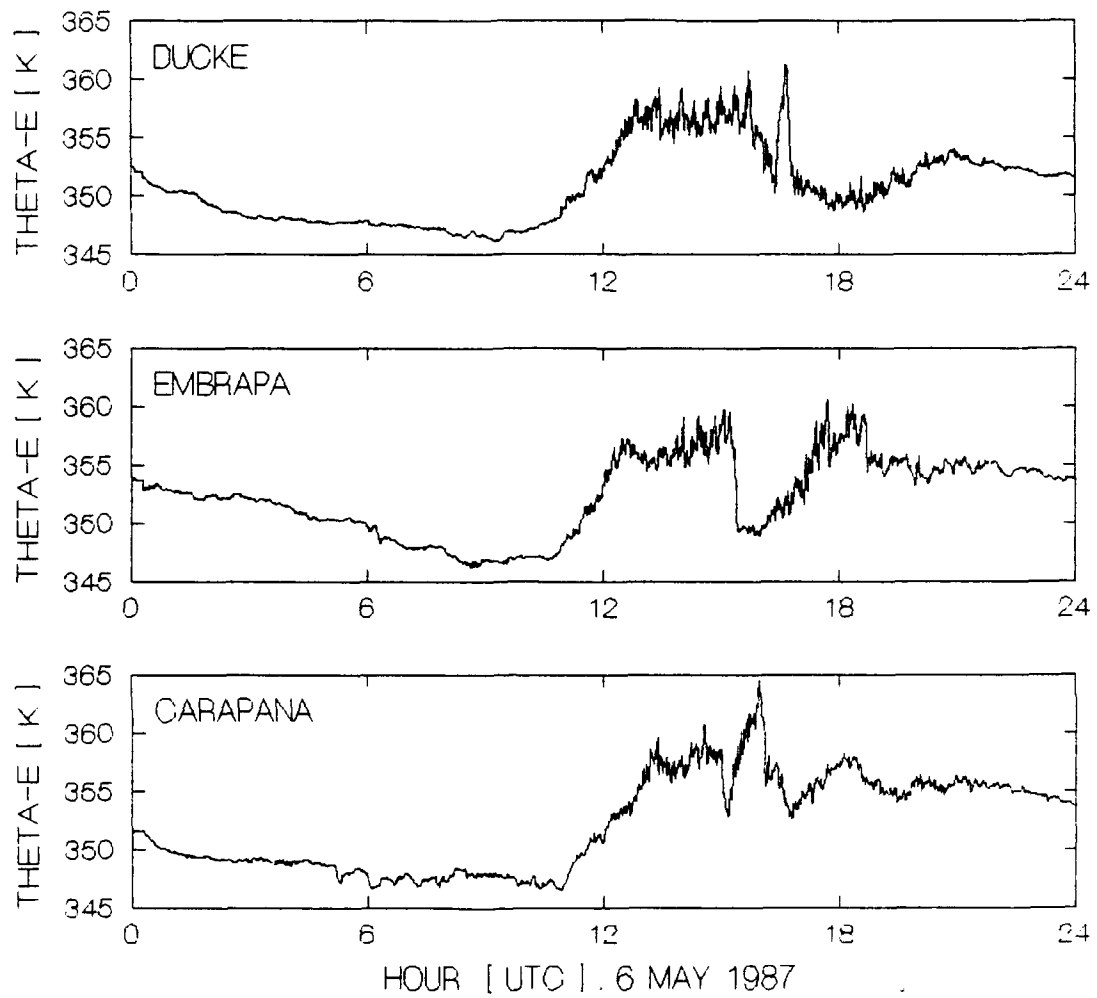


Figure 73. PAM time series of  $\theta_e$  (deg K) on 6 May 1987.

little difference between the beginning and the end of the period.

The rawinsonde time cross-sections of  $u$  (Figure 74),  $v$  (Figure 75), and  $\theta_e$  (Figure 76) show little change after squall front passage. In contrast to the systems occurring on 26 April and 1 May,  $u$  and  $v$  at the lower levels show no pronounced directional shifts, weaker vertical shear, and no distinct low level easterly jet maximum behind the squall front, although a low level jet is clearly present. The changes in  $\theta_e$  at the lower levels follow a trend like that expected with the diurnal heating cycle instead of the one associated with storm downdrafts.

Weak low level convergence between 925 and 700 mb in the vicinity of the squall front at 1500 UTC (Figure 77) produces weak upward vertical motion in the lower and mid troposphere (Figure 78). The rawinsonde network does not resolve the relatively narrow convective component of the 6 May COS, but the stratiform component is well-defined in both the divergence and vertical motion fields at 1800 UTC.

Relative humidity (Figure 79) exhibits a pronounced upper-level dry layer ahead of the disturbance line, a deep moist layer near the convective component, and drier air under the stratiform anvil. The upper-level dry layer in the pre-storm environment and the lower-level dry layer in the anvil region coincide with areas of enhanced mesoscale subsidence.

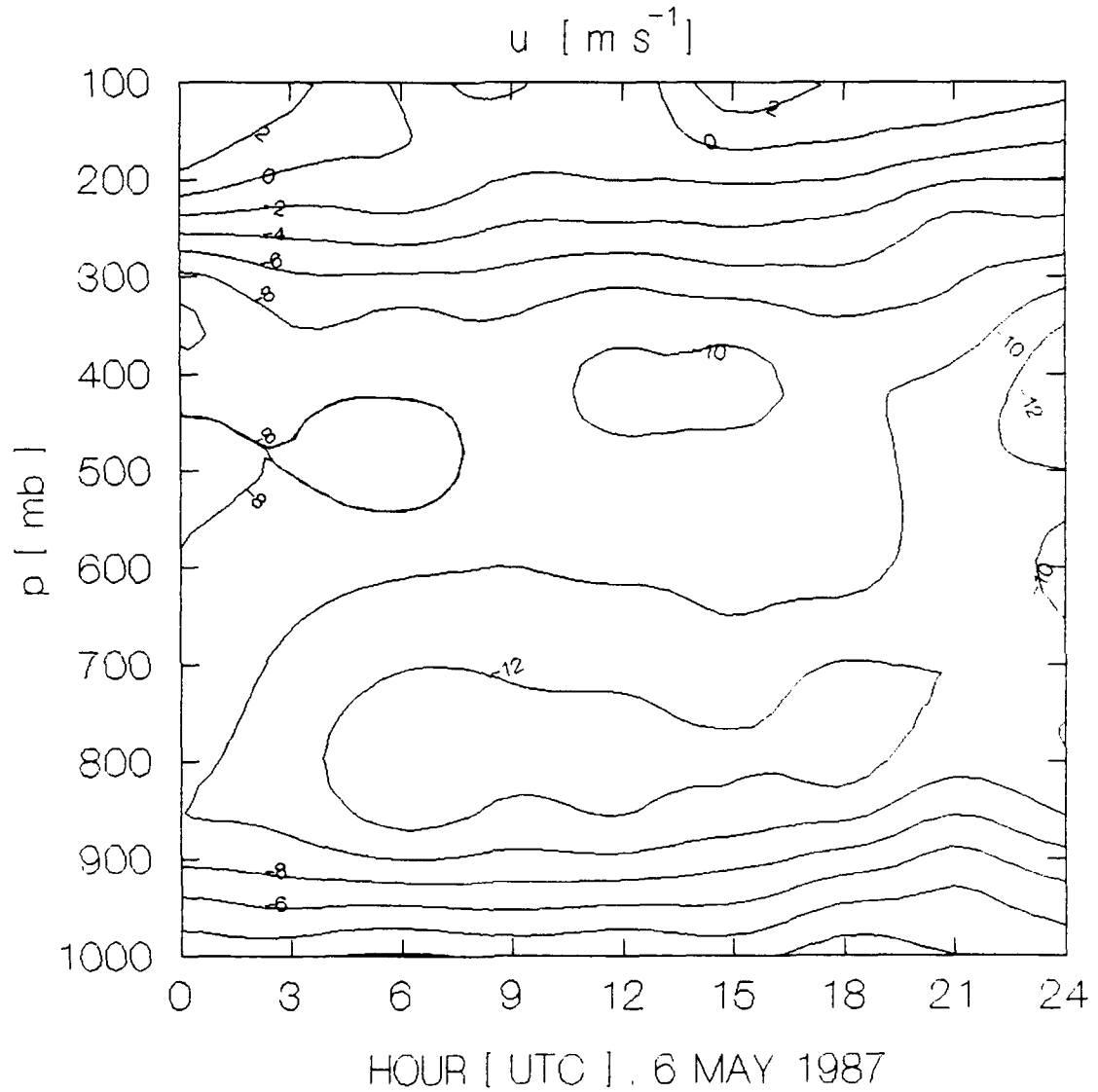


Figure 74. Vertical time cross section of  $\bar{u}$  ( $\text{m s}^{-1}$ ) in the mesoscale triangle on 6 May 1987. The contour interval is  $2 \text{ m s}^{-1}$ .

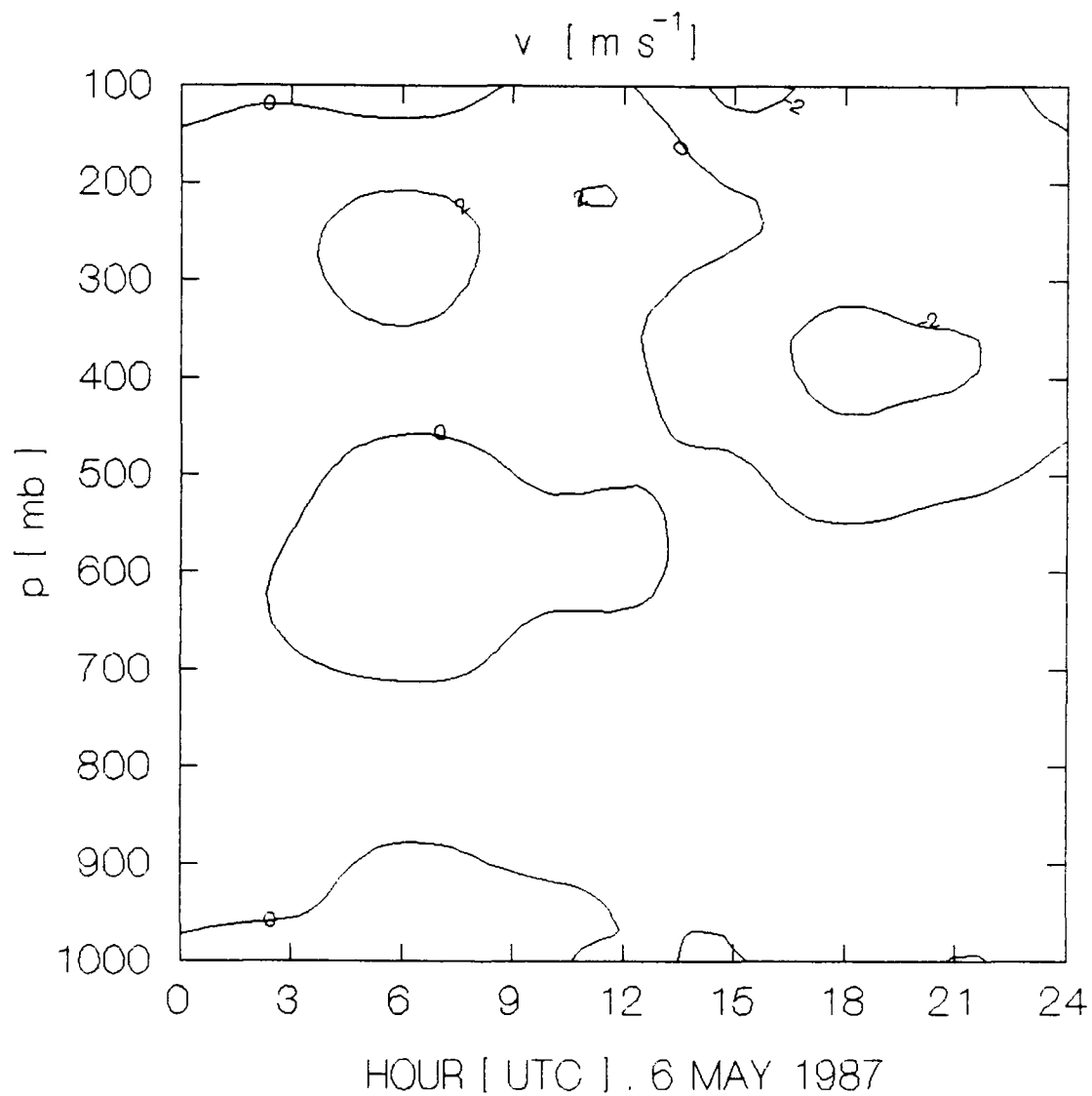


Figure 75. Vertical time cross section of  $v$  ( $\text{m s}^{-1}$ ) in the mesoscale triangle on 6 May 1987. The contour interval is 2  $\text{m s}^{-1}$ .

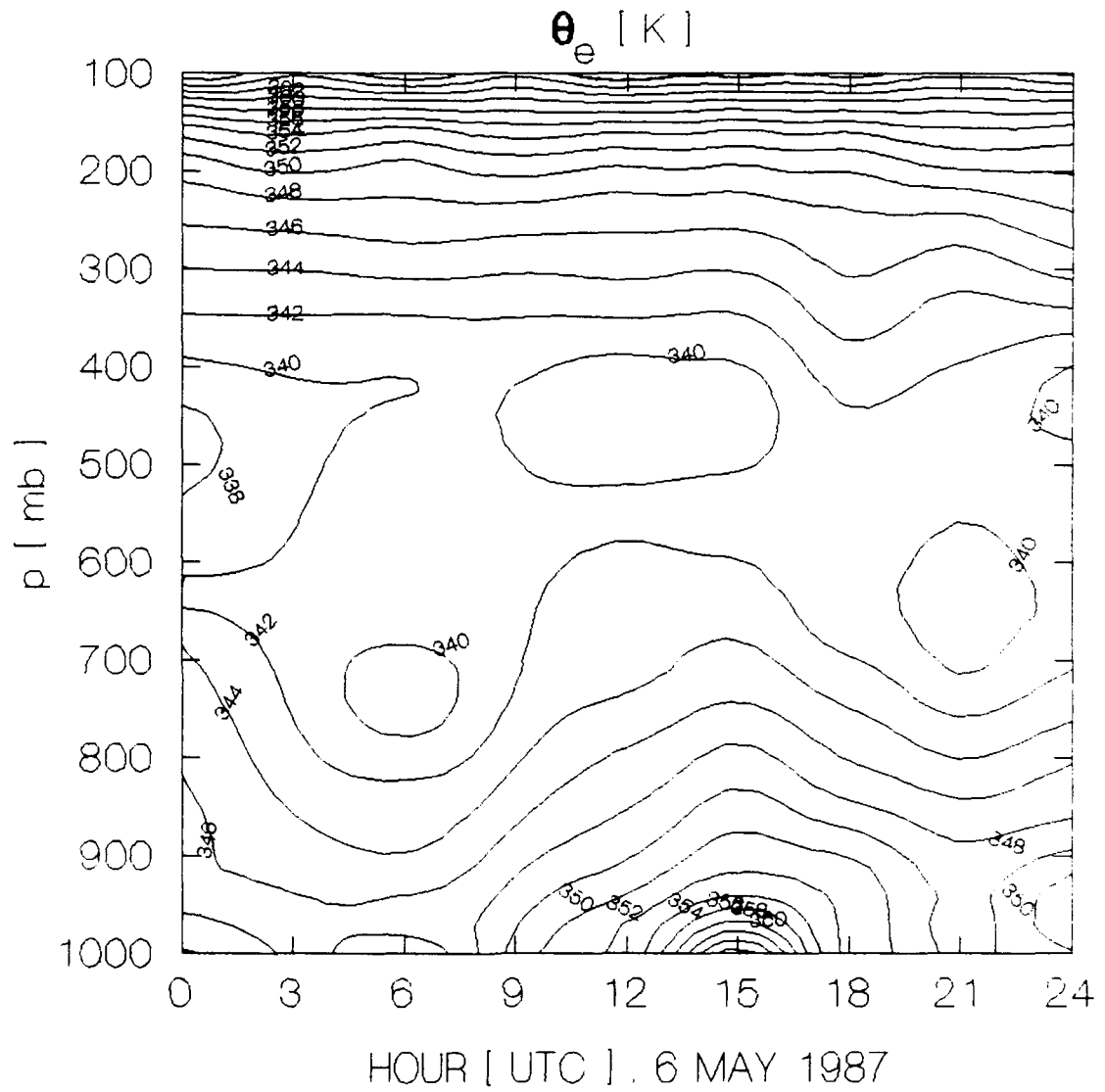


Figure 76. Vertical time cross section of  $\theta_e$  (K) in the mesoscale triangle on 6 May 1987. The contour interval is 2 K.

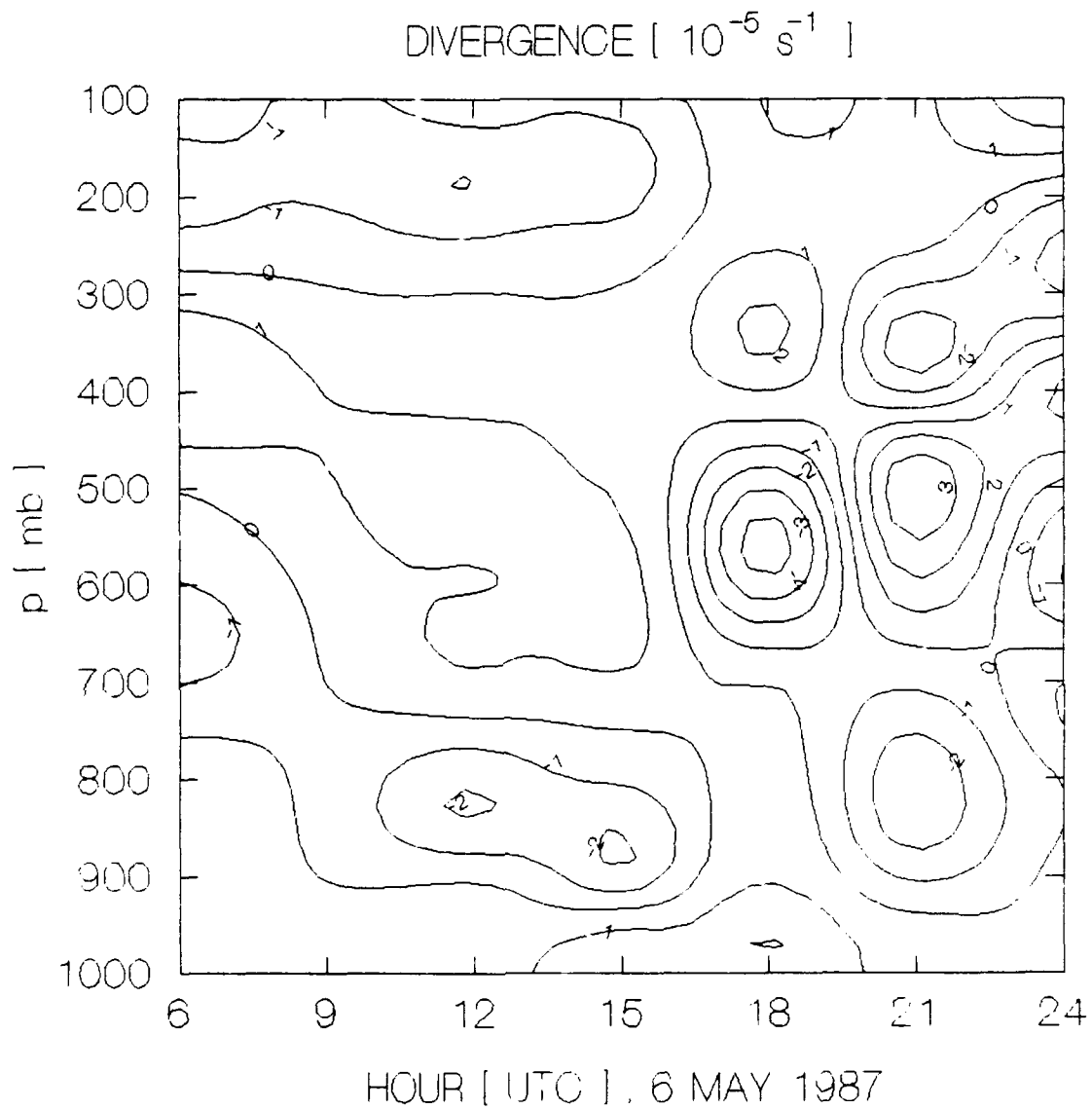


Figure 77. Vertical time cross section of divergence ( $10^{-5} \text{ s}^{-1}$ ) in the mesoscale triangle on 6 May 1987. The contour interval is  $1 \times 10^{-5} \text{ s}^{-1}$ .

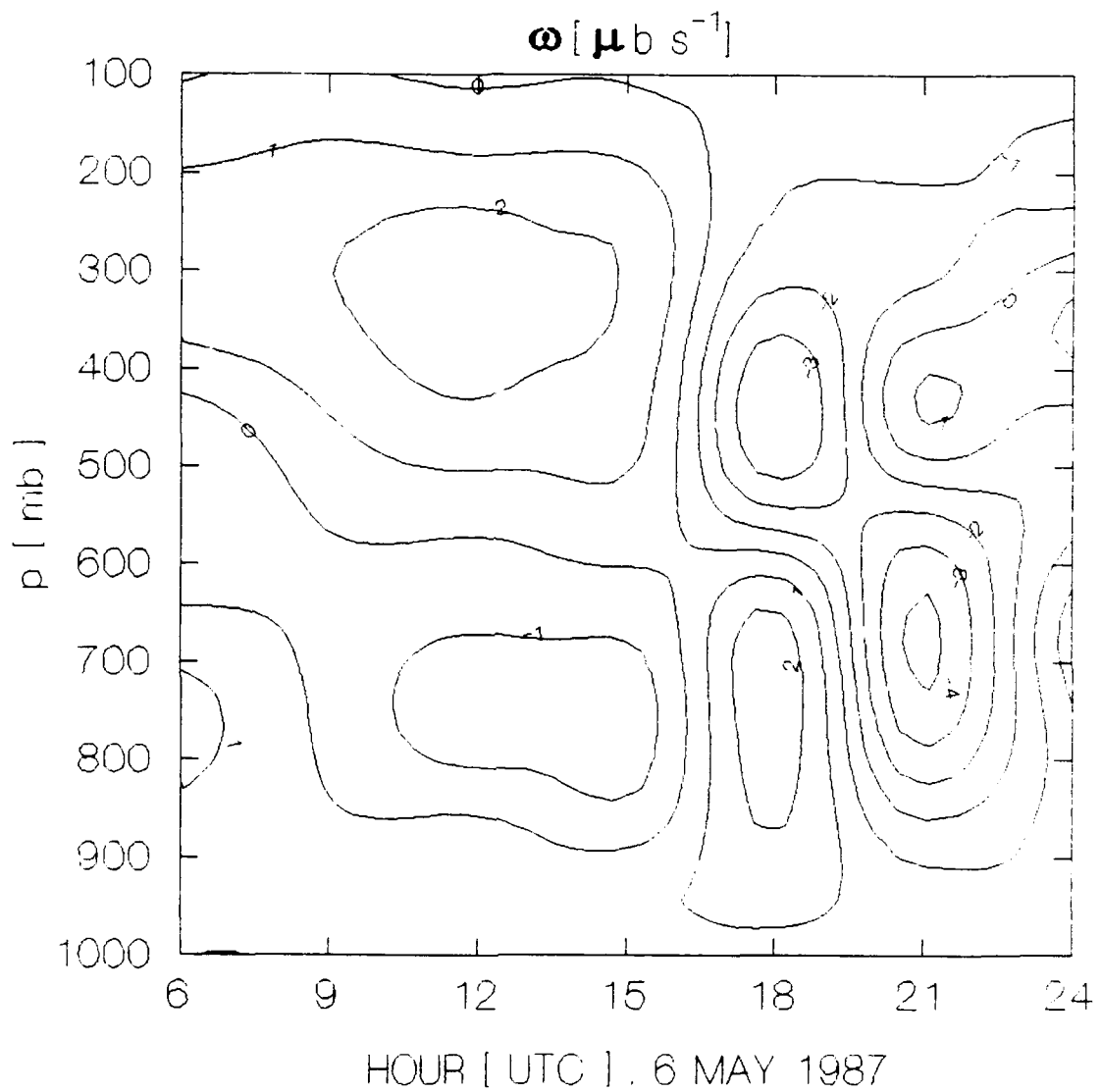


Figure 78. Vertical time cross section of  $\omega$  (microbars  $\text{s}^{-1}$ ) in the mesoscale triangle on 6 May 1987. The contour interval is 1 microbar  $\text{s}^{-1}$ .

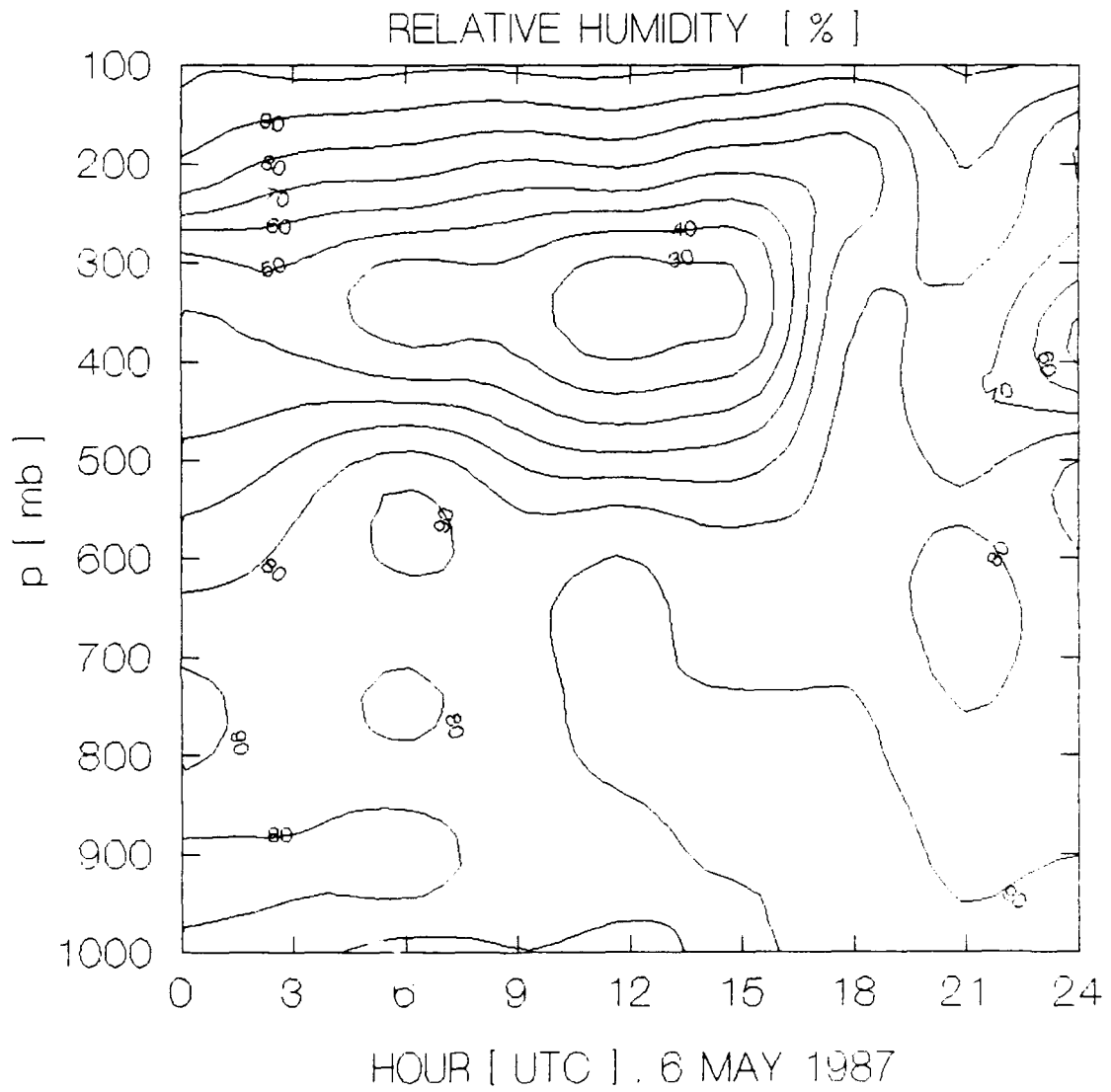


Figure 79. Vertical time cross section of mean relative humidity (%) in the mesoscale triangle on 6 May 1987. The contour interval is 10%.

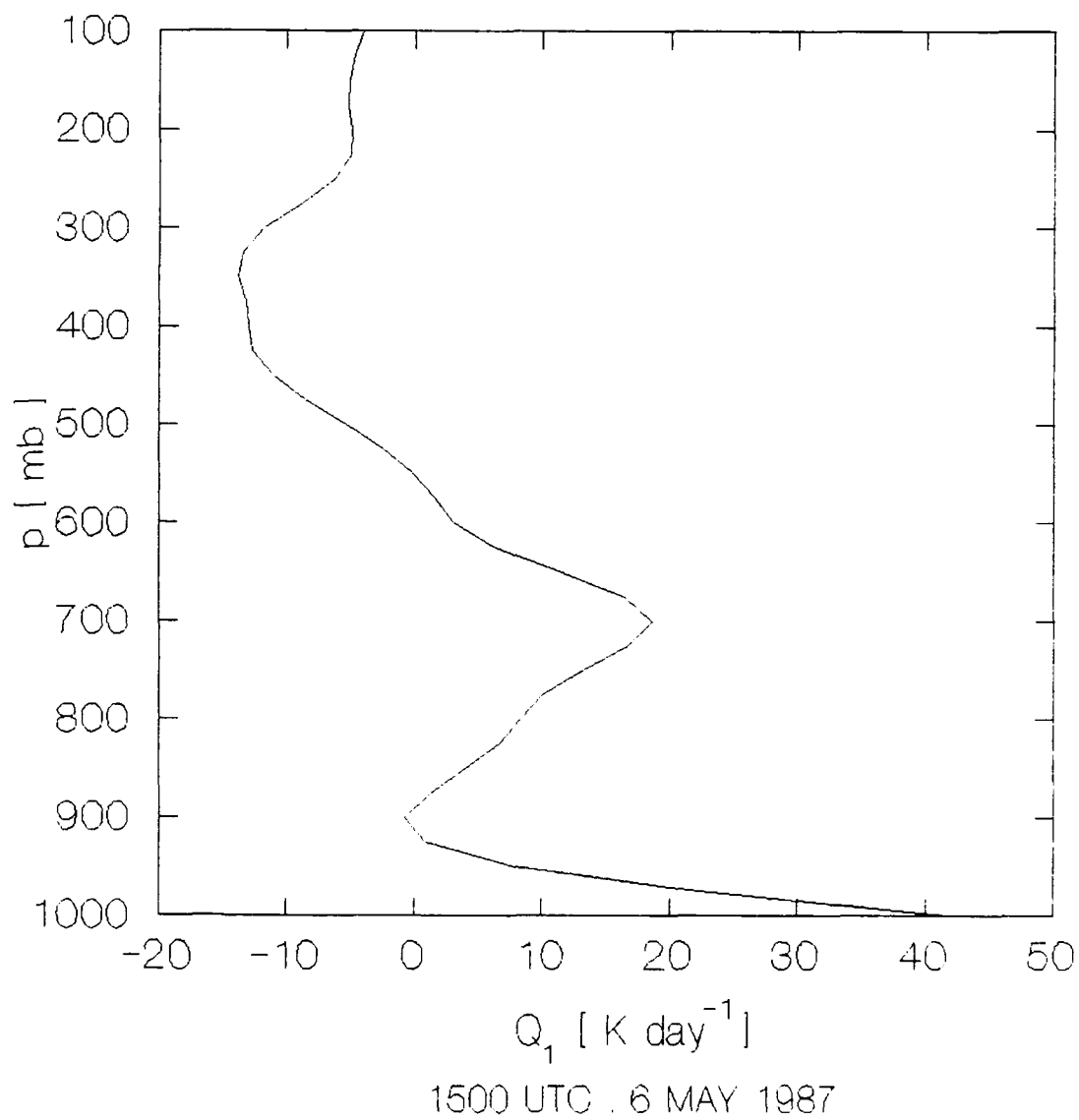


Figure 80. Apparent sensible heat source ( $\text{K day}^{-1}$ ) in the mesoscale triangle during the COS building cumulus component at 1500 UTC, 6 May 1987.

The 1500 UTC soundings meet the criteria for pre-squall towering cumulus. The sensible heat source (Figure 80) shows strong surface heat flux and pronounced mid-level heating at heights occupied by towering cumulus. Cooling occurs above the cloud tops, analyzed from relative humidities to be near 600 mb. The  $Q_2$  profile (Figure 81) indicates strong surface and low level moistening. Pre-storm radiation profiles (Figures 82-83) show net cooling of the troposphere. The  $F$  profile (Figure 84) is positive below 800 mb and negative in the mid and upper levels.

The heat and moisture budgets of the anvil component (1800 UTC) are shown in Figures 85-86. In the subcloud layer,  $Q_1$  (Figure 85) is negative with maximum cooling being at the surface and near 675 mb. Moistening (Figure 86) occurs below the anvil cloud base and is strongest at 700 and 900 mb. There is strong drying at the surface and drying at the mid levels. The radiative rates of temperature change (Figures 87-88) indicate net cooling of the lower troposphere in the anvil region. The vertical eddy flux of total heat (Figure 89) resembles that in the 26 April anvil component as low surface values increase to a mid-level maximum and then decrease through the upper troposphere. The mid-level maximum suggests the anvil component plays an important role in vertical heat transport on 6 May.

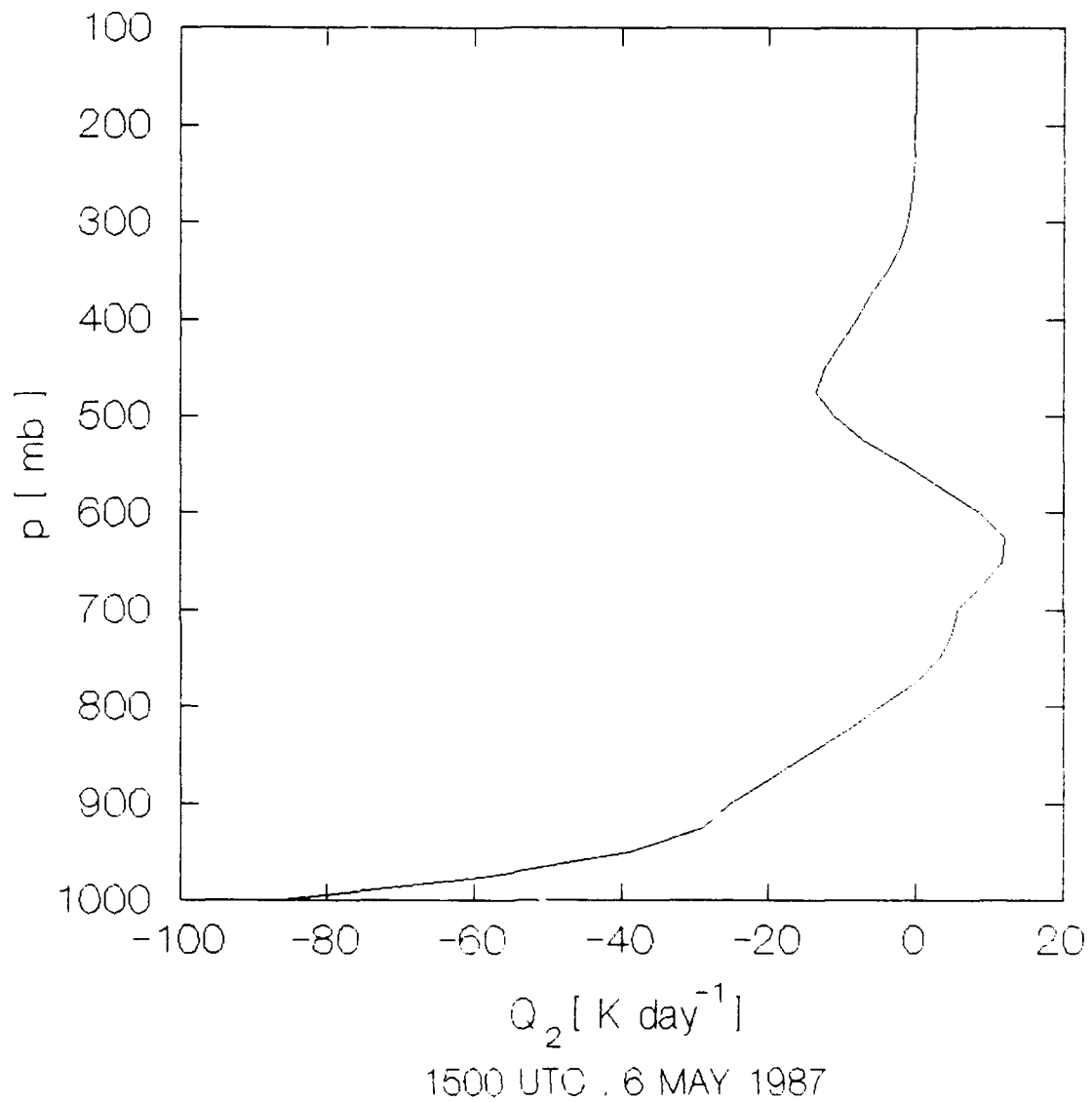


Figure 81. Apparent moisture sink ( $\text{K day}^{-1}$ ) in the meso-scale triangle during the COS building cumulus component at 1500 UTC, 6 May 1987.

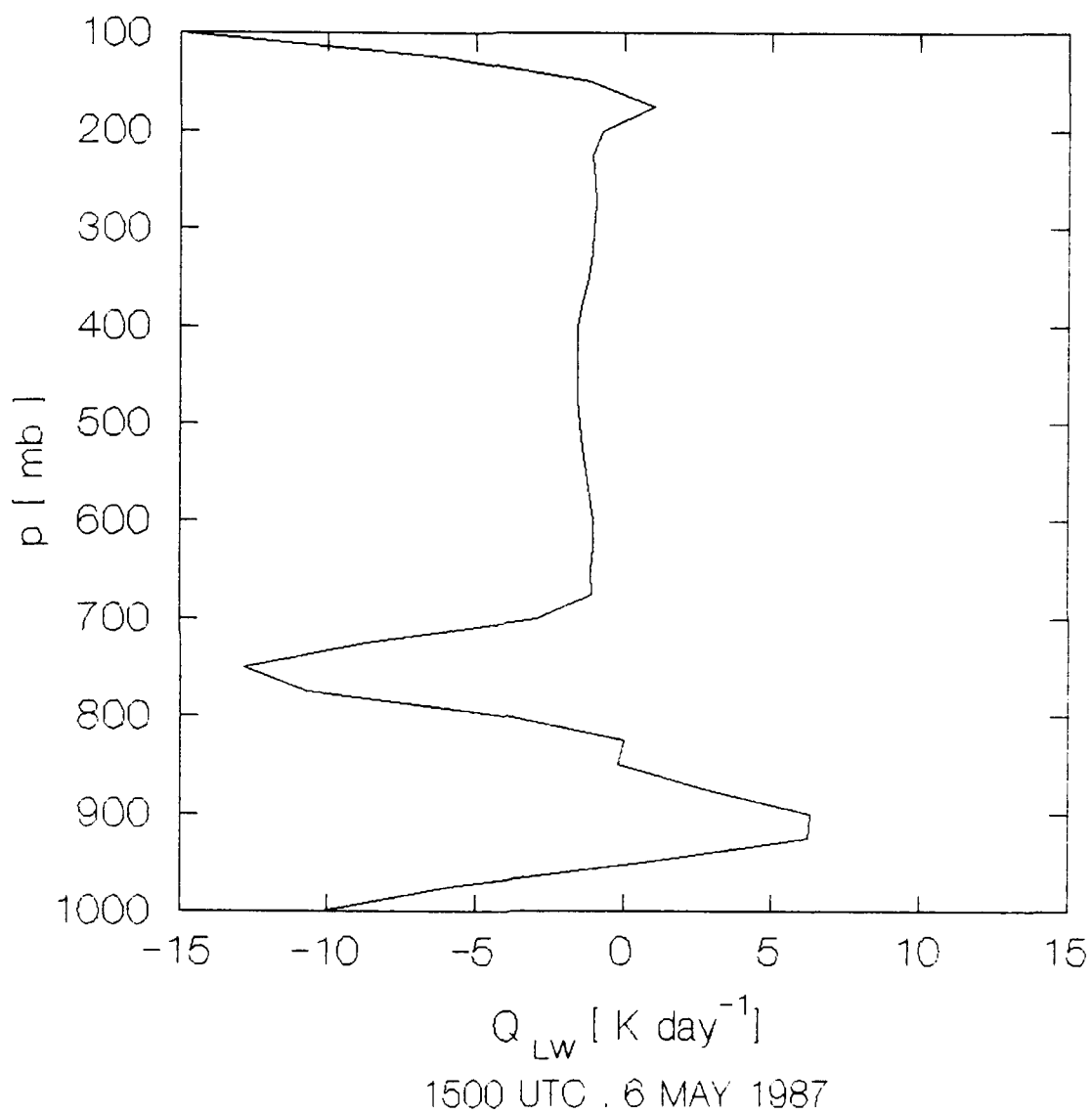


Figure 82. Rate of temperature change (K day<sup>-1</sup>) due to longwave radiation in the mesoscale triangle during the COS building cumulus component at 1500 UTC, 6 May 1987.

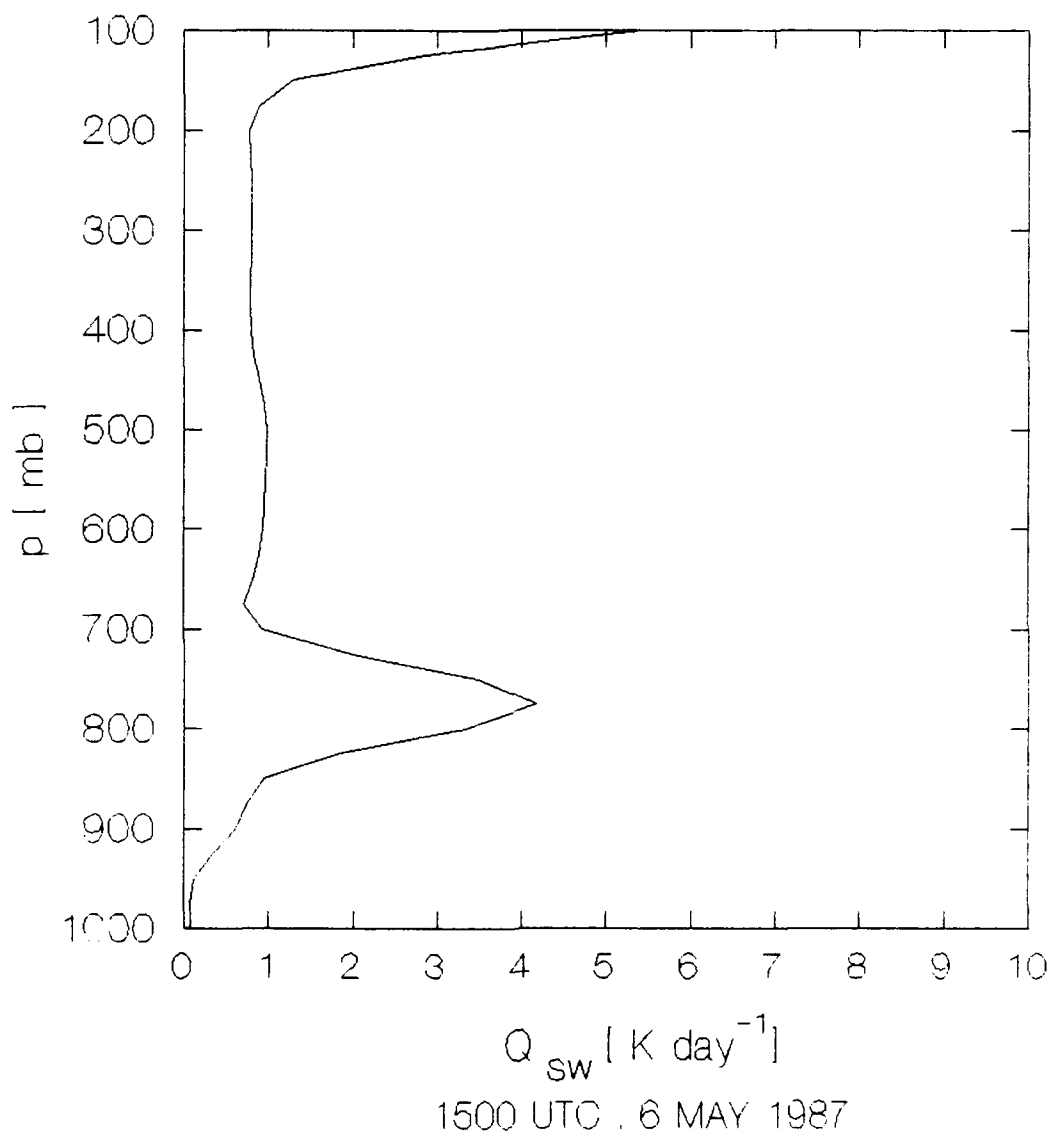


Figure 83. Rate of temperature change ( $\text{K day}^{-1}$ ) due to shortwave radiation in the mesoscale triangle during the COS building cumulus component at 1500 UTC, 6 May 1987.

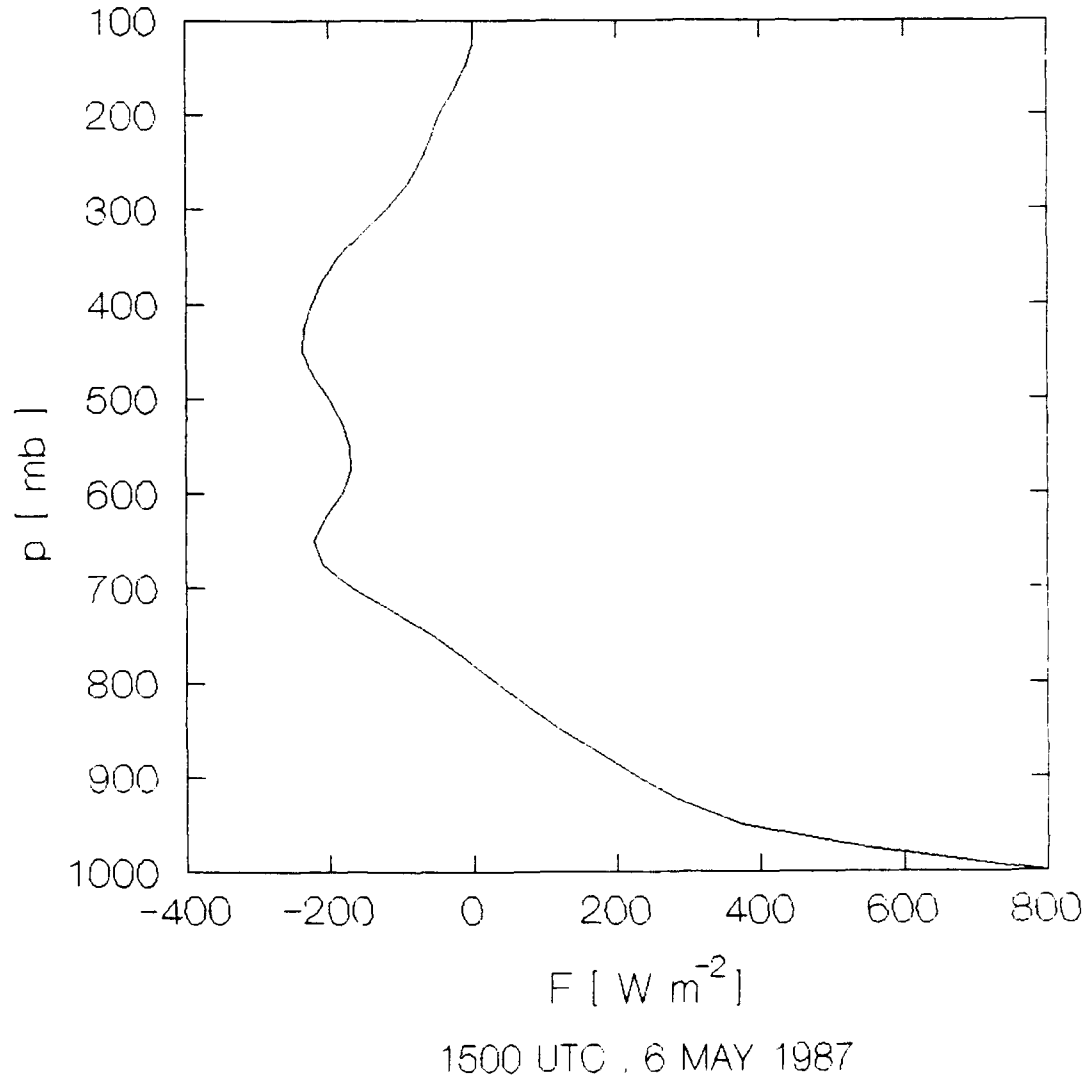


Figure 84. Vertical eddy flux of total heat ( $\text{W m}^{-2}$ ) in the mesoscale triangle during the COS building cumulus component at 1500 UTC, 6 May 1987.

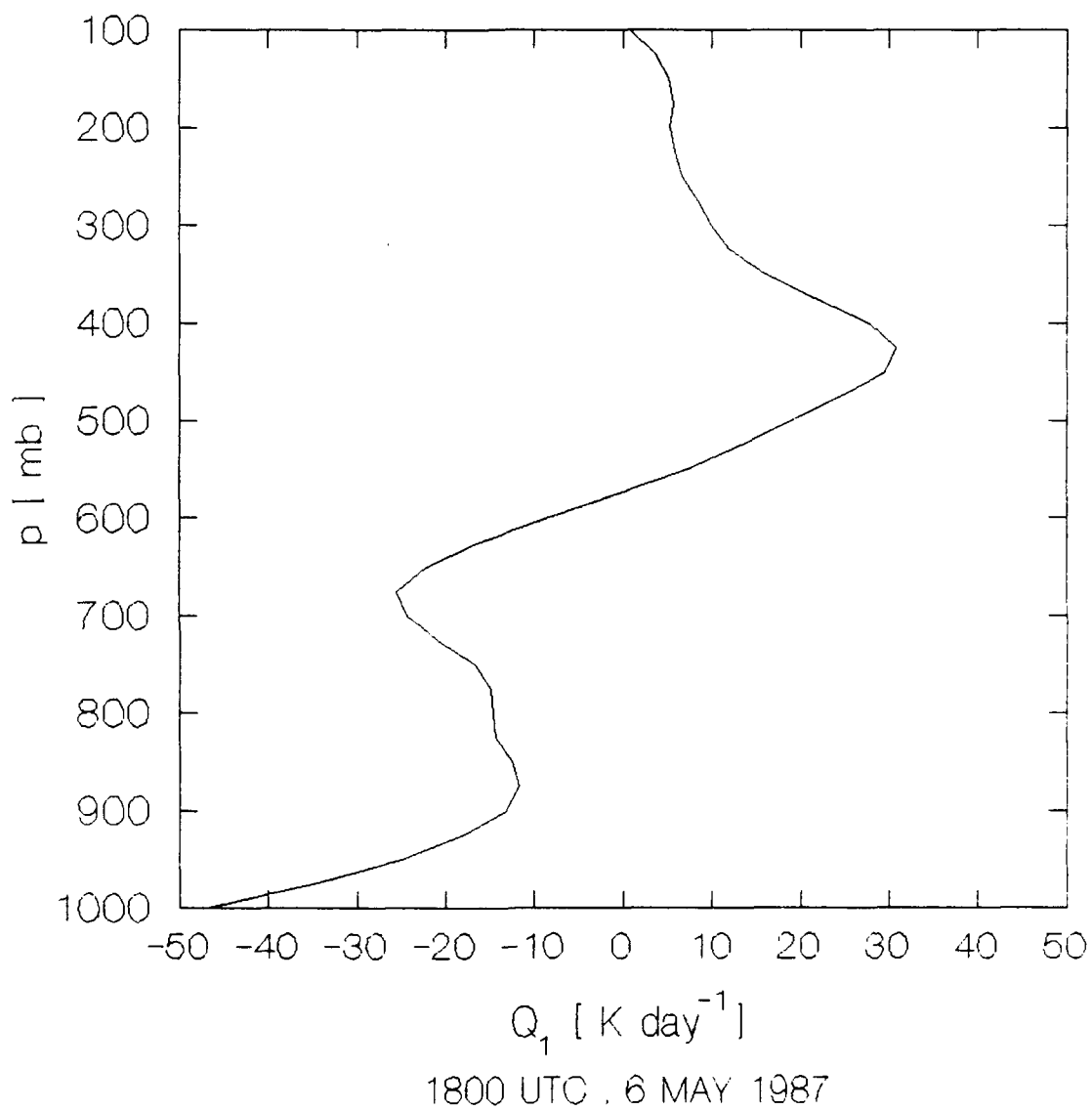


Figure 85. Apparent sensible heat source ( $\text{K day}^{-1}$ ) in the mesoscale triangle during the regenerating COS anvil component at 1800 UTC, 6 May 1987.

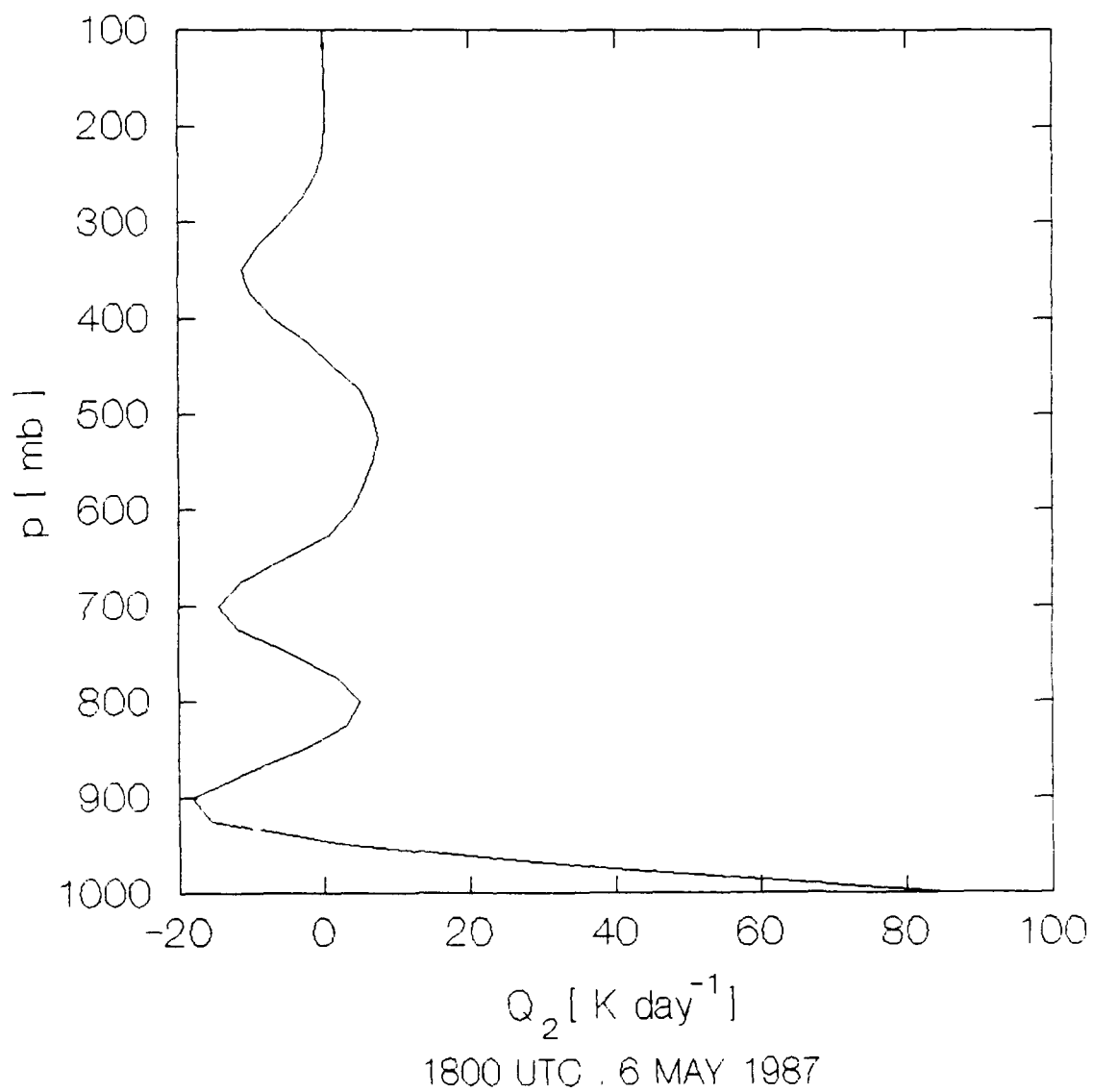


Figure 86. Apparent moisture sink ( $K \text{ day}^{-1}$ ) in the meso-scale triangle during the regenerating COS anvil component at 1800 UTC, 6 May 1987.

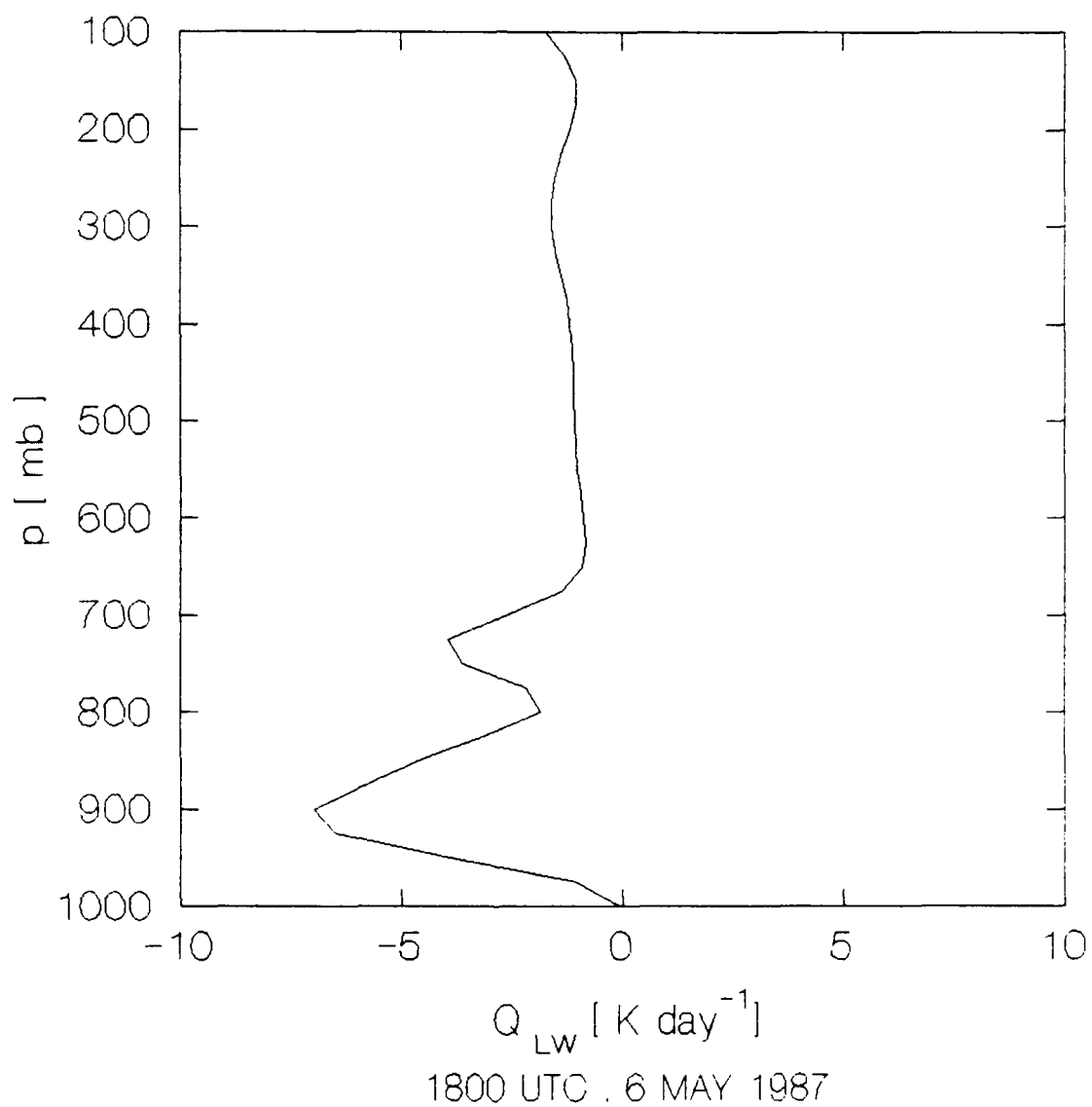


Figure 87. Rate of temperature change (K day<sup>-1</sup>) due to longwave radiation in the mesoscale triangle during the regenerating COS anvil component at 1800 UTC, 6 May 1987.

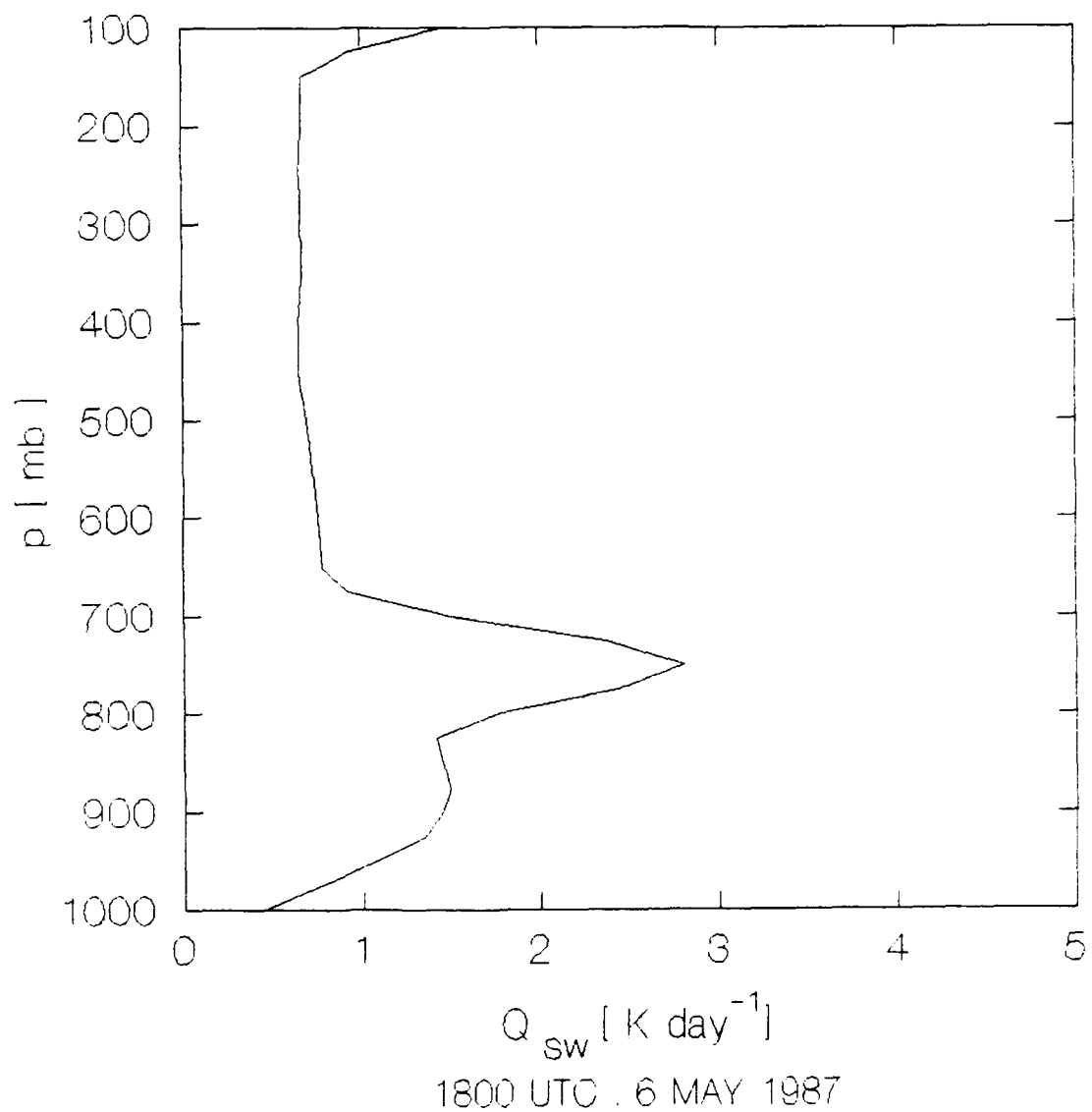


Figure 88. Rate of temperature change ( $K \text{ day}^{-1}$ ) due to shortwave radiation in the mesoscale triangle during the regenerating COS anvil component at 1800 UTC, 6 May 1987.

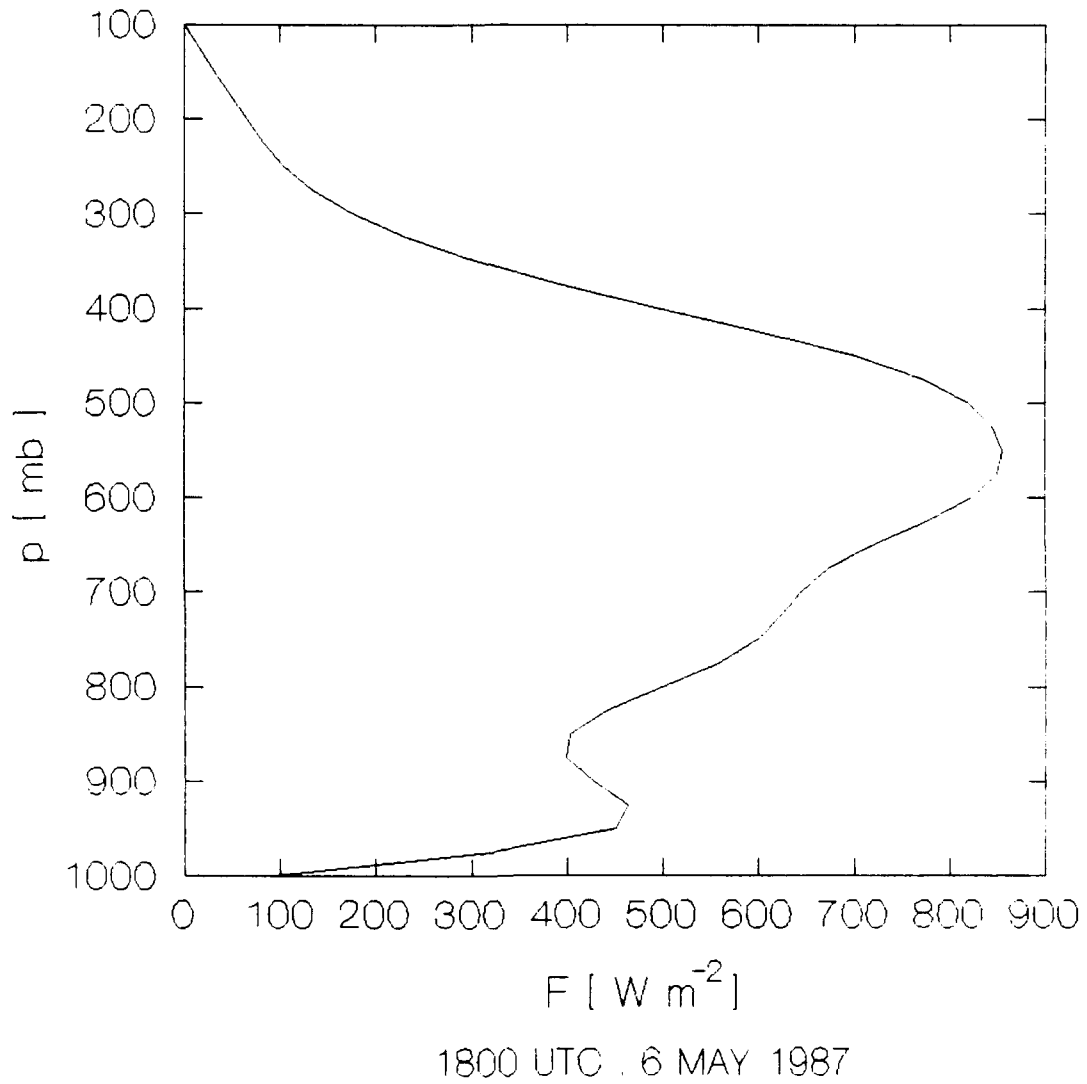


Figure 89. Vertical eddy flux of total heat ( $\text{W m}^{-2}$ ) in the mesoscale triangle during the regenerating COS anvil component at 1800 UTC, 6 May 1987.

**D. Fair Weather Cumulus, 4 May 1987**

On 4 May 1987, fair weather prevailed over the central Amazon basin. The sky conditions were scattered-to-broken cumulus, altocumulus, and cirrus with a trend towards decreasing cloudiness in the afternoon.

This case provides a comparison of Type 1 undisturbed fair weather conditions to the disturbed Type 2-4 conditions described in sections 4.A.-4.C. Undisturbed conditions on 4 May followed the occurrence of a mature COS in the network on 3 May. However, the 4 May is dominated by undisturbed fair weather as indicated by the PAM time series, GOES images, and surface observations.

The GOES IR images (Figures 90-91) show fair skies over the central Amazon basin and mesoscale triangle network at 1200 UTC and 1830 UTC, respectively. At 1200 UTC, mesoscale convective clusters appear only in northern and eastern sections of the basin. At 1830 UTC, the only thunderstorms over the Amazon basin occur in regions well to the east of the mesoscale network.

The GOES visible image at 1230 UTC (Figure 92) indicates layered, scattered-to-broken low, mid, and high clouds over the triangle. The 1731 UTC visible image (Figure 93) shows widespread scattered-to-broken cumulus over the central Amazon basin. The image shows the confluence of the Rio Negro and Rio Solimoes, main Amazon river tributaries which meet near Manaus.

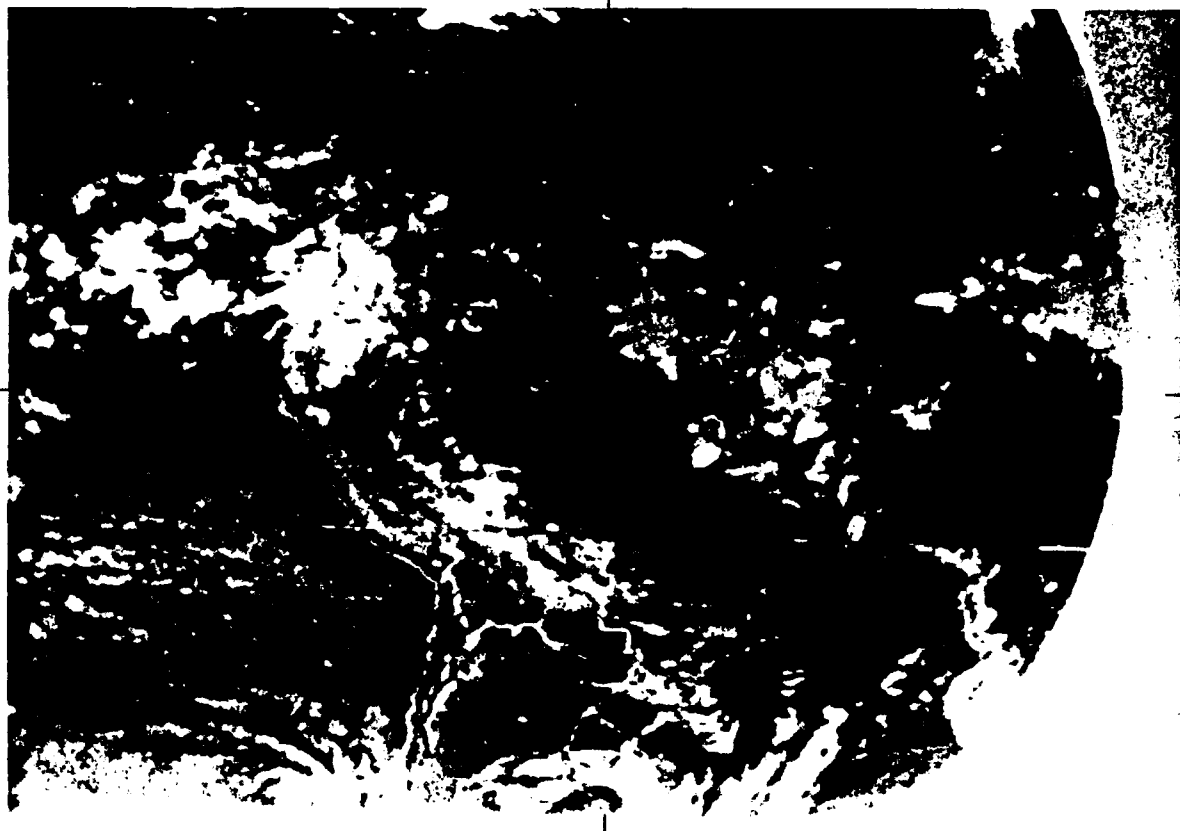


Figure 90. The GOES full disk IR image at 1200 UTC,  
4 May 1987. The + denotes 3°S, 60°W.

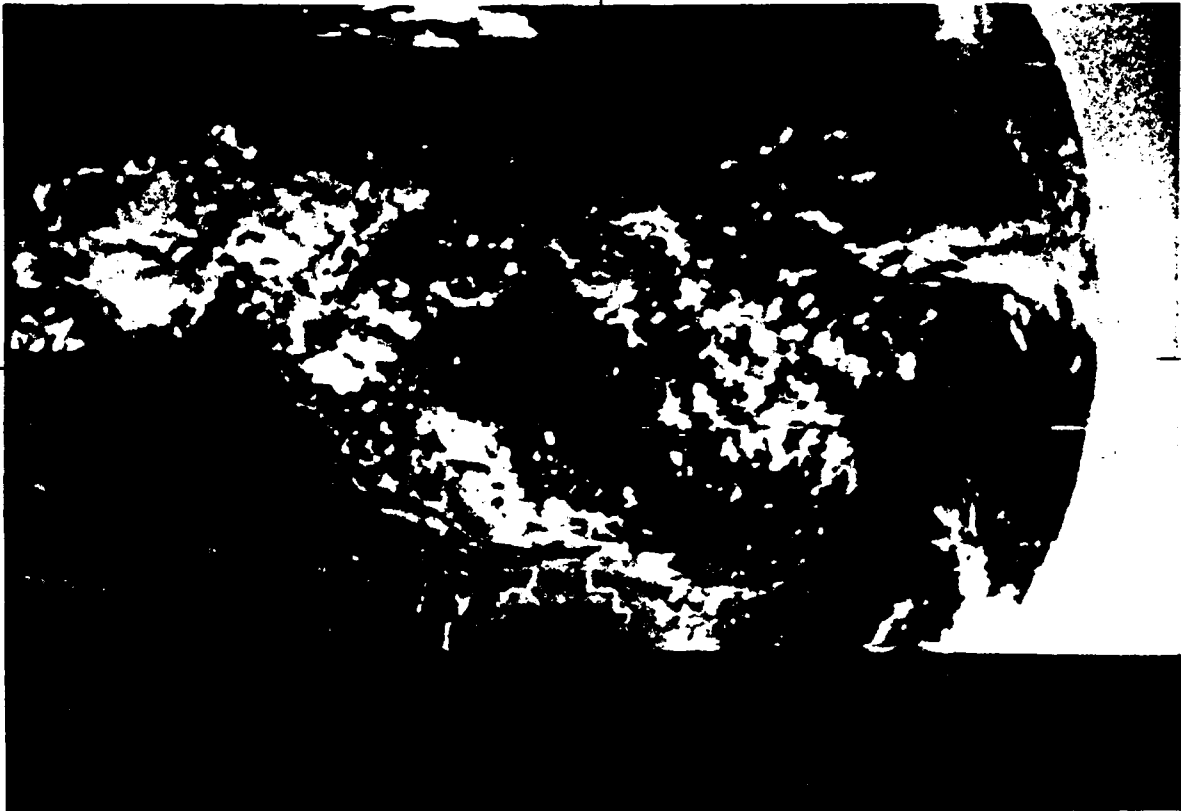
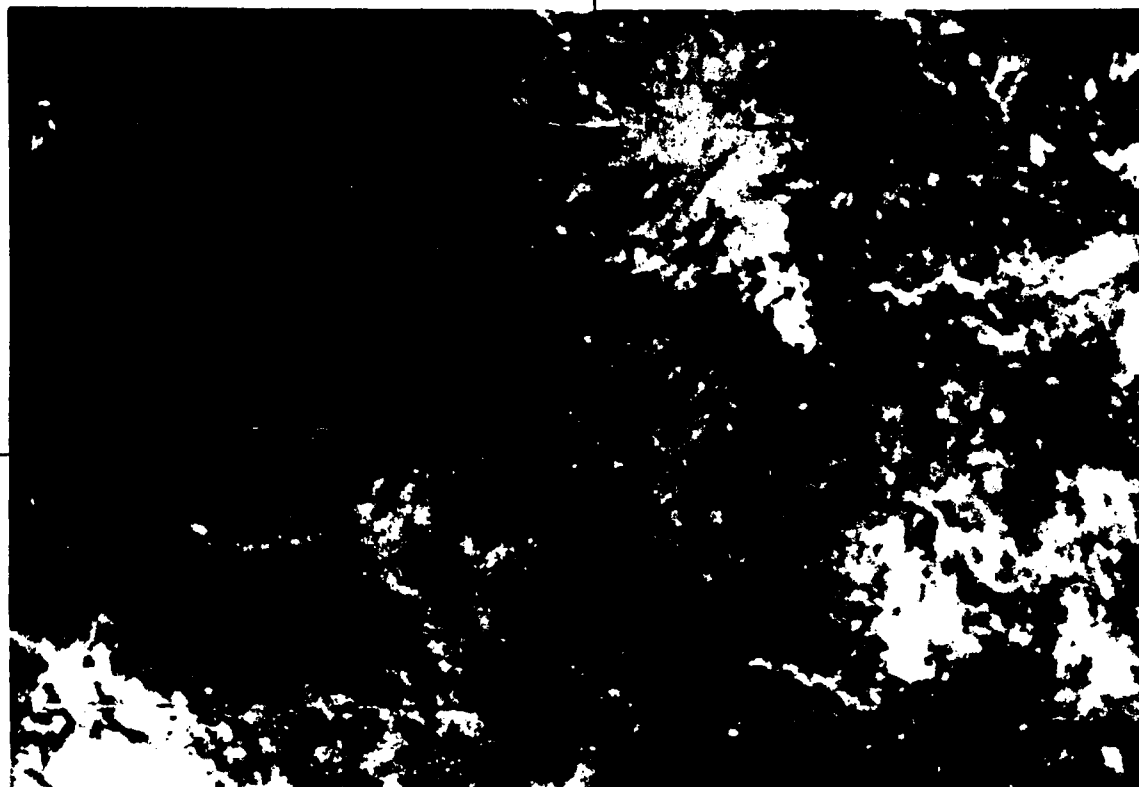


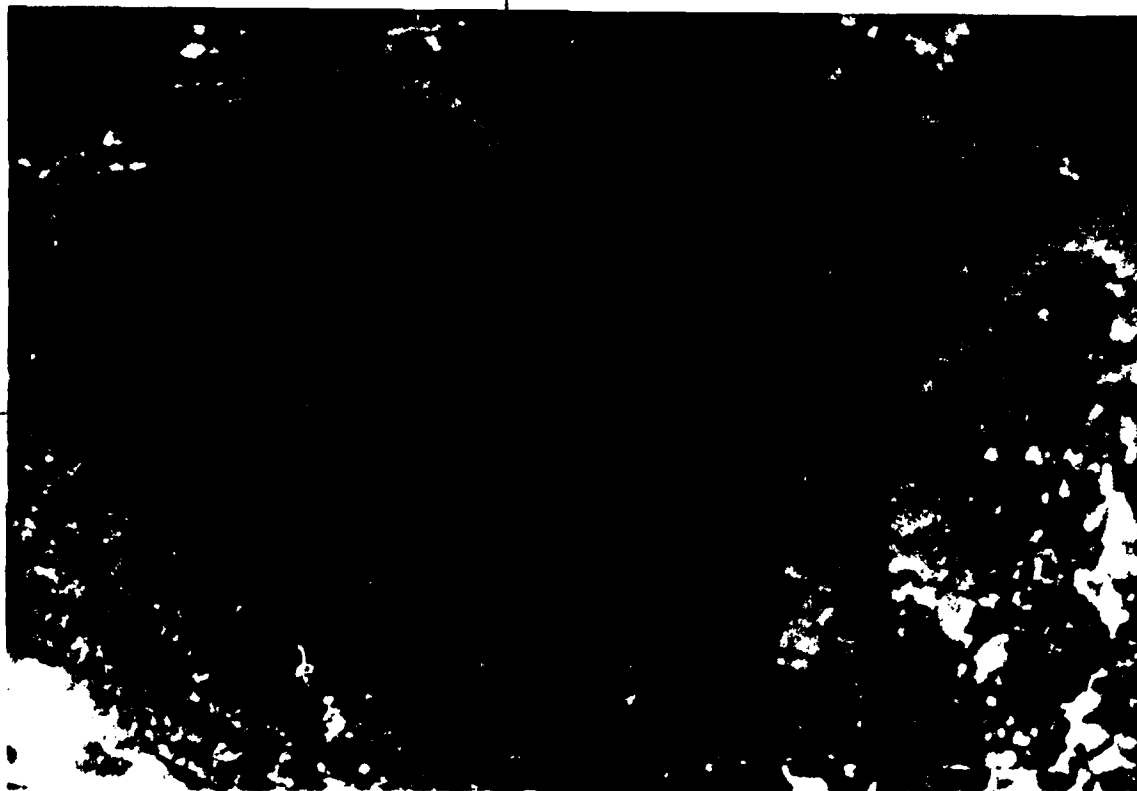
Figure 91. The GOES full disk IR image at 1831 UTC,  
4 May 1987. The + denotes 3°S, 60°W.



500 km

---

Figure 92. The GOES .5 NM-resolution visible image at 1230 UTC, 4 May 1987. The + denotes 3°S, 60°W.



500 km

Figure 93. The GOES .5 NM-resolution visible image at 1731 UTC, 4 May 1987. The + denotes 3°S, 60°W.

No rain fell in the mesoscale triangle on 4 May. The time series of  $u$ ,  $v$ , peak wind,  $q$ ,  $T$ , and  $\theta_e$  (Figures 94-99) show no significant changes other those related to the turbulent mixing of heat and moisture in the boundary layer during diurnal heating.

The 24-hour changes in  $T$ ,  $q$ , and  $\theta_e$  support the hypothesis of Garstang et al. (1990) that heavy precipitation downdrafts in COS suppress diurnal heating for protracted periods. In the 3 May COS, heavy convective precipitation occurred before sunrise while stratiform precipitation occurred after sunrise. COS average total rainfall in the PAM network on 3 May was 4.3 cm.

The PAM mean  $T$  and  $q$  ( $22.3^\circ\text{C}$  and  $17.0 \text{ g kg}^{-1}$ , respectively) in the 3 May anvil stage are nearly equal to those at 0000 UTC on 4 May. Stratiform anvil clouds, still present in the triangle long after passage of the squall front, apparently suppress surface heat and moisture fluxes during the afternoon of 3 May. It appears these effects are influencing the trends in the PAM temperature and moisture observed on 4 May.

The PAM time series of temperature show significant end-of-period (0000 UTC, 5 May) increases of  $3\text{-}4^\circ\text{C}$  compared to the start of the period (0000 UTC, 4 May). The maximum afternoon temperatures are approximately  $5^\circ\text{C}$  warmer than those observed during the afternoon on 3 May. In contrast,  $q$  recovers slower than  $T$ . Moisture budget results presented

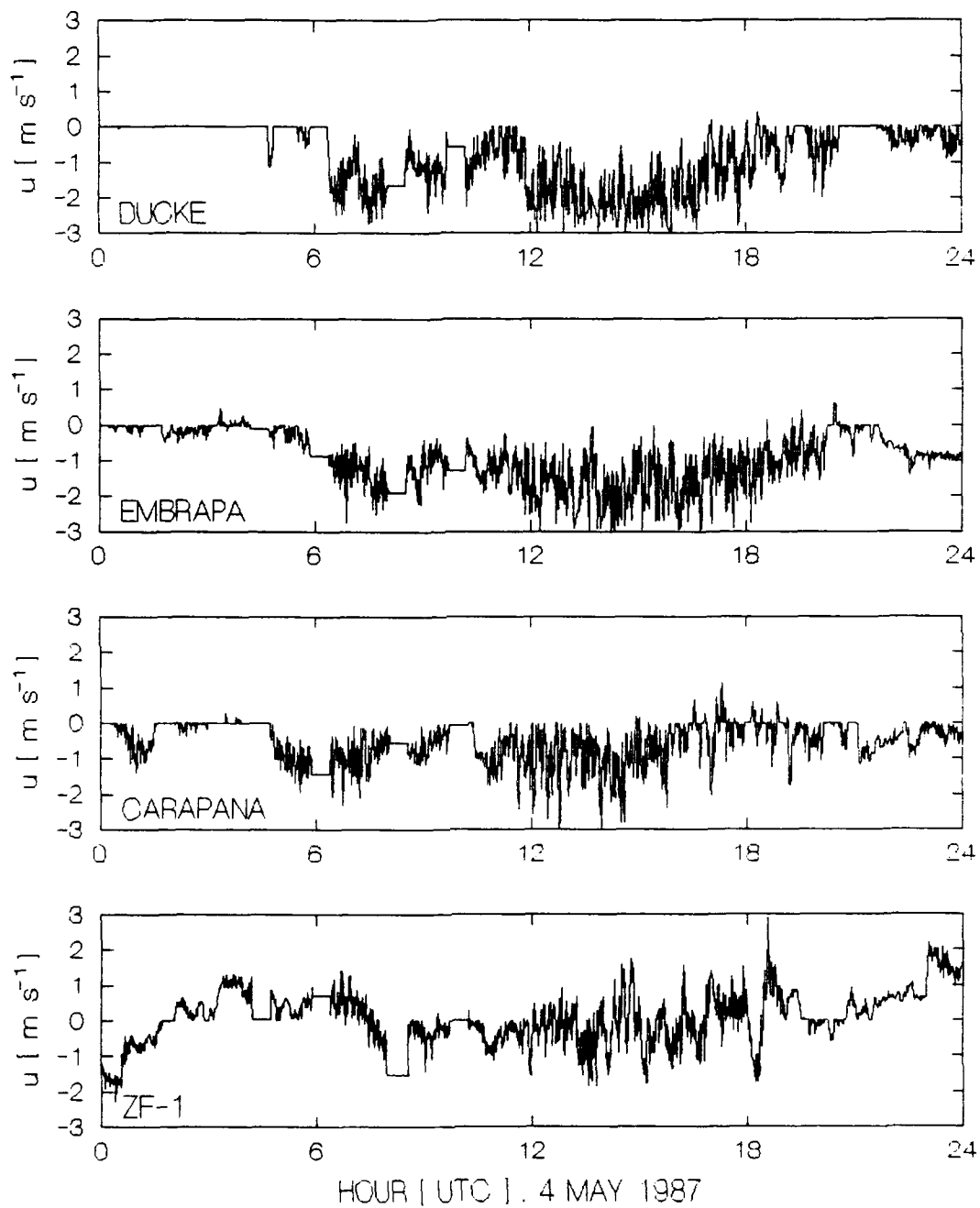


Figure 94. PAM time series of  $u$  ( $\text{m s}^{-1}$ ) on 4 May 1987.

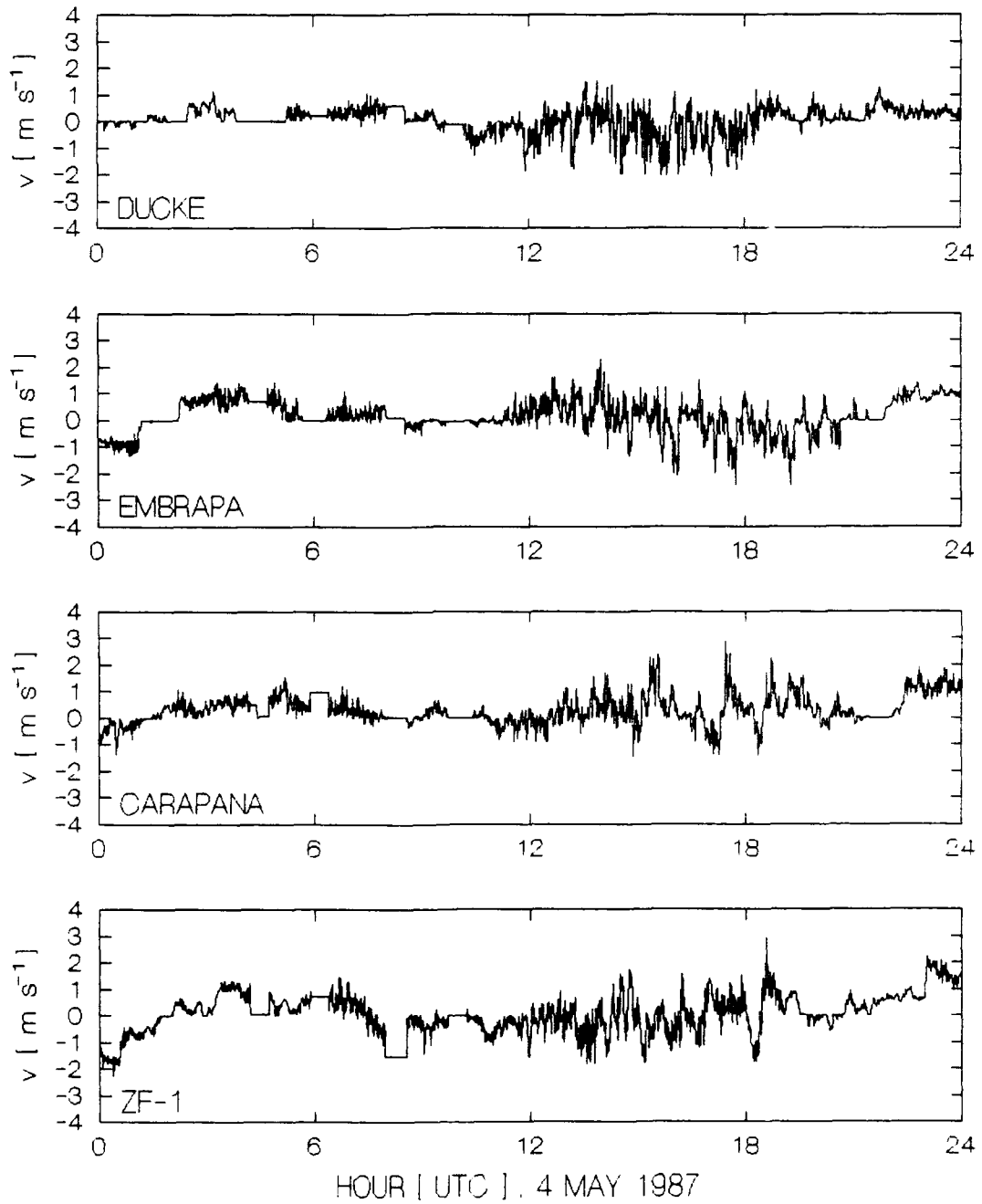


Figure 95. PAM time series of  $v$  ( $m s^{-1}$ ) on 4 May 1987.

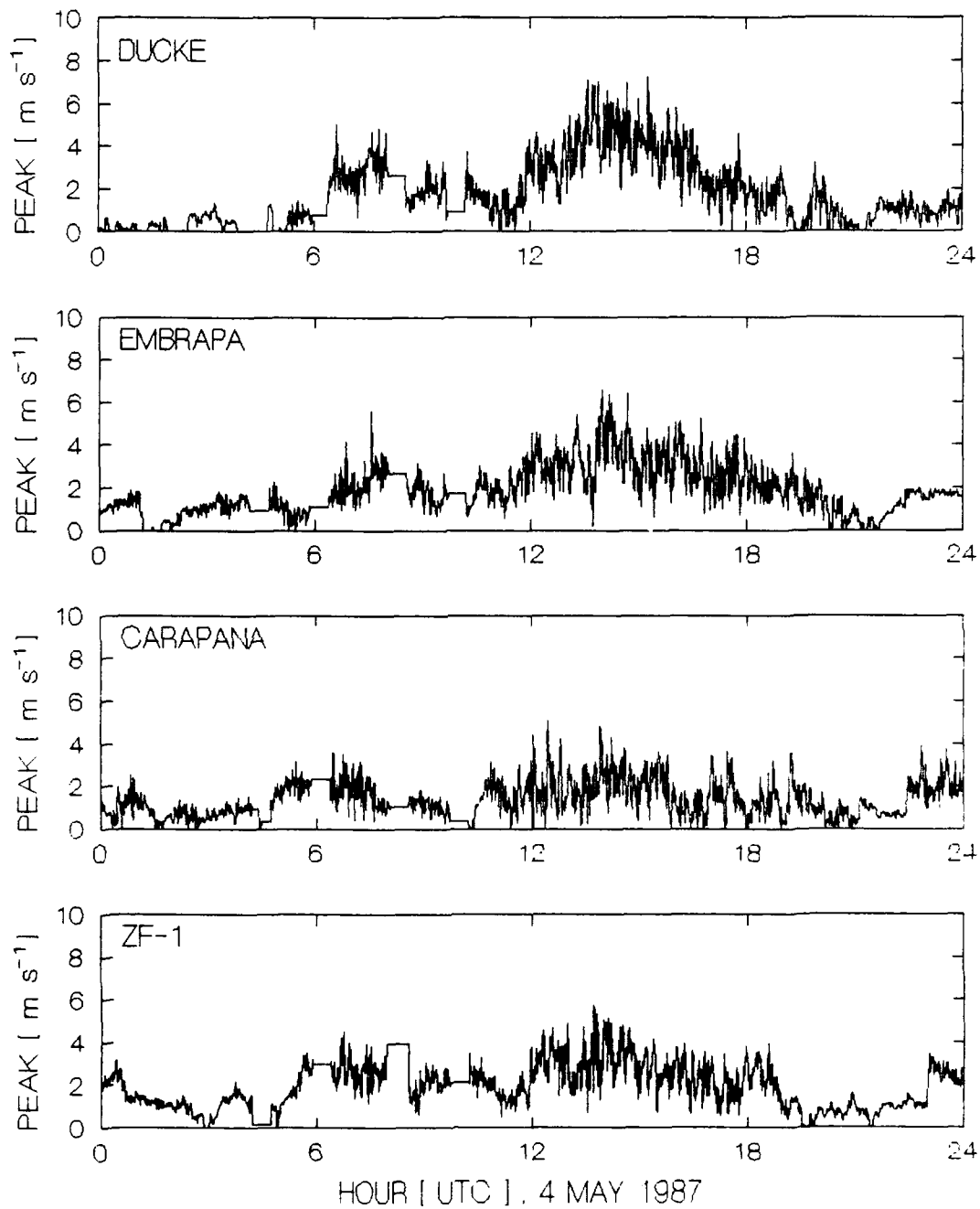


Figure 96. PAM time series of peak winds ( $\text{m s}^{-1}$ ) on  
4 May 1987.

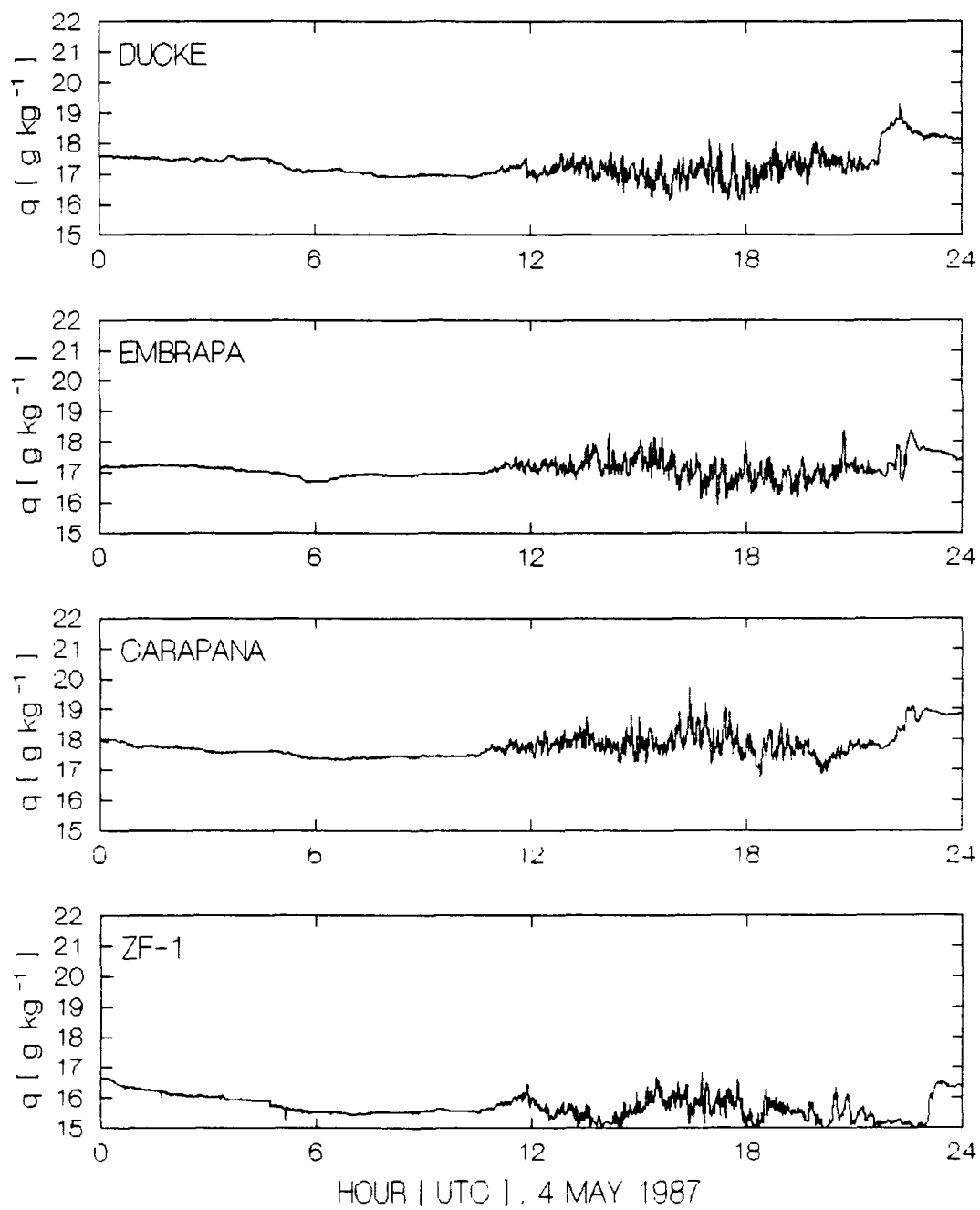


Figure 97. PAM time series of  $q$  ( $\text{g kg}^{-1}$ ) on 4 May 1987.

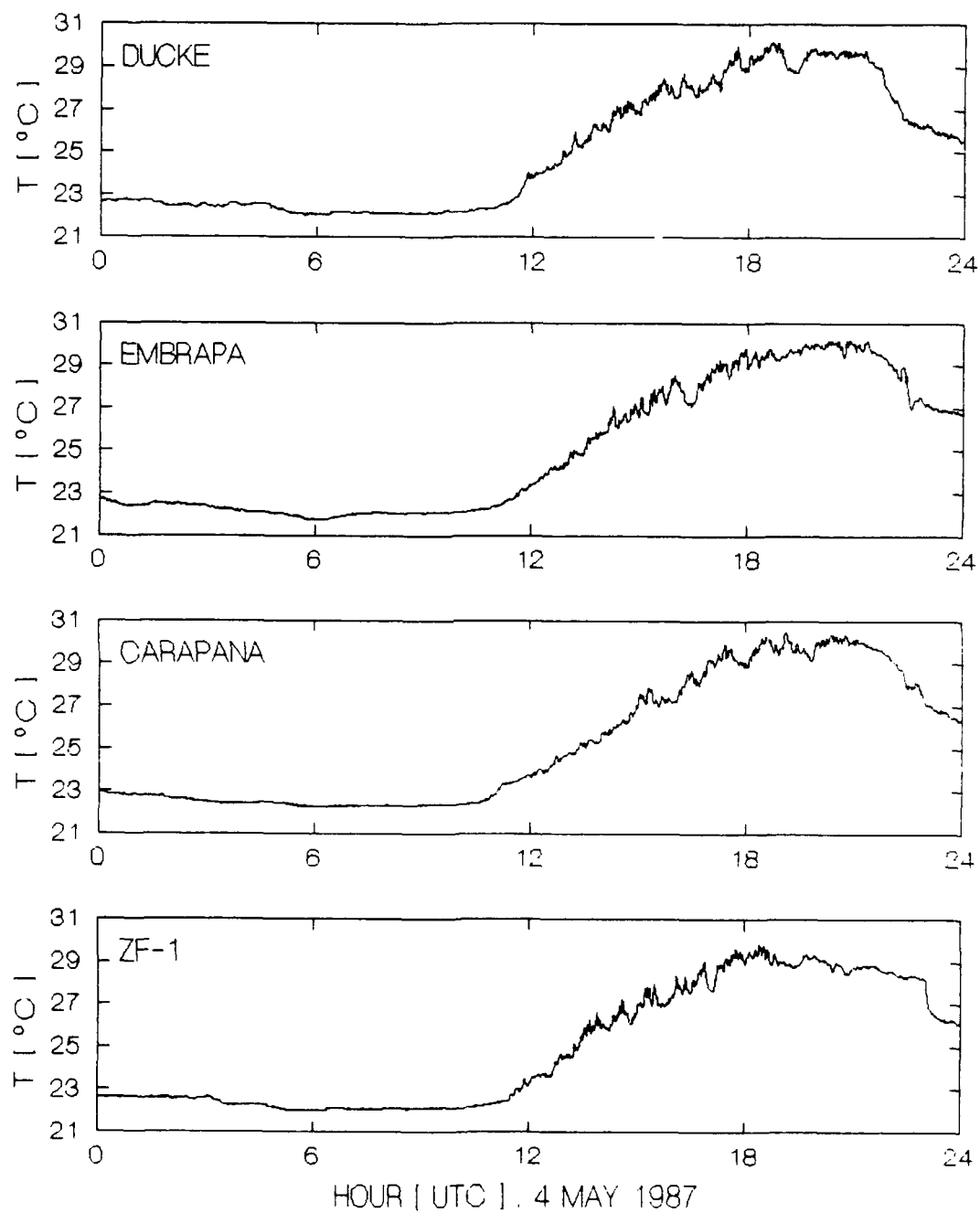


Figure 98. PAM time series of  $T$  (deg C) on 4 May 1987.

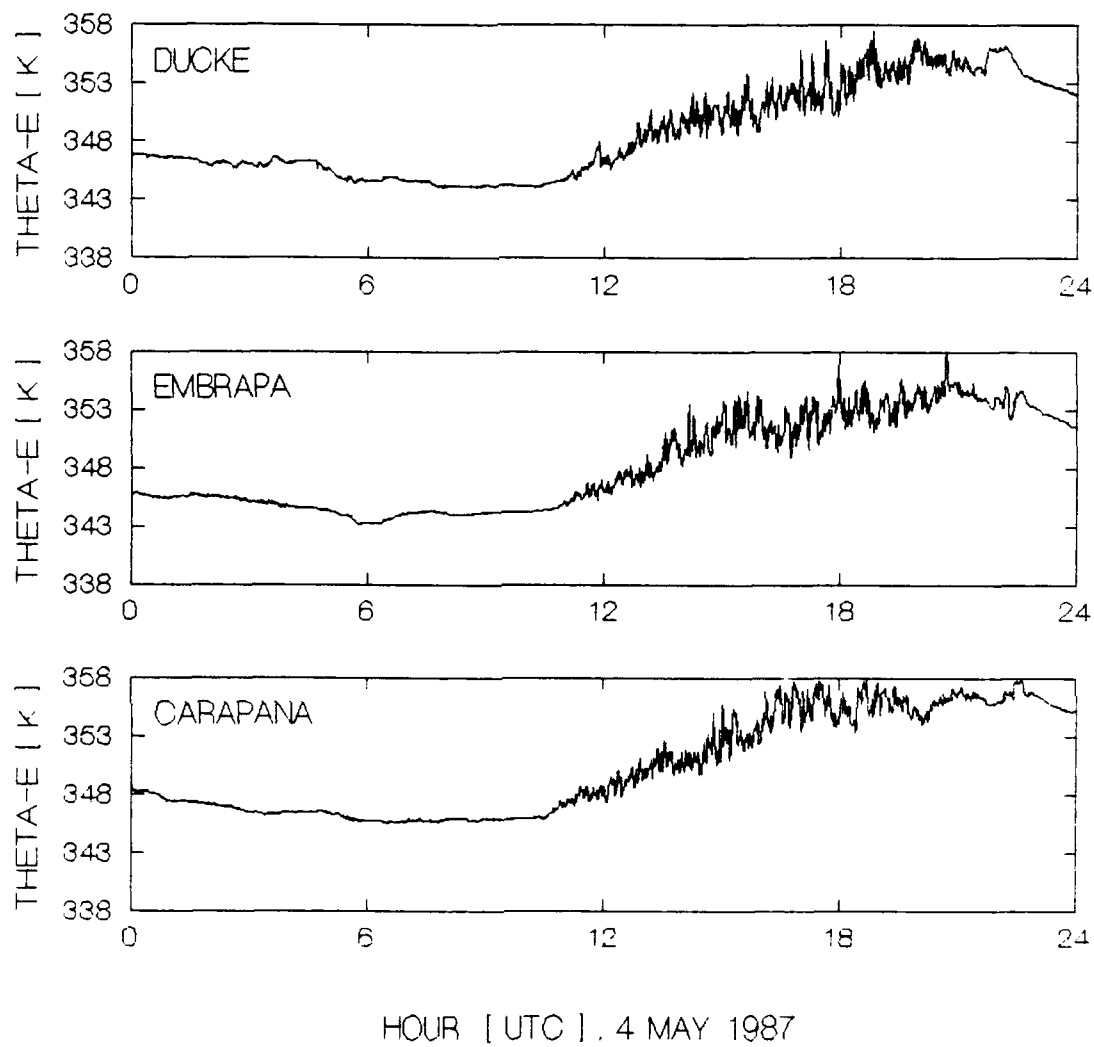


Figure 99. PAM time series of  $\theta_e$  (K) on 4 May 1987.

later in this section show that losses through cumulus cloud top detrainment may explain the slower recovery of surface moisture.

At 1200 UTC,  $u$  (Figure 100) has easterly maxima of  $\sim 10 \text{ m s}^{-1}$  near 900 and 200 mb. At 1800 UTC (Figure 101), the low level maximum shifts upward to 700 mb and decreases to  $\sim 6 \text{ m s}^{-1}$ .

The  $v$  profile at 1200 UTC (Figure 102) has northerly maxima at the low and mid levels. At 1800 UTC (Figure 103), the double maxima are replaced by a single northerly peak near 550 mb. Both  $u$  and  $v$  have much weaker vertical shear on 4 May than in the three COS cases.

The  $\theta_e$  profile at 1200 UTC (Figure 104) has a minimum of  $\sim 337 \text{ K}$  near the 800 mb level. The relatively uniform distribution of  $\theta_e$  between 600 and 350 mb may still be a result of the 3 May anvil component. By 1800 UTC (Figure 105), the  $\theta_e$  minimum shifts upward to 700 mb while a significant increase occurs at the lower levels.

Relative humidity at 1200 UTC (Figure 106) has maxima near 950, 600, 400, and 100 mb. During strong surface heating at 1800 UTC (Figure 108), the low level maximum moves to a higher level near 850 mb. From the 1200 UTC relative humidities, satellite images, and surface observations, it is surmised that sky conditions over the mesoscale triangle include fog, scattered-to-broken low level stratus, scattered-to-broken mid level altocumulus, and scattered

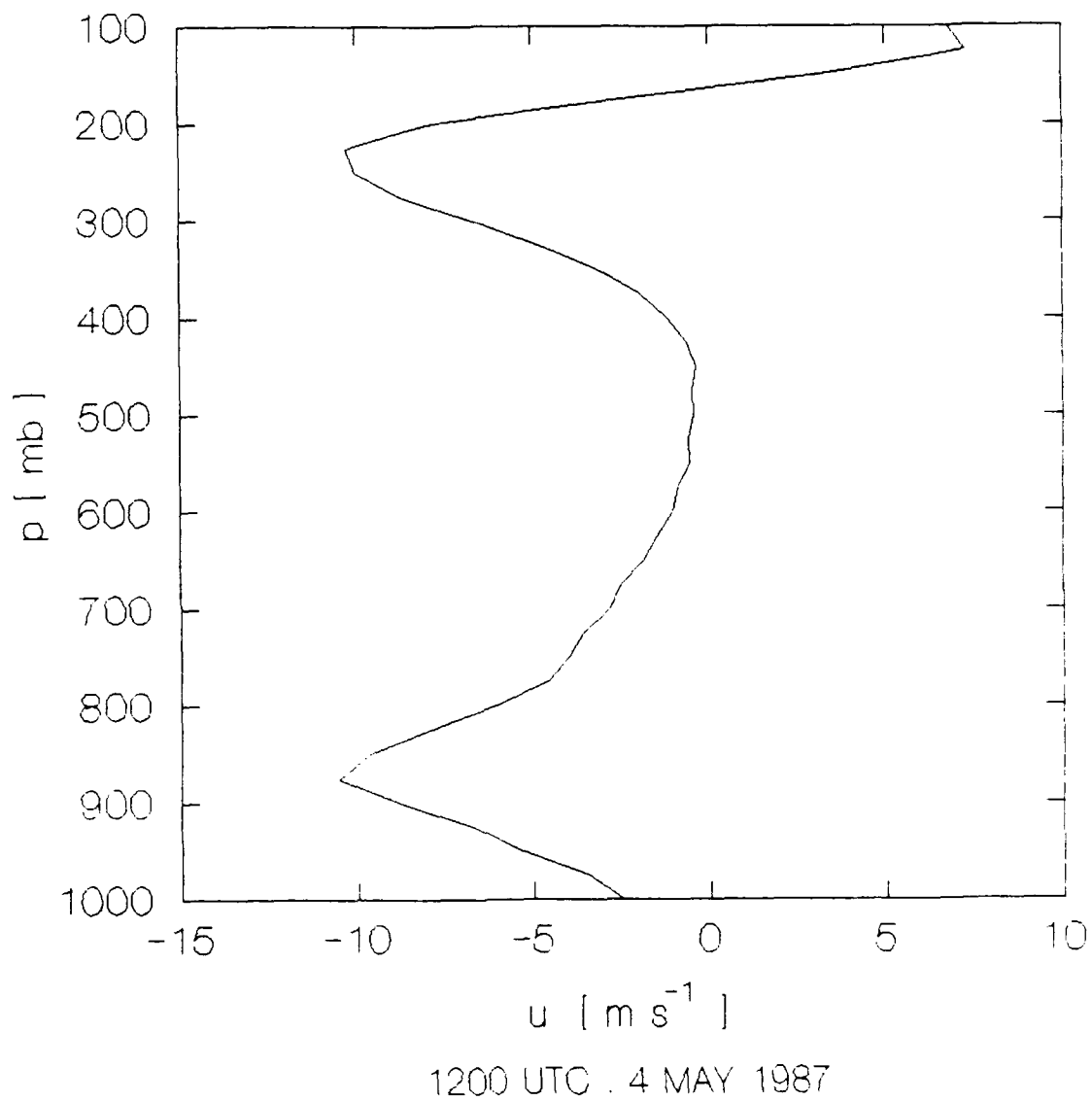


Figure 100. Vertical profile of  $u$  ( $\text{m s}^{-1}$ ) in the mesoscale triangle at 1200 UTC, 4 May 1987.

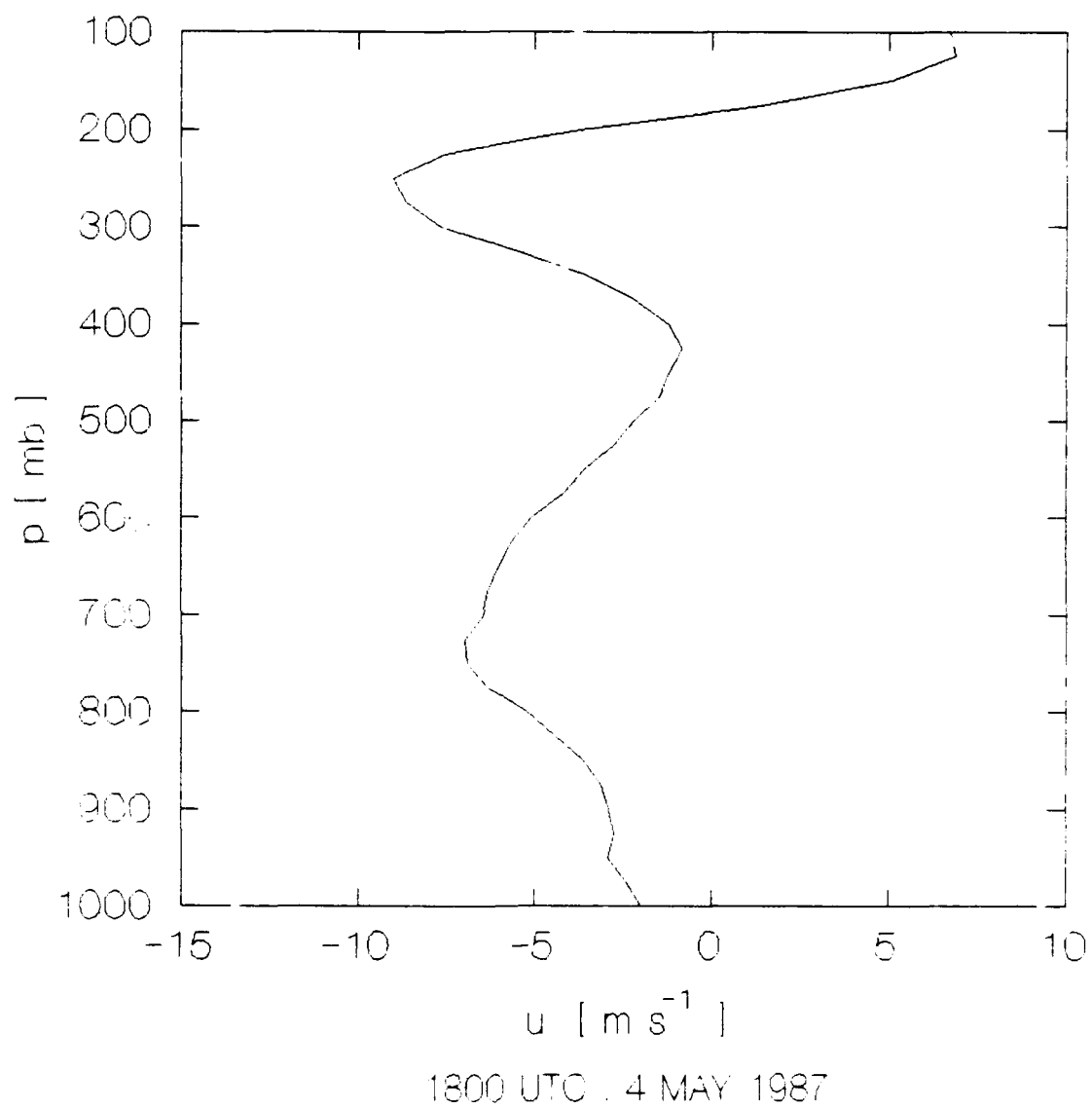
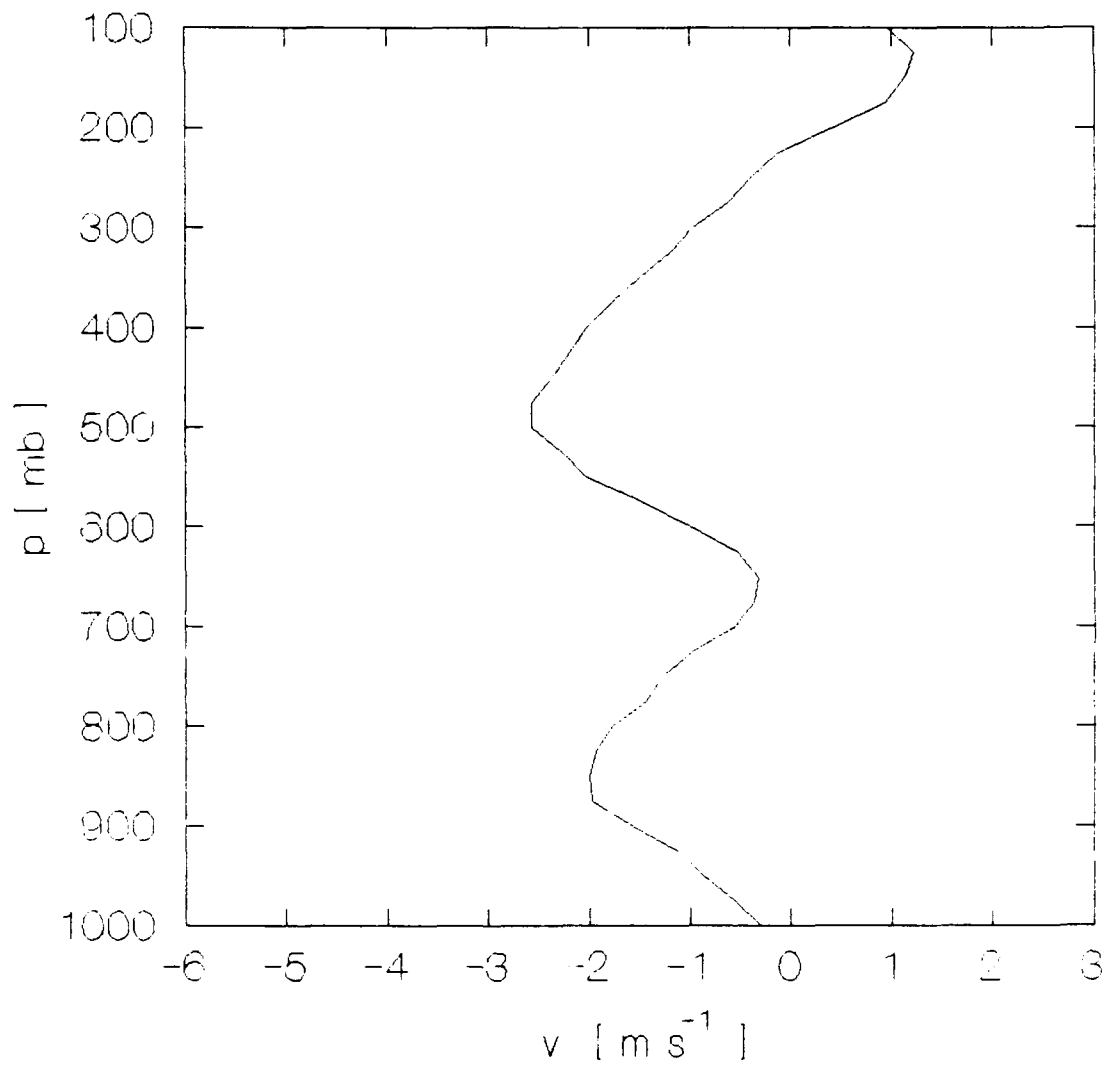
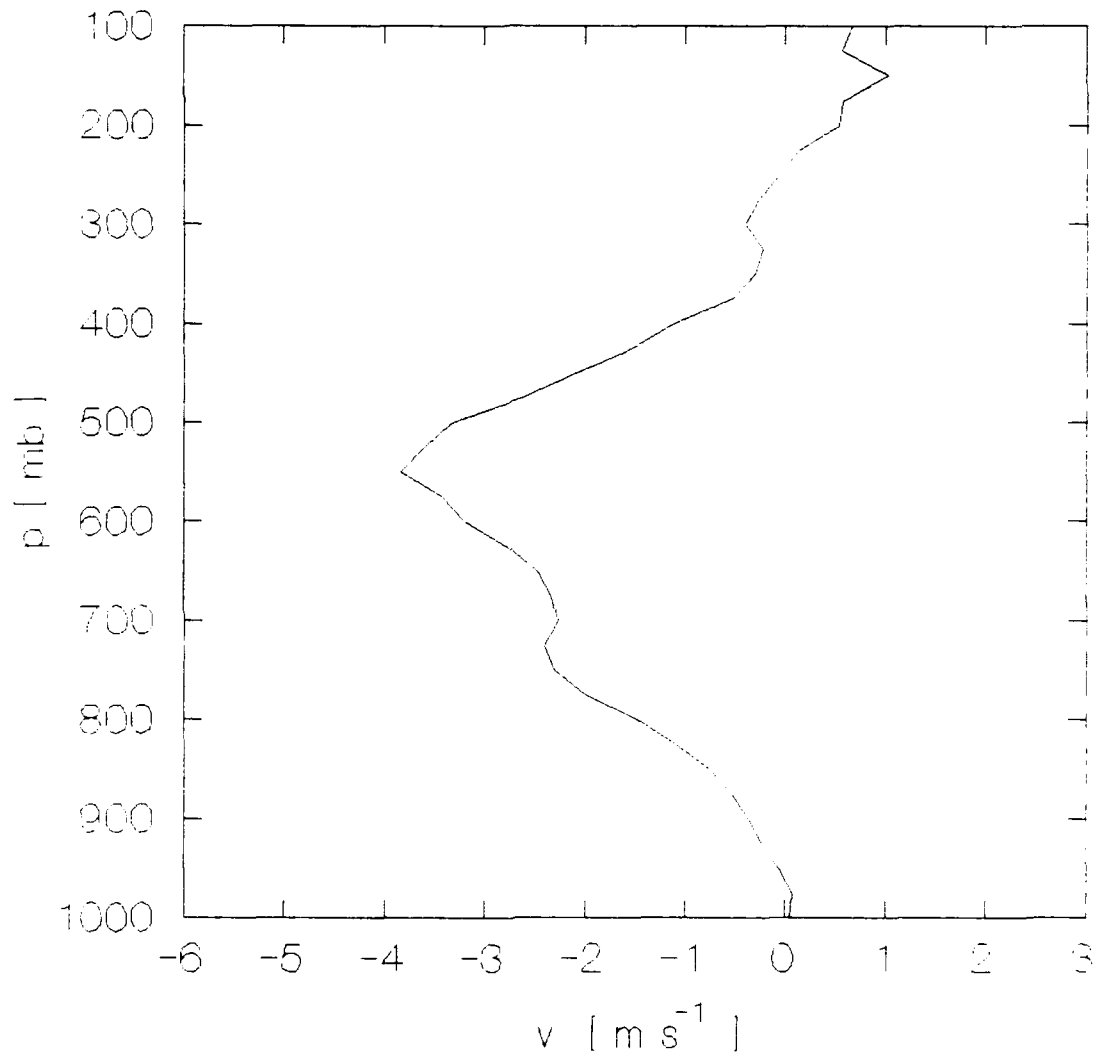


Figure 101. Vertical profile of  $\bar{u}$  ( $\text{m s}^{-1}$ ) in the mesoscale triangle at 1800 UTC, 4 May 1987.



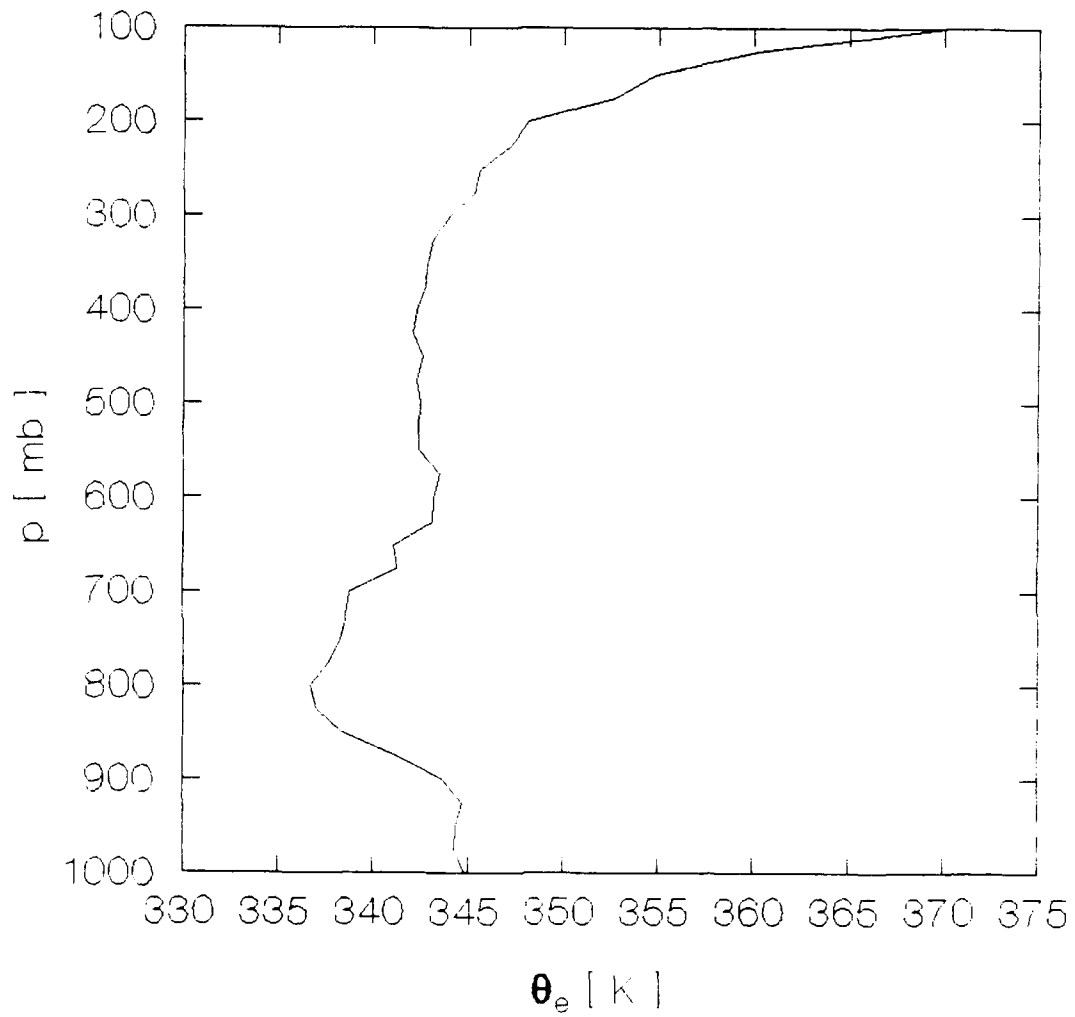
1200 UTC . 4 MAY 1987

Figure 102. Vertical profile of  $\bar{v}$  ( $\text{m s}^{-1}$ ) in the mesoscale triangle at 1200 UTC, 4 May 1987.



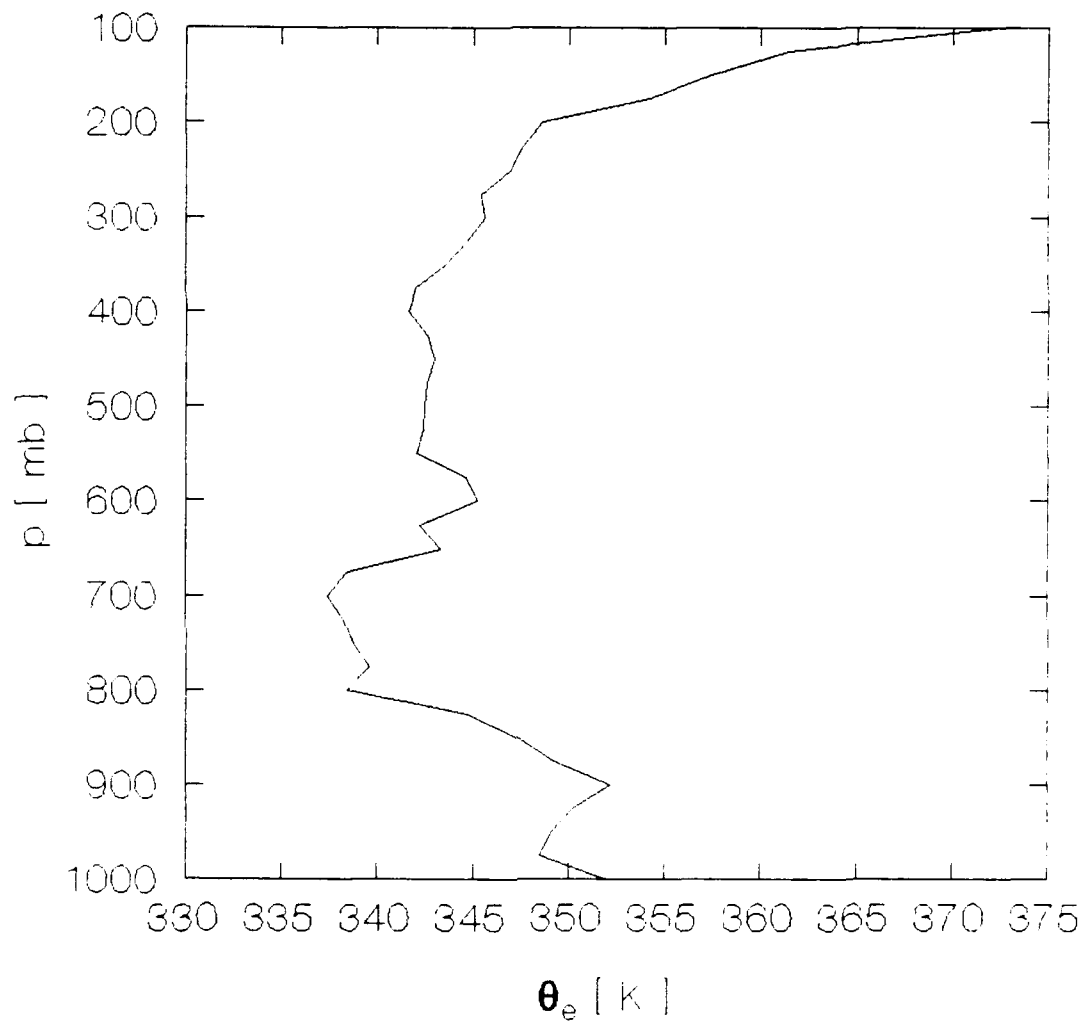
1800 UTC, 4 MAY 1987

Figure 103. Vertical profile of  $\bar{v}$  ( $\text{m s}^{-1}$ ) in the mesoscale triangle at 1800 UTC, 4 May 1987.



1200 UTC . 4 MAY 1987

Figure 104. Vertical profile of mean  $\theta_e$  (K) in the meso-scale triangle at 1200 UTC, 4 May 1987.



1800 UTC . 4 MAY 1987

Figure 105. Vertical profile of mean  $\theta_e$  (K) in the meso-scale triangle at 1800 UTC, 4 May 1987.

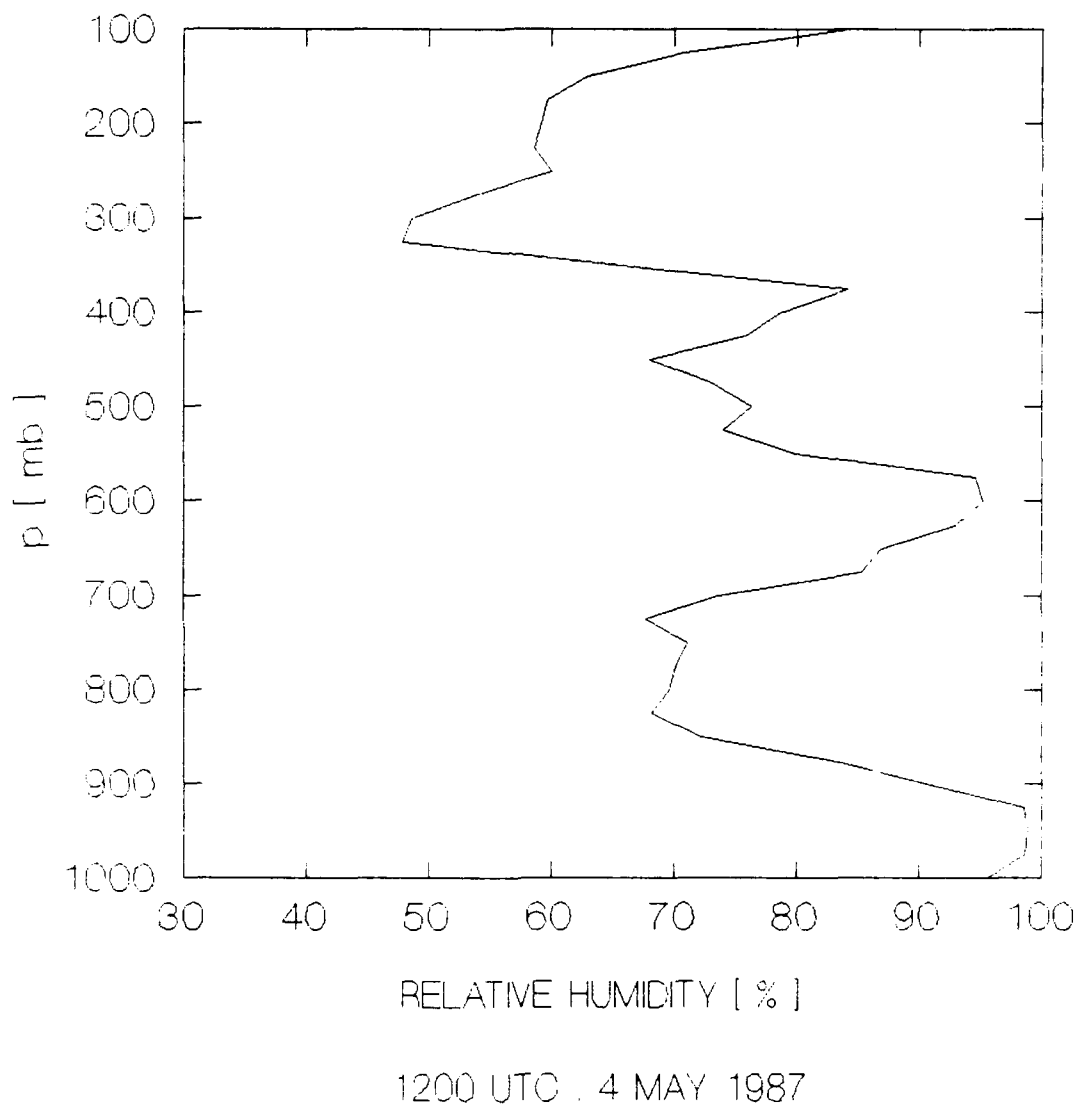


Figure 106. Vertical profile of mean relative humidity (%) in the mesoscale triangle at 1200 UTC, 4 May 1987.

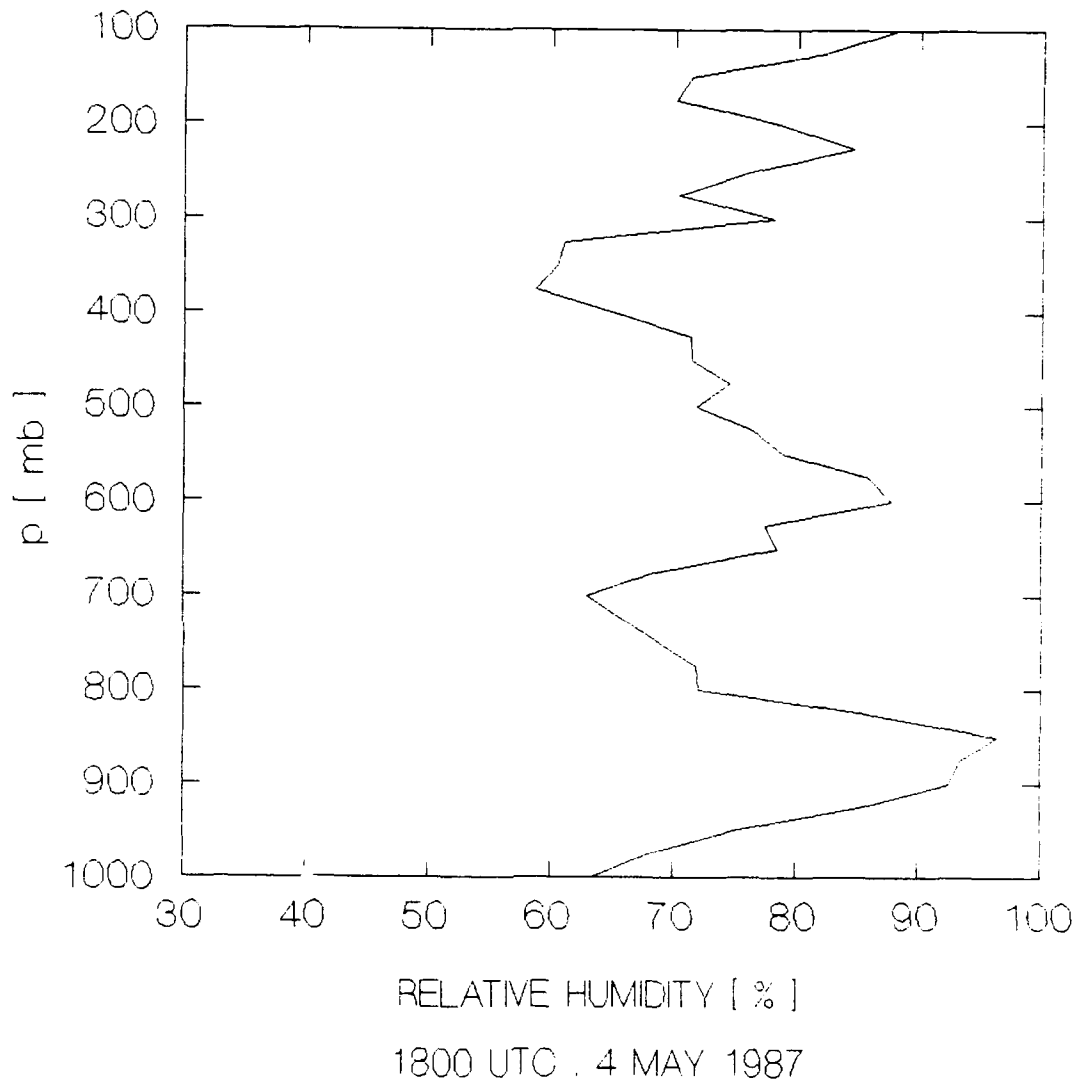


Figure 107. Vertical profile of mean relative humidity (%) in the mesoscale triangle at 1800 UTC, 4 May 1987.

high level cirrus. By 1800 UTC, these same types of data indicate scattered-to-broken cumulus and widely scattered altocumulus and cirrus are present over the triangle. The bulk of the day is dominated by fair weather, as clearly shown by the PAM time series.

At 1200 UTC, shallow layers of weak convergence (Figure 108) in the low and mid levels produce weak upward vertical motion near 775 and 450 mb, respectively (Figure 109). Both regions of upward motion are located below relative humidity maxima (Figure 106) associated with clouds. The remnants of a mesoscale anvil updraft from the 3 May COS most likely accounts for upward motion in the upper levels.

At 1800 UTC, divergence (Figure 110) from the surface to 700 mb produces downward vertical motion through the entire column (Figure 111). Maximum subsidence at 700 mb provides is limiting the vertical development of convective clouds.

The  $Q_1$  profile at 1200 UTC (Figure 112) shows a pattern of low-level cooling and upper-level warming like that commonly found in stratiform anvils. At the same time,  $Q_2$  (Figure 113) shows low-level moistening and upper-level drying features typical of those in anvils. The  $F$  profile (Figure 114) decreases sharply from a surface maximum of about  $275 \text{ W m}^{-2}$ , becomes negative at 900 mb, and remains negative through the rest of the column. If an anvil up-

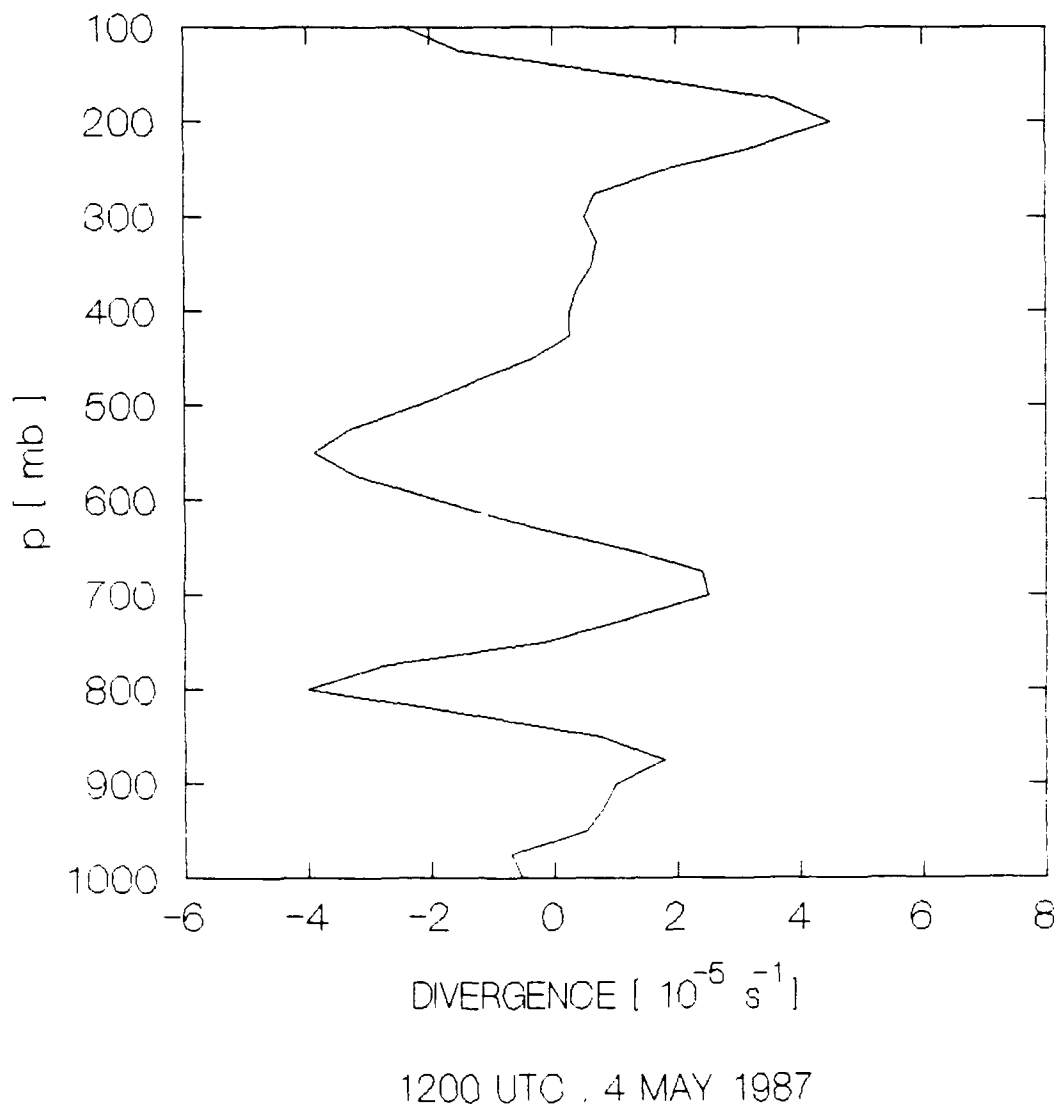
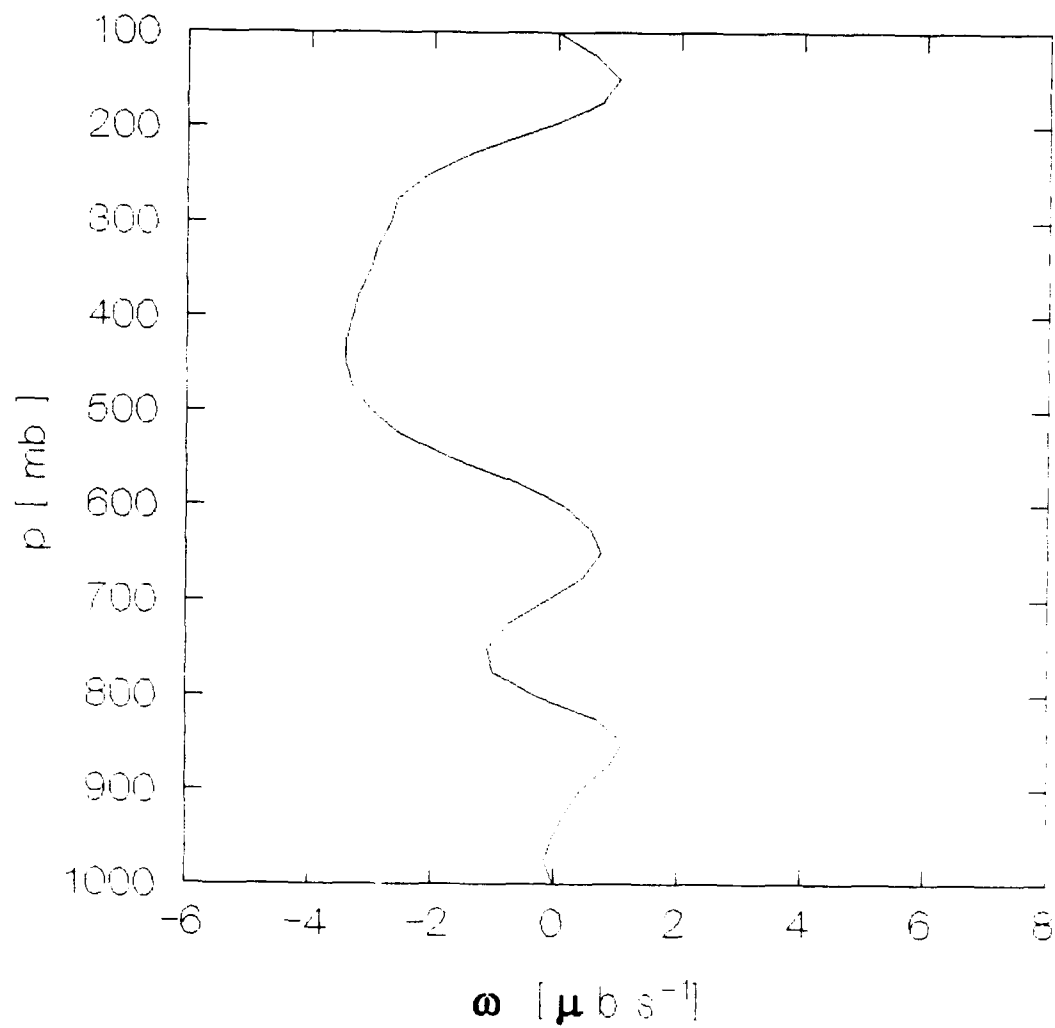


Figure 108. Vertical profile of divergence ( $10^{-5} \text{ s}^{-1}$ ) in the mesoscale triangle at 1200 UTC, 4 May 1987.



1200 UTC . 4 MAY 1987

Figure 109. Vertical profile of  $\omega$  (microbars  $\text{s}^{-1}$ ) in the mesoscale triangle at 1200 UTC, 4 May 1987.

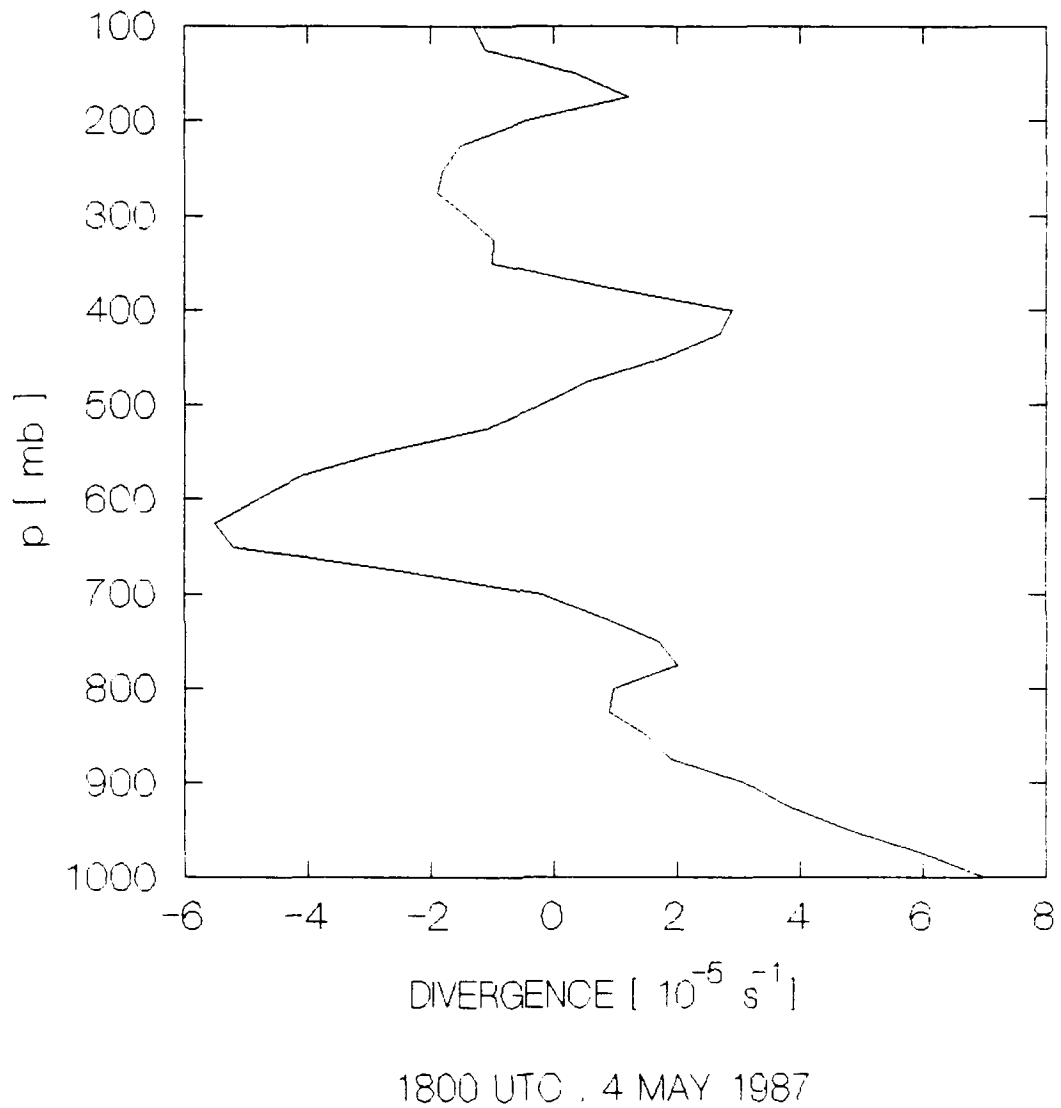
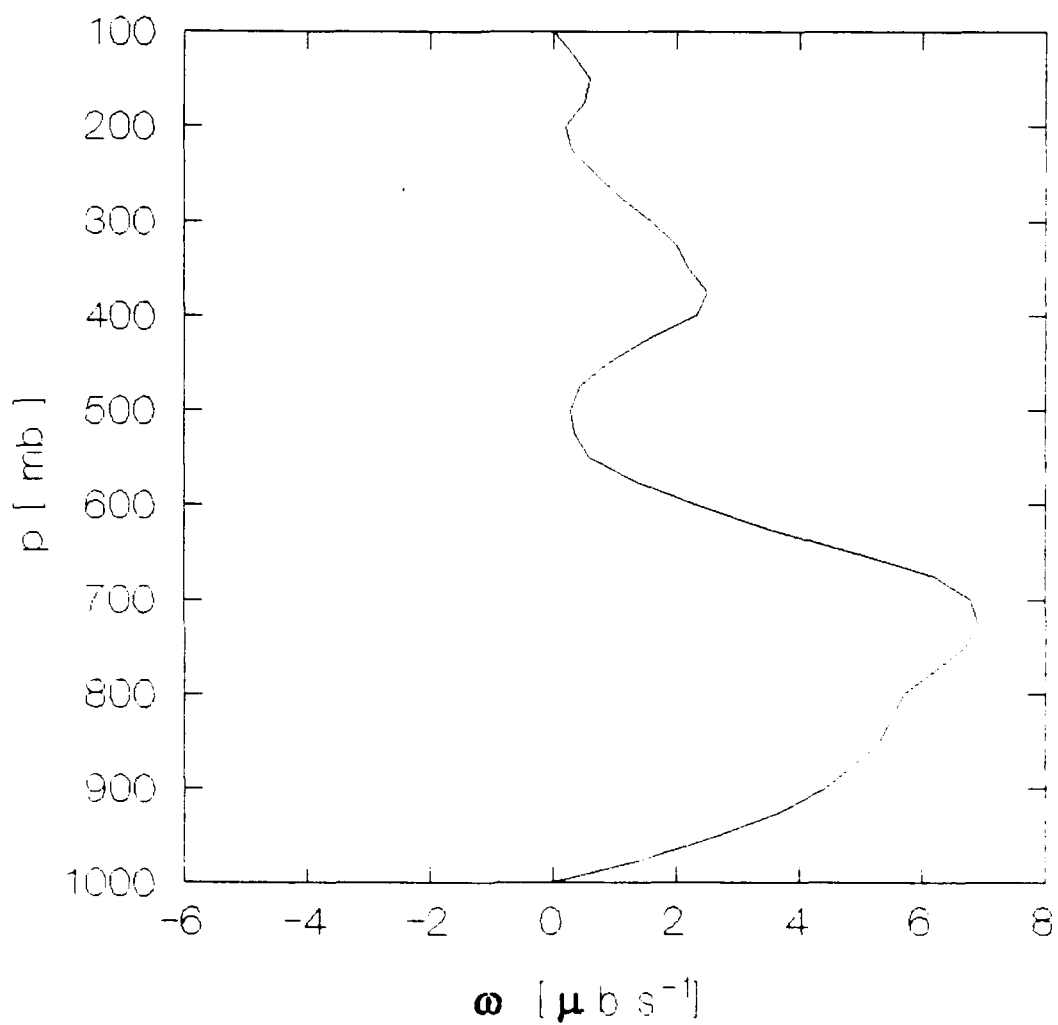


Figure 110. Vertical profile of divergence ( $10^{-5} \text{ s}^{-1}$ ) in the mesoscale triangle at 1800 UTC, 4 May 1987.



1800 UTC . 4 MAY 1987

Figure 111. Vertical profile of  $\omega$  (microbars  $\text{s}^{-1}$ ) in the mesoscale triangle at 1800 UTC, 4 May 1987.

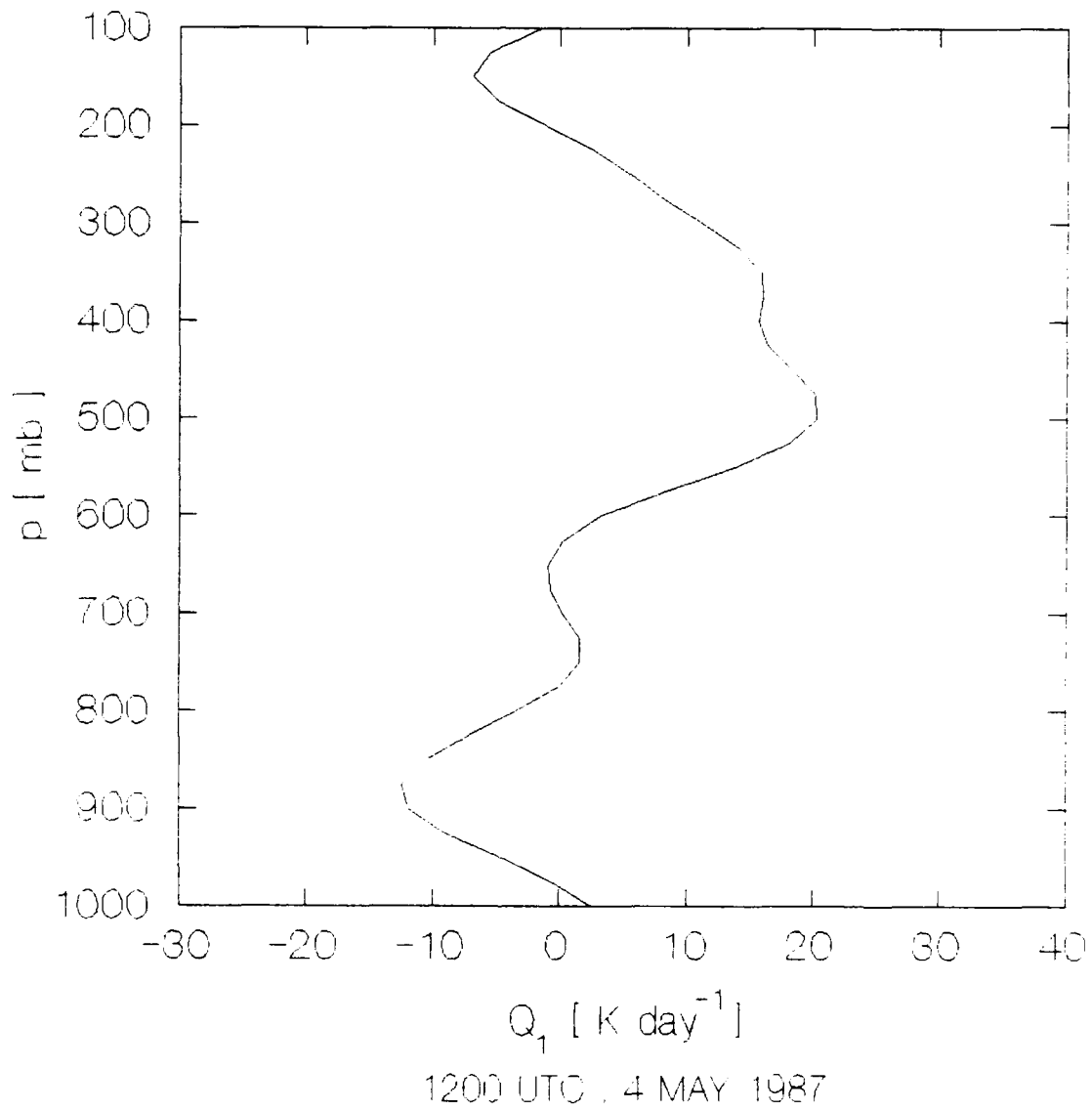


Figure 112. Apparent sensible heat source ( $K \text{ day}^{-1}$ ) in the mesoscale triangle at 1200 UTC, 4 May 1987.

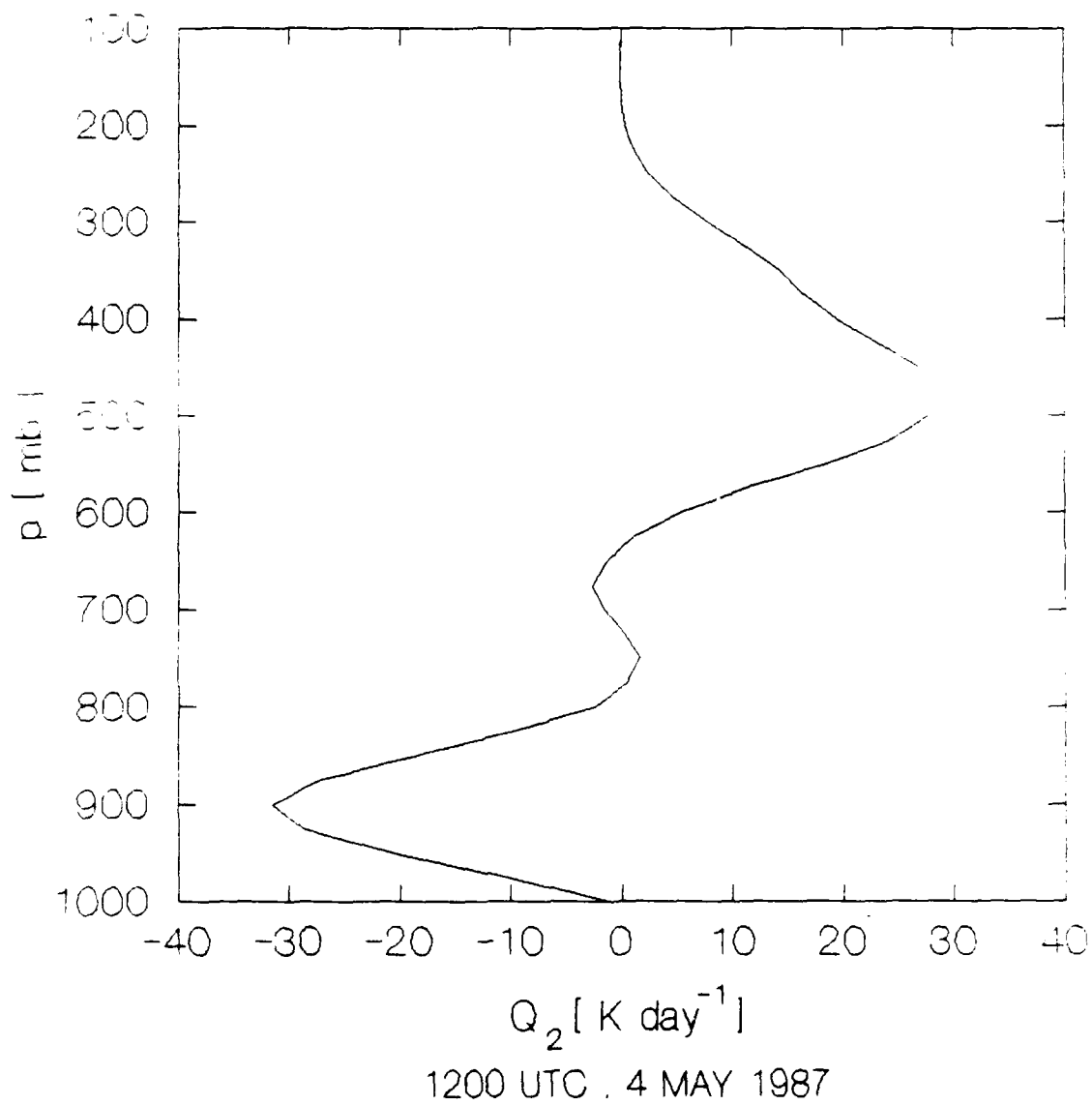
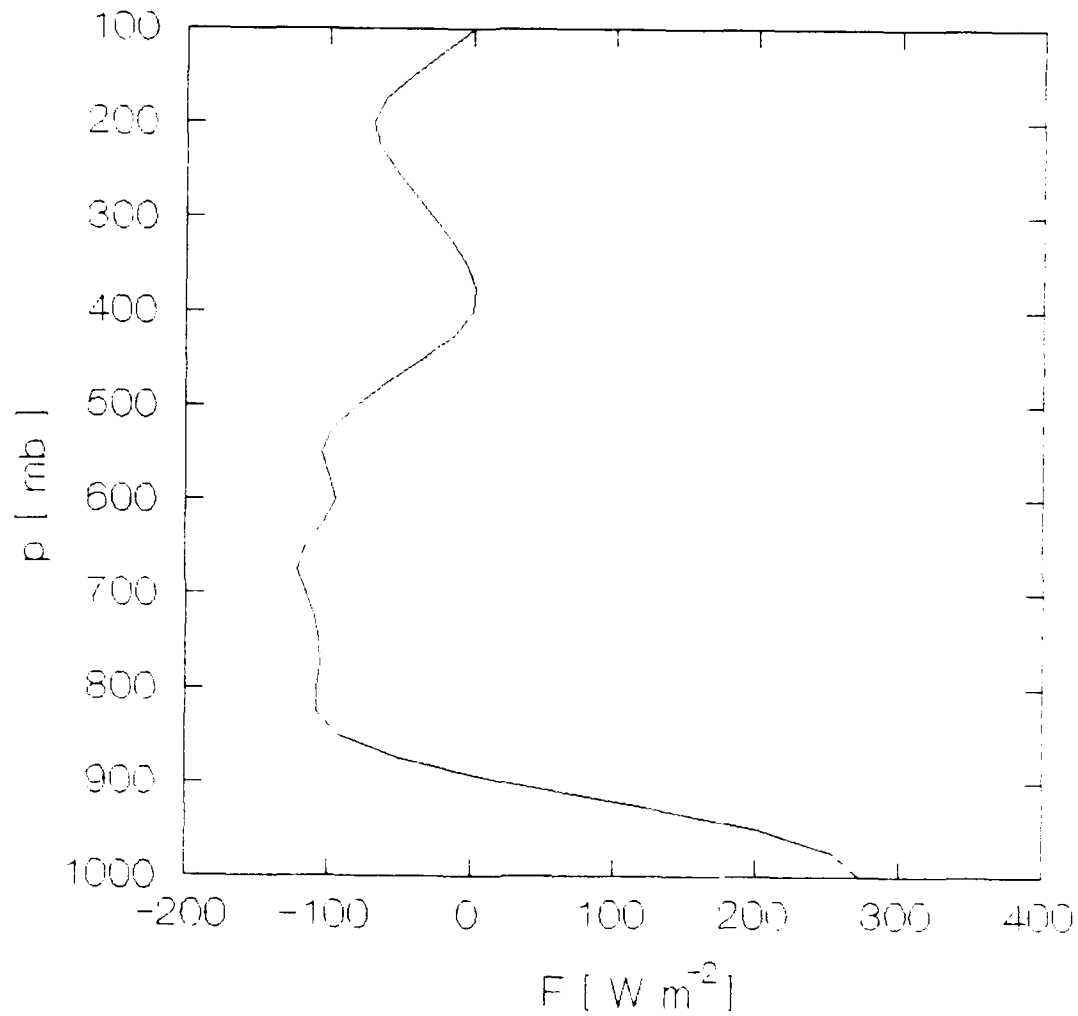


Figure 113. Apparent latent heat sink (K day<sup>-1</sup>) in the mesoscale triangle at 1200 UTC, 4 May 1987.



1200 UTC . 4 MAY 1987

Figure 114. Vertical eddy flux of total heat ( $\text{W m}^{-2}$ ) in the mesoscale triangle at 1200 UTC, 4 May 1987.

draft still exists, the distribution of  $F$  shows it no longer transports heat upwards.

At 1800 UTC, near the time of maximum solar heating, the  $Q_1$  profile (Figure 115) shows low-level heating in layers containing active cumulus and strong cooling of the air just above the cloud tops. The sensible heat source remains slightly negative through the mid and upper levels to the tropopause. The distribution of  $Q_2$  (Figure 116) shows drying at the surface, strong low-level moistening in the region of active cumulus, and weak mid-level moistening of the air just above the cloud tops. The values of  $F$  (Figure 117) decrease from an afternoon maximum of nearly  $800 \text{ W m}^{-2}$  and become negative at 800 mb, located near the top of the active cumulus layer.

The observed heat and moisture budgets on 4 May are consistent with expected patterns of boundary-layer recovery for low-level heat and moisture in the absence of any organized deep convection after the 3 May COS. In particular, the results suggest that detrainment cools and moistens the atmosphere above the cumulus cloud tops. The surface heat and moisture fluxes help create instability and supply the water vapor needed for convective clouds to form.

The fair weather mid-level subsidence maximum ensures that most of the heat and moisture added from the surface contributes to recovery in the lower levels. This process continues to warm and moisten air at the lower and

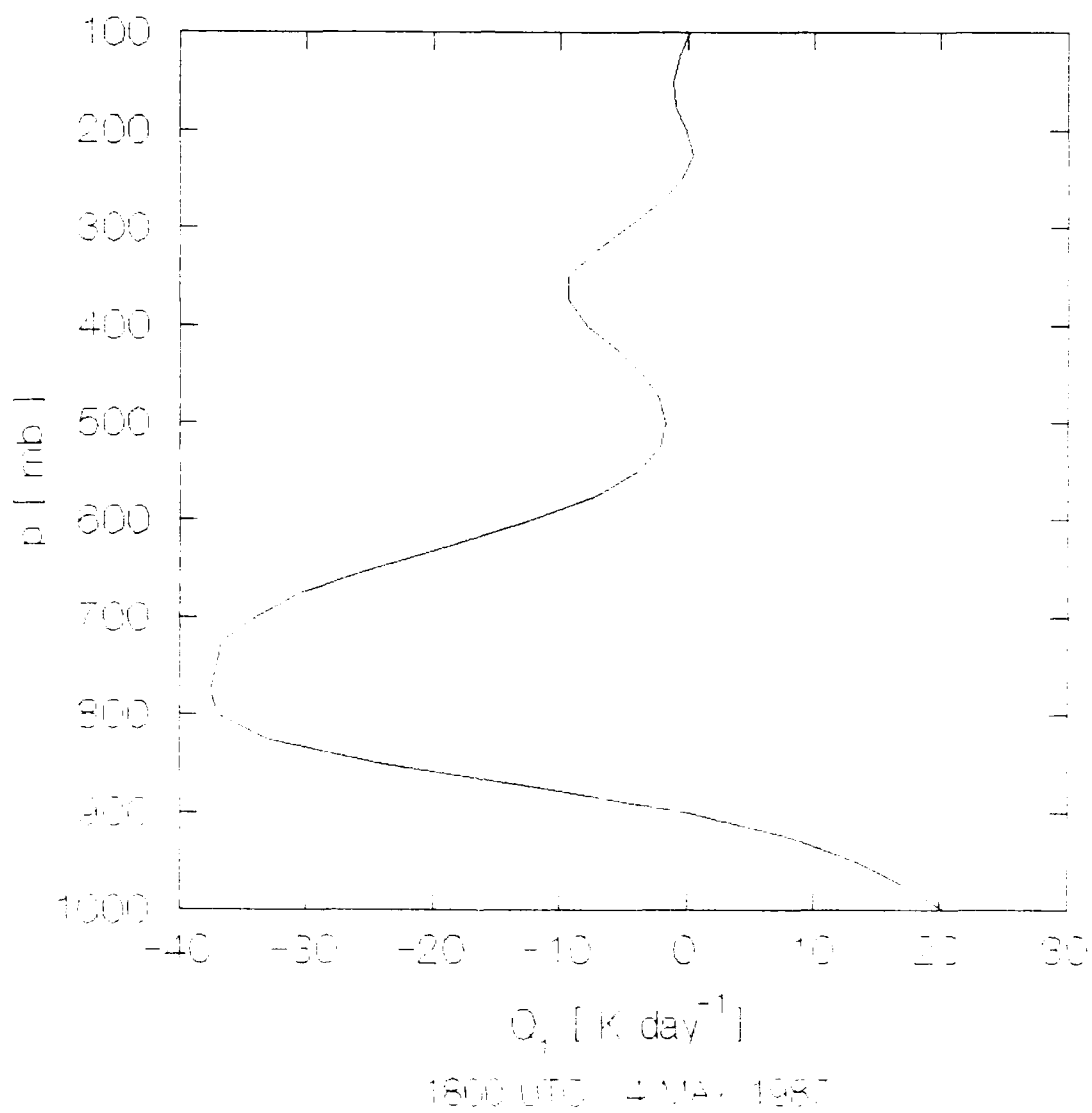


Figure 115. Apparent sensible heat source ( $K \text{ day}^{-1}$ ) in the mesoscale triangle at 1800 UTC, 4 May 1987.

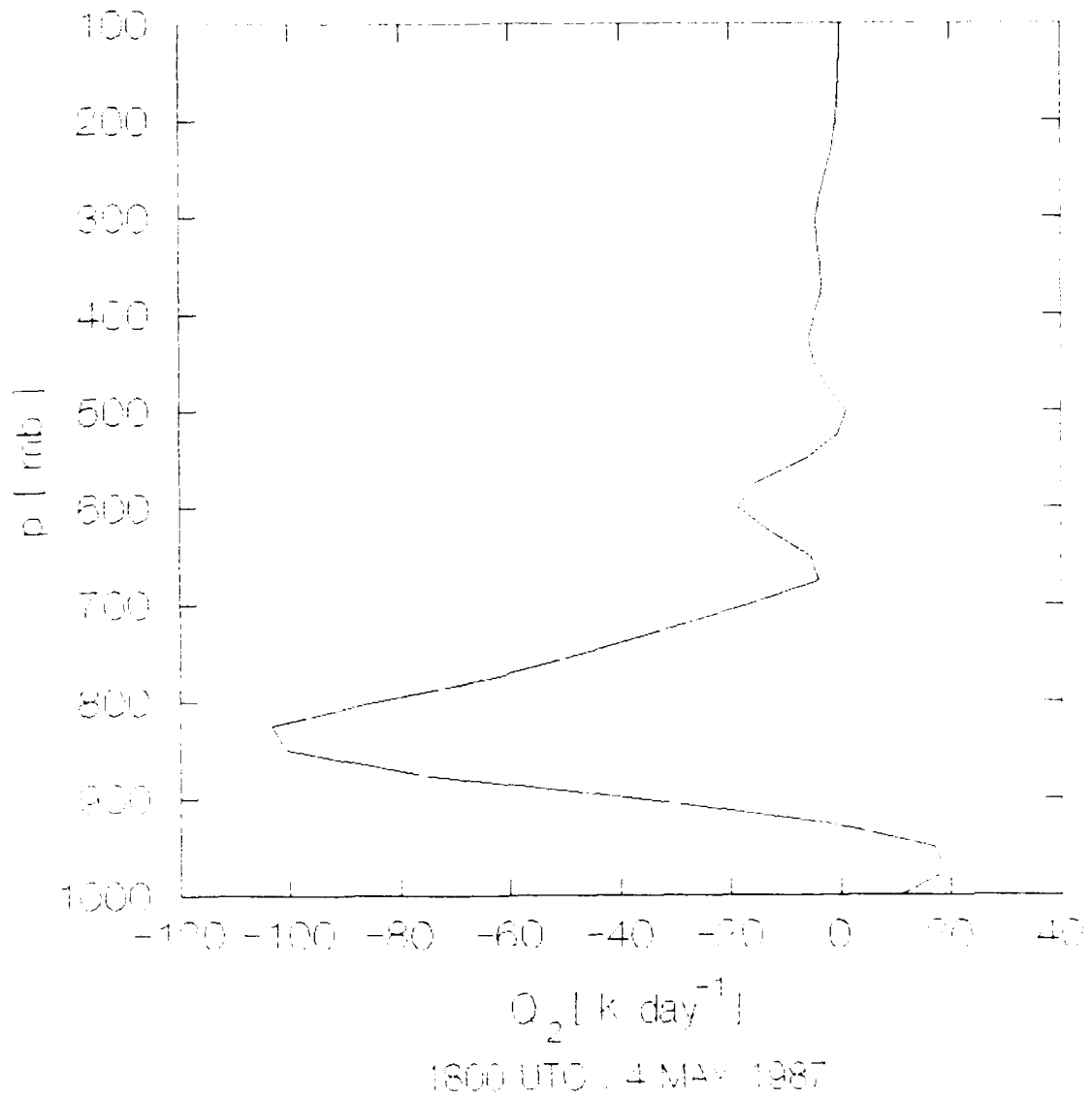


Figure 116. Apparent latent heat sink (K day<sup>-1</sup>) in the mesoscale triangle at 1800 UTC, 4 May 1987.

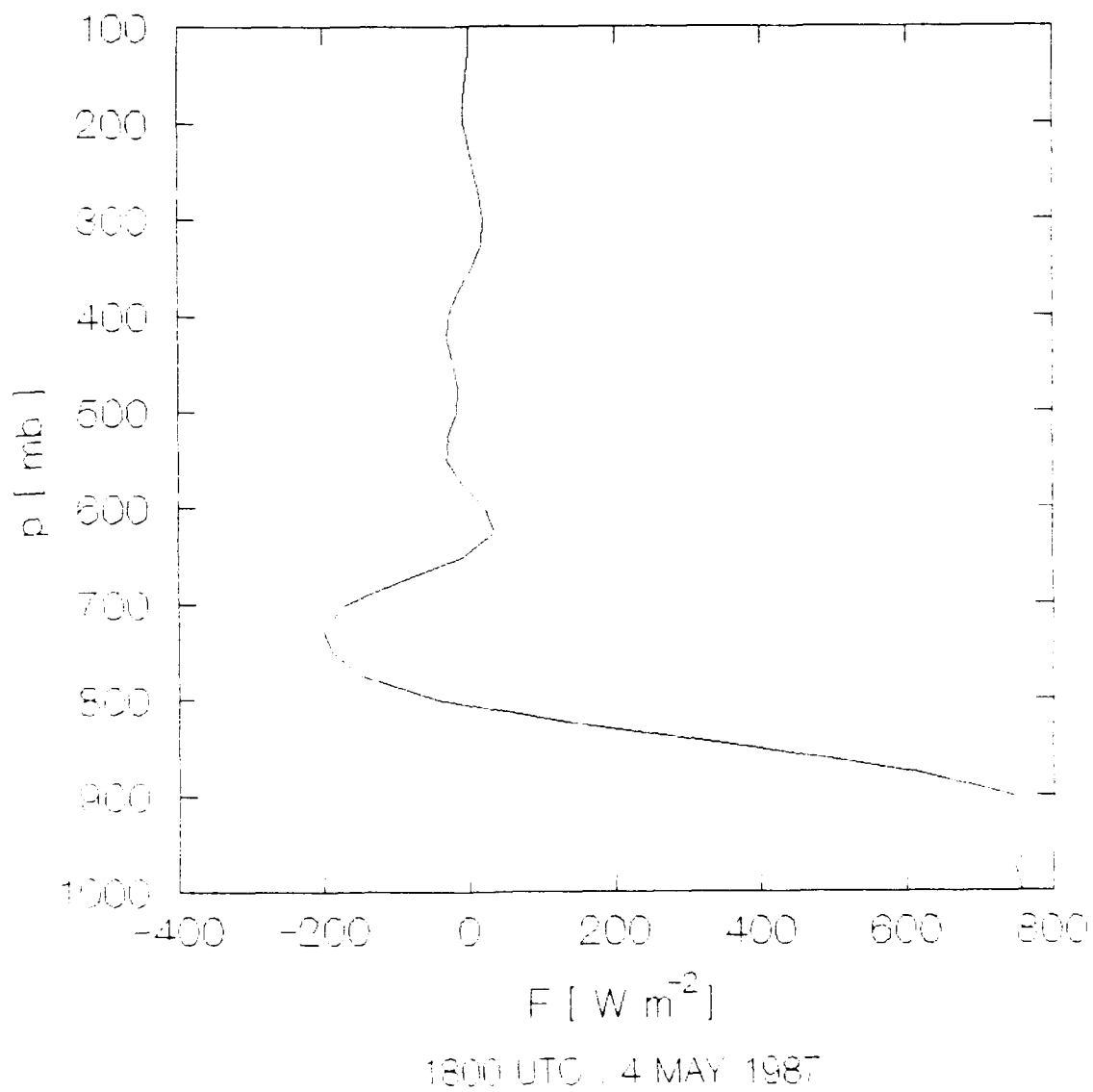


Figure 117. Vertical eddy heat flux ( $\text{W m}^{-2}$ ) in the meso-scale triangle at 1800 UTC, 4 May 1987.

middle levels until the atmosphere returns to a state of thermodynamic conditional instability and can again support deep convection in the presence of an adequate lifting mechanism.

## CHAPTER 5

### APPRAISAL OF RESULTS

I will now address vertical heat transport by COS clouds in general and by COS anvils in particular in the context of the global heat balance. This chapter begins with a taxonomy of the COS life cycle, followed by an appraisal of their structure, heat transport characteristics, and global importance.

The system-wide heat transport is evaluated as a function of cloud components and life cycle with a model developed from the triangle network heat transport calculations and satellite analysis of active cloud area. I will show that upper level heat transport by COS can equal a substantial amount of the lateral heat export requirement for the tropics estimated by Riehl and Simpson (1979). Furthermore, it is revealed that the dynamically active COS anvil plays an important role in system-wide heat transport.

Coastal occurring systems are often a dominant synoptic-scale cloud feature over the third of the tropics appearing on GOES full-disk images during the Amazon wet season (Molion, 1987; Cavalcanti, 1982). Greco *et al.* (1990) have shown these massive, long-lived convective systems account for much of the total rainfall in the mesoscale network during ABLE-2B. It is therefore appropriate and important to quantify their role in the heat balance of the equatorial trough zone.

### A. COS life cycle

The GOES visible and IR images collected during ABLE-2B indicate that patterns, sizes, intensities of clouds and rainfall change dramatically during the lifetime of a COS. The satellite images from April and May 1987 have been studied to define a COS life cycle of six possible stages. These stages are:

#### 1. COASTAL GENESIS

During this stage, a line of thunderstorms, oriented from northwest to southeast, forms during the afternoon in the sea-breeze zone along the northern coast of Brazil. The number, size, and intensity of cells increase with time, followed by selective merging into thunderstorm clusters that share anvils.

#### 2. INTENSIFICATION

Small cloud clusters merge into larger clusters, oriented in a quasi-linear pattern that follows the coastal outline of northeastern Brazil. The strongest clusters, comprised of hot towers and anvils, are resolved by segment number 7 (black) on the GOES images enhanced with the MB curve (Carlson, 1981). The more mature clusters have sharply defined outer edges and cloud-top temperatures of less than  $-59.2^{\circ}\text{C}$ , indicating an altitude of approximately 13-14 km above mean sea level (MSL). At this stage, the system propagates inland at a speed of 50-70 km h<sup>-1</sup>.

### 3. MATURATION

At this stage, the system reaches maximum length and width. Individual cloud clusters have their largest size and greatest intensity on the MB images. A mature COS often has a length of 3500 km of which 500-1000 km is active deep convection. The width of the system is typically 200-400 km. Patches of white (MB segment 9) in the mesoscale clusters indicate cumulonimbi with cloud top temperatures less than  $-80.2^{\circ}\text{C}$  and heights of about 16-17 km MSL. Clouds comprising the mesoscale clusters merge to give the COS massive synoptic features on the GOES full disk images.

### 4. WEAKENING

The thunderstorm clusters shrink and their outer definition becomes ragged on the MB images. Areas previously appearing in black on the MB images change to dark and light gray (segment numbers 6 and 5, respectively), indicating warmer cloud-top temperatures and weaker thunderstorms. The width of the system markedly decreases to 100-200 km.

### 5. REGENERATION

COS regeneration, usually occurring during afternoon surface heating, may follow weakening. During regeneration, clusters appearing in black (segment 7) grow and redevelop their sharp outer definition, indicating intensifying cumulonimbus activity. The system's synoptic-scale features become more pronounced on the full disk IR images.

## 6. DISSIPATION

After a period of weakening, individual clusters become more ragged and finally dissipate. The system loses its synoptic-scale definition on the full disk images.

The above definition of the COS life cycle follows taxonomies developed for individual cumulonimbus clouds (e.g. Byers and Braham, 1949; Houze, 1977) and for complexes of thunderstorms comprising mesoscale tropical squall lines (e.g. Frank, 1978; Leary and Houze, 1979). My taxonomy is unique in that it defines the life cycle of a synoptic-scale convective disturbance. I have used the life cycle definitions in Chapter 4 to classify the COS on 26 April as weakening, the one on 1 May system as mature, and the one on 6 May system as regenerating.

### **B. Kinematic and thermodynamic structure**

I will now combine the results of the case studies to assess the kinematic and thermodynamic structure of COS in general. Efforts are made to relate how convective feedback and other interscalar processes may contribute to kinematic and thermodynamic features observed during the COS life cycle.

The COS propagate faster than the environmental winds at all levels. This typical characteristic of fast-moving tropical squall lines results in storm-relative inflow on the forward edge and storm-relative outflow on the

rear flank (Cotton and Anthes, 1989). The GATE studies by Barnes (1980) and the model simulations by Tao and Simpson (1984) show propagation results from continuous development of new convective cells along the cold outflow boundary at the leading edge of the squall front. According to Gamache and Houze (1982), new cells intensify and form a new line of convection as old convective line elements weaken and blend into the trailing anvil cloud.

Marked changes in  $T$ ,  $q$ ,  $p$ ,  $\theta_e$ , and horizontal winds with squall front passage resemble those typically observed in tropical squall lines (Miller and Betts, 1977; Zipser, 1977). As the squall front passes, there are large, sudden decreases in  $T$  (Figure 14),  $q$  (Figure 15), and  $\theta_e$  (Figure 16) and large, sudden increases in wind speed (Figure 12).

Downward transport of cold, dry air by convective downdrafts in the mature stage suppresses  $T$  and  $q$  until surface fluxes can replenish the total heat in the lower atmosphere. Surface recovery times of 12-24 hours after a mature COS are considerably longer than the 1-6 hours observed after a regenerating system. Quicker recovery in regenerating COS indicates its convective-scale downdrafts are much weaker than those in mature systems.

In the region of the COS squall front, an easterly jet of 8-13  $\text{m s}^{-1}$  and a vertical wind shear of .003-.008  $\text{s}^{-1}$  dominate the 950-700 mb layer. A low-level easterly wind maximum occurs behind the squall front during the mature

stage but not in the regenerating stage. Low-level westerlies occur ahead of mature squall fronts while easterlies are found ahead of regenerating systems. In fair weather conditions, the low-level easterlies and vertical wind shear are notably weaker than they are on COS days.

The low-level meridional winds shift from south to north (Figure 21) with passage of a mature squall front. The opposite is true for GATE squall lines, where a north to south shift in meridional winds after passage of the squall front signifies an easterly wave (McGarry and Reed, 1978). With the exception of the regenerating case, COS sampled during ABLE-2B show wind shifts indicative of wave passage.

The horizontal winds in COS are consistent with the model results of Moncrieff and Miller (1976) for tropical squall lines. According to their results, steady convection in propagating tropical squall lines enhances vertical wind shear as westerly momentum increases at the surface and decreases at the mid levels. It is hypothesized that these same effects occur during the mature stage of long-lived Amazon COS.

Large decreases in  $\theta_e$  at the lower levels behind the mature squall front (Figure 22) indicate strong overturning of air between the lower and mid troposphere by convective-scale updrafts and downdrafts. Small low-level decreases in  $\theta_e$  behind the regenerating squall front suggests little

overturning of mid- and lower-tropospheric air occurs during the early stages of regeneration.

Higher pre-squall humidity at all levels indicates mature COS (Figure 43) feed upon moister air than weakening (25) and regenerating (Figure 79) systems. Lower humidity beneath the mature anvil signifies stronger convective drafts and overturning of air than in weakening and regenerating COS.

Enhanced low-level convergence promotes lifting ahead of mature squall fronts. Satellite images and radar scans validate the presence of convective cell development as conditionally unstable air is lifted ahead of the COS squall front. At all stages, low-level divergence and subsidence occur under the anvil while convergence and upward motion are found in the anvil.

Abnormally dry air at the mid and upper levels ahead of the mature squall front (Figure 25) coincides with meso-scale subsidence (Figure 24). Collocation of these features support the argument for interscalar feedback between the COS and its environment at scales of 300-400 km.

Tao and Soong (1986) note that cumulus cloud ensembles, by means of collective feedback, must modify the kinematic and thermodynamic structure of their nearby environment. In the case of long-lived, steady COS convection, compensating subsidence ahead of squall line may account for the pronounced upper level drying. Since COS propagate

faster than the environmental winds at all levels (Figures 20-21), storm-relative inflow at the mid and upper levels would cause convective towers to entrain mid-level dry air ahead of the line. Model experiments by Scala (1991, personal communication) have shown that entrainment of dry air into the leading edge of the squall line can have an important negative effect on convective cell dynamics.

### C. Heat transfer characteristics

Total heat budget results from Chapter 4 are now combined with GOES images to develop a model for vertical heat transport in each COS cloud component as a function of the life cycle. The model will be used to evaluate system-wide heat transport by each cloud component. "Component" refers to part of the COS having features that can be resolved by ABLE-2B sampling and analysis methods.

Table 2 gives total heat transport per unit area in each COS component (Columns 2-4) by integrating  $F$  over the pressure levels in Column 1. The integrations, based on five cases, are carried out for the entire tropospheric column (1000-100 mb), the upper troposphere (500-100 mb), and the layer of strongest Hadley export from the equatorial trough zone (300-100 mb) (Palmen and Vuorela, 1963).

Massive amounts of heat are transported upwards through the entire tropospheric column in all three COS components with the hot towers being the strongest in heat transport per unit area. There is a substantial decrease in

vertical heat transport when the integration is performed over 500-100 mb. This decrease shows the COS uses much of energy originating at the surface and converted in the column to maintain the hot towers and anvils. The heat reaching the 300-100 mb layer is only 1-3% of the column total but it takes on global importance when integrated over the area of an entire COS.

**Table 2. Vertical transport of total heat ( $W m^{-2}$ ) in COS cloud components based on vertical integration of  $F$  for five ABLE-2B cases.**

Pressure (mb)	Building Cu ( $W m^{-2}$ )	Hot Tower ( $W m^{-2}$ )	Anvil ( $W m^{-2}$ )
1000-100	261,500	497,500	337,367
500-100	17,500	127,500	79,333
300-100	2,000	12,500	3,333

\*Derived from the following ABLE-2B cases:

Building cumulus: 26 April 1987, 1500 UT

Hot Tower: 1 May 1987, 1200 UT

Anvil: 26 April 1987, 1800 UT

1 May 1987, 1800 UT

6 May 1987, 1800 UT

The general result of Table 2 for the COS anvil is unmistakable: it is dynamically active. Riehl and Simpson (1979) conclude that tropical thunderstorms provide the vertical heat transport needed to meet the heat balance requirements of the equatorial trough zone. In their previ-

ous study (Riehl and Malkus, 1958), they show a mid-level total heat minimum, existing throughout the tropics, prohibits vertical heat transport via a steady, large-scale upward circulation like that envisioned by Hadley (1735).

Riehl and Malkus (1958) invoke undilute transport in the hot tower conduits of tropical thunderstorms as the mechanism providing the needed transfer of heat to the upper levels of the atmosphere. Budget studies by Johnson (1984) and model experiments by Scala et al. (1990) show that undilute transport is not the only means of vertical heat transport in tropical squall lines.

Gamache and Houze (1982) and Cohen and Frank (1987) have shown the anvil shield is dynamically active. They indicate system-wide vertical transport is shared by cloud components consisting of more than hot towers. The results in Table 2 substantiate Johnson's (1984) recommendation to partition heating and moistening between the hot tower and anvil components.

Only 1-3% of the total column heat transport reaches the 300-100 mb layer for export from the Amazon Basin. It will now be shown that these relatively small amounts of upper level heating are significant compared to the tropical heat export requirements if they are integrated over the large area of an entire COS.

The results of Table 2 are extrapolated to the scale of an entire COS with the aid of the MB-enhanced satellite

images. First, the length and width of each convectively active cloud cluster appearing in black (segment 7) is measured on the MB images. Then the lengths and widths of all active clusters are summed over the length of the entire COS to obtain the total active cloud area for the system.

The widths of the building cumulus and hot tower components are derived from ground observations and the measured duration of convective rainfall at the PAM stations. The widths obtained by these procedures are consistent with the Gamache and Houze (1982) structural morphology for tropical squall lines.

The anvil width is obtained by subtracting the combined widths of the building cumulus and hot towers from the satellite measurement of the total active width of the system. Large differences in anvil width at different stages of system maturity result in large differences in total active cloud area during the COS life cycle. In the three COS evaluated, each had an active length of about 750 km while passing over the mesoscale network.

Tables 3-5 show the horizontally integrated system-wide heating in the 1 May, 26 April, and 6 May COS for the same layers appearing in Table 2. In these tables, it is assumed that vertical heat transport per unit area is uniform throughout each cloud component and does not vary as a function of the COS life cycle.

Table 3. Total heat transport in a mature COS over the central Amazon basin on 1 May 1987, 1300 UTC.

Pressure (mb)	Building Cu (W)	Convective (W)	Anvil (W)	Total (W)
1000-100	$4.9 \times 10^{15}$	$1.9 \times 10^{16}$	$6.3 \times 10^{16}$	$8.7 \times 10^{16}$
500-100	$3.3 \times 10^{14}$	$4.8 \times 10^{15}$	$1.5 \times 10^{16}$	$2.0 \times 10^{16}$
300-100	$3.8 \times 10^{13}$	$4.7 \times 10^{14}$	$6.2 \times 10^{14}$	$1.1 \times 10^{15}$
Width (km)	25	50	250	325
Length (km)	750	750	750	750

Table 4. Total heat transport in a weakening COS over the central Amazon basin on 26 April 1987, 1700 UTC.

Pressure (mb)	Building Cu (W)	Convective (W)	Anvil (W)	Total (W)
1000-100	$4.9 \times 10^{15}$	$1.9 \times 10^{16}$	$2.5 \times 10^{16}$	$4.9 \times 10^{16}$
500-100	$3.3 \times 10^{14}$	$4.8 \times 10^{15}$	$6.0 \times 10^{15}$	$1.1 \times 10^{16}$
300-100	$3.8 \times 10^{13}$	$4.7 \times 10^{14}$	$2.5 \times 10^{14}$	$7.6 \times 10^{14}$
Width (km)	25	50	100	175
Length (km)	750	750	750	750

Table 5. Total heat transport in a regenerating COS over the central Amazon basin on 6 May 1987, 1700 UTC.

Pressure (mb)	Building Cu (W)	Convective (W)	Anvil (W)	Total (W)
1000-100	$2.0 \times 10^{15}$	$9.3 \times 10^{15}$	$1.9 \times 10^{16}$	$3.0 \times 10^{16}$
500-100	$1.3 \times 10^{14}$	$2.4 \times 10^{15}$	$4.5 \times 10^{15}$	$7.0 \times 10^{15}$
300-100	$1.5 \times 10^{13}$	$2.3 \times 10^{14}$	$1.9 \times 10^{14}$	$4.4 \times 10^{14}$
Width (km)	10	25	75	110
Length (km)	750	750	750	750

The maximum poleward-directed mass flow in the upper-level leg of the Hadley circulation occurs near 200 mb (Palmén and Vuorela, 1963). Riehl and Simpson (1979) calculate an upper-level requirement of  $6.6 \times 10^{15}$  W for the lateral heat export from a  $10^\circ$ -wide belt adjoining the equatorial trough line. Table 6 compares the COS vertical heat transport in the 300-100 mb layer to the Riehl-Simpson export requirement. The upper-level transport in a mature COS equals 17.1% of the tropical requirement compared to 11.5% in the weakening COS and 6.6% in the regenerating COS.

**Table 6. The 300-100 mb COS heat transport in percent of the equatorial heat export requirement.\***

Stage	Building Cu (%)	Tower (%)	Anvil (%)	Total (%)
Mature	0.6	7.1	9.4	17.1
Weakening	0.6	7.1	3.8	11.5
Regenerating	0.2	3.5	2.9	6.6
Total	1.4	17.7	16.1	35.2

\*  $6.6 \times 10^{15}$  W (Riehl and Simpson, 1979)

Riehl and Malkus (1958) conclude that 1600-2400 hot towers, distributed among approximately 30 tropical synoptic disturbances meet the heat export requirements of the equatorial trough at any one time. My results indicate that 6-15 COS-scale disturbances can meet the instantaneous upper-level heat transport requirement for the tropics.

According to satellite analyses during ABLE-2B, up to three COS at different stages of their life cycle may exist at once over tropical South America. Occasionally, two mature COS are observed at the same time. During such periods, Table 6 shows that upper level heat transport due to Amazon COS may equal about one-third of the tropical heat export requirement.

The global importance of COS during ABLE-2B is substantiated by GOES full disk analyses of the frequency and total areal coverage of deep convection in three centers of deep convection: the Amazon basin (AB), the equatorial western Atlantic (EWA), and the equatorial eastern Pacific (EEP). Using full disk IR images from 12 April-9 May, 1987, the total area and frequency of deep convection is analyzed for each of the three areas. The results appear in Table 7.

**Table 7. The GOES analysis of equatorial trough convective activity from 12 April to 9 May 1987.**

Area	Hours of Dominance	% of Total
Amazon Basin	210	32.7
Equatorial E. Pacific	180	28.0
Equatorial W. Atlantic	24	3.7
Shared	228	35.6
Amazon Basin	(222)	(34.6)
Pacific	(224)	(34.9)
Atlantic	(72)	(11.2)
<b>Total</b>	<b>642</b>	<b>100.0</b>

The AB dominated 32.7% of the time compared to 28.0% for the EEP and 3.7% for the EWA. The AB+PCZ regions dominated equally 24.3% of the time compared to 10.3% for the AB+EEP+EWA at 10.3% and 1.0% for the EEP+EWA. Coastal Occurring Systems were the dominant mode of convection over the Amazon basin 65.4% of the time.

During ABLE-2B there were frequent shifts in maximum deep convection within the equatorial Western Hemisphere. Tyson (1986) relates tropical deep convection to the Walker Circulation (Walker, 1923, 1924) during the "high" and "low" phases (Bjerknes, 1969) of the Southern Oscillation. Each phase lasts about 18-24 months. In the high phase, a rising branch of the Walker Circulation produces maximum convection over the Amazon basin. At the same time, minimum convection occurs in descending branches over the eastern Pacific and central Atlantic. In the low phase, maximum convection occurs in ascending limbs over the eastern Pacific and eastern Atlantic while minimum convection occurs in a descending limb over the Amazon basin.

The ABLE-2B satellite analysis indicates high day-to-day variability in the location of convective centers of action in the Western Hemisphere tropics. It is likely that non-linear interscalar feedback associated with this shifting of maximum convection between centers of action affects the dynamics of the Southern Oscillation over time scales of at least several days.

## CHAPTER 6

### SUMMARY AND CONCLUSIONS

This study has shown that the Amazon Basin is a substantial, concentrated equatorial source of convective heating during periods of maximum COS activity. Globally important vertical heat transport occurs within the COS anvil shields, particularly during the system's mature stage. The existence of dynamically active COS anvils substantiates Houze's (1982) statement that deep convection in the equatorial tropics involves more than cumulus-scale hot towers.

System-wide instantaneous heat transport by a mature COS can equal nearly 20% of the upper level heat export requirement for the equatorial trough zone. About 55% of the vertical transport in the 300-100 layer in a mature COS can occur in extensive anvil layers.

The observed structure and energetics of COS are consistent with the general characteristics of tropical squall lines described by Houze (1982). The cloud structure consists of pre-squall building cumuli, convective hot towers, and stratiform anvils. The hot towers and anvils both play an important role in the vertical transport of total heat, with the role of the anvil depending directly upon its spatial extent relative to the whole system. Maximum heat transport in the system and in the anvil occurs during the

mature stage of the COS life cycle when all cloud components achieve their maximum spatial extent.

It is hypothesized that vertical heat transport in the equatorial trough zone is more regionally concentrated and requires fewer active hot towers than suggested by Riehl and Malkus (1958). It has been shown that basin-wide vertical heat transport during maximum COS activity, when up to three systems may be active at once, can equal about one-third of the equatorial heat export requirement. The combined upper-level heating of six tropical systems having the transport characteristics of a mature COS would equal the equatorial heat export requirement.

From the time they form in the sea-breeze zone along the northeastern coast of Brazil, COS undergo a sequence of dramatic cloud changes that have been used to define a life cycle consisting of six possible stages. At maturity, they often reach lengths of 3500 km, of which 500-1000 km is active deep convection, and propagate at speeds of 50-70 km h<sup>-1</sup>. As in GATE squall lines (Barnes, 1980), new cells continuously form ahead of the COS squall front, intensify, and establish a new line of convective towers at the leading edge of the system. As older convective cells weaken, they are displaced to the rear and blend into the trailing anvil region (Gamache and Houze, 1982).

At all stages, COS propagate faster than the environmental winds at any level. This characteristic, combined

with a low-level easterly jet, imparts downshear (eastward) tilt to the convective updrafts and cloud components. A tilted structure prevents heavy convective rainfall from interfering with low-level inflow into the convective cells, thereby enabling the system to tap existing reservoirs of environmental moisture in order to maintain steady, propagating convection (Cotton and Anthes, 1989). Model experiments by Scala (1991, personal communication) show all phases of the COS life cycle are represented in runs initialized with the thermodynamic and kinematic structure present during COS periods.

Cold, dry air deposited at the lower levels by convective downdrafts creates a more stable environment behind the squall front. The PAM observations show the time needed for surface energy fluxes to replenish low-level heat and moisture is directly related to the COS life cycle, taking substantially longer behind a mature squall front in any other stage.

The time scale of suppressed conditions in the triangle varies from 1-12 h in the wake of a weakening or regenerating COS to 12-24 h after the passage of a mature COS. If the average system speed is  $50 \text{ km h}^{-1}$ , the scale of the area affected by suppressed conditions is 50-600 km behind the weakening and regenerating systems and 600-1200 km behind mature systems. The area behind the squall front cannot support deep convection again until low-level heating

and moistening restore conditional instability in the lower and middle troposphere. Therefore, it is hypothesized that the effects of antecedent storm downdrafts, which vary as a function of system maturity, must play a role in determining the timing and location of future convection. This negative feedback, combined with the positive diurnal forcing of the sea breeze on the coast of northeastern South America, may play a strong role in governing the periodic generation of the COS.

The effects of COS upon the horizontal wind field depend upon the system's maturity. Following periods of long-lived steady convection at or near the mature stage, low-level westerlies appear ahead of the squall front. This feature has two effects upon the disturbance kinematics: (1) it enhances low-level convergence and upward vertical motion ahead of the squall front, and (2) it enhances the vertical wind shear.

During periods of COS activity, the vertical motion field consistently shows enhanced mid- and upper-level subsidence ahead of the squall front. Convergence appears in the lower levels about 1-6 hours before the hot towers enter the triangle. Upward motion increases with height and time within the anvil cloud while subsidence occurs in the sub-cloud region under the anvil. Collocation of dry mid- and upper-level air with enhanced subsidence ahead of the system

represents a form of interscalar feedback involving COS heat and mass transport and the environment at larger scales.

As in squall-line disturbances elsewhere in the tropics (Johnson, 1984; Houze, 1989), COS exhibit markedly different profiles of heating and moistening in each cloud component. Some important features of these distributions are: (1) in the convective component, warming and drying of the entire troposphere with strong peaks at the mid levels, and (2) in the anvil component, warming and drying in the anvil cloud layer and cooling and moistening in the subcloud region.

The GOES satellite analysis of equatorial trough activity during ABLE-2B shows that COS rank among the largest synoptic-scale cloud features in the tropics. During the eight-month Amazon wet season, they occur at an average frequency of 10 per month, or at about twice the frequency of synoptic disturbances in the GATE region. Based on the larger scale and greater frequency of COS, it is hypothesized that the Amazon Basin during the wet season has more than twice the impact of the GATE region in terms of total heat transport.

This study confirms and extends the convective hot tower hypothesis of Riehl and Malkus (1958). The results show that deep cumulus towers are the primary agents responsible for energy conversion and vertical transport in the equatorial trough region. According to the ABLE-2B budget

analyses, undilute transport in the cumulus hot towers of mature COS account for no more than half of the total system transport. The remaining transport takes place in extensive, dynamically active stratiform anvils. The overall view that emerges is consistent with the statement by Houze (1982) that: "...the effect of these stratiform regions is to lead to more heating of the environment in the upper troposphere and less in the lower troposphere than would be the case if the precipitation were all convective in nature."

Future research should use computer cloud models to study the different roles of the COS hot tower and anvil components in system-wide heat transport. The experiments should examine how variations in the environmental wind and moisture structure affect the COS life cycle. This work is presently under way at the NASA Goddard Space Flight Center (personal communication with Scala, 1990).

## REFERENCES

- Air Weather Service Manual 105-24, 1969: Use of the Skew T, log P Diagram in Analysis and Forecasting. Dept. of the Air Force, Headquarters Air Weather Service, Scott AFB, IL.
- Atwater, M.A., 1974: *The Radiation Model*, Sect. 4, Vol. I, CEM Report No. 5131-4099, pp. 67-82. A description of a general three-dimensional model of a coupled air-water and/or air-land boundary. Center for the Environment and Man, Hartford, CT.
- Atwater, M.A. and P. Brown, Jr., 1974: Numerical calculations of the latitudinal variations of solar radiation for an atmosphere of varying opacity. *J. Appl. Meteorol.*, **13**, 289-297.
- Barnes, G.M., 1980: Subcloud layer energetics of precipitating convection. Ph.D dissertation, University of Virginia, 212 pp.
- Barnes, G.M. and M. Garstang, 1982: Subcloud layer energetics of precipitating convection. *Mon. Wea. Rev.*, **110**, 102-117.
- Betts, A.K., 1986: A new convective adjustment scheme. Part I: Observational and theoretical basis. *Quart. J. R. Met. Soc.*, **112**, 677-691.

- Brümmer, B., 1978: Mass and energy budgets of a 1 km high atmospheric box over the GATE C-scale triangle during undisturbed and disturbed weather conditions. *J. Atmos. Sci.*, **35**, 997-1011.
- Byers, H.R. and R.R. Braham, Jr., 1949: *The Thunderstorm*. U.S. Government Printing Office, Washington, D.C., 287 pp.
- Carlson, D.C., 1981: Weather Satellite Interpretation - Introduction to Satellite Imagery. NOAA Technical Memorandum NWS SR-103, 47 pp.
- Chen, Y.-L., 1987: Thermodynamic effects of mesoscale convective systems on the environment over the eastern Atlantic. *J. Meteor. Soc. Japan*, **65**, 391-400.
- Chong, M., P. Amayenc, G. Scialom, and J. Testud, 1987: A tropical squall line observed during the COPT81 experiment in West Africa. Part I: Kinematic structure inferred from dual-Doppler radar data. *Mon. Wea. Rev.*, **115**, 670-694.
- Chong, M. and D. Hauser, 1990: A tropical squall line observed during the COPT81 experiment in West Africa Part III: Heat and moisture budgets. *Mon. Wea. Rev.*, **118**, 1696-1706.
- Cohen, C. and W.M. Frank, 1987: Simulation of tropical convective systems. Part II: Simulations of moving cloud lines. *J. Atmos. Sci.*, **44**, 3800-3820.

- Cotton, W.R. and R.A. Anthes, 1989: *Storm and Cloud Dynamics*. Academic Press, 883 pp.
- Cox, S.K. and K.T. Griffith, 1979: Estimates of radiative divergence during Phase III of the GARP Atlantic Tropical Experiment. Part I: Methodology. *J. Atmos. Sci.*, **36**, 576-585.
- Davis, J.C., 1986: *Statistics and Data Analysis in Geology*. John Wiley and Sons, New York, 646 pp.
- Duvedal, T., 1962: Upper-level wind computation with due regard to both the refraction of electromagnetic rays and the curvature of the earth. *Geophysica*, **8**, 115-124.
- Esbensen, S., 1975: An analysis of subcloud layer heat and moisture budgets in the western Atlantic trades. *J. Atmos. Sci.*, **32**, 1921-1933.
- Frank, W.M., 1978: The life cycle of GATE convective systems. *J. Atmos. Sci.*, **35**, 1256-1264.
- Gallus, W.A., Jr. and R.H. Johnson, 1991: Heat and moisture budgets of an intense mid latitude squall line. *J. Atmos. Sci.*, **48**, 122-146.
- Gamache, J.F. and R.A. Houze, Jr., 1982: Mesoscale air motions associated with a tropical squall line. *J. Atmos. Sci.*, **110**, 118-135.

- Garstang, M., S. Ulanski, S. Greco, J. Scala, R. Swap, D. Fitzjarrald, D. Martin, E. Browell, M. Shipham, V. Connors, R. Harris, R. Talbott, 1990: The Amazon Boundary-Layer Experiment (ABLE-2B): A meteorological perspective. *Bull. Amer. Meteor. Soc.*, **71**, 19-32.
- Greco, S., R. Swap, M. Garstang, S. Ulanski, M. Shipham, R.C. Harris, R. Talbott, M.O. Andreae, and P. Artaxo, 1990: Rainfall and surface kinematic conditions over central Amazonia during ABLE-2B. *J. Geophys. Res.*, **93**, No. D10, 17001-17014.
- Hadley, G., 1735: Concerning the cause of the general trade winds. *Phil. Trans. Roy. Soc. London*, **39**, 58; reprinted in *Smithsonian Inst. Misc. Collections*, **51**, 5-7 (1910).
- Haltiner, G.J. and F.L. Martin, 1957: *Dynamical and Physical Meteorology*. McGraw-Hill, 470 pp.
- Harris, R.C., M. Garstang, S.C. Wofsy, S.M. Beck, R.J. Bendura, J.R.B. Coelho, J.W. Drewry, J.M. Hoell, P.A. Matson, R.J. McNeal, L.C.B. Molion, R.L. Navarro, V. Rabine, and R.L. Snell, 1990: The Amazon Boundary Layer Experiment: Wet season 1987. *J. Geophys. Res.*, **93**, No. D10, 16721-16736.

- Houze, R.A., Jr., 1977: Structure and dynamics of a tropical squall-line system. *Mon. Wea. Rev.*, **105**, 1540-1567.
- Houze, R.A., Jr., 1982: Cloud clusters and large-scale vertical motions in the tropics. *J. Meteorol. Soc. Japan*, **60**, 396-410.
- Houze, R.A., Jr., 1989: Observed structure of mesoscale convective systems and implications for large-scale heating. *Quart. J. R. Met. Soc.*, **115**, 425-461.
- Johnson, R.H., 1984: Partitioning tropical heat and moisture budgets into cumulus and mesoscale components: Implications for cumulus parameterization. *Mon. Wea. Rev.*, **112**, 1590-1601.
- Johnson, R.H. and G.S. Young, 1983: Heat and moisture budgets of tropical of tropical mesoscale anvil clouds. *J. Atmos. Sci.*, **40**, 2138-2147.
- Leary, C.A. and R.A. Houze, Jr., 1980: The contribution of mesoscale motions to the mass and heat fluxes of an intense tropical convective system. *J. Atmos. Sci.*, **37**, 784-796.
- Kondratyev, J., 1969: *Radiation in the Atmosphere*. Academic Press, New York, pp.
- Miller, M.J. and A.K. Betts, 1977: Travelling convective storms over Venezuela. *Mon. Wea. Rev.*, **105**, 833-848.

- McCumber, M.C., 1980: A numerical simulation of the influence of heat and moisture fluxes upon mesoscale circulations. Ph.D. dissertation, University of Virginia, Charlottesville.
- McDonald, J., 1960: Direct absorption of solar radiation by atmospheric water vapor. *J. Meteorol.*, **17**, 319-328.
- McGarry, M.M. and R.J. Reed, 1978: Diurnal variations in convective activity and precipitation during Phase II and III of GATE. *Mon. Wea. Rev.*, **106**, 101-113.
- Molion, L.C.B., 1987: On the dynamic climatology of the Amazon basin and associated rain-producing mechanisms, in *The Geophysiology of Amazonia: Vegetation and Climate Interactions*, edited by R. Dickerson, pp. 391-407, John Wiley, New York.
- Moncrieff, M.W. and M.J. Miller, 1976: The dynamics and simulation of tropical cumulonimbus and squall lines. *Quart. J. R. Met. Soc.*, **102**, 373-394.
- Newell, R.E., J.W. Kidson, D.G. Vincent, and G.J. Boer, 1972: *The General Circulation of the Tropical Atmosphere and Interactions with Extratropical Latitudes*, vols. 1 and 2, MIT Press, Cambridge, MA.
- O'Brien, J.J., 1970: Alternative solutions to the classical vertical velocity problem. *J. Appl. Meteor.*, **9**, 197-203.

- Paegle, J., 1987: Interaction between convective and large-scale motions over Amazonia, in *The Geophysiology of Amazonia: Vegetation and Climate Interactions*, edited by R. Dickerson, pp. 347-387, John Wiley, New York.
- Palmen, E. and L.A. Vuorela, 1963: On the mean meridional circulations in the Northern Hemisphere during the winter season. *Quart. J. R. Met. Soc.*, **89**, 131-138.
- Pielke, R.A., 1984: *Mesoscale Meteorological Modeling*. Academic Press, New York, 612 pp.
- Reed, R.J. and E.E. Recker, 1971: Structure and properties of synoptic-scale wave disturbances in the equatorial western Pacific. *J. Atmos. Sci.*, **28**, 1117-1133.
- Riehl, H. and J.S. Malkus, 1958: On the heat balance in the equatorial trough zone. *Geophysica*, **6**, 503-538.
- Riehl, H. and J.M. Simpson, 1979: The heat balance in the equatorial trough zone, revisited. *Contr. Atmos. Phys.*, **52**, 287-305.
- Scala, J.R., 1991: Personal communication.
- Scala, J.R., M. Garstang, W. Tao, K.E. Pickering, A.M. Thompson, J. Simpson, V.W.J.H. Kirchhoff, E.V. Browell, G.W. Sachse, A.L. Torres, G.L. Gregory, R.A. Rasmussen, and M.A.K. Khalil, 1990: Cloud draft structure and trace gas transport. *J. Geophys. Res.*, **93**, No. D10, 16721-16736.

- Shuttleworth, W.J., J. Gash, C.R. Lloyd, C.J. Moore, J. Roberts, A. Filho, G. Fisch, V. Filho, M. Ribeiro, L. Molion, L. Abreu Sa, C. Nobre, O. Cabral, S. Patel, J. Moraes, 1984: Eddy correlation measurements of energy partition for Amazonian forest. *Quart. J. R. Met. Soc.*, **110**, 1143-1162.
- Staley, D.O. and G.M. Jurica, 1970: Flux emissivity tables for water vapor, carbon dioxide, and ozone. *J. Appl. Meteorol.*, **9**, 365-372.
- Stephens, G.L., 1978: Radiation profiles in extended water clouds. II. Parameterization schemes. *J. Atmos. Sci.*, **35**, 2123-2132.
- Tao, W.-K. and J. Simpson, 1984: Cloud interactions and merging: Numerical simulations. *J. Atmos. Sci.*, **41**, 2901-2917.
- Tao, W.-K. and S.-T. Soong, 1986: A study of the response of deep tropical clouds to mesoscale processes: Three-dimensional numerical experiments. *J. Atmos. Sci.*, **43**, 2653-2676.
- Thompson, R.M., Jr., S.W. Payne, E.E. Recker, and R.J. Reed, 1979: Structure and properties of synoptic-scale wave disturbances in the intertropical convergence zone of the eastern Atlantic. *J. Atmos. Sci.*, **36**, 53-72.

- Tyson, P.D., 1986: *Climatic Change and Variability in Southern Africa*. Oxford University Press, Cape Town, 220 pp.
- Webster, P.J. and G.L. Stephens, 1980: Tropical upper-tropospheric extended clouds: Inferences from Winter MONEX. *J. Atmos. Sci.*, 37, 1521-1541.
- Yanai, M., S. Esbensen, and J.H. Chu, 1973: Determination of bulk properties of tropical cloud clusters from large-scale heat and moisture budgets. *J. Atmos. Sci.*, 30, 611-627.
- Zipser, E.J., 1977: Mesoscale and convective-scale downdrafts as distinct components of squall-line structure. *Mon. Wea. Rev.*, 105, 1568-1593.